EXPERIMENTS AND MATHEMATICAL MODELS FOR ELECTROCHEMICAL SYSTEMS

By

CHEN YOU

A DISSERTATION PRESENTED TO THE GRADUATE SCHOOL
OF THE UNIVERSITY OF FLORIDA IN PARTIAL FULFILLMENT
OF THE REQUIREMENTS FOR THE DEGREE OF
DOCTOR OF PHILOSOPHY

UNIVERSITY OF FLORIDA

2022

To my parents, and to all the people I love

ACKNOWLEDGEMENTS

I would like to express my appreciation to Professor Mark Orazem for his invaluable guidance, support, and expertise during my doctoral study. I could not have undertaken this journey without his encouragement and inspiration. Not only I was taught how to conduct professional research, but also I have been deeply influenced by his valuable life experiences. I feel myself being valued and cared so much in the research group. Many thanks to my committee members, Professor Peng Jiang, Professor Charles Hages, and Professor Jiangeng Xue, for their guidance. I would like to express my thanks to program manager of this project, Scott Briggs for his help and involvement with the research. I would also like to thank Prof. Burak Ulgut and Prof. Vincent Vivier for their valuable insights and opportunities to work together.

I'm grateful to my former lab mates for their mentoring and help. Special thanks to Arthur Dizon for getting me started in modeling using COMSOL Multiphysics software. My thanks should also go to Morgan Hazelbaker for teaching me to use FORTRAN. I would like to extend my sincere thanks to Ming Gao for being a study and research companion when I began to learn electrochemical impedance spectroscopy and electrochemistry. I am thankful to my undergraduate mentees, Fiki Owhoso and Letícia Moreira for assisting me with my research. I also had the great pleasure of working with my current group members, Sam Jacobs, Cythia Ezeh, Jie Min Goh and Yunhan Chuai.

I would like to express my deepest gratitude to Jennifer Patterson for caring for me as a big family member. I would be remiss in not mentioning all my friends. Special thanks to Yifan Yu, Ruwen Tan, Bo Yu, Yixi Shen and Shuyu Wang for their moral support and company.

Lastly, this endeavor would not have been possible without heartfelt love and tremendous support received from my parents, Xinghua You and Li Wang. I also deeply acknowledge my family members for their support and encouragement.

The work was supported by the Nuclear Waste Management Organization, Canada, under project 2000904, and by Nanophotonica and a matching grant from the University of Florida Industry Partnership (UFLIPS) under Grant# OR-DRPD-UFLIPS-G-2018.

TABLE OF CONTENTS

LIST OF TABLES

LIST OF FIGURES

Figures page

Roman

A	constants to account for the influence of temperature diffusion coefficient given in equation (3-80), A = 2.414 $\times 10^{-5}$ Pa s
A_i	analytic constants to account for the influence of temperature on homogeneous reaction rate constant
A	coefficient in velocity expansion, $A = 0.934$
A_i	area of the film i, cm^2
A_{dp}	surface area of the droplet, cm^2
a	coefficient in velocity expansion, $a = 0.510232618867$
B	constants to account for the influence of temperature diffusion coefficient given in equation (3-80), B = 247.8 K
B	coefficient in velocity expansion, $B = 1.208$
b	lumped kinetic parameters, $b = \alpha_a n\mathrm{F}/\mathrm{R}T$ or $b = \alpha_c n\mathrm{F}/\mathrm{R}T$, V^{-1}
b	coefficient in velocity expansion, $b = -0.615922014399$
C	constants to account for the influence of temperature diffusion coefficient given in equation (3-80), C = 140.0 K
C	coefficient in velocity expansion, C = 0.88447
C	capacitance, F/cm^2
C_{dl}	double-layer capacitance, F/cm^2
C_0	interfacial capacitance, F/cm^2
C_{xy}	a real number between 0 and 1 that measures the correlation between the input signal $x(t)$ and the output signal $y(t)$, see equation (6-6)
c_i	volumetric concentration of species i, mol/cm^3
$c_{m,d}$	concentration of one molecule in the droplet, mol/cm^3
D_i	diffusion coefficient of species i, cm^2/s

E	activation energy
F	Faraday's constant, 96,487 C/equiv
$F(\zeta)$	dimensionless radial velocity, see equation (7-12)
F_0	dimensionless radial velocity expansion near the electrode, see equation (7-14)
F_∞	dimensionless radial velocity expansion far from the electrode, see equation (7-16)
f	velocity interpolation formula, see equation (7-19)
f_c	characteristic frequency associated with the ohmic impedance, Hz
f_i	reaction rate constant factors influenced by film i
f_{R_t}	characteristic frequency associated with the faradic reaction, Hz
g	dimensionless parameter used for the power-law model, see equation (2-20)
$H(\zeta)$	dimensionless axial velocity, see equation (7-11)
H_i	Henry's law constant of species i, mol/cm^3 atm
H_0	dimensionless axial velocity expansion near the electrode, see equation (7-13)
H_∞	dimensionless axial velocity expansion far from the electrode, see equation (7-15)
i	current density, A/cm^2
$i_{F,i}$	faradaic current density, A/cm^2
i_{total}	total current, A
J	dimensionless exchange current density which may be written as $J = 4R_{e,HF}/\pi R_t$
j	the imaginary number, $j = \sqrt{-1}$

k	reaction rate constant
k_{B}	Boltzman constant, k_{B}= 1.380649 $\times 10^{-23}$ J/K
K	dimensionless frequency given by equation (7-5)
K_{sp}	solubility product constant
K_{eq}	equilibrium rate constant
$L_{\mathrm{corr,local}}$	local corrosion depth
$M_{\mathrm{W,i}}$	molecular weight for species i, g/mol
N_{A}	Avogadro's number, $N_{\mathrm{A}} = 6.02214 \times 10^{23}$ mol^{-1}
$\mathbf{N_i}$	flux of species i, mol/cm s
$N_{\mathrm{d}} - N_{\mathrm{a}}$	doping level, mol/cm^3
n	the number of electrons transferred in electrochemical reactions
n_{i}	intrinsic concentration, mol/cm^3
$\mathbf{n}$	unit vector normal to the surface
OA	diameter of the droplet, OA = 1 mm
OB	height of the droplet, OA = 0.4 mm
P_{xx}	power spectra of $x(t)$, see equation (6-6)
P_{xy}	power spectra of $y(t)$, see equation (6-6)
P_{yy}	average cross-power spectrum of $x(t)$ and $y(t)$
p	pressure in the repository air, atm
Q	CPE parameter that is equal to capacitance when $\alpha = 1$, F/cm^{2}s$^{1-\alpha}$
Q_{H}	CPE parameter for high-frequency loop given in equation (2-19), F/cm^{2}s$^{1-\alpha}$
Q_{L}	CPE parameter for low-frequency loop given in equation (5-1), F/cm^{2}s$^{1-\alpha}$

q	surface charge density, C/cm^2
R	universal gas constant, 8.3143 J/mol K
R	radius corresponding to the location of the counterelectrode, see Figure 7-1
R_{e}	ohmic resistance, Ωcm^2
$R_{\mathrm{e,HF}}$	high-frequency ohmic resistance, Ωcm^2
$R_{\mathrm{e,LF}}$	low-frequency ohmic resistance, Ωcm^2
R_{H}	resistance associated with the high-frequency loop given in equation (5-1), Ωcm^2
R_{i}	homogeneous reaction rate for species i, mol/cm^{3}s
R_{L}	resistance associated with the high-frequency loop given in equation (5-1), Ωcm^2
R_{t}	charge-transfer resistance, Ωcm^2
$R_{\mathrm{corr,local}}$	local corrosion rate
r	radial coordinate
r_0	radius of the disk electrode, cm
Sc	Schmidt number for species i, Sc $= \nu/D_{\mathrm{i}}$
s_{i}	stoichiometric coefficient for species i
T	temperature, K
T_0	room temperature, $T_0 = 298.15$ K
T'	period of an integer number of cycles
t	elapsed time, s
$t_{0.1\%}$	elapsed time associated with 0.1% O_2 remaining in the repository, s
V_{d}	volume of the droplet, cm^3

v_r radial velocity, cm/s

v_y axial velocity, cm/s

y axial coordinate

y_i gaseous species fraction

Z impedance, Ωcm^2

Z_e ohmic impedance, Ωcm^2

$Z_{(0)}$ zeroth term in the expansion for dimensionless diffusion impedance, see equation (7-49)

$Z_{(0)}$ interfacial impedance, Ωcm^2

$Z_{(1)}$ first term in the expansion for dimensionless diffusion impedance, see equation (7-49)

$Z_{(2)}$ second term in the expansion for dimensionless diffusion impedance, see equation (7-49)

z_i the number of charge for species i

Greek

α exponent for a constant-phase element

α_a apparent anodic transfer coefficient

α_c apparent cathodic transfer coefficient

α_H exponent for a constant-phase element in high-frequency loop, see equation (2-19)

α_L exponent for a constant-phase element in low-frequency loop, see equation (5-1)

ζ_0 coefficient in velocity interpolation formula given in equation (7-19), $\zeta_0 = 1$

β exponent used in the Havriliak–Negami equation, see equation (2-36)

γ	surface coverage
Γ_{DB}	boundary of the droplet, see Figure 3-1
Γ_{I}	insulating surface, see Figures 3-1 and 7-1
Γ_{REF}	Farthest location from the working electrode to define the reference potential, see Figure 3-1
Γ_{WE}	surface associated with the working electrode, see Figures 3-1 and 7-1
$\Delta_r H^{\theta}$	change of enthalpy for species i, kJ/mol
δ	film thickness, cm
$\delta_{m,i}$	monolayer thickness of the film i, cm
ε	dielectric constant
ε_{CuCl}	porosity of CuCl film
ε_0	permittivity of vacuum, $\varepsilon_0 = 8.8542 \times 10^{-14}$ F/cm
ζ	dimensionless axial position, $\zeta = y\sqrt{\Omega/\nu}$
ζ_0	coefficient in velocity interpolation formula given in equation (7-19), $\zeta_0 = 1$
η	influence factor of CuCl film on potentials, $\eta = \Phi_0/\Phi(\mathrm{CuCl})$
θ_i	dimensionless concentration phasor for species i, $\theta_i = \widetilde{c_i}/\widetilde{c_i}(0)$
κ	conductivity, S cm^{-1}
λ	influence factor of CuCl film on surface oxygen concentration, $\lambda = c_{O_2}(0)/c_{O_2}(\mathrm{CuCl})$
μ_i	mobility of species i, mol/cm^2 s J
μ	mean, Ωcm^2
ν	kinematic viscosity, cm^{2}s^{-1}
ν	degree of freedom

ξ	coefficient in velocity interpolation formula given in equation (7-19), $\alpha = 25$
ρ	resistivity, Ωcm
ρ	mass density, g/cm^3
ρ	charge density, C/cm^3
ρ_0	resistivity when y = 0 given in equation (2-18), Ωcm
ρ_δ	resistivity, the value of the resistivity when y = δ given in equation (2-18), Ωcm
ρ'	resistivity of CuCl film, Ωcm
σ	standard deviation of impedance, Ωcm^2
τ	time constant
Φ	potential
$\Phi^{\theta}_{\text{ref}}$	potential
ω	angular frequency, s^{-1}
Ω	disk rotation speed, s^{-1}
χ^2/ν	weighted regression statistic, $\chi^2/\nu = 1 + \sqrt{2/\nu}$ for a good fit
ψ	parameter to distinguish the limiting current behavior for oxygen reduction, $\psi = D_{H_2O_2}k_2/D_{O_2}k_3$

Subscript

a	anodic
b	backward
c	cathodic
eff	effective
f	forward

j	imaginary
m	electrode
n	electron
p	hole
r	real
ref	reference
0	location just outside the diffuse double layer
3	ferricyanide, $Fe(CN)_6^{3-}$
4	ferrocyanide, $Fe(CN)_6^{4-}$

General

$\mathrm{Im}\{X\}$	imaginary part of X
$\mathrm{Re}\{X\}$	real part of X
$\overline{X}$	steady-state of variable X
$\widetilde{X}$	phasor of variable X
$< X >$	average value for variable X

Abstract of Dissertation Presented to the Graduate School
of the University of Florida in Partial Fulfillment of the
Requirements for the Degree of Doctor of Philosophy

EXPERIMENTS AND MATHEMATICAL MODELS FOR ELECTROCHEMICAL SYSTEMS

By

Chen You

August 2022

Chair: Mark E. Orazem
Major: Chemical Engineering

Copper coatings are used as the protecting material for the Canadian used nuclear fuel containers. A 2-D axisymmetric time-dependent model for the localized corrosion of copper under an Evans droplet was developed using the finite-element method. Some unique features of the model are that it includes 6 heterogeneous and 15 homogeneous reactions, it provides implicit calculation of nm-scale films, and it accounts for the influence of the film on surface concentrations, potentials, and reaction rate constants. The influence of temperature is included on model parameters. The model shows time-dependent radial distributions for current density, surface coverage of films, and localized corrosion rates and depths. The model provides distributions of pH, potential, and concentrations of dissolved gaseous and ionic species through the entire droplet. Preliminary results show that the corrosion of copper is almost uniform on the electrode surface. Temperature and oxygen concentration are shown to have a strong contribution to copper corrosion over a simulation period of 10 years.

Electrochemical impedance spectroscopy (EIS) is used to study red and green QLED devices. The high-frequency loop is interpreted in terms of the thickness, dielectric constant, and resistivity distribution of the hole-injection layer. The work presents a first ever analysis that employs the device capacitance obtained from a measurement model analysis, the film thickness measured by scanning electron microscopy, and an interpretation of the impedance based on a power-law model. Impedance measurements performed on hole-transport–only devices yield

results that are consistent with the interpretation of the high-frequency capacitive loop in terms of the properties of the hole-injection layer.

Additional work involves fundamental studies of EIS. In collaboration with Prof. Burak Ulgut and his students, impedance spectra obtained by multi-sine potential perturbation are shown to automatically satisfy with the Kramers–Kronig relations, even for systems that are nonlinear and nonstationary. In collaboration with Dr. Vincent Vivier, a step-by-step analysis is demonstrated for frequency-dependent complex ohmic impedance observed by experiments. Another work describes the use of measurement model to interpret the impedance data complicated by the ohmic impedance.

CHAPTER 1
INTRODUCTION

Several works presented in this dissertation emphasize different electrochemical systems. Physics and chemistry in real applications were investigated and explained from fundamental prospect of view using both experimental and simulation approaches.

The objective for the first work was to develop a mathematical model for localized corrosion of copper under a droplet. Background for Canadian deep geological repository and literature review for past copper corrosion models on used nuclear fuel container are introduced in Section 2.1 of Chapter 2. Part of evaluating the long-term performance and safety of the repository system is understanding the behavior of the copper-coated container with respect to localized corrosion. The Canadian Deep Geological Repository (DGR) system does not lend itself to passivation of the copper surface. However, the system will transition from dry to wet conditions, which may produce different localized environments, and as a result, localized corrosion damage. There is still a need to develop a mathematic model for localized corrosion of copper.

The mathematical model was developed using the finite-element method (COMSOL Multiphysics) and the development of the mathematical model for localized copper corrosion is presented in Chapter 3. The model includes coupled, nonlinear, diffusion equations for ionic species, which include the contribution of migration, local electroneutrality, and homogeneous reactions. The anodic and cathodic regions are not predefined but, instead, are determined by values of local concentration and potential from the simulation results. The growth of nm-scale films was calculated implicitly without using finite-element meshing and surface coverage was expressed in terms of the thickness in units of monolayers. The model also accounted for the effect of porous CuCl film thickness on the surface oxygen concentration and potential applied on electrochemical reactions. The influence of temperature was included on model parameters. A total of 28 dependent spatial-temporal variables including species' concentrations, potentials and local corrosion rate were solved in this model.

Results for 10-year time dependent simulations for localized corrosion of copper are discussed in Chapter 4. Two extreme conditions were chosen such that droplet boundary has a faster or slower rate of oxygen decay for an initially air-saturated droplet. The model shows a

time-dependent radial distribution of anodic and cathodic current density, surface coverage of CuCl film and Cu_2O film, and localized corrosion rates and depths. It also shows a distribution of pH, potential, and concentrations of dissolved gaseous and ionic species through the entire droplet. Temperature and oxygen concentration is shown to have a strong contribution to the simulation results.

The second work used electrochemical impedance spectroscopy to study quantum-dot light-emitting diodes (QLED) devices. Quantum-dot light-emitting diodes (QLED) are used in the new generation of electronic displays. A QLED based display can offer superior performance, including brightness, color purity, color gamut, and efficiency, at a lower cost as compared to existing technology. Work is needed, however, to improve the interpretation of the EIS response of QLED devices. The objective of the second main project is to interpret the high-frequency impedance response on red and green QLED devices in terms of the physical properties of the device. In section 2.2 of Chapter 2, background for quantum dot light-emitting devices and basic knowledge for electrochemical impedance spectroscopy are introduced.

Analysis of high-frequency loops in terms of material properties from impedance measurements on QLED devices is discussed in Chapter 5. The high-frequency loop is interpreted in terms of the thickness, dielectric constant, and resistivity distribution of the hole-injection layer. The analysis employed the device capacitance obtained from a measurement model analysis, the film thickness measured by scanning electron microscopy, and an interpretation of the impedance based on a power-law model. Impedance measurements performed on hole-transport only devices yielded results that were consistent with the interpretation of the high-frequency capacitive loop in terms of the properties of the hole-injection layer.

Application of the Kramers–Kronig relations to multi-sine electrochemical impedance measurements is discussed in the third work. Impedance spectra obtained by fast Fourier transformation of the response to a multi-sine potential perturbation were shown to be consistent with the Kramers–Kronig relations, even for systems that are nonlinear and nonstationary. The present work demonstrates that application of the Kramers–Kronig relations to the results of

multi-sine measurements cannot be used to determine whether the experimental system satisfies the conditions of linearity, causality and stability. In Section 2.3 of Chapter 2, multi-sine electrochemical impedance measurements and Kramers-Kronig relations are introduced. In Chapter 6, these results, observed for measurements on a $Li/SOCl_2$ battery, were confirmed by numerical simulations. Consistency with the Kramers–Kronig relations was confirmed by use of the measurement model developed by Agrawal et al. [1, 2, 3] and by a linear measurement model approach developed by Boukamp [4] and implemented by Gamry. This work demonstrates that application of the Kramers–Kronig relations to the results of multi-sine measurements cannot be used to determine whether the experimental system satisfies the conditions of linearity, causality and stability.

Ohmic impedance response on the disk electrode is investigated for the fourth work. Background for ohmic impedance and applications of measurement model are described in Section 2.4 of Chapter 2. Experimental observation of ohmic impedance is discussed in Chapter 7. The ohmic impedance was obtained by Levenberg-Marquardt regression of a process model that used the Havriliak-Negami equation to account for the ohmic impedance. Experimental results obtained by Vincent Vivier (CNRS) for the ferri/ferrocyanide redox species on a gold disk used as a model system were interpreted using a physical description expressed in terms of an ohmic impedance and an expression that accounted for the influence of a local constant-phase element on the faradaic reaction and the convective diffusion impedance. Regressions were weighted by the experimentally determined error structure of the data, and the resulting parameters characteristic of the ohmic impedance were in excellent agreement with numerical simulations.

In Chapter 8, the method of using measurement model to interpret the impedance data complicated by ohmic impedance is discussed. The measurement model was shown to give the correct value of the capacitance for the system with a capacitance, but a wrong value for the system having a local constant-phase-element (CPE) behavior. The ohmic impedance could also be fitted by the process model including the Cole-Davidson or Havriliak-Negami equation. The

value of the effective capacitance for the system with a CPE could be calculated by the Brug formula using regressed parameters. Even though the measurement model could not give the correct value of the interface capacitance in case of local CPE, it could be used to identify which portion of the data was affected by the ohmic impedance and to calculate the effective capacitance by eliminating the frequencies above the geometry-induced dispersion frequency.

Conclusions are drawn for each work in Chapter 9. For future work discussed in chapter 10, possible extensions for the mathematic model for localized corrosion of copper are discussed and the development of a 1-D mathematic model for N-type semi-conductor is presented, which could be extended to a mathematic model for QLED devices with multiple layers. The MATLAB code for single-sine and multi-sine impedance calculations is shown in Appendix A. The FORTRAN code to calculate steady-state and impedance in the one-dimensional model for n-type semi-conductor is shown in Appendix B.

CHAPTER 2
BACKGROUND

Background information for different works is presented in this Chapter. For the development of mathematical model for localized corrosion of copper in underground repositories shown in section 2.1, Canadian deep geological repository is introduced and associated possible copper corrosion reactions are introduced. Past Copper corrosion models for nuclear fuel containers and models using Evans droplet are reviewed. Background for the work of impedance of quantum-dot light-emitting diodes is introduced in section 2.2. It covers the basic introduction of quantum-dot light-emitting diode devices, electrochemical impedance spectroscopy, and application of EIS on QLED devices. In section 2.3, Multi-sine impedance spectroscopy's background is introduced including the technique of sing-sine and multi-sine impedance measurements, applications of multi-sine EIS, and Kramers-Kronig relations. Background knowledge for the ohmic impedance on disk electrodes is introduced in section 2.4. The ohmic impedance, frequencies dispersion and application of the measurement model are discussed.

2.1 Corrosion of Copper in Underground Repositories

Nuclear fuel has became a sustainable energy and been used to generate electric power among different countries. The Canada Deuterium Uranium (CANDU), a heavy-water moderated power reactor design, was firstly developed in the 1950s by Atomic Energy of Canada Limited (AECL), Ontario Hydro, and Canadian General Electric (CGE).[5] The first commercial CANDU units became available in 1960s and CANDU is currently operating in Ontario, Quebec and New Brunswick. During the operation, used nuclear fuel became a by-product. The radiation of the used fuel will decay rapidly initially and it will taken 10 million years to reach the radiation level that is equivalent to uranium in the nature.[6] This highly radioactive waste needs to be stored properly to avoid any exposure to the environment and people.

2.1.1 Canadian Deep Geological Repository

Canada's used nuclear fuel is temporarily safely stored in dry storage containers with a minimum lifetime of fifty years.[7] After fifty years of storage, life of the container could be extended or the used nuclear fuel could be repackaged. Adaptive Phased Management (APM) plan, the federally-approved plan for the safe long-term management of Canada's used nuclear

fuel, was selected by the government of Canada in 2007 and the Nuclear Waste Management Organization (NWMO) is responsible for the implementation of APM.[8]

Under APM, used nuclear fuel will ultimately be placed within a deep geological repository (DGR) in a suitable host rock formation and the schematic representation of the Canadian DGR conceptual design is shown in Figure 2-1. [9] It shows a two kilometers by three kilometers conceptual layout and the repository will be constructed at a depth of about 500 meters below the ground surface. On the ground surface, surface facilities labeled as A will be used for operation, maintainable and long-term monitoring, and rock pile labeled as B will be used to properly manage the unused excavated rock [10]. Under the ground surface, services area labeled as C will provide support for DGR operations, and placement rooms labeled as D will safely store the used nuclear fuel container. The schematic representation of the Canadian multiple-barrier system is shown in Figure 2-2[11]. The fuel pellet labeled as 1 are made from uranium dioxide powder and will serve as the first barrier. Fuel bundle labeled as 2 will consist of a number of fuel elements made from Zircaloy that contain the fuel pellets. Used nuclear fuel bundle will be stored in the used fuel container (UFC) labeled as 3. The container has a height of 2.5 meters and a width of 0.6 meters with a spherical head welded to the core of the container. The container is made from carbon steel and coated with a 3-mm-thick copper layer. A highly compacted bentonite clay buffer box labeled as 4 will encapsulate the UFC. Open spaces between each bentonite buffer box will be filled with bentonite clay and the entrance of each placement room will be sealed by the concrete bulk head. The host rock labeled as 5 will serve as a natural barrier that protect the UFC from extreme situations.

2.1.2 Possible Copper Corrosion during Different Stages in DGR

Once the used fuel container is placed in the Canadian DGR, the environment will go from dry and warm to wet and cold conditions. For the long-term management, copper known as one of the inert noble material is the best practical choice to be coated on the carbon steel UFC and Copper will be likely to remain stable under well known conditions. There will be four major post-closure stages.[12] Stage I is called immediate post-placement period. There will be trapped

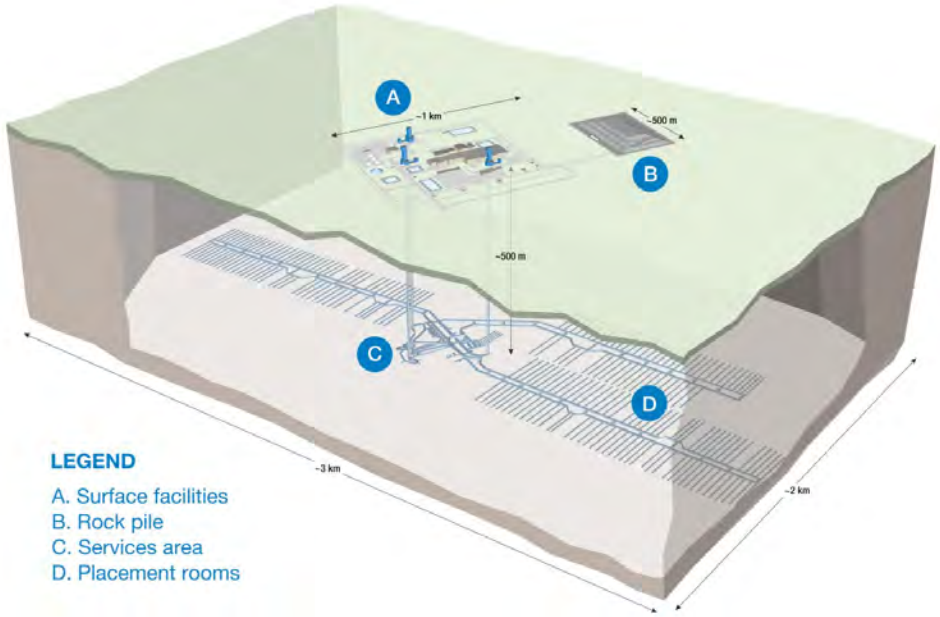

Figure 2-1. Schematic representation of the Canadian DGR conceptual design. (Image credited to NWMO [9])

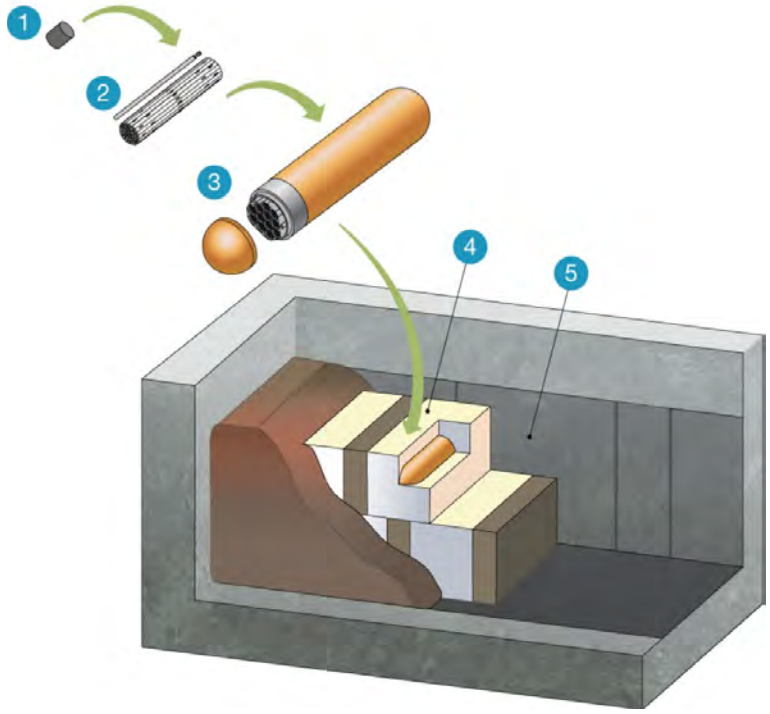

Figure 2-2. Schematic representation of the Canadian multiple-barrier system. (Image credited to NWMO [11])

oxygen and moisture that favours the aqueous corrosion. Cuprous oxide or cuprous salts could be formed. One of the conservative assumption for reaction between oxygen and copper could be expresses as

$$4Cu + O_2 \rightarrow 2Cu_2O \tag{2-1}$$

The γ radiation rate will be at the highest level in this stage. Nitric acid could be produced through γ radiation in the humid air and the reaction could be expressed as

$$O_2(g) + N_2(g) + H_2O(g) \xrightarrow{\gamma} HNO_3(g) \tag{2-2}$$

Copper could be corroded by nitric acid in different reactions shown as

$$2Cu + NO_3^- + 2H^+ \rightarrow 2Cu^+ + H_2O + NO_2^- \tag{2-3}$$

$$2Cu + NO_3^- \rightarrow Cu_2O + H_2O \tag{2-4}$$

$$Cu + NO_3^- + 2H^+ \rightarrow Cu^{2+} + H_2O + NO_2^- \tag{2-5}$$

This stage could last from a few days to several months.

As temperature becomes higher due to the thermal influence from radiation, the DGR will transit to the second stage, which is called dried-out period. The container surface will be completely dry and atmospheric corrosion could take place instead of aqueous corrosion. The duration of this stage will be varied on different types of host rock. It could last about fifty years for the crystalline host rock and five thousand years for the sedimentary rock.[13] As the radiation decays and temperature cools down, the environment will jump into the third stage, which is called the re-wetting and highly compacted bentonite saturation stage. The humidity will increase and the UFC surface will become fully wetted eventually. Oxic corrosion shown in equation (2-1) could still occur if oxygen has not been completely consumed in the previous two stages. Radiation reaction shown in equations (2-3) (2-5) and (2-4) could also occur if the level of the radiation is still very high. After the oxygen is consumed, the DGR will be in the forth stage and also the final stage. This stage is the long-term anoxic phase such that temperature will continue

to cool down. Two types of corrosion could occur in this stage, which are anoxic corrosion and microbiologically-influenced corrosion. For anoxic corrosion, the reaction could be expressed in a similar conservative way as the oxic corrosion and shown as

$$2Cu + H_2O \rightarrow 2Cu_2O + H_2 \tag{2-6}$$

This reaction could occur spontaneously when the pressure of H2 is very low. Sulphate could be produced by sulphate-reducing bacterial and sulphate is expected to corrode copper in the following reaction shown as

$$2Cu + SH^- + H^+ \rightarrow Cu_2S + H_2 \tag{2-7}$$

Besides sulphate could be produced microbiologically, it could also be produced by minerals that contains sulphate.

2.1.3 Copper Corrosion Models for Nuclear Fuel Containers

Different modeling approaches could be taken to predict the long-term copper corrosion and there are two types of models in general. The first type of model is the phenomenological model that requires the empirical relationship by observation and experiment. The phenomenological model has been used in many applications to predict different parameters related to copper corrosion. Swedish corrosion institute studied the corrosion resistance of a copper canister for the nuclear fuel [14]. Pitting corrosion of copper was most concerned that could happen in the copper canister due to the developed oxidants. Pitting factor of copper was derived using an empirical expression for the pit depth as a function of time to describe the ratio between maximum pit depth and average penetration. Werme et al. [15] performed a corrosion analysis of copper canister for Swedish nuclear high level waster disposal. Pitting factor was also used to evaluate the performance of copper respect to pitting corrosion. Björkbacka et al. [16] investigated the radiation induced corrosion of copper for Swedish spent nuclear fuel storage. The maximum possible corrosion rate caused by gamma radiolysis of the aqueous phase was estimated by numerical simulations of radiolysis of pure water. King and Kolar [17] proposed a conceptual

model to address the surface roughening that was observed on copper exposed to compacted buffer environment and surface roughening is the result from pits initiation, growth and death.

Phenomenological model could help explain existing data with fewer parameters, but it becomes less useful as a predictive tool to guide new designs or experiments. The second type of model is the mechanistic model which requires inclusion of all relevant phenomena and has many parameters. When it comes to guide new designs and experiments, the mechanistic model is useful to gain insight into consequences of the coupled behavior of physical and chemical process. A mechanistically-based mixed-potential copper corrosion model has been continuously developed by King and Kolar [18, 19, 20, 21, 22, 17, 23, 24] since 1995. The initial version of the model [18] accounted for the mechanisms of electrochemical reactions and mass-transfer characteristic on the rotating disk electrode and on membrane and compacted-clay electrodes. A total of 6 species were considered including dissolved oxygen, cuprous chloride ($CuCl_2^-$), cuprous oxide (Cu_2O) precipitate, and one dissolved, one adsorbed and one precipitated cupric complex, which are unspecified. The model was used to analyze the effects of unsaturated conditions on the corrosion of copper containers in a Canadian disposal vault.[22]

A second version of the copper corrosion model was developed in 1996 by King et al. [19, 20] and four more species including dissolved chloride (Cl^-), dissolved and precipitated ferrous complex and biotite or other ferrous solid were added compared to the initial version. The early second version was assumed to be isothermal and the later version introduced the effects of the spital and temporal temperature. The second version of the copper corrosion model was used to predict the long-term corrosion behavior of copper nuclear fuel waste containers, which is in support of Atomic Energy of Canada's second case study.[25]

A more advanced and the most recent version of copper corrosion model was developed in 2006 by King et al.[23, 24] The major improvement was the model introduced time-dependent degree of saturation to address the evolution of the repository environment and gaseous oxygen was added to the model. This version of model accounted for the various chemical, microbiological, electrochemical, precipitation/dissolution, adsorption/desorption, redox, and

mass-transport processes at the container surface and in the compacted bentonite-based sealing materials within the repository. A validated COMSOL version of the copper model was developed in 2022 by King and Briggs [26] and this model is the conversion of the previous copper corrosion model to the COMSOL Multiphysics platform.

2.1.4 Models Using Evans Droplet

Evans droplet approach was first used by Evans in 1926 [27] to study the corrosion and oxidation of metals. In his experiments, a sodium chloride droplet was placed on the steel. Under the droplet, periphery region was found to be cathodic with more available oxygen from the atmosphere and droplet center was found to be anodic due to a limited amount of oxygen. The Evans droplet approach has been used in many numerical models to study different corrosion systems.

Jiang et al. [28] studied the effect of length three-phase boundary zone on cathodic and corrosion behavior of metals in Sandy soil systems. An analytical steady-state model was developed under a droplet that accounted for the influence of liquid dispersion on sandy soil corrosion rates and cathodic limiting current. The model showed a strong relationship between the geometric parameters, such as the length and width of the three-phase region, and the cathodic current density. Venkatraman et al. [29] developed a 3-D finite element model for corrosion of Zinc under an Aerosol droplet. The model solves for the Nerst-Planck equation without convection. It was assumed that there was no gas generation and no formation of oxide or films on the metal surface. Zinc dissolution was the only anodic reaction and oxygen reduction was the only cathodic reaction. The results showed the distributions of zinc concentrations and current density distributions, but the separation of anodic and cathodic regions were not described. Chang et al. [30] developed a axial symmetric time-dependant mathematical model to study the under-deposit corrosion of steel. In their model, the anodic and cathodic regions were not predefined and it included the contribution of migration, local electroneutrality, homogeneous reactions and formation of primary precipitates. The model provided an insight into studies among systems reactions, deposition of films,and species transport.

2.2 Impedance of Quantum-Dot Light-Emitting Diodes

Electrochemical impedance spectroscopy(EIS) is used to study red and green quantum-dot light-emitting diodes devices. The high-frequency loop is interpreted in terms of the thickness, dielectric constant, and resistivity distribution of the hole-injection layer. The analysis employed the device capacitance obtained from a measurement model analysis, the film thickness measured by scanning electron microscopy, and an interpretation of the impedance based on a power-law model. Impedance measurements performed on hole-transport only devices yielded results that were consistent with the interpretation of the high-frequency capacitive loop in terms of the properties of the hole-injection layer.

2.2.1 Quantum Dots

Quantum dots are nanoscaled semiconductor particles and are initially discovered by Alexey I. Ekimov [31] and Louis Brus [32, 33] in the early 80s. The schematic structure representation of a quantum dot is shown in Figure 2-3 and the quantum dot has three major properties called core, shell, and ligands. The core is sitting inside the quantum dot, which can adsorb and emit light with pure and bright colors. The shell surrounding the core could protect from moisture, oxygen and heat. The ligands could ensure the quantum dot will be stable and suspended in the solution during the manufacturing. The size of a quantum dot is around 3$\sim$10 nm in diameter and it is 10 thousand times smaller than a human hair. Emission colors strongly depend on the size of the quantum dots. Increasing quantum dot size will decrease the bandgap energy and increase the wavelength of the emitting light. Therefore, the color-changing phenomenon is the result of different bandgaps between different sized quantum dots.

Quantum dots have been widely used in many fields, such as biomedical imaging and biosensing [34], photovoltaic devices [35], computing [36], and photocatalysts [37]. One of the most popular applications is called colloidal quantum-dots light-emitting diode (QLED), in which the quantum dots are synthesized from solutions and used in the new generation of TV displays. The first QLED based device was developed by Colin et al. [38] in 1994. The device was made from cadmium selenide nanocrystals and a semiconducting polymer. The color of the emitting

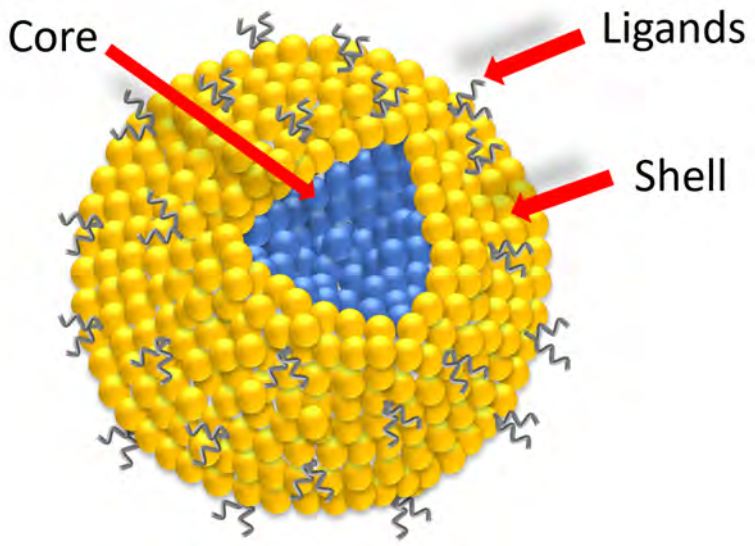

Figure 2-3. Schematic representation of a quantum dot with blue dot representing the core, yellow dot representing the shell and silver tail representing the ligand.

light could be tuned by a degree of voltage. However, this device had a high operating voltage of 4 V and the efficiency needed to be improved. After the following two decades, different quantum-dots emitting layers have been studied to improve the device performance. Anikeeva et al. [39] enhanced the QLED performance by use of different colloidal QLED for the different parts of the visible spectrum, and by utilizing a recently demonstrated robust quantum-dots deposition. One of the major factors to evaluate the QLED devices is called external quantum efficiency (EQE). By this method, EQE was obtained as 1% for green QLED devices with 4 times larger and 2.5 % for red QLED devices with a 30 % increase, but blue QLED devices were still a challenge. Qian et al. [40] reported that high brightness, solution processability, colour tunability, and narrow emission bandwidth could be achieved by using a multi-layer QLED structure. The quantum-dots emissive layer was sandwiched between an organic hole transport layer and an electron transport layer made of ZnO nanoparticles. Ding et al. [41] showed that EQE and current efficiency could be improved by introducing a thermally evaporated organic cathode interfacial material (CIM) Phen-NaDPO. With the organic CIM/LiF/Al cathode, EQE and current efficiency of the QLED device could increase by 44 % and 52 %, respectively.

2.2.2 Electrochemical Impedance Spectroscopy

Electrochemical impedance spectroscopy can be described as transfer function that relates the input signal and the output signal. It becomes a popular technique that has been applied to different electrochemical systems including corrosion, battery, semi-conductor, bio-sensors and etc. As shown in Figure 2-4(a), a sinusoidal time-dependent potential is applied to the electrochemical cell as the input and the response is a sinusoidal time-dependent current density as the out put during the EIS measurement. For a steady-state system, current density is plotted as a function of potential in Figure 2-4(b), which is called the polarization curve. Sinusoidal time-dependent potential can be expressed as

$$V(t) = \overline{V} + |\Delta V|\cos(\omega t) \tag{2-8}$$

where $\overline{V}$ is the steady-state potential, $|\Delta V|$ is the potential amplitude, and ω is the angular frequency. Time-dependent potential $V(t)$ can also be expressed as

$$V(t) = \overline{V} + \mathrm{Re}\{\widetilde{V}\exp(\mathrm{j}\omega t)\} \tag{2-9}$$

where j is the complex number equal to $\sqrt{-1}$ and $\widetilde{V}$ is potential phasor, which can be expressed as

$$\widetilde{V}(\omega) = |\Delta V|\exp(\mathrm{j}\varphi_{\mathrm{V}}) \tag{2-10}$$

where φ_{V} is the phase angle associated with the potential. The response of the current density from the system is also sinusoidal, which can be expressed as

$$i(t) = \overline{i} + \mathrm{Re}\{\widetilde{i}\exp(\mathrm{j}\omega t)\} \tag{2-11}$$

Associated current density phasor can be expressed as

$$\widetilde{i}(\omega) = |\Delta i|\exp(\mathrm{j}\varphi_{\mathrm{i}}) \tag{2-12}$$

The impedance of the steady-state system is the ratio of potential phasor and current density phasor given by

$$Z(\omega) = \frac{\widetilde{V}(\omega)}{\widetilde{i}(\omega)} = \frac{|\Delta V|}{|\Delta i|}\exp(\mathrm{j}(\varphi_{\mathrm{V}} - \varphi_{\mathrm{i}})) \tag{2-13}$$

Impedance can also be expressed in the complex form as

$$Z(\omega) = Z_{\mathrm{r}} + \mathrm{j}Z_{\mathrm{j}} \tag{2-14}$$

where Z_{r} is the real part of the impedance and Z_{j} is the imaginary part of the impedance.

For system having a simple electrochemical reaction without considering mass-transfer effect, associated equivalent circuit model could be a resistance in series with a parallel combination of a resistance and a capacitance shown in Figure 2-5. Impedance could be expressed as

$$Z = \frac{\widetilde{V}}{\widetilde{i}} = R_{\mathrm{e}} + \frac{R_{\mathrm{t}}}{1 + \mathrm{j}\omega R_{\mathrm{t}} C_{\mathrm{dl}}} \tag{2-15}$$

where R_{e} is the ohmic resistance corresponding to the resistance between the reference electrode and location near the working electrode in the electrolyte, R_{t} is the charge-transfer resistance corresponding to the electrochemical reactions on the electrode surface and C_{dl} is the double-layer capacitance corresponding to the interface between the working electrode and electrolyte. Since impedance is a complex number, it could be presented in the Nyquist format, where real part of the impedance could be plotted as a function of imaginary part of the impedance as shown in Figure 2-6. Each point represents the impedance at a single frequency and the shape is a semi circle. The value of impedance tends toward to the value of R_{e} as $\omega \to \infty$ and it tends toward to the value of $R_{\mathrm{e}} + R_{\mathrm{t}}$ as $\omega \to 0$. A characteristic frequency could be expressed as

$$f_{\mathrm{c}} = \frac{1}{2\pi R_{\mathrm{t}} C_{\mathrm{dl}}} \tag{2-16}$$

2.2.3 Constant-Phase Element

Constant-phase-element (CPE) behavior is often observed in EIS response of electrochemical and solid-state systems. As shown in Figure 2-7(a), pure capacitance was

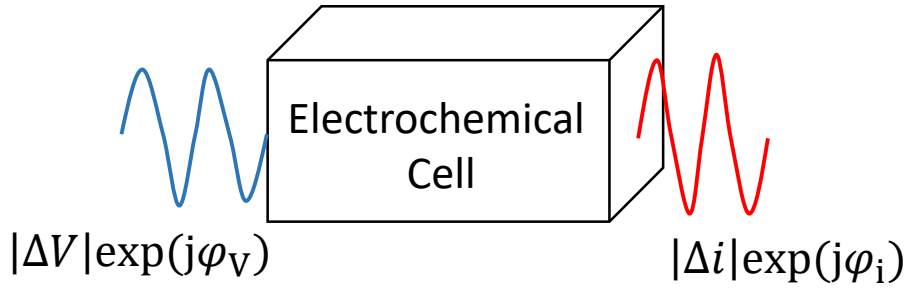

(a)

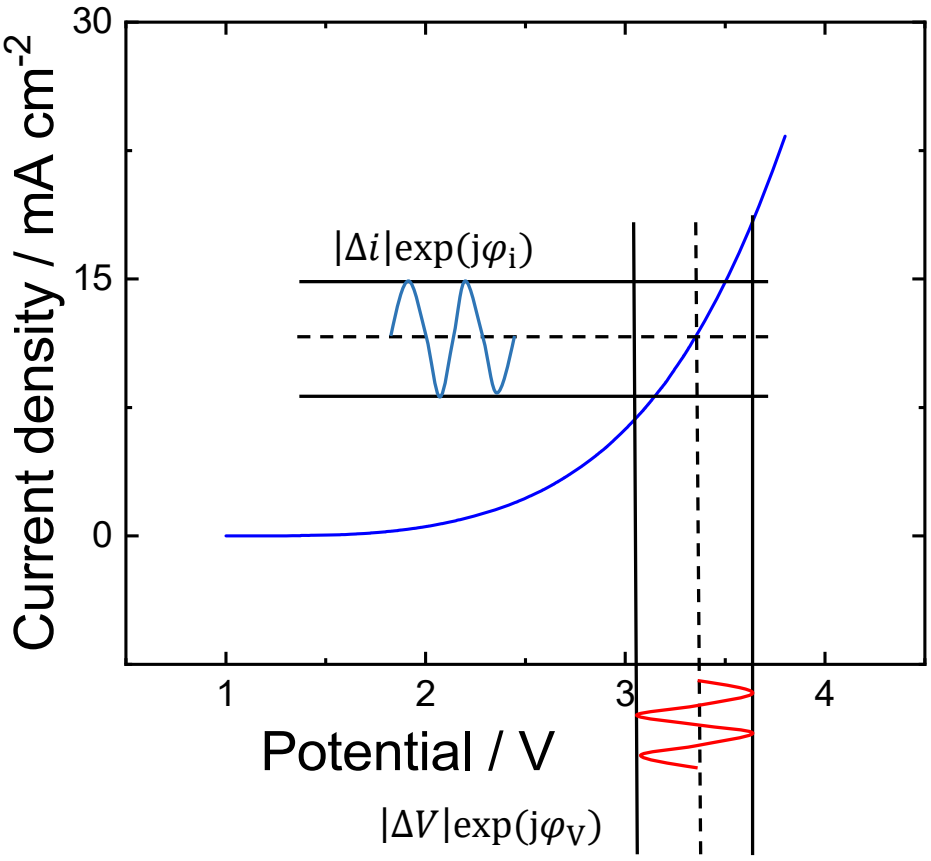

(b)

Figure 2-4. Schematic representation of a sinusoidal perturbation of a input potential with a response of the current density: a) electrochemical cell and b) polarization curve.

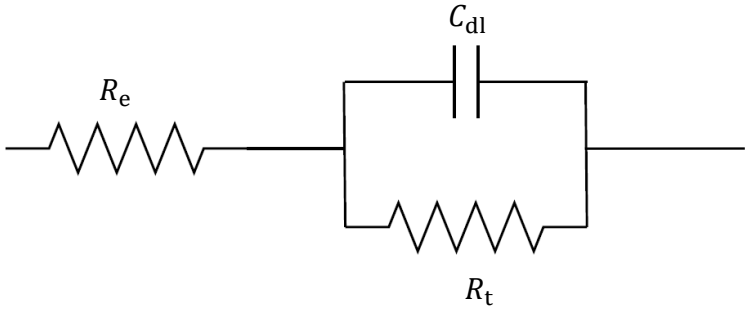

Figure 2-5. Equivalent circuit model of a resistance R_{e} in series with a parallel combination of a resistance R_{t} and a capacitance C_{dl}

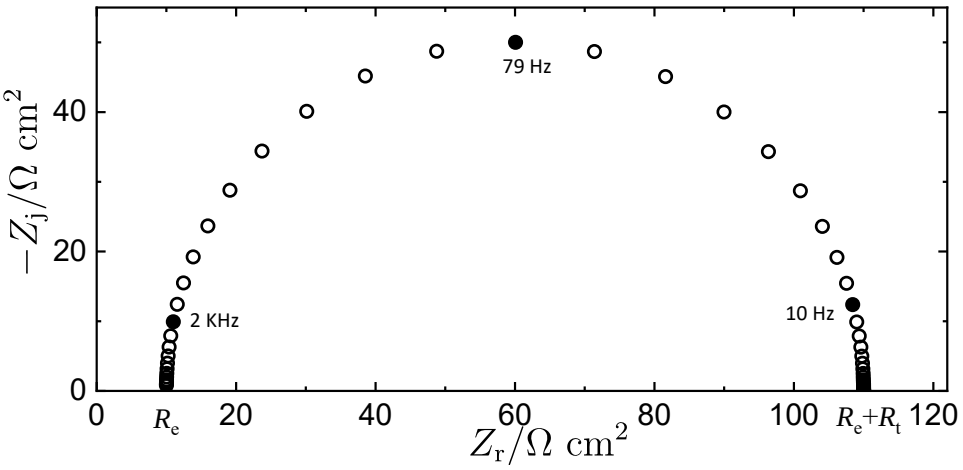

Figure 2-6. Nyquist plot for an equivalent circuit model of a resistance R_{e} in series with a parallel combination of a resistance R_{t} and a capacitance C_{dl}

replaced by the constant phase element in the associated equivalent circuit model and the impedance can be expressed as

$$Z = R_{\mathrm{e}} + \frac{R_{\mathrm{t}}}{1 + (\mathrm{j}\omega)^{\alpha} Q R_{\mathrm{t}}} \tag{2-17}$$

where α is the CPE exponent and Q is the CPE coefficient. The shape of the impedance is a depressed semi-circle shown in Figure 2-7(b) and a smaller α will make the semi-circle more depressed. The CPE can be used to improve the fit of the equivalent circuit model to the impedance data. However, interpretation of the CPE parameters to extract physical meaning requires an understanding of the time-constant distribution in each individual system. Hirschorn et al. [42, 43] developed a power-law model that could relate the CPE parameters to the physical properties of the film by regression of the measurement model [1, 2, 3] to synthetic data. The distribution of resistivity was identified by assuming a uniform dielectric constant. The power-law model has been validated in many applications such as aluminum oxide, oxide film on stainless steel, human skin, and water uptake in coatings.[43, 44, 45]

2.2.3.1 Power-Law Model

Under the assumption that the CPE behavior can be attributed to a distribution of time constants within a layer, Hirschorn et al. [42, 43], found that the distribution of resistivity can be expressed as

$$\frac{\rho}{\rho_{\delta}} = \left(\frac{\rho_{\delta}}{\rho_0} + \left(1 - \frac{\rho_{\delta}}{\rho_0} \right) \left(\frac{y}{\delta} \right)^{\gamma} \right)^{-1} \tag{2-18}$$

where y is the axial position through the film, δ is the film thickness, ρ_0 is the value of the resistivity when $y = 0$, and ρ_{δ} is the value of the resistivity when $y = \delta$. Hirschorn et al. [42, 43], found that, in the frequency range in which a CPE behavior is found, a relationship between film properties and CPE parameters Q_{H} and α_{H} can be expressed as

$$Q_{\mathrm{H}} = \frac{(\varepsilon \varepsilon_0)^{\alpha_{\mathrm{H}}}}{\mathrm{g} \delta \rho_{\delta}^{1-\alpha_{\mathrm{H}}}} \tag{2-19}$$

where g is a function of α_{H}, i.e.,

$$\mathrm{g} = 1 + 2.88(1 - \alpha_{\mathrm{H}})^{2.375} \tag{2-20}$$

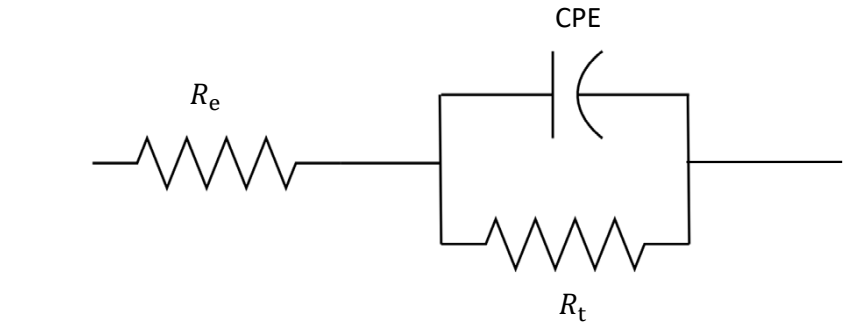

(a)

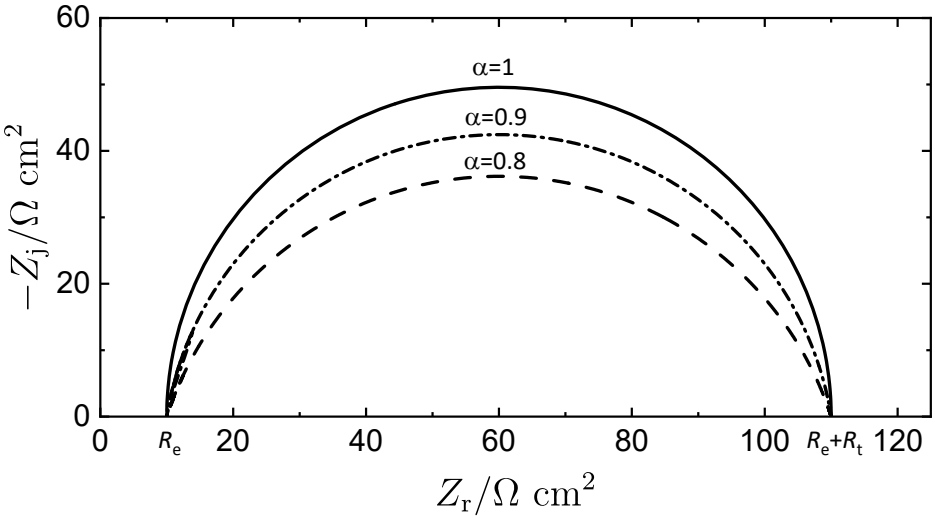

(b)

Figure 2-7. System with constant-phase element behavior: a) equivalent circuit and b) Nyquist plot.

The general expression for capacitance can be written as

$$C = \frac{\varepsilon \varepsilon_0}{\delta} \tag{2-21}$$

and effective capacitance in terms of CPE parameters can be obtained from

$$C_{\text{eff,PL}} = \text{g} Q_{\text{H}} (\rho_\delta \varepsilon \varepsilon_0)^{1-\alpha_{\text{H}}} \tag{2-22}$$

Equation (2-19) has been used to extract film thickness for oxide films on metals,[44] but, as discussed by Orazem et al.,[46] with known values of Q_{H} and α_{H}, equation (2-19) represents one equation with three unknowns. Independent measurement of layer thickness provides an additional parameter. Another parameter may be obtained from the recent observation that the measurement model can be used to identify the capacitance of an electrochemical system.[47]

2.2.3.2 Measurement Model

A circuit representation of the measurement model is shown in Figure 2-8. Liao et al. [47] showed, by regression to synthetic data, that a Voigt measurement model

$$Z = R_0 + \sum_{\text{k}=1}^{\text{K}} \frac{R_{\text{k}}}{1 + \text{j}\omega\tau_{\text{k}}} \tag{2-23}$$

can be used to extract capacitance, ohmic resistance, and polarization resistance values from impedance data, where τ_{i} is the time constant. Agarwal et al. [1] showed that, by including a sufficient number of terms, a general measurement model based on equation (2-23) can fit impedance data for typical stationary electrochemical systems. The number of Voigt elements K was increased sequentially under the constraint that the 95.4% ($\pm 2\sigma$) confidence interval for each

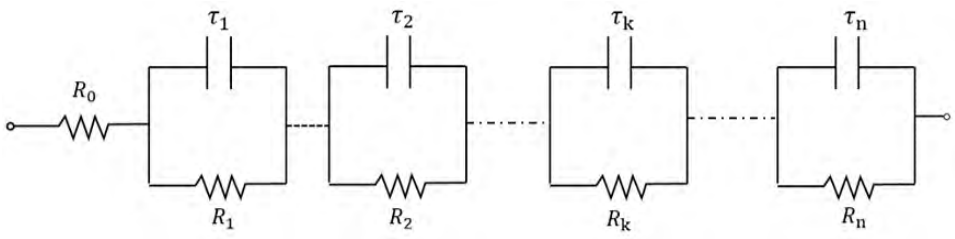

Figure 2-8. A circuit representation of the measurement model

regressed parameter does not include zero. The same value for K can be obtained by minimization of the Akaike information criterion, which penalizes each added parameter.[48] A capacitance for each element k can be expressed as

$$C_{\mathrm{k}} = \frac{\tau_{\mathrm{k}}}{R_{\mathrm{k}}} \tag{2-24}$$

and the effective capacitance can be obtained as

$$\frac{1}{C_{\mathrm{eff}}} = \sum_{\mathrm{k}} \frac{1}{C_{\mathrm{k}}} \tag{2-25}$$

The confidence interval for the effective capacitance can be obtained from the estimated standard errors of the regressed parameters using a linear propagation of error analysis (see Section 3.2 of Orazem and Tribollet[49]).

2.2.4 Application of EIS to QLED Devices

Electrochemical impedance spectroscopy (EIS) has been applied over the decades to study the light-emitting diode (LED) devices and could provide an ability to characterize the electrical properties of the material and the interfaces inside the device. Cho et al. [50] studied the effects of plasma treatment on the surface of indium-tin oxide (ITO) anodes on the OLEDs using different gases. Different values of the contact resistance, the parallel resistance, and the parallel capacitance inferred by the EIS analysis were attributed to the removal of contaminants and to changes in the work function of ITO. Nowy et al. [51] used EIS to investigate the charge-carrier injection properties with different anodes and anode treatments in bottom-emitting OLEDs. Capacitance, trapped and interfacial charges, and the dynamics of injected charges were analyzed to study degradation processes. Hsiao et al. [52] used EIS to study the interfacial capacitance of polymer light-emitting diode devices, and an additional capacitive loop was associated with the bulk of the PEDOT layer. Kwak et al. [53] proposed a method to examine the thermal degradation of OLEDs by EIS and infrared imaging. The OLED with poor electrical properties showed a fairly high temperature during the operation and a short lifetime. Cai et al. [54] and Chulkin et al. [55, 56] measured impedance spectroscopy on OLED devices to study the charge

transfer in the charge-transport layer. The values of the capacitance and the resistance obtained from the regression were used to estimate the mobility and concentration of charge carriers, the parameters responsible for charge transfer and charge density. Tyagi et al. [57] related changes in OLED impedance to degradation caused by heat generation. So and Kondakov [58] reviewed degradation mechanisms for OLED devices, including the extrinsic (cathode) and intrinsic (operation) degradation. They stated that, for polymer OLED devices, charge-transport and injection properties and charge balance controlled by interlayers at the anode contact affect the device lifetime. Zheng et al. [59] suggested that the space-charge-limited current (SCLC) with an exponential trap distribution theory can be used to explain the relationship between the resistance and the applied potential. The value of the resistance in the degraded device was much larger than in the un-degraded device due to the moisture and oxygen diffusion or heat associated with operation. The reported half lifetime is 3000 hours for the red QLED devices, 1000 hours for the green QLED devices, and only 20 hours for the blue QLED devices by Chen et al. [60]. The half lifetime is based on that the value of the luminescence decreased to 50% of its original value, which is equal to 1000 cd/m^2. So far, the external quantum efficiency, the operation time, and the synthesis method are mostly discussed. However, QLED does not have a long history and the degradation mechanism are still lack of explanations. The EIS is very sensitive to the condition of the QLED and it may provide a useful tool to study and understand the possible failure mechanisms.

2.3 Multi-Sine Impedance Spectroscopy

Electrochemical Impedance Spectroscopy, namely measuring the frequency-dependent complex impedance as a function of frequency, has become a fundamental technique for analyzing electrochemical systems. The information-rich response of EIS enables the determination of properties for various electrochemical phenomena in broadly varying systems.

The power of EIS relies on the ability to study the electrochemical phenomena on a wide timescale. It is utilized very heavily in all areas of electrochemistry, from energy storage and conversion[61, 62, 63, 64, 65] to coatings[66, 67], from physical electrochemistry [68, 69, 70] to

corrosion studies [71, 72]. In all cases, EIS data allows decoupling phenomena occurring at different timescales in the system. As examples, for batteries and fuel cells, the area difference of the electrodes allow separation of the behavior of two electrodes [73, 74], for corrosion studies, the polarization resistance of the metal can be obtained without any contribution from the solution resistance [75] and, in cases where the metal is coated, the coating properties can be isolated [72, 76]. These separations are only possible because characteristic timescales (typically RC time constants) for these phenomena are clearly separated.

Since the resolving power of the technique comes from the ability to interrogate events occurring at different timescales, the accessible range of frequencies is an important parameter to discuss. The range of frequencies is rarely limited by instrumentation. On the high-frequency side, manufacturers of electrochemical impedance spectroscopy equipment specify instruments to have a maximum frequency as high as 8 MHz with a potentiostat [77] and 32 MHz [77] without. While it is true that, with the correct resistor connected across the instrument cables and correct geometry, there may be an accurate measurement at such high frequencies, measurements with practical systems including cable limitations are typically only useful up to 50kHz or less. The low-frequency side is more interesting. Instrumentally, there is no limitation on how slow a measurement can be made. Manufacturers' limits on the low side, when they exist, are bound by factors such as time between data points, USB sleep times, etc., which can be modified easily if/when necessary. However, most of the time, the principal limitation is sample stability and, more often, stationarity. Instrument software typically allow for frequencies as low as 10μHz, which corresponds to 105 seconds per period, roughly 27.8 hours. Given the need for measurement of multiple cycles, at least 56 hours are necessary for a measurement at a frequency of 10µHz. Most electrochemical system are not stationary over a period of days to weeks.

2.3.1 Single-Sine EIS

Single-frequency Fourier analysis could be used for the single-sine EIS measurements and the outline of the approach could be seen in Section 7.3.3 of Orazem and Tribollet[49] For

example, the input potential to a system could be expressed as

$$V(t) = \Delta V \cos(\omega t) \tag{2-26}$$

and the output current density could be expressed as

$$i(t) = \Delta i \cos(\omega t + \varphi_{\mathrm{i}}) \tag{2-27}$$

To transform a signal from time domain to the frequency domain, a Fourier analysis could be used. The real and imaginary part of the current density signal could be expressed as

$$i_{\mathrm{r}}(\omega) = \frac{1}{T'} \int_0^{T'} i(t) \cos(\omega t) \mathrm{d}t \tag{2-28}$$

and

$$i_{\mathrm{j}}(\omega) = -\frac{1}{T'} \int_0^{T'} i(t) \sin(\omega t) \mathrm{d}t \tag{2-29}$$

where T' is the period of an integer number of cycles at frequency ω. The real and imaginary part of the potential signal could be expressed as

$$V_{\mathrm{r}}(\omega) = \frac{1}{T'} \int_0^{T'} V(t) \cos(\omega t) \mathrm{d}t \tag{2-30}$$

and

$$V_{\mathrm{j}}(\omega) = -\frac{1}{T'} \int_0^{T'} V(t) \sin(\omega t) \mathrm{d}t \tag{2-31}$$

The impedance was calculated as

$$Z(\omega) = \frac{V_{\mathrm{r}} + jV_{\mathrm{j}}}{i_{\mathrm{r}} + ji_{\mathrm{j}}} \tag{2-32}$$

2.3.2 Multi-Sine EIS

In an effort to decrease the measurement time, multi-sine, or more generally, Fourier Transform techniques have emerged as an alternative. Multi-Sine Electrochemical Impedance Spectroscopy (MS-EIS) was introduced in the late 1970s [78, 79] as a technique that can improve data acquisition and can shorten the experiment duration. It has been implemented by instrument manufacturers [80, 81] and used by several research groups to obtain impedance results of various

electrochemical systems[82, 83, 84, 85, 86]. Unlike the conventional step-sine EIS in which excitation signals are applied at each frequency separately, MS-EIS excites the sample by one composite signal containing numerous frequencies intended for investigation. Application of the Fast Fourier Transform (FFT) on the full signal yields a frequency response from the multi-sine signal. The impedance is calculated from ratio of the voltage to the current at each frequency. Fourier Transform techniques are routinely used in analytical chemistry, especially in techniques where a large number of averages are necessary. Instruments that perform FTIR [87] and FTNMR [88] are commonplace in chemistry laboratories.

2.3.3 Application of Multi-Sine EIS

The first application of MS-EIS in the literature was reported by Smith et al. , who applied pseudorandom white noise excitation signals to measure the self-exchange rate constants for $Cr(CN)_6^{4-}/Cr(CN)_6^{3-}$ system [78]. The technique was named Fourier Transform Admittance due to the reliance on FFT to obtain the admittance values. They also described the data processing involved for FFT impedance and highlighted the advantages of using the technique [79].

Later several studies utilized the technique to obtain the electrochemical impedance of various systems. Smyrl [89] and Smyrl and Stephenson [90] describe "digital impedance for faradaic analysis" (DIFA), an input spectrum consisting of superimposed sinusoids such that the higher frequency members are harmonics of the lowest frequency, and applied the technique to study corrosion of copper in HCl. Later Wiese et al. . [91] described the working principles of Fourier Transform Impedance spectrometer in the frequency range from 1 Hz to 105 Hz. They report that impedance spectra were obtained within few seconds. Few years later, Schindler et al. developed phase-optimization for the excitation signal to optimize the response. The perturbation signal used was a superposition of sine waves with properly chosen frequencies [92]. Gabrielli et al. did a comparison study for the impedance results of single sine wave and white noise excitation [93]. They stated that the both techniques allow for accurate impedance measurements and that the white noise yields shorter measurement time only if linear spaced frequencies are tolerable in the lowest decade.

Another approach was taken by Gheem et al. in which a broadband periodic excitation signal, called odd random phase multi-sine, was introduced as a technique to characterize non-linear and non-stationary systems [94, 95]. As stated by the authors, the technique allows for differentiation between non-stationarity and non-linearity in the system and has been applied to coatings and corrosion systems [96, 97].

In addition to the MS-EIS techniques, there have been numerous studies involving signals that are not generated by adding sine waves. Relaxation Voltammetry [98] is one of the early examples where a simple open circuit voltage decay measurement has been employed as the signal used in order to calculate the impedance at low frequencies. The voltage measured can be Fourier transformed into the frequency domain in order to obtain the spectrum. Though this measurement is simple, the frequency domain signal is very broad and continuous, decreasing the signal power at any given frequency, and thus creating issues with signal-to-noise. The extreme case for signal-to-noise issues come in cases where the signal is simply a potential step function [83]. Once the derivative of the step is taken, the result is a Dirac function, which is effectively white in the frequency domain. Though this is shown to work in very-low-impedance systems where there is plenty of current signal, it is also shown to have problems [99].

There are several commercial implementations of MS-EIS. In all implementations, the goal has been to decrease the time requirement of the measurement [80, 81, 100]. In the low-frequency region, properly designed signals have been shown to decrease the time requirement of the measurement by up to factors of 4.

2.3.4 Kramers-Kronig Relations

The fundamental assumptions behind any EIS measurement are that the measurements are linear, stable, and causal [49]. The causality and the stationarity conditions can be checked through compatibility with the Kramers–Kronig relations. The Kramers–Kronig relations relate the real and the imaginary component of the obtained impedance values, e.g.,

$$Z_{\mathrm{r}}(\omega) = Z_{\mathrm{r},\infty} - \frac{2}{\pi}\int_0^{\infty} \frac{xZ_{\mathrm{j}}(x) - Z_{\mathrm{j}}(\omega)}{x^2 - \omega^2}\mathrm{d}x \tag{2-33}$$

Equation (2-33) shows that real component of impedance Z_r can be predicted from an analytical function of the imaginary component if the conditions of linearity, stability and causality are not violated. Any deviation from the Kramers–Kronig transform can be attributed to the presence of nonlinearity or non-stationarity in the measurement.

As can be seen from equation (2-33), direct application of the Kramers–Kronig relations requires integration over frequency ranging from zero to infinity. Due to the finite frequency range accessible in practical EIS measurements, various approximations are employed in order to check compatibility with Kramers–Kronig relations. The implementations either rely on fitting the data to generic Kramers–Kronig-compatible circuit elements, or extrapolations of the data to the rest of the frequency domain. Two implementations that rely on fitting generic Kramers–Kronig-compatible models to the data are the measurement model method [1, 2, 2] and the Boukamp method [4]. The measurement model is based on fitting electrical circuits corresponding to the Voigt model, which is consistent with the Kramers–Kronig relations. The Boukamp method is also based on fitting Voigt circuit elements but is linear in its parameters.

Another approach to test for compatibility with the Kramers Kronig relations is to perform the integration by fitting polynomials to the data. This allows interpolation for getting a better estimation of the true integral with more points between the frequencies and extrapolation in order to calculate the regions of frequency that are not experimentally accessible. This approach has been shown to work, as long as a properly chosen model is accessible [101].

The sensitivity of the Kramers–Kronig relations in the determination of the linearity and stationarity for the impedance data set has been discussed in the literature. Compatibility with the Kramers–Kronig relations is known to be sensitive to non-linear behavior only if the measurement is done for a sufficiently wide frequency range that covers the time constants of the system [102]. In the case of stationarity, the Kramers–Kronig relation is found to be very sensitive to non-stationary behaviors in electrochemical systems [103, 104].

The issue of whether the Kramers–Kronig relations may be used to validate multi-sine impedance data is not fully resolved. Srinivasan et al. [105] state that the Kramers–Kronig

relations may be used to identify multi-sine data affected by potential drift. Sacci et al. [106] used the Kramers–Kronig relations to validate dynamic electrochemical impedance spectroscopy data that employs a multi-sine technique. The results presented by Macdonald [107] suggest that multi-sine signals treated by fast Fourier and related transformations yield results that automatically satisfy the Kramers–Kronig relations. The objective of this work is to use experiments and numerical simulations to test for the compliance of the Kramers–Kronig relations to the non-stationary behaviors utilizing single-sine and multi-sine excitation signals.

2.4 Ohmic Impedance of Disk Electrodes

The electrode geometry often constrains the distribution of current density and potential in the electrolyte adjacent to the electrode in such a way that both cannot simultaneously be uniform. The primary and secondary current and potential distributions associated with a disk embedded in an insulating plane were developed by Newman.[108, 109] Current distributions have been calculated as well for planar electrodes in channel flow.[110, 111] Newman showed that the potential distribution on the disk electrode is not uniform under conditions where the current density is uniform and, conversely, the current distribution is non-uniform under the primary condition where the solution potential is uniform.[109, 112]

2.4.1 Frequency Dispersion

The presence of frequency dispersion associated with the current and potential distributions on the working electrode was introduced by Newman.[113] He performed numerical simulations for a disk electrode under three conditions: the electrode was purely capacitive ($J = 0$) and the electrode was subject to a faradaic reaction with $J = 0.1$ and $J = 1$. The dimensionless parameter J may be expressed as[114, 115]

$$J = \frac{4R_{\mathrm{e,HF}}}{\pi R_{\mathrm{t}}} \tag{2-34}$$

where $R_{\mathrm{e,HF}}$ is the high-frequency or primary ohmic resistance and R_{t} is the charge-transfer resistance associated with a faradaic reaction. For a pure capacitor, $R_{\mathrm{t}} = \infty$ and $J = 0$. Newman presented his results in terms of frequency-dependent resistance and capacitance, showing that, for a purely capacitive electrode, the ohmic resistance could be described as having a value at

high frequency that differed from a value at low frequency. The solution to Laplace's equation was performed using a transformation to rotational elliptic coordinates and a series expansion in terms of Lengendre polynomials.

Nisancioglu and Newman[116, 117] used a similar mathematical development to find the transient potential response of a disk electrode subject to step changes in current. Their treatment considered a secondary current distribution for which the electrode was subject to faradaic reactions. Antohi and Scherson expanded the solution to the transient problem by expanding the number of terms used in the series expansion.[118]

The location of reference electrodes within a nonuniform current and potential distribution were shown to influence the impedance of thin solid electrolytes[119] and lithium batteries.[120] Córdoba–Torres et al. suggested that geometry-induced current and potential distributions influence interpretation of constant-phase element behavior.[121]

2.4.2 Ohmic Impedance

The effect of electrode geometry on impedance was explored further by Huang et al. [114, 122, 123] who suggested that the influence of nonuniform distributions of current and potential can be described in terms of an ohmic impedance. The ohmic impedance becomes an ohmic resistance for geometries yielding uniform current and potential distributions such as a recessed electrode. The complex character of the ohmic impedance is evident above a characteristic frequency that can be expressed as

$$f_c = \frac{1}{2\pi R_{e,HF} C_0} \tag{2-35}$$

where C_0 is the interfacial capacity and the high-frequency ohmic resistance $R_{e,HF}$ is that obtained as the primary resistance. The characteristic frequency given by equation (2-35) depends on the electrode size and electrolyte conductivity (through $R_{e,HF}$).

Gharbi et al. [124] showed that a process model including the Havriliak–Negami equation

$$Z = R_{e,HF} + \frac{R_{e,LF} - R_{e,HF}}{(1 + (j\omega\tau)^{\alpha})^{\beta}} \tag{2-36}$$

could account for the high-frequency dispersion or complex ohmic impedance associated with the disk electrode. Equation (2-36) was fit to synthetic data obtained by finite-element simulations of a disk electrode. The value of α was found to be that associated with local CPE behavior of the electrode, and β had a value on the order of 0.7. They reported the regression of a model accounting for ohmic impedance and the power-law impedance[125], i.e.,

$$Z = R_{\mathrm{e,HF}} + \frac{R_{\mathrm{e,LF}} - R_{\mathrm{e,HF}}}{(1+(\mathrm{j}\omega\tau)^{\alpha})^{\beta}} + \int_0^{\delta} \frac{\rho(y)}{1+\mathrm{j}\omega\varepsilon\varepsilon_0\rho(y)}\mathrm{d}y \tag{2-37}$$

to data collected on aluminum oxide. The regression was performed using an in-house regression program that employed a Simplex routine; thus, while the fits showed good agreement with the data, confidence intervals for parameter estimates could not be obtained. Subsequent efforts to perform this regression using a Levenberg–Marquardt algorithm were unsuccessful.

2.4.3 Application of the Measurement Model

The measurement model was proposed by Agawal et al. [1, 3] in 1990s to check for the consistency of the experimental impedance data with the Kramers-Kronig relations. By use of a series of Viogt elements, the measurement model is able to provide a statistically significant fit to different impedance spectra. The measurement model can also be used to identify the error structure of the impedance measurements. [2] Boukamp and Macdonald also proposed a distribution of relaxation-times fitting method to test whether the impedance data satisfies the Kramers-Kronig relations.[126] A linear method was suggested by Boukamp [127] that the impedance data at each frequency was fitted to an individual Viogt element by a linear regression. You et al. [128] showed that the measurement model developed by Agawal et al. was more sensitive to failures of causality of impedance data caused by the nonstationary behavior than the approach proposed by Boukamp and implemented by Gamry instruments.

The use of measurement model could not only check for the impedance data that are consistent with the Kramers-Kronig relations, but also provided a useful tool for understanding the physics for the system. Orazem et al. [129]showed that zero and high-frequency limits obtained from the measurement model were used to determine the polarization resistance. The

results followed by this procedure could be used to monitor the systems involving the transient growth of corrosion-product films on copper in synthetic water and on cast iron in Evian water. You et al. [130] used the measurement model to calculate the effective capacitance of the hole-injection layer for the quantum-dot light-emitting diode devices. The useful parameters of physical properties, such as dielectric constant or layer thickness, could be obtained under the assumption of a power-law resistivity distribution.[43, 42] Liao et al. [47] showed that the measurement model was able to yield an accurate capacitance by removing the contribution of the ohmic impedance from the regressed data for systems showing geometry-induced frequency dispersion. High frequency and low frequency ohmic resistances could be extracted. However, the effect of mass transfer was not included in the presence of the geometry-induced frequency dispersion.

CHAPTER 3
MATHEMATICAL DEVELOPMENT FOR COPPER CORROSION MODEL

Part of evaluating the long-term performance and safety of the Canadian repository system is to understand the behavior of the copper coated container with respect to localized corrosion. The Canadian Deep Geological Repository (DGR) system does not lend itself to passivation of the copper surface, owing to the nature of copper and the environment, so conventional pitting corrosion is not expected. However, the system will transition from dry to wet conditions, and there is a possibility that deliquescent species may be present on the container surface, which may produce different localized environments, and, as a result, localized corrosion damage. The objective of this work was to develop a time-dependent model for localized corrosion of copper using the concept of an Evans droplet.[27] The mathematical approach was similar to that developed by Chang et al. [30] for corrosion of iron under a droplet or under a deposit.

The model included coupled nonlinear conservation equations for ionic species, which included the contribution of diffusion, migration, local electro-neutrality, and homogeneous reactions. The anodic and cathodic regions were not predefined but were rather determined by values of local concentration and potential from the simulation results. The surface coverage of film was calculated implicitly and expressed in terms of the thickness in units of monolayers. The model also accounted for the effect of porous CuCl film thickness on the surface oxygen concentration and potential applied on electrochemical reactions. The influence of temperature was included on model parameters.

3.1 Numerical Methods

Numerical simulations was performed using COMSOL Multiphysics® 6.0, and the hardware used was a Dell precision workstation T7920 with dual Intel® Xeon® Gold 6242R 3.1 GHz processors with 256G of RAM. The model was built using the basic module called mathematics and a physics module called Nernst-Planck Equations. Non-linear governing equations were solved by the fully-coupled approach in the time-dependent study.

The geometry of the droplet was assumed to be axisymmetric and a quarter ellipse was used to represent the water droplet on the copper metal surface, as shown in Figure 3-1. Γ_{WE} is the cooper metal surface, Γ_I is the insulating surface, and Γ_{DB} is the interface between the droplet and

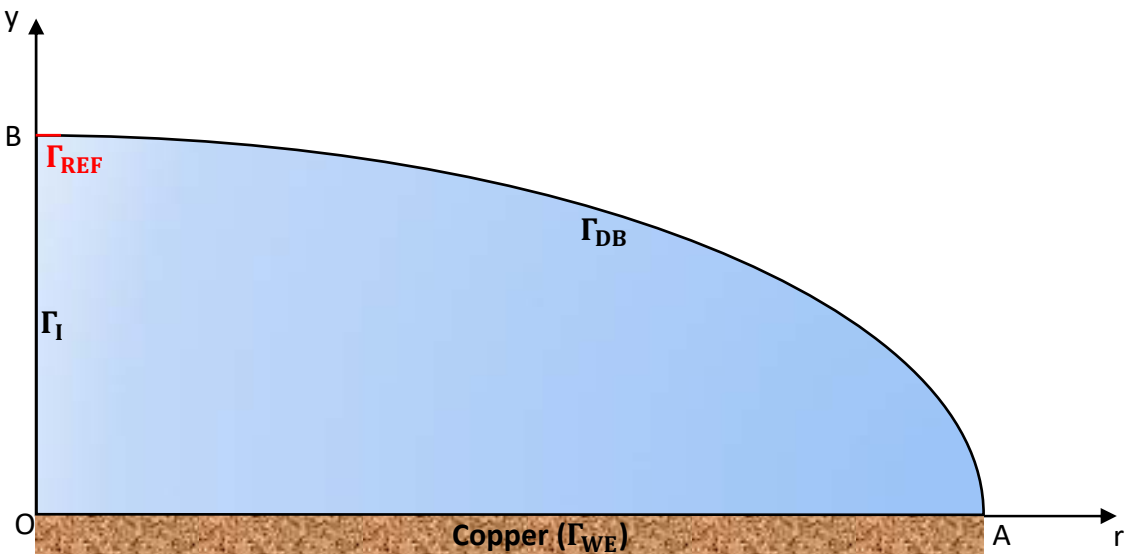

Figure 3-1. Schematic representation of water droplet on the copper surface.

the repository air. The droplet has a radius OA = 1 mm and a height OB = 0.4 mm. Γ_{REF} is the farthest location from the copper metal surface within the droplet. Nonuniform distributed triangular-element meshing was used in the current geometry shown in Figure 3-2 and maximum element sizes were defined in the droplet domain and at different droplet boundaries. The maximum element size near the center of the droplet labeled as ① is 200 times smaller than the droplet radius, which is OA/200 = 5 μm and length of ① is 95% of OA. The maximum element size near the periphery of the droplet labeled as ② and ③ was set to 400 times smaller than the droplet radius, which is OA/400=2.50 μm, and the farthest distance of ③ from the metal surface is 5% of OA. The maximum element size far away from the metal surface labeled as ④ is 150 times smaller than the droplet radius, which is OA/150 = 6.67 μm. The maximum element size for the domain of the droplet labeled as ⑤ was set to 50 times smaller than the droplet radius equal to OA/50=20 μm. The model has about 4,400 finite elements.

3.2 Electrochemical Reactions

Sodium chloride was chosen as the supporting electrolyte, and several electrochemical reactions were considered in the current model. Copper was assumed to oxidize to cuprous ions in the anodic direction, and cuprous ions could be also plated in the cathodic direction. The

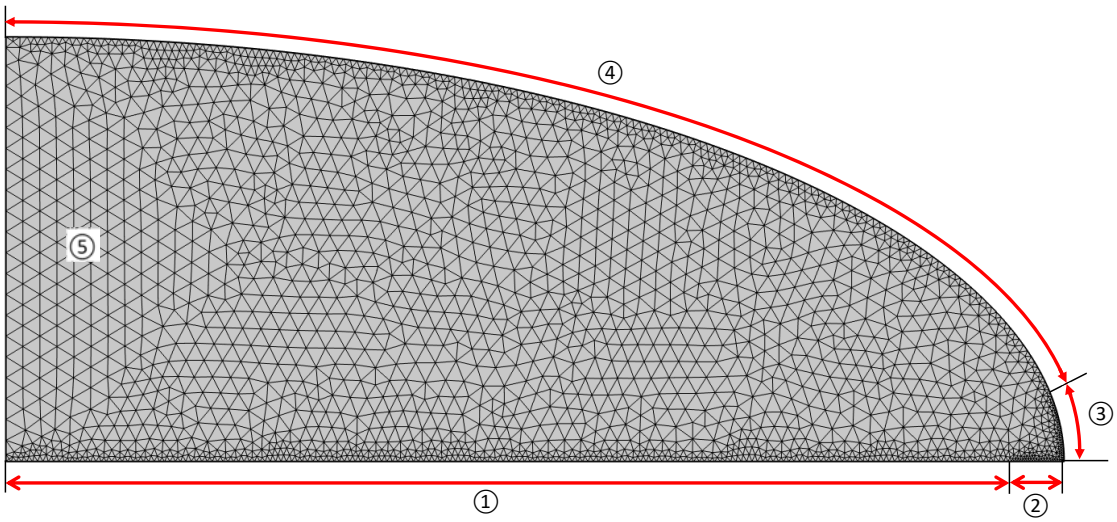

Figure 3-2. Schematic representation of nonuniform triangular meshing in the model

reversible reaction could be expressed as

$$\mathrm{Cu} \rightleftarrows \mathrm{Cu}^{+} + \mathrm{e}^{-} \tag{3-1}$$

The corresponding current density for reaction (3-1) following the Tafel expression could be expressed as

$$i_{\mathrm{F,Cu^+}} = k_{\mathrm{Cu^+,a}} \exp(b_{\mathrm{Cu^+,a}}(\Phi_{\mathrm{m}} - \Phi_0)) - k_{\mathrm{Cu^+,c}} c_{\mathrm{Cu^+}}(0) \exp(-b_{\mathrm{Cu^+,c}}(\Phi_{\mathrm{m}} - \Phi_0)) \tag{3-2}$$

where $k_{\mathrm{Cu^+,a}}$ and $k_{\mathrm{Cu^+,c}}$ are reaction rate constants including the equilibrium potential information, $b_{\mathrm{Cu^+,a}}$ and $b_{\mathrm{Cu^+,c}}$ are lumped parameters, $c_{\mathrm{Cu^+}}(0)$ is the cuprous ion concentration on the metal surface, Φ_{m} is the potential on the metal surface, and Φ_0 is the potential outside the diffuse part of the double layer. The kinetic parameters b_{i} was given by

$$b_{\mathrm{i}}(T) = \frac{\alpha_i \mathrm{F}}{\mathrm{R}T} \tag{3-3}$$

where α_i is the symmetry factor for single electron step reactions and α_i is the apparent transfer coefficient for more complicated reactions. Cuprous ions produced by reaction (3-1) could

transform to cupric ions, which could be expressed as

$$Cu^{+} \rightleftarrows Cu^{2+} + e^{-} \tag{3-4}$$

The associated current density for reaction (3-4) could be expressed as

$$i_{F,Cu^{2+}} = k_{Cu^{2+},a} c_{Cu^{+}}(0) \exp(b_{Cu^{2+},a}(\Phi_m - \Phi_0)) - k_{Cu^{2+},c} c_{Cu^{2+}}(0) \exp(-b_{Cu^{2+},c}(\Phi_m - \Phi_0)) \tag{3-5}$$

Cupric ions could be reduced to cuprous chloride ions by chloride ions shown as

$$Cu^{2+} + 2Cl^{-} + e^{-} \rightarrow CuCl_2^{-} \tag{3-6}$$

The current density for reaction (3-6) could be expressed as

$$i_{F,CuCl_2^{-}} = -k_{CuCl_2^{-}} c_{Cu^{2+}}(0)(c_{Cl^{-}}(0))^2 \exp(-b_{CuCl_2^{-}}(\Phi_m - \Phi_0)) \tag{3-7}$$

The oxygen reduction reaction in the acidic conditions is generally expressed as

$$O_2 + 4H^{+} + 4e^{-} \rightarrow 2H_2O \tag{3-8}$$

As discussed by Newman [131], oxygen reduction may follow two elementary steps under the acidic conditions, i.e.,

$$O_2 + 2H^{+} + 2e^{-} \rightarrow H_2O_2 \tag{3-9}$$

and

$$H_2O_2 + 2H^{+} + 2e^{-} \rightarrow 2H_2O \tag{3-10}$$

A parameter $\psi = D_{H_2O_2} k_2 / D_{O_2} k_3$ was defined to distinguish the limiting current behavior, where k_2 and k_3 are reaction rate constants for reactions (3-9) and (3-10), and $D_{H_2O_2}$ and D_{O_2} are diffusion coefficients. As $\psi \rightarrow 0$, reaction (3-10) is much faster as compared to reaction (3-9). A single limiting current plateau is observed at cathodic potentials. For $\psi \rightarrow \infty$, the polarization curve shows a smaller limiting current plateau, which is half of the bigger plateau for $\psi \rightarrow 0$. For $0 < \psi < \infty$, polarization curve falls in between two limiting current conditions and the reactions are more distinguishable. For alkaline conditions[132], the overall reaction for oxygen reduction

can be expressed as

$$O_2 + 2H_2O + 4e^- \rightarrow 4OH^- \tag{3-11}$$

Elementary steps for reaction (3-11) could be expressed as

$$O_2 + H_2O + 2e^- \rightarrow HO_2^- + OH^- \tag{3-12}$$

and

$$HO_2^- + H_2O + 2e^- \rightarrow 3OH^- \tag{3-13}$$

in which HO_2^- is the intermediate. Current densities for reactions (3-12) and (3-13) could be expressed as

$$i_{F,O_2} = -k_{O_2} c_{O_2}(0) \exp(-b_{O_2}(\Phi_m - \Phi_0)) \tag{3-14}$$

and

$$i_{F,HO_2^-} = -k_{HO_2^-} c_{HO_2^-}(0) \exp(-b_{HO_2^-}(\Phi_m - \Phi_0)) \tag{3-15}$$

Hydrogen ions could react cathodically to generate hydrogen, and hydrogen could also be oxidized to form hydrogen ions. Reversible reactions for hydrogen evolution and reduction could be expressed as

$$2H^+ + e^- \rightleftarrows H_2 \tag{3-16}$$

The current density for reaction (3-16) could be expressed as

$$i_{F,H_2} = k_{H_2,a} c_{H^+}(0) \exp(b_{H_2,a}(\Phi_m - \Phi_0)) - k_{H_2,c} \exp(-b_{H_2,c}(\Phi_m - \Phi_0)) \tag{3-17}$$

Equations 3-1, 3-4, 3-6, 3-12, 3-13 and 3-16 were used to represent heterogeneous electrochemical reactions on the copper surface.

3.3 Film Formation

Two kinds of films were assumed to form in the current model. One is cuprous chloride salt film that served as a diffusion barrier. The other is a cuprous oxide film that partially blocks the electrode surface. Dissolved Cu^+ was assumed to react in a second chemical step to form the

CuCl film, and the reaction could be expressed as[133, 134]

$$Cu^{+} + Cl^{-} \rightleftarrows CuCl \tag{3-18}$$

The reaction rate for reaction (3-18) could be expressed as

$$R_{CuCl} = k_{f,CuCl}(c_{Cu^{+}} c_{Cl^{-}} - K_{sp,CuCl}) \tag{3-19}$$

where $K_{sp,CuCl}$ is the solubility product constant. The CuCl salt film could further react with Cl^{-} to form dissolved $CuCl_2^{-}$, and the reaction could be expressed as

$$CuCl + Cl^{-} \rightleftarrows CuCl_2^{-} \tag{3-20}$$

The reaction rate for reaction (3-20) could be expressed as

$$R_{CuCl_2^{-}} = k_{f,CuCl_2^{-}} c_{Cl^{-}} - k_{b,CuCl_2^{-}} c_{CuCl_2^{-}} \tag{3-21}$$

Dissolved Cu^{+} could also react to form the Cu_2O film and the reaction could be expressed as[135, 134]

$$2Cu^{+} + H_2O \rightleftarrows Cu_2O + 2H^{+} \tag{3-22}$$

The reaction rate for reaction (3-22) could be expressed as

$$R_{Cu_2O} = k_{f,Cu_2O}((c_{Cu^{+}})^2 - K_{sp,Cu_2O}(c_{H^{+}})^2) \tag{3-23}$$

The surface coverage for CuCl and Cu_2O films was calculated implicitly and expressed in terms of the thickness in units of monolayers given as

$$\gamma_i = \frac{A_i}{A_{dp}} = \frac{c_i M_{w,i}}{\rho_i \delta_{m,i}} \frac{1}{A_{dp}} \tag{3-24}$$

where A_{dp} is the surface area of the droplet, A_i is the surface area of the film, $M_{w,i}$ is the molecule weight, ρ_i is the density of film, and $\delta_{m,i}$ is the monolayer thickness of the film.

3.4 Homogeneous Reactions

Multiple homogenous reactions were also assumed to take place in the droplet. Reversible homogeneous reactions were assumed to reach equilibrium at longer elapsed time, and equilibrium constants were used to govern species concentrations. The equilibrium constant is generally defined based on the reaction stoichiometry and species concentrations, and it could be expressed as

$$K_{\mathrm{eq}} = \frac{\prod_{\mathrm{i}} c_{\mathrm{p,i}}^{s_{\mathrm{i}}}}{\prod_{\mathrm{i}} c_{\mathrm{r,i}}^{-s_{\mathrm{i}}}} \tag{3-25}$$

where s_{i} is stoichiometric coefficient, and subscripts p and r stand for products and reactants.

Water dissociation was included in the current model to account for the pH effect and the reaction could be expressed as

$$\mathrm{H_2O} \rightleftarrows \mathrm{H^+ + OH^-} \tag{3-26}$$

The elementary steps for most homogeneous reactions were guided by the database from the thermodynamic speciation program PHREEQC, which contained information on the aqueous geochemistry.[136, 137, 138] Dissolved $\mathrm{Cu^+}$ and $\mathrm{Cu^{2+}}$ could react with chloride, carbonate, and hydroxide ions to produce dissolved copper chloride, copper carbonate and copper hydroxide complex. Homogeneous reactions were removed from the model when associated product concentrations were smaller than concentration of one molecule in the droplet, which could be expressed as

$$c_{\mathrm{m,d}} = \frac{1}{N_{\mathrm{A}} V_d} \tag{3-27}$$

where $N_{\mathrm{A}} = 6.02214 \times 10^{23}$ $\mathrm{mol^{-1}}$ is the Avogadro's number, and $V_d = 8.38 \times 10^{-4}$ $\mathrm{cm^3}$ is the volume of the droplet. Species involving copper chloride complex in the current model are $\mathrm{CuCl_3^{-2}}$, $\mathrm{CuCl^+}$ and $\mathrm{CuCl_2}$. Associated reactions could be expressed as

$$\mathrm{CuCl_2^- + Cl^- \rightleftarrows CuCl_3^{2-}} \tag{3-28}$$

$$\mathrm{Cu2^+ + Cl^- \rightleftarrows CuCl^+} \tag{3-29}$$

and

$$CuCl^{+} + Cl^{-} \rightleftarrows CuCl_2 \tag{3-30}$$

As shown by Yuan et al. [139], dissolved $CuCl_2^-$ and $CuCl_3^{2-}$ could react with O_2 to produce hydrogen peroxide and superoxide species, and the associated reactions could be expressed as

$$CuCl_2^- + O_2 \rightleftarrows O_2^{2-} + Cu^{2+} + 2Cl^{-1} \tag{3-31}$$

$$CuCl_3^{2-} + O_2 \rightleftarrows O_2^{2-} + Cu^{2+} + 3Cl^{-1} \tag{3-32}$$

$$CuCl_2^- + O_2 + 2H^{+} \rightarrow H_2O_2 + Cu^{2+} + 2Cl^{-1} \tag{3-33}$$

and

$$CuCl_3^{2-} + O_2 + 2H^{+} \rightarrow H_2O_2 + Cu^{2+} + 3Cl^{-1} \tag{3-34}$$

Reaction rates for reactions (3-31), (3-32), (3-33) and (3-34) could be expressed as

$$R_{CuCl_2^-,O_2^{2-}} = k_{f,CuCl_2^-,O_2^{2-}} c_{CuCl_2^-} c_{O_2} - k_{b,CuCl_2^-,O_2^{2-}} c_{O_2^{2-}} c_{Cu^{2+}} (c_{Cl^-})^2 \tag{3-35}$$

$$R_{CuCl_3^{-2},O_2^{2-}} = k_{f,CuCl_3^{-2},O_2^{2-}} c_{CuCl_3^{-2}} c_{O_2} - k_{b,CuCl_3^{-2},O_2^{2-}} c_{O_2^{2-}} c_{Cu^{2+}} (c_{Cl^-})^3 \tag{3-36}$$

$$R_{CuCl_2^-,H_2O_2} = k_{f,CuCl_2^-,H_2O_2} c_{CuCl_2^-} c_{O_2} (c_{H^+})^2 \tag{3-37}$$

and

$$R_{CuCl_3^{-2},H_2O_2} = k_{f,CuCl_3^{-2},H_2O_2} c_{CuCl_3^{2-}} c_{O_2} (c_{H^+})^2 \tag{3-38}$$

Available CO_2 in the repository air could be dissolved into the electrolyte where it could transform to HCO_3^- and CO_3^{2-}. Corresponding reactions could be expressed as

$$HCO_3^- + H^{+} \rightleftarrows CO_2 + H_2O \tag{3-39}$$

and

$$CO_3^{2+} + H^{+} \rightleftarrows HCO_3^- \tag{3-40}$$

Species involving copper carbonate complex in the current model are $CuCO_3$ and $CuHCO_3^+$ and Associated reactions could be expressed as

$$Cu^{2+} + CO_3^{2-} \rightleftarrows CuCO_3 \tag{3-41}$$

and

$$Cu^{2+} + HCO_3^- \rightleftarrows CuHCO_3^+ \tag{3-42}$$

Species involving copper hydroxide complex in the current model are $CuOH^+$, $Cu(OH)_2$, and $Cu_2(OH)_2^{2+}$. Associated reactions could be expressed as

$$Cu^{2+} + H_2O \rightleftarrows CuOH^+ + H^+ \tag{3-43}$$

$$CuOH^+ + H_2O \rightleftarrows Cu(OH)_2 + H^+ \tag{3-44}$$

and

$$Cu^{2+} + CuOH^+H_2O \rightleftarrows Cu_2(OH)_2^{2+} + H^+ \tag{3-45}$$

11 out of 17 homogeneous reactions from PHREEQC database were kept after the concentration check over a 10-year simulation.

3.5 Governing Equations

Nonlinear partial differential equations were solved in the cylindrical coordinates and the governing equation for the mass transfer within the droplet could be expressed as

$$\frac{\partial c_\mathrm{i}}{\partial t} = -\nabla \cdot \mathbf{N_i} + R_\mathrm{i} \tag{3-46}$$

where c_i is species concentration, t is the elapsed time, $\mathbf{N_i}$ is the species flux, and R_i is the homogeneous reaction rate. Species flux could be expressed as

$$\mathbf{N_i} = -z_\mathrm{i} \mathrm{F} u_\mathrm{i} c_\mathrm{i} \nabla \Phi - D_\mathrm{i} \nabla c_\mathrm{i} \tag{3-47}$$

where z_i is the number of charge, F is the Faraday constant, Φ is the electrical potential, D_i is the diffusion coefficient, and u_i is the mobility. The relation between mobility and diffusion

coefficient was assumed to follow the Nernst-Einstein equation as

$$u_{\mathrm{i}} = \frac{D_{\mathrm{i}}}{\mathrm{R}T} \tag{3-48}$$

where R is the ideal gas constant and T is the temperature. The first term in Equation (3-47) is migration and the second term is diffusion. The governing equation for conservation of charge could be expressed as

$$\nabla \cdot i = 0 \tag{3-49}$$

The current density is the result of motion of ionic species in the electrolyte, which could be expressed as

$$i = \mathrm{F}\sum_{\mathrm{i}} z_{\mathrm{i}}\mathbf{N}_{\mathrm{i}} \tag{3-50}$$

Substitution of equation (3-47) into equation (3-50) yields

$$i = -\mathrm{F}^2\nabla\Phi\sum_{i} z_{\mathrm{i}}u_{\mathrm{i}}c_{\mathrm{i}} - \mathrm{F}\sum_{i} z_{\mathrm{i}}D_{\mathrm{i}}\nabla c_{\mathrm{i}} \tag{3-51}$$

Substitution of equation (3-51) into equation (3-49) yields

$$0 = -\nabla\cdot(\kappa\nabla\Phi) - \mathrm{F}\sum_{i} z_{\mathrm{i}}\nabla\cdot(D_{\mathrm{i}}\nabla c_{\mathrm{i}}) \tag{3-52}$$

where κ is the electrolyte conductivity, which can be expressed as

$$\kappa = \mathrm{F}^2\sum_{i} z_{\mathrm{i}}u_{\mathrm{i}}c_{\mathrm{i}} \tag{3-53}$$

There are several reasons to account for the migration in the current model. The location of anodic and cathodic regions is controlled by nonuniform concentrations in the droplet, and values for potential applied on electrochemical reactions need to be obtained. As shown in Equation (3-52), Laplace's equation $\nabla^2\Phi = 0$ is only valid for uniform concentration and conductivity. The value of the total current on the electrode surface is defined using an integral equation, which could be expressed as

$$\int_0^{\mathrm{r}} i2\pi r\mathrm{dr} - \mathrm{a} = 0 \tag{3-54}$$

where r is the radial coordinate and a is the constant used to control the value of the total current. The open-circuit condition was chosen in the current model such that value of a is equal to zero. Local electroneutrality was also applied, which could be expressed as

$$\sum_{\mathrm{i}} z_{\mathrm{i}} c_{\mathrm{i}} = 0 \tag{3-55}$$

The local corrosion rate for copper was defined to be

$$R_{\mathrm{corr,local}} = \frac{\mathrm{d}L_{\mathrm{corr,local}}}{t} = \frac{i_{\mathrm{Cu^+}} M_{\mathrm{Cu}}}{\mathrm{nF}\rho_{\mathrm{Cu}}} \tag{3-56}$$

where $L_{\mathrm{corr,local}}$ is the local corrosion depth, M_{Cu} is the molecular weight of Copper, and ρ_{Cu} is the density of copper.

3.6 Boundary Conditions

The boundary conditions used to solve the set of non-linear governing equations are presented in this section. At the top of droplet labelled as Γ_{REF} in Figure 3-1, which is the furthest location from the copper metal surface, the reference potential Φ_{ref} was defined. Under the assumption that the copper plating reaction shown in reaction (3-1) and the cuprous ion oxidation shown in reaction (3-4) reached the equilibrium conditions for longer elapsed time, the value of Φ_{ref} was calculated as

$$\Phi_{\mathrm{ref}}|_{\Gamma_{\mathrm{REF}}} = \Phi^{\theta}_{\mathrm{ref}} + \frac{\mathrm{R}T}{\mathrm{F}} \ln\left(\frac{< c_{\mathrm{Cu^{2+}}} >}{(< c_{\mathrm{Cu^+}} >)^2}\right) \tag{3-57}$$

where $\Phi^{\theta}_{\mathrm{ref}}$ is the standard cell potential between copper plating and cuprous ion oxidation, and $< c_{\mathrm{Cu^+}} >$ and $< c_{\mathrm{Cu^{2+}}} >$ are average concentrations. The droplet was assumed to be initially air saturated, and concentrations for gaseous species O_2, CO_2, and H_2 in the droplet were assumed to be in equilibrium with concentrations in the repository air. The value of initial concentration for gaseous species could be calculated using Henry's law, i.e.,

$$c_{\mathrm{O_2}}(t = 0s) = H_{\mathrm{i}} p y_{\mathrm{i}} \tag{3-58}$$

where H_{i} is Henry's law constant, p is the pressure in the air and y_{i} is species fraction in the air. Available O_2 was assumed to follow an exponential decay in the repository air as described by

Scott et al. [140], and the time-dependent concentration for O_2 at the droplet boundary labeled as Γ_{DB} could be expressed as

$$c_{O_2}|_{\Gamma_{DB}} = c_{O_2}(t = 0s)\exp\left(\frac{-t}{\tau_{O_2}}\right) \tag{3-59}$$

where τ_{O_2} is time constant associated with O_2 decay. The time constant was expressed as

$$\tau_{O_2} = \frac{t_{0.1\%}}{3\ln(10)} \tag{3-60}$$

where $t_{0.1\%}$ is elapsed time associated with 0.1% O_2 remaining in the repository. For CO_2 and H_2 concentration at the droplet boundary Γ_{DB}, fixed concentration conditions were applied that could be expressed as

$$c_{CO_2}|_{\Gamma_{DB}} = H_{CO_2} p y_{CO_2} \tag{3-61}$$

and

$$c_{H_2}|_{\Gamma_{DB}} = H_{H_2} p y_{H_2} \tag{3-62}$$

Zero fluxes were assumed for ionic species at the droplet boundary Γ_{DB} that were shown as

$$\mathbf{N}_i|_{\Gamma_{DB}} = 0 \tag{3-63}$$

At the copper metal surface Γ_{WE}, fluxes for reacting species in electrochemical reactions could be expressed as

$$\mathbf{N}_i|_{\Gamma_{WE}} = \frac{-s_i i_{F,i}}{n\mathrm{F}} \tag{3-64}$$

where n is the number of electrons transfer in the electrochemical reactions and the total current density on the copper metal surface Γ_{WE} was the sum of each individual current density shown as

$$i|_{\Gamma_{WE}} = \sum_i i_{F,i} \tag{3-65}$$

Expressions of the current density for each electrochemical reactions are described in section 3.2.

3.7 Influence of CuCl and Cu_2O Films on Current Density

With the presence of CuCl and Cu_2O film on the copper metal surface, electrochemical reactions were assumed to be slowed down. As Shown in Figure 3-3, four differen scenarios for

surface coverage were considered. No films were formed on the copper metal surface initially and surface coverage for both films were zero shown in Figure 3-3(a). CuCl film was found to be developed first on the copper metal surface shown in Figure 3-3(b) such that $0 < \gamma_{CuCl} < 1$ and $0 < \gamma_{Cu_2O} \ll 0$. Cu_2O film was assumed to grow underneath CuCl film. The third scenario was when $\gamma_{CuCl} > 1$ and $0 < \gamma_{Cu_2O} < 1$ shown in Figure 3-3(c), and the last scenario was when surface coverage for both films became larger than one such that $\gamma_{CuCl} > 1$ and $\gamma_{Cu_2O} > 1$. Coupled switched reaction rate constant was used for each individual current density under different scenarios and associated reaction rate constant could be adjusted shown as

$$k_i = \begin{cases} ((1-\gamma_{CuCl}) + f_{CuCl}\gamma_{CuCl})k_{i,bare} & 0 < \gamma_{CuCl} < 1 \text{ and } 0 < \gamma_{Cu_2O} \ll 1 \\ (f_{CuCl}(1-\gamma_{Cu_2O}) + f_{Cu_2O}\gamma_{Cu_2O})k_{i,bare} & \gamma_{CuCl} > 1 \text{ and } 0 < \gamma_{Cu_2O} < 1 \\ f_{Cu_2O}k_{i,bare} & \gamma_{CuCl} > 1 \text{ and } \gamma_{Cu_2O} > 1 \end{cases} \tag{3-66}$$

where $f_{CuCl} = 50\%$ and $f_{Cu_2O} = 2\%$ are reaction rate constant factors influenced by CuCl and Cu_2O films respectively.

3.8 Influence of CuCl Film on Surface Oxygen Concentration and Potential

As shown in Figure 3-4, potential and surface oxygen concentration were adjusted to account for the presence of CuCl film. The Bruggeman equation [141] was used to calculate the effective diffusion coefficient for oxygen.

$$D_{O_2,eff} = \varepsilon_{CuCl}^{1.5} D_{O_2} \tag{3-67}$$

where ε_{CuCl} is the porosity of CuCl film. The current density for oxygen reduction (3-12) could be expressed in terms of oxygen flux given as

$$i_{O_2} = -nFD_{O_2,eff} \left.\frac{dc_{O_2}}{dy}\right|_{y=0} \tag{3-68}$$

where y is the axial coordinate. In the presence of a thin film on the metal surface, equation 3-68 could be expressed as[142]

$$i_{O_2} = -nFD_{O_2,eff} \frac{c_{O_2}(\delta_{CuCl}) - c_{O_2}(0)}{\delta_{CuCl}} \tag{3-69}$$

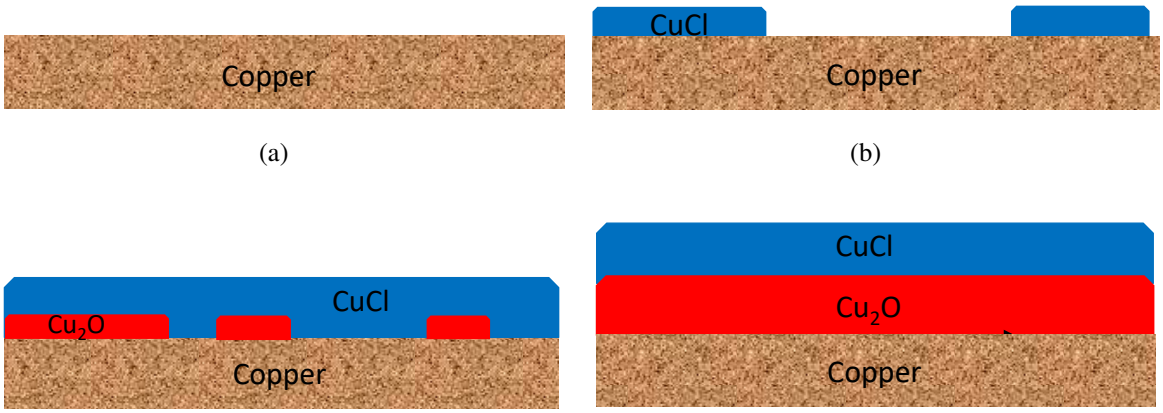

Figure 3-3. Schematic representation of CuCl and Cu_2O film developed on copper metal surface: a) $\gamma_{CuCl} = 0$ and $\gamma_{Cu_2O} = 0$, b) $0 < \gamma_{CuCl} < 1$ and $0 < \gamma_{Cu_2O} \ll 1$, c) $\gamma_{CuCl} > 1$ and $0 < \gamma_{Cu_2O} < 1$ d)$\gamma_{CuCl} > 1$ and $\gamma_{Cu_2O} > 1$.

Figure 3-4. Schematic representation of CuCl Film on the copper metal surface.

where δ_{CuCl} is thickness of CuCl film. The current density for oxygen reduction could be expressed using either kinetic expression or mass-transfer expression. Thus, the O_2 concentration on the metal surface could be obtained by setting equation (3-14) equal to equation (3-69).

$$c_{O_2}(0) = \frac{c_{O_2}(\delta_{CuCl})}{\frac{k_{O_2}\delta_{CuCl}}{nFD_{O_2,eff}}\exp(-b_{O_2}(\Phi_m - \Phi_0)) + 1} \tag{3-70}$$

The influence factor of CuCl film on surface oxygen concentration was defined as

$$\lambda = \frac{c_{O_2}(0)}{c_{O_2}(\delta_{CuCl})} = \frac{c_{O_2}(\delta_{CuCl})}{\frac{k_{O_2}\delta_{CuCl}}{nFD_{O_2,eff}}\exp(-b_{O_2}(\Phi_m - \Phi_0)) + 1} \tag{3-71}$$

The approach to account for the influence of CuCl film on potential was similar to that used by Riemer et al. [143] in the cathodic protection model for long pipelines. Potential drop through the CuCl thin film was assumed to follow the Ohm's law given as

$$i = \frac{\Phi(\delta_{CuCl}) - \Phi_0}{\rho'_{CuCl}\delta_{CuCl}} \tag{3-72}$$

where ρ'_{CuCl} is the resistivity of CuCl film that was given by

$$\rho'_{CuCl} = \frac{1}{\varepsilon^{1.5}\kappa} \tag{3-73}$$

Thus, a relation between potential outside the diffuse part of the double layer and outside CuCl film was given by

$$\Phi_0 = \Phi(\delta_{CuCl}) - i\rho'_{CuCl}\delta_{CuCl} \tag{3-74}$$

As shown in equations (3-74) and (3-70), oxygen would decrease from outside CuCl film to metal surface, but potential would either decrease or increase depending on the sign of total current density. Instead of directly solving for Φ_0 and $c_{O_2}(0)$, $\Phi(\delta_{CuCl})$ and $c_{O_2}(\delta_{CuCl})$ became dependent variables. For example, current density for oxygen reduction shown in equation (3-14) could be expressed as

$$i_{F,O_2} = -k_{O_2}\lambda c_{O_2}(\delta_{CuCl})\exp(-b_{O_2}(\Phi_m - (\Phi(\delta_{CuCl}) - i_{t_{i-1}}\rho'_{CuCl}\delta_{CuCl})) \tag{3-75}$$

where $i_{t_{i-1}}$ is the total current density in previous time step to avoid circular dependence issue.

3.9 Influence of Temperature on Model Parameters

A simplified 3-D finite element model was built by Guo [144] that accounted for the thermal response on the Canadian used nuclear fuel container surface. The model was based on previously developed models, but using modified near-filed boundary conditions. The temperature on the container surface was calculated for a million years and the transient temperature is shown in Figure 3-5. The initial temperature in DGR is 284 K, and it is expected to increase to a peak value of 357 K in 45 years. The temperature on the container surface is then expected to cool down to 284 K in one million years, which is the same as the initial temperature.

The transient temperature shown in Figure 3-5 was implemented as a uniform value through the droplet for every time step using an interpolation function. The influence of temperature was considered on several model parameters, including equilibrium constants and reaction rate constants for homogeneous reactions, diffusion coefficients, rate constants and kinetic parameters for electrochemical reactions, solubility product constants, and Henry's law constants. The Van't Hoff equation [145] was used to account for the influence of temperature on homogeneous reaction equilibrium constant, reaction rate constant for film formation, solubility product constant and Henry's law constant, as

$$K_{\mathrm{eq,i}}(T) = K_{\mathrm{eq}}(T_0)\exp\left(\frac{-\Delta_{\mathrm{r}}\mathrm{H}_{\mathrm{i}}^{\theta}}{\mathrm{R}}\left(\frac{1}{T}-\frac{1}{T_0}\right)\right) \tag{3-76}$$

$$k_{\mathrm{f/b,i}}(T) = K_{\mathrm{f/b,i}}(T_0)\exp\left(\frac{-\Delta_{\mathrm{r}}\mathrm{H}_{\mathrm{i}}^{\theta}}{\mathrm{R}}\left(\frac{1}{T}-\frac{1}{T_0}\right)\right) \tag{3-77}$$

$$K_{\mathrm{sp,i}}(T) = K_{\mathrm{sp}}(T_0)\exp\left(\frac{-\Delta_{\mathrm{r}}\mathrm{H}_{\mathrm{i}}^{\theta}}{\mathrm{R}}\left(\frac{1}{T}-\frac{1}{T_0}\right)\right) \tag{3-78}$$

and

$$H_{\mathrm{i}}(T) = H_{\mathrm{i}}(T_0)\exp\left(\frac{-\Delta_{\mathrm{r}}\mathrm{H}_{\mathrm{i}}^{\theta}}{\mathrm{R}}\left(\frac{1}{T}-\frac{1}{T_0}\right)\right) \tag{3-79}$$

respectively, where $\Delta_{\mathrm{r}}\mathrm{H}^{\theta}$ is that change of enthalpy and $T_0 = 298.15K$ is the room temperature. An analytic expression suggested by PHREEQC [136, 137, 138] was also used to account for the

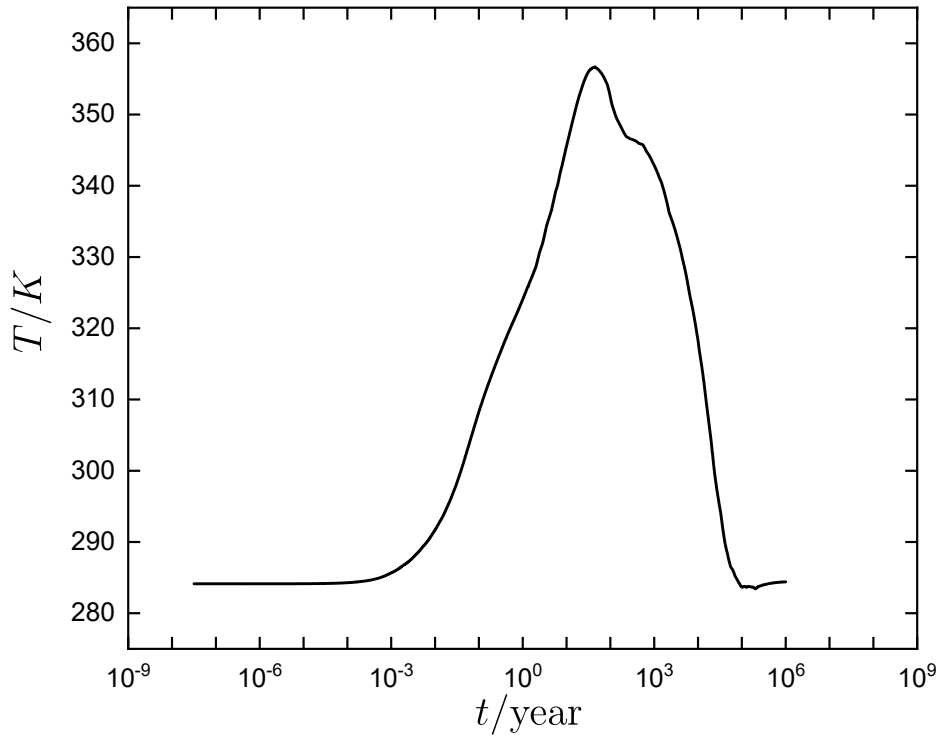

Figure 3-5. Temperature on the container surface in Canadian DGR.

influence of temperature on homogeneous reaction equilibrium constant, which was given by

$$\log_{10} K_{\mathrm{eq}}(T) = \mathrm{A}_1 + \mathrm{A}_2 T + \frac{\mathrm{A}_3}{T} + \mathrm{A}_4 \log_{10} T + \frac{\mathrm{A}_5}{T^2} \tag{3-80}$$

where A_1, A_2, A_3, A_4 and A_5 are analytic constants. For the dilute solutions, diffusion coefficients could be expressed as a function of temperature using the Stokes-Einstein equation [146] given as

$$D_{\mathrm{i}}(T) = \frac{\mathrm{k_B} T}{6\pi \nu_{\mathrm{s}}(T) r_{\mathrm{i}}} \tag{3-81}$$

where $\mathrm{k_B}$ is the Boltzman constant, r_{i} is the dynamic solvent viscosity, and r_{i} is the radius of diffusing particle. Water is the solvent in the current model, and the temperature-dependent viscosity of water could be expressed using Vogel–Fulcher–Tammann equation [147, 148, 149] as

$$\nu_{\mathrm{H_2O}}(T) = \mathrm{A} \times 10^{\frac{\mathrm{B}}{T - \mathrm{C}}} \tag{3-82}$$

where A $= 2.414 \times 10^{-5}$Pa.s, B $= 247.8$K and C $= 140.0$K are constants. The expression to account for influence of temperature on diffusion coefficient was given by

$$D_{\mathrm{i}}(T) = \frac{BD_{\mathrm{i}}(T_0)T}{T_0} 10^{\left(\frac{1}{T-\mathrm{C}} - \frac{1}{T_0-\mathrm{C}}\right)} \tag{3-83}$$

As discussed by Bard and Faulkner [150], a relation close to Arrhenius equation could be used to account for the influence of temperature on electrochemical reaction rate constant, which was expressed as

$$k_{\mathrm{i}}(T) = k_{\mathrm{i}}(T_0) \exp\left(\frac{-E}{\mathrm{R}}\left(\frac{1}{T} - \frac{1}{T_0}\right)\right) \tag{3-84}$$

where E is the activation energy. As shown in equation (3-3), kinetic parameters for electrochemical reactions were inverse linear to the temperature and the relation between two temperatures for b_{i} could be expressed as

$$b_{\mathrm{i}}(T) = \frac{b_{\mathrm{i}}(T_0)T_0}{T} \tag{3-85}$$

Values of parameters that were used to account for the influence of temperature will be given in Chapter 4.

CHAPTER 4
10-YEAR SIMULATION FOR COPPER CORROSION MODEL

In the current study, two extreme conditions were chosen such that oxygen concentration in the repository air would reach 0.1% of initial oxygen concentration either in $t_{0.1\%} = 5$ years or $t_{0.1\%} = 5$ weeks, corresponding to $\tau_{O_2} = 0.73$ years or $\tau_{O_2} = 0.73$ weeks in equation (3-60). As shown in Figure 4-1, the oxygen concentration at the droplet boundary was plotted in right y-axis as functions of elapsed time in Figure 4-1. The oxygen concentration decreased from 3.39×10^{-7} mol/cm^3 with $t_{0.1\%} = 5$ years in 10 years. For smaller $t_{0.1\%} = 5$ weeks, the oxygen concentration became smaller than concentration of one molecule in the droplet $c_{m,d}$ in 0.53 years. Temperature, plotted on the left y-axis as functions of elapsed time increased from 284 K to 346 K in 10 years. Parameters used in the simulations at room temperature $T_0 = 298.15$ K are shown in Table 4-1, and parameters used to account for the influence on model parameters are shown in Table 4-2.

4.1 Simulation Results

The model showed a 10-year time-dependent radial distribution of anodic and cathodic current density, surface coverage of CuCl film and Cu_2O film, and localized corrosion rates and depths. It also showed a distribution of pH, potential, and concentrations of dissolved gaseous and ionic species through the entire droplet. Temperature and oxygen concentration were shown to have a strong contribution to the simulation results.

4.1.1 Current Density and Potential

The open-circuit condition was chosen in the current model. To confirm that this condition was satisfied, ratios of maximum current in the individual current and the total current were checked. Ratios of absolute value of maximum current and absolute value of total current are presented in Figure 4-2(a) as a functions of elapsed time for both oxygen decay cases. $|i_{total}|/|i_{max}|$ has a largest value of 3.5×10^{-4} and a smallest value of 9.8×10^{-15}, which indicates the open-circuit condition is satisfied at every time step. Ratios of absolute value of maximum current and absolute value of total current $|i_{total}|/|i_{max}|$, presented in Figure 4-2(b), follow a pseudo log-normal distribution with a mean value of 3.5×10^{-6} for faster oxygen decay and a mean value of 8.9×10^{-6} for slower oxygen decay.

Table 4-1. Parameters used in the simulations at $T_0 = 298.15$K

Parameter Symbol	Value	Parameter Symbol	Value
$b_{Cu^+,a}$	19.5 V^{-1}	$k_{Cu^{2+},c}$	0.1 A cm/mol
$b_{Cu^+,c}$	19.5 V^{-1}	$k_{CuCl_2^-}$ [134] ⋆	1.63×10^{10} A cm^7/mol^3
$b_{CuCl_2^-,c}$	19.5 V^{-1}	$k_{H^+,a}$ [151] ⋆	4.15×10^{5} A cm/mol
$b_{Cu^{2+},a}$	19.5 V^{-1}	$k_{H^+,c}$ [151] ⋆	3.28×10^{12} A cm^4/mol^2
$b_{Cu^{2+},c}$	19.5 V^{-1}	k_{O_2} [134] ⋆	6.57 A cm/mol
$b_{H^+,a}$ [151]	38.4 V^{-1}	$k_{HO_2^-}$	1×10^{-4} A cm/mol
$b_{H^+,c}$ [151]	24.2 V^{-1}	$k_{f,CuCl}$	10 cm^3/ mol s
b_{O_2}	19.5 V^{-1}	$k_{f,CuCl_2^-}$ [134]	1×10^{-5} cm^3/ mol s
$b_{HO_2^-}$	19.5 V^{-1}	$k_{b,CuCl_2^-}$ [134]	1370 s^{-1}
D_{Cl^-} [49]	2.03×10^{-5} cm^2/s	k_{f,Cu_2O}	1×10^{-6} cm^3/ mol s
D_{CO_2} [152]	2.02×10^{-5} cm^2/s	$K_{sp,CuCl}$ [153]	1.72×10^{-1} mol^2/cm^6
$D_{CO_3^{2-}}$ [152]	8.10×10^{-6} cm^2/s	K_{sp,Cu_2O} [154]	1.72×10^{-14}
D_{Cu^+}	1.64×10^{-5} cm^2/s	$k_{f,CuCl_2^-,O_2^{2-}}$ [139]	1.20×10^{2} cm^3/ mol s
$D_{Cu^{2+}}$ [49]	7.33×10^{-6} cm^2/s	$k_{b,CuCl_2^-,O_2^{2-}}$ [139]	1.83×10^{17} cm^9/mol^3 s
$D_{CuCl_2^-}$ [155]	1.20×10^{-5} cm^2/s	$k_{f,CuCl_3^{-2},O_2^{-2}}$ [139]	4.40×10^{2} cm^3/ mol s
$D_{CuCl_3^{2-}}$ [155]	1.19×10^{-5} cm^2/s	$k_{b,CuCl_3^{-2},O_2^{-2}}$ [139]	3.06×10^{18} cm^12/mol^4 s
D_{CuCl^+} [156]	1.30×10^{-5} cm^2/s	$k_{f,CuCl_2^-,H_2O_2}$ [139]	2.00×10^{32} cm^9/mol^3 s
D_{CuCl_2} [156]	1.30×10^{-5} cm^2/s	$k_{f,CuCl_3^{-2},H_2O_2}$ [139]	2.00×10^{32} cm^{12}/mol^4 s
D_{CuCO_3} [157]	1.27×10^{-5} cm^2/s	$K_{eq,CuCl_3^{-2}}$ [137]	1.58×10^{3} cm^3/mol
$D_{CuHCO_3^+}$ [157]	1.27×10^{-5} cm^2/s	$K_{eq,CuCl^+}$ [137]	2.69×10^{3} cm^3/mol
D_{CuOH^+} [157]	4.50×10^{-5} cm^2/s	$K_{eq,CuCl_2}$ [137]	2.57×10^{2} cm^3/mol
$D_{Cu(OH)_2}$ [157]	4.50×10^{-5} cm^2/s	K_{eq,CO_2} [137]	2.25×10^{9} cm^3/mol
$D_{Cu_2(OH)_2}$ [157]	4.50×10^{-5} cm^2/s	K_{eq,HCO_3^-} [137]	2.13×10^{13} cm^3/mol
D_{H^+} [49]	9.31×10^{-5} cm^2/s	$K_{eq,CuCO_3}$ [137]	5.37×10^{9} cm^3/mol
D_{H_2} [158]	5.11×10^{-5} cm^2/s	$K_{eq,CuHCO_3^+}$ [137]	5.01×10^{5} cm^3/mol
$D_{HO_2^-}$ [159]	2.30×10^{-5} cm^2/s	$K_{eq,CuOH^+}$ [137]	1×10^{-11} mol/cm^3
$D_{H_2O_2}$ [160]	2.00×10^{-5} cm^2/s	$K_{eq,Cu(OH)_2}$ [137]	2.09×10^{-12} mol/cm^3
$D_{HCO_3^-}$ [152]	1.17×10^{-5} cm^2/s	$K_{eq,Cu2(OH)_2}$ [137]	4.38×10^{-3}
D_{Na^+} [49]	2.02×10^{-5} cm^2/s	K_{eq,H_2O} [137]	1×10^{-20} mol^2/cm^6
D_{O_2} [161]	1.97×10^{-5} cm^2/s	y_{O_2}	0.21
$D_{O_2^{2-}}$ [162]	4.40×10^{-8} cm^2/s	y_{H_2}	5×10^{-7}
D_{OH^-} [49]	5.26×10^{-8} cm^2/s	y_{CO_2}	4×10^{-4}
H_{O_2} [163]	1.22×10^{-6} mol/cm^3 atm	$\delta_{m,CuCl}$	1 nm
H_{H_2} [163]	7.90×10^{-7} mol/cm^3 atm	δ_{m,Cu_2O} [164]	0.98 nm
H_{CO_2} [163]	3.34×10^{-5} mol/cm^3 atm	ρ_{Cu}	8.96 g/cm^3
$k_{Cu^+,a}$ [151] ⋆	1×10^{-7} A/cm^2	ρ_{Cu_2O}	6 g/cm^3
$k_{Cu^+,c}$ [151] ⋆	1×10^{-7} A cm/mol	ρ_{CuCl}	4.14 g/cm^3
$k_{Cu^{2+},a}$	1×10^{-4} A cm/mol	ε_{CuCl}	0.1

⋆ denotes values of parameters were adjusted from literature

Table 4-2. Parameters used to account for the influence of temperature on model parameters

Activation energy E_i	Value	units	change of enthalpy $\Delta_r H_i^\theta$	Value	Units
$E_{k_{Cu^+,a}}$ [165]	39.74	kJ/mol	$\Delta_r H^\theta_{k_{f,CuCl}}$ [137]	-17.32	kJ/mol
$E_{k_{Cu^+,c}}$ [166]	40	kJ/mol	$\Delta_r H^\theta_{K_{sp,CuCl}}$ [153]	57.65	kJ/mol
$E_{k_{Cu^{2+},a}}$ [167]	40	kJ/mol	$\Delta_r H^\theta_{k_{f,Cu_2O}}$ [134]	60	kJ/mol
$E_{k_{Cu^{2+},c}}$ [167]	40	kJ/mol	$\Delta_r H^\theta_{K_{sp,Cu_2O}}$ [134]	-20	kJ/mol
$E_{k_{CuCl_2^-}}$ [134]	45	kJ/mol	$\Delta_r H^\theta_{k_{f,CuCl_2^-}}$ [137]	-1.75	kJ/mol
$E_{k_{H_2,a}}$ [168]	20	kJ/mol	$\Delta_r H^\theta_{k_{b,CuCl_2^-}}$ [137]	-1.75	kJ/mol
$E_{k_{H_2,c}}$ [168]	20	kJ/mol	$\Delta_r H^\theta_{K_{eq,CuCl^+}}$ [137]	36.2	kJ/mol
$E_{k_{O_2}}$ [169]	20	kJ/mol	$\Delta_r H^\theta_{K_{eq,CuCl_2}}$ [137]	7.99	kJ/mol
$E_{k_{HO_2^-}}$ [169, 134]	40	kJ/mol	$\Delta_r H^\theta_{H_{O_2}}$ [163]	-14.13	kJ/mol
			$\Delta_r H^\theta_{H_{H_2}}$ [163]	-4.41	kJ/mol
			$\Delta_r H^\theta_{H_{CO_2}}$ [163]	-19.95	kJ/mol

Constants A_i

Equilibrium constant	A_1	A_2 (K^{-1})	A_3 (K)	A_4	A_5(K^2)
K_{eq,CO_2} [137]	107.887	0.0325	-5151.790	-38.926	563714
K_{eq,HCO_3^-} [137]	356.309	0.0609	-21834.370	-126.834	1684915
K_{eq,H_2O} [137]	-283.971	-0.0507	13323.000	102.244	-1119669

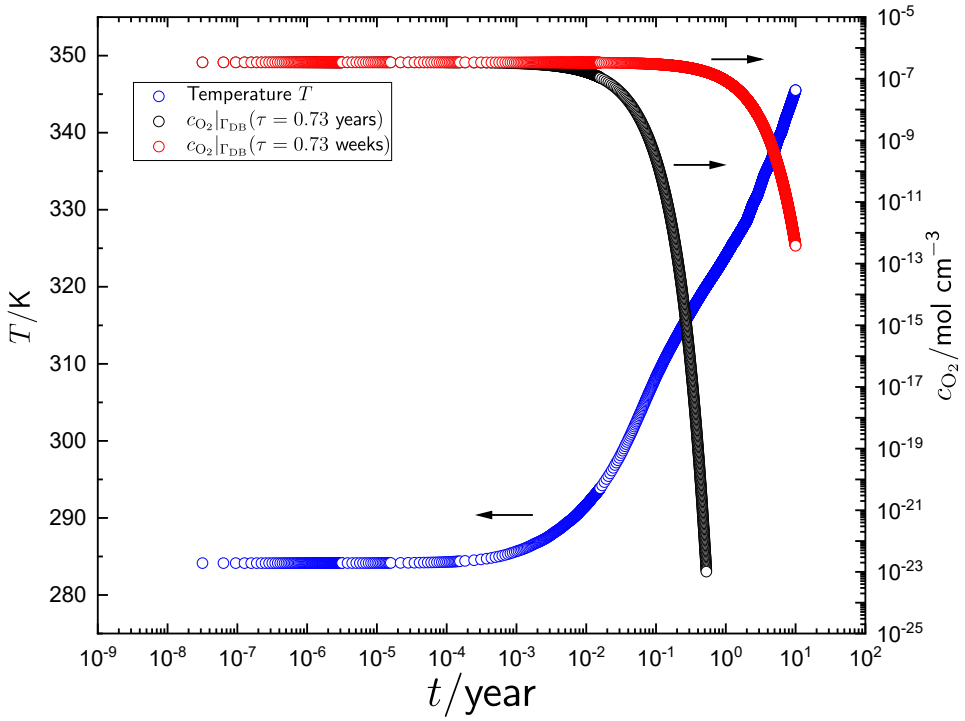

Figure 4-1. Temperature and oxygen concentration at the droplet boundary as functions of elapsed time for 10-year simulation

The absolute value of current for each individual electrochemical reaction $|i_{F,i}|$ as functions of elapsed time for slower oxygen decay with $t_{0.1\%} = 5$ years is shown in Figure 4-3(a) and $|i_{F,i}|$ for system with faster oxygen decay with $t_{0.1\%} = 5$ weeks is shown in Figure 4-3(b). For $t_{0.1\%} = 5$ weeks, copper dissolution was the dominant anodic reaction and oxygen reduction reaction was the dominant cathodic reaction in early elapsed times. At $t = 1.54 \times 10^{-4}$ years, both dominant currents became slightly smaller because CuCl film was formed on the copper metal surface with surface coverage γ_{CuCl} larger than one monolayer thickness. Then, the dominant current became larger due to the elevation of temperature. At $t = 0.12$ years, the dominant currents became much smaller due to the formation of Cu_2O film with a surface coverage γ_{CuCl} larger than one monolayer thickness. As oxygen was gradually consumed by electrochemical and homogeneous reactions and oxygen supply from the repository air decays, HO_2^- reduction became the dominant cathodic reaction to balance the copper dissolution at $t = 2.67$ years. In even longer elapsed time, copper dissolution and HO_2^- reduction were the dominant reactions and associated currents

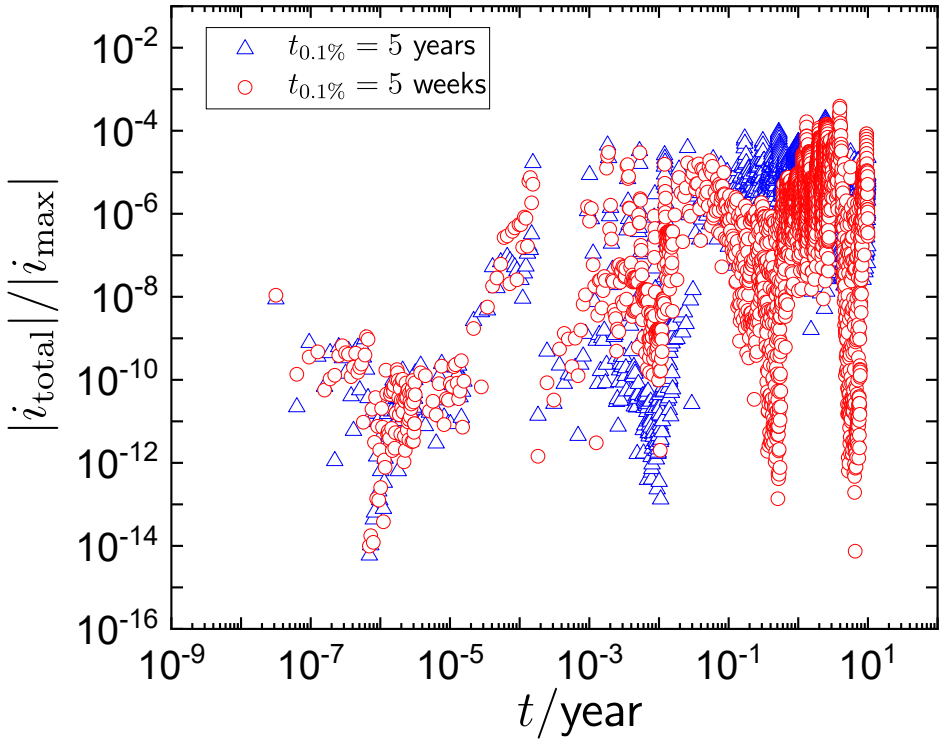

(a)

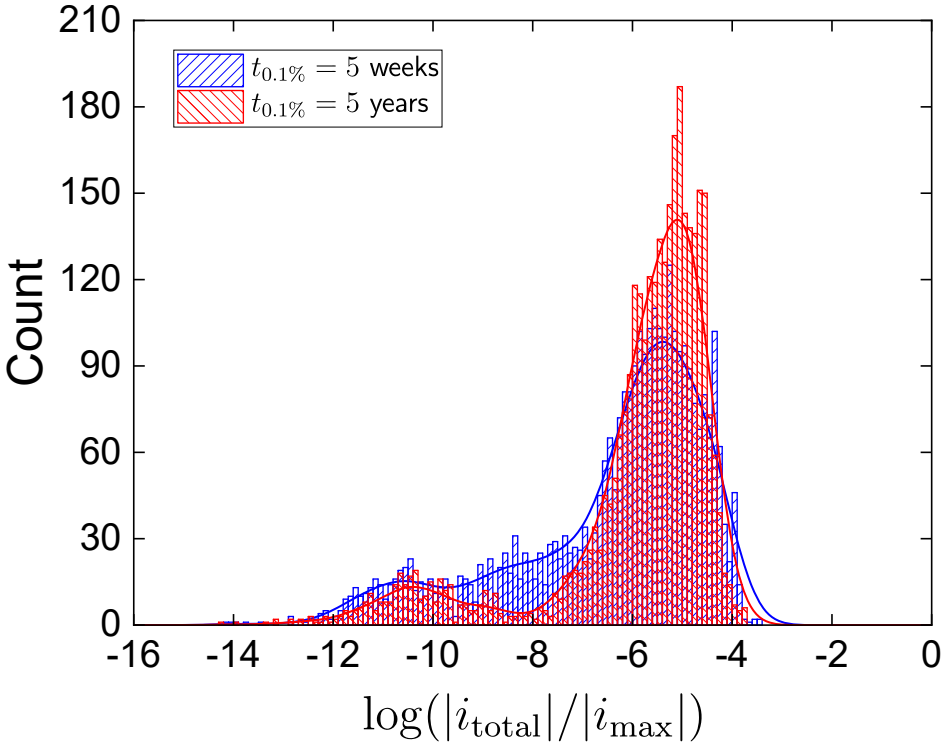

(b)

Figure 4-2. Current accuracy check for two oxygen decays: a) Ratio of absolute value of maximum current and absolute value of total current as functions of elapsed time and b) Histograms of $\log(|i_{\text{total}}|/|i_{\max}|)$, where the solid line is Kernel Smooth distribution curve.

gradually decreased in 10 years. For other reactions within 10 years, the current for Cu^{2+} reduction and $CuCl_2^-$ reduction initially increased to a peak and then decreased, but the current for $CuCl_2^-$ reduction was much smaller compared to other currents. The current for the H_2 reaction initially kept constant and then decreased to a smaller value in 10 years. For $t_{0.1\%} = 5$ weeks, the oxygen concentration decayed faster and the current for HO_2^- reduction starts to balance the current for copper dissolution at an earlier elapsed time $t = 0.09$ years. As HO_2^- was consumed in the droplet, Cu^+ plating and Cu^+ oxidation became dominant cathodic and anodic reactions respectively at $t = 4.43$ years and associated currents tended to decrease in 10 years. Other reactions behaved very similar as compared to reactions with $t_{0.1\%} = 5$ years. Some currents showed discontinuity such as current for $CuCl_2^-$ reduction since any current smaller than the total current was set to zero in Figure 4-3.

Average values of potential applied on electrochemical reactions are plotted as functions of elapsed time in Figure 4-4 for two extreme conditions. Potential $< \Phi_m - \Phi_0 >$ became more cathodic for both cases, in which the value of $< \Phi_m - \Phi_0 >$ changed from 0.08 V to -0.30 V for $t_{0.1\%} = 5$ years and changed from 0.08 V to -0.13 V for $t_{0.1\%} = 5$ weeks in 10-year simulation. At $t = 1.54 \times 10^{-4}$ years, a small potential jump was due to the formation of CuCl film with the surface coverage larger than one monolayer thickness.

Absolute values of anodic and cathodic current for reversible electrochemical reactions (3-1) (3-4) and (3-16) are plotted as functions of elapsed time shown in Figure 4-5. For $t_{0.1\%} = 5$ years, current for copper dissolution was much larger than current for copper plating for all the time as shown in Figure 4-5(a), current for Cu^+ oxidation was much larger than Cu^{2+} reduction all the time as shown in Figure 4-5(b) and, current for H_2 reduction was larger than current for H_2 evolution as shown in Figure 4-5(c). For currents with $t_{0.1\%} = 5$ weeks presented in Figures 4-5(d), 4-5(e) and 4-5(f), it showed similar behavior compared to currents with $t_{0.1\%} = 5$ years in early elapsed time, but anodic current and cathodic current became overlapped to each other as elapsed time t approached 10 years.

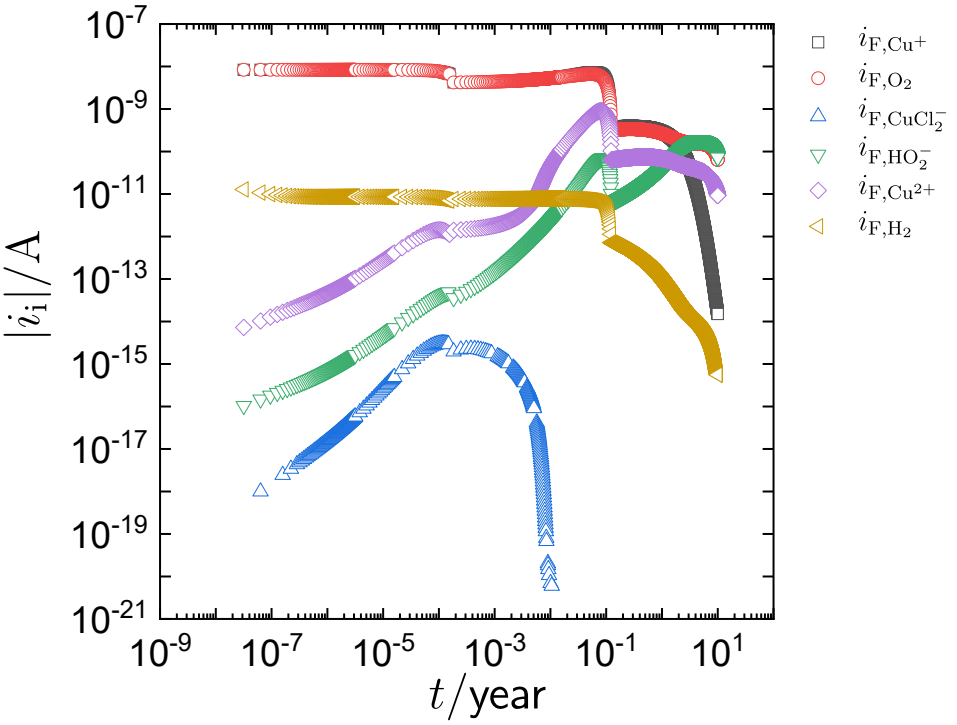

(a)

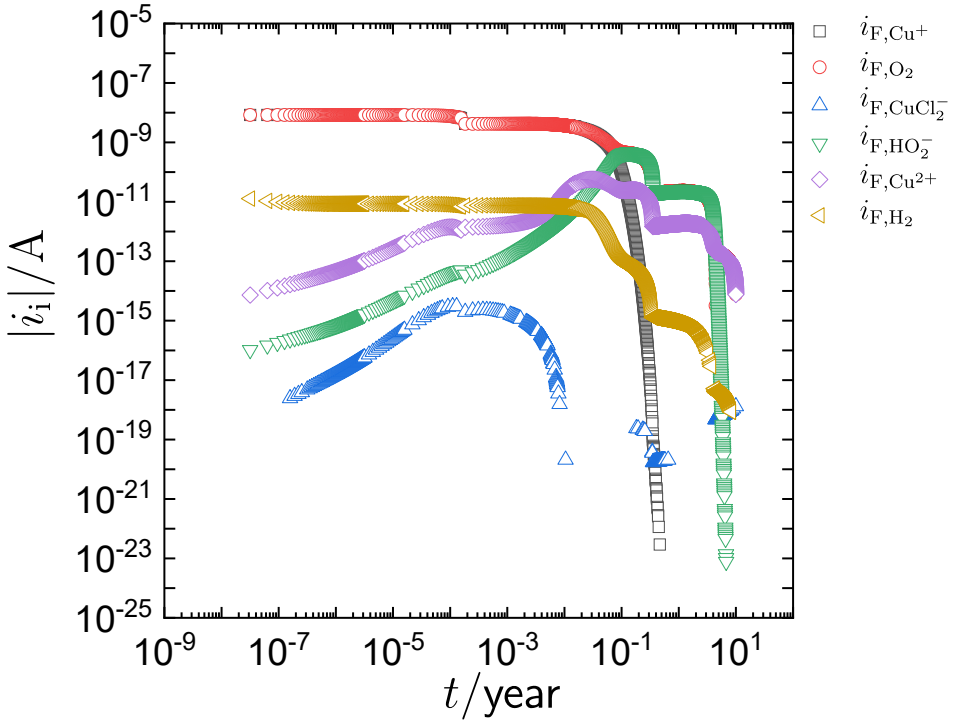

(b)

Figure 4-3. The absolute value of current as functions of elapsed time for each individual electrochemical reaction: a) $t_{0.1\%} = 5$ years, b) $t_{0.1\%} = 5$ weeks

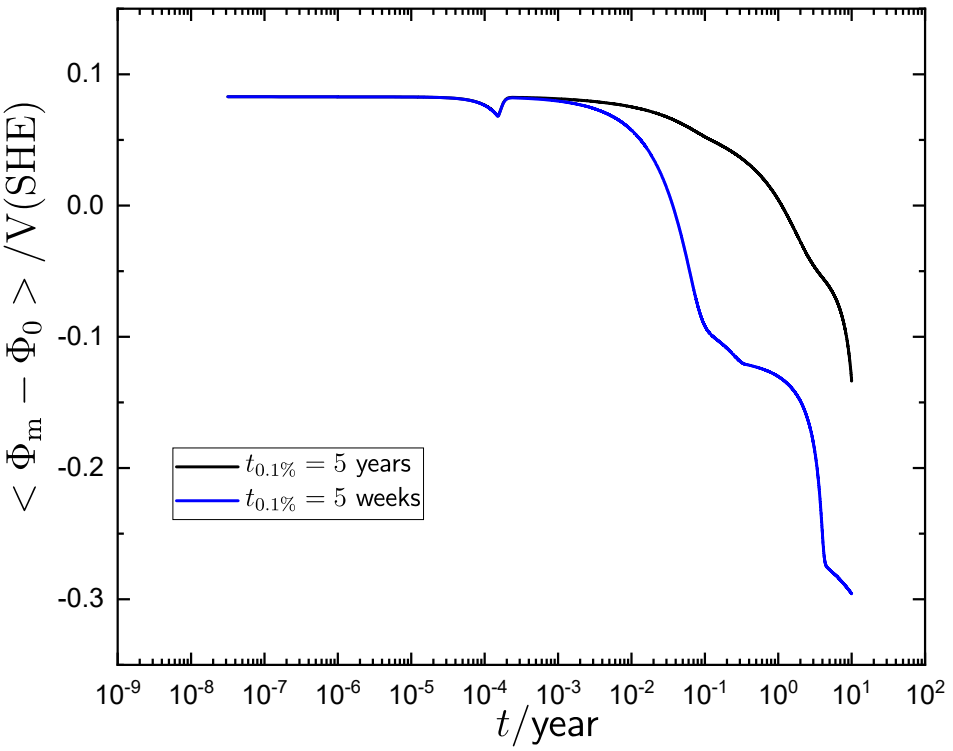

Figure 4-4. Potentials applied on electrochemical reactions as functions of elapsed time for $t_{0.1\%} = 5$ years and $t_{0.1\%} = 5$ weeks

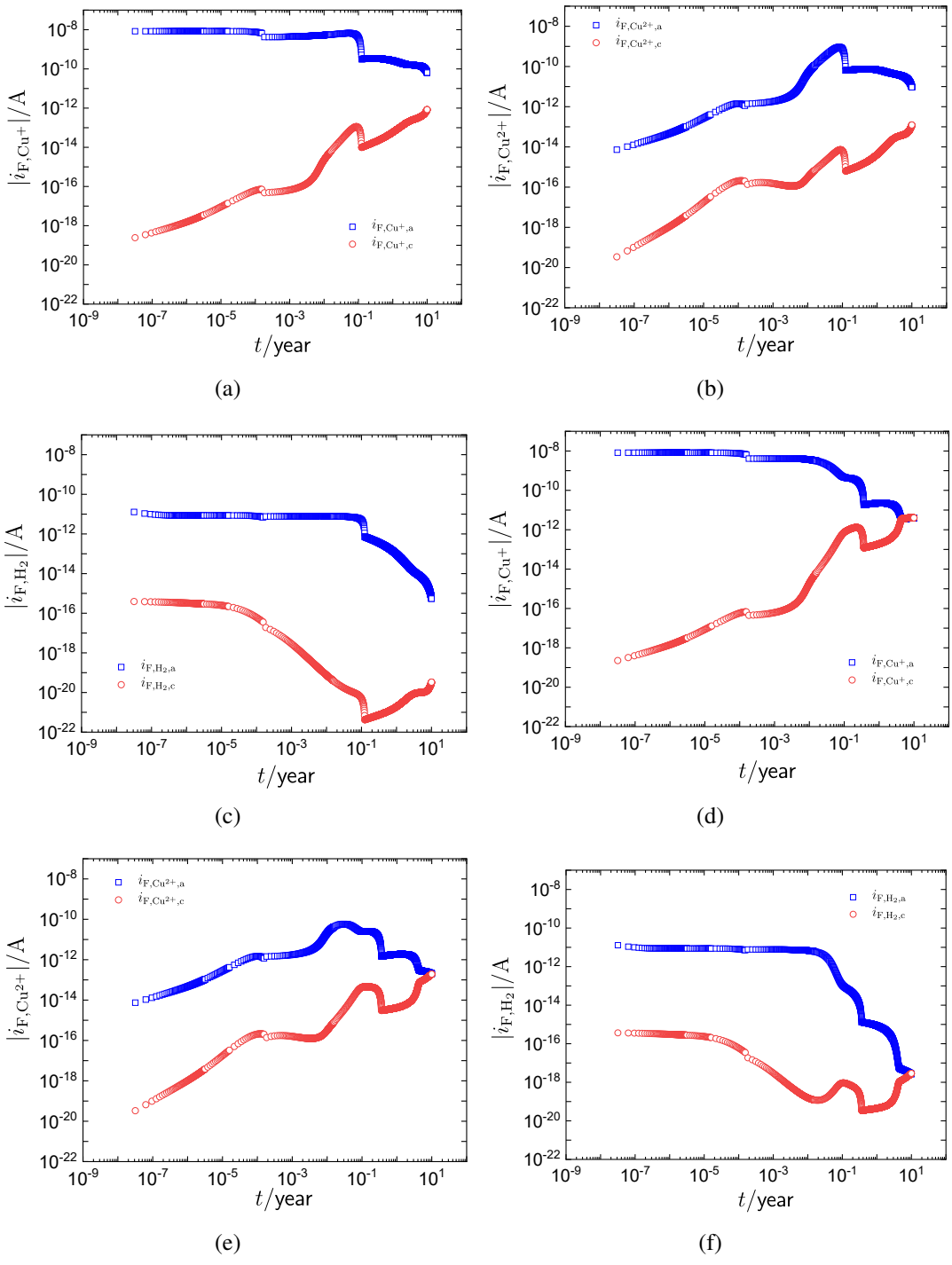

Figure 4-5. The absolute value of anodic and cathodic current as functions of elapsed time for reversible electrochemical reactions: a) reaction (3-1) with $t_{0.1\%} = 5$ years, b) reaction (3-4) with $t_{0.1\%} = 5$ years, c) reaction (3-16) with $t_{0.1\%} = 5$ years, d) reaction (3-1) with $t_{0.1\%} = 5$ weeks, and f) reaction (3-4) with $t_{0.1\%} = 5$ weeks, e) reaction (3-16) with $t_{0.1\%} = 5$ weeks.

Anodic and cathodic regions on the copper metal surface were not predefined, but were calculated from locally non-uniform potentials and concentrations. The ratio of anodic current density and absolute cathodic current density $i_a/|i_c|$ is presented in Figure 4-6(a) as a function of normalized radial position with elapsed times as a parameter for slower oxygen decay. A value for $i_a/|i_c|$ larger than 1 represents the anodic region, and $i_a/|i_c|$ smaller than 1 represents the cathodic region. To identify transient changes of anodic and current regions more easily, $i_a/|i_c|$ was plotted as functions of elapsed time at droplet center, periphery and at $r/r_0 = 0.9$, as shown in Figure 4-6(b). At the center of the droplet, a cathodic region is seen initially, then $i_a/|i_c|$ increased to a anodic region with a peak value of 1.003 at $t = 4.4 \times 10^{-6}$ years, $i_a/|i_c|$ decreased to a cathodic region with a peak value of 0.992 at $t = 1.5 \times 10^{-4}$ years, and $i_a/|i_c|$ increased to another anodic region with a peak value of 1.003 at $t = 0.07$ years. The periphery of the droplet moved initially from an anodic region with a peak value of 1.05 to a cathodic region with a peak value of 0.998 at 0.07 years. At $t = 1.5 \times 10^{-4}$ years, the sudden jump of the current ratio at the droplet periphery was due to the surface coverage of CuCl film becoming larger than 1 monolayer thickness. For a location between the center and periphery of $r/r_0 = 0.9$, a cathodic region was observed initially when an anodic current was seen at the periphery. At longer elapsed times, $i_a/|i_c|$ tended toward to a value close to 1 at $t = 5$ years, and it was hard to distinguish the cathodic and anodic regions on the copper metal surface. For faster oxygen decay, the radial distribution of $i_a/|i_c|$ is shown in Figure 4-7(a), and $i_a/|i_c|$ is shown in Figure 4-7(b) for the droplet boundary, periphery and $r/r_0 = 0.9$. Transitions of current density were similar compared to slower oxygen decay, but $i_a/|i_c|$ became close to 1 at $t = 0.19$ years.

The radial distribution of total current density for slower oxygen decay is shown in Figure 4-8 with elapsed time as a parameter. For $t = 2.7 \times 10^{-3}$ years in Figure 4-8(a), both droplet center and periphery showed a anodic region with a maximum anodic current density of 5 nA/cm^2, and locations in between showed an cathodic region with a maximum cathodic current density of -0.2 nA/cm^2. As shown in Figures 4-8(b) 4-8(c) and 4-8(d), the magnitude of current density became smaller as elapsed time increased. Cathodic and anodic regions were more

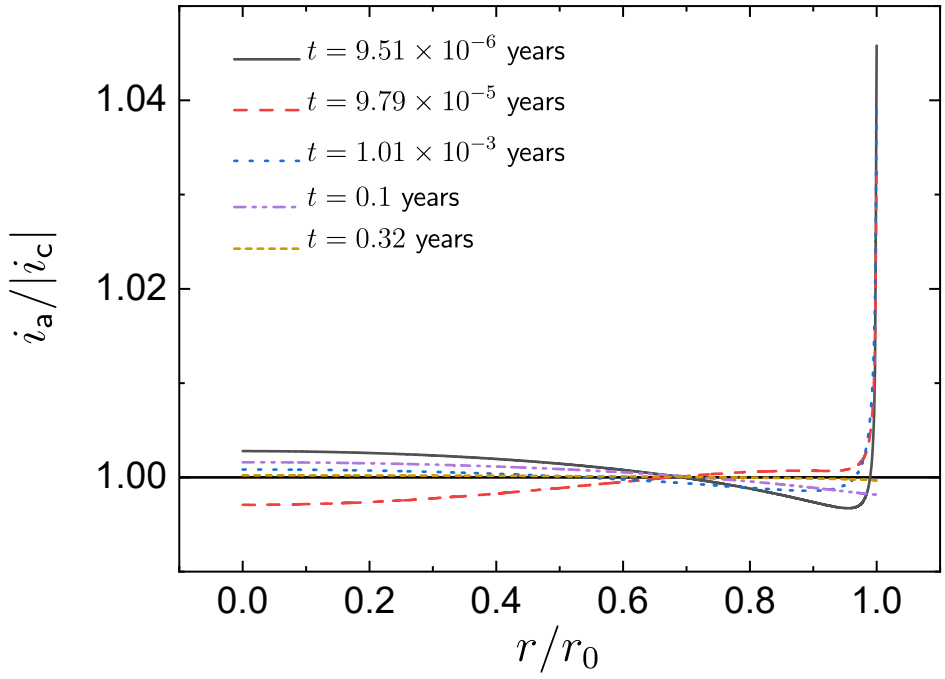

(a)

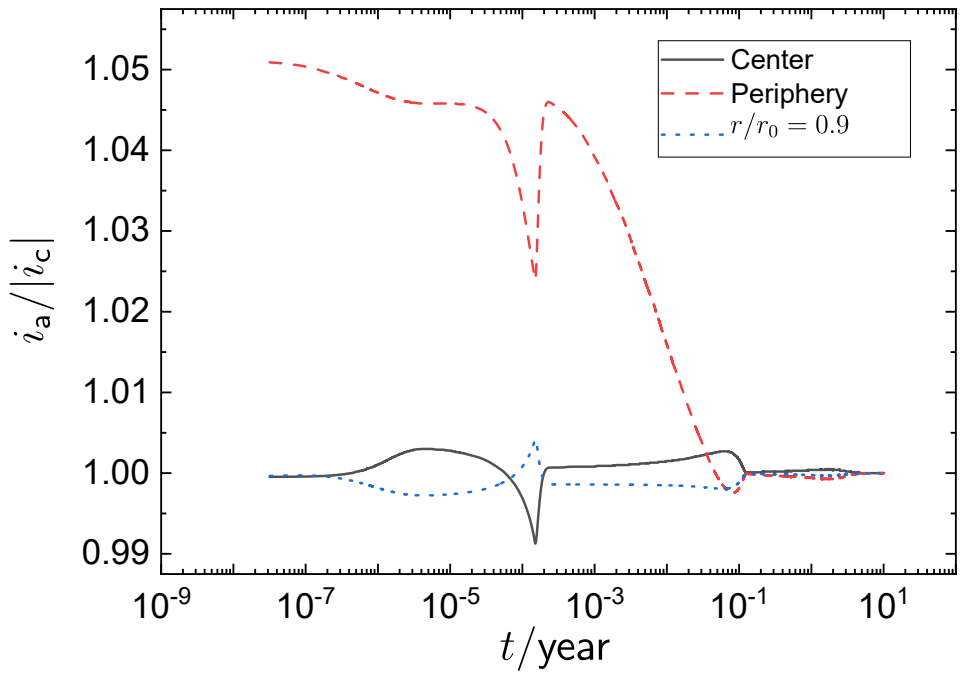

(b)

Figure 4-6. The ratio of anodic current density and absolute cathodic current density $i_a/|i_c|$ for slower oxygen decay: a) $i_a/|i_c|$ as a function of normalized radial position with elapsed time as a parameter and b) $i_a/|i_c|$ as functions of elapsed time at droplet center, droplet periphery and location at r/r_0=0.9

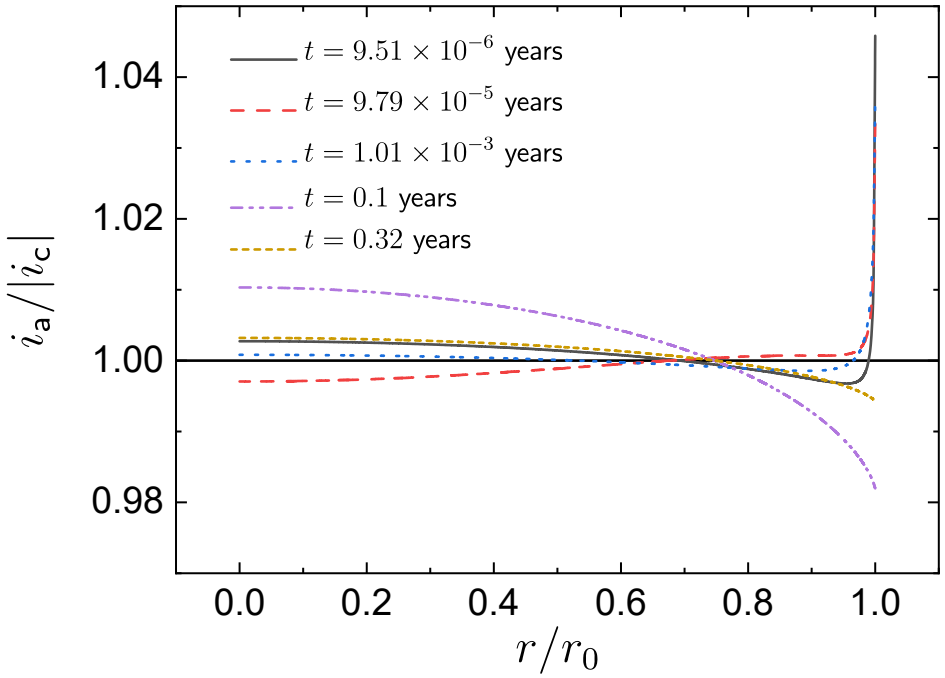

(a)

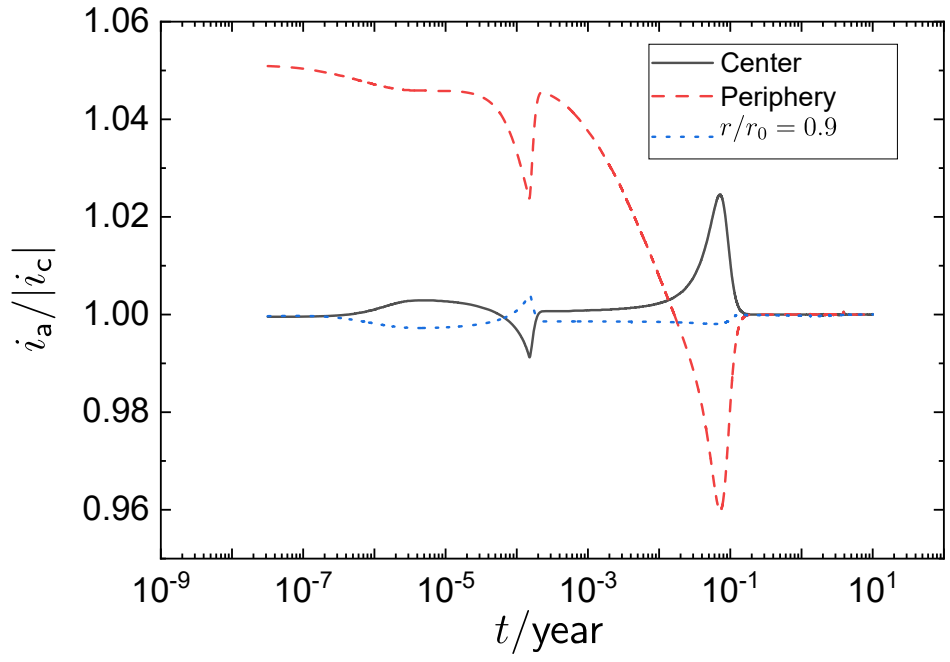

(b)

Figure 4-7. The ratio of anodic current density and absolute cathodic current density $i_a/|i_c|$ for faster oxygen decay: a) $i_a/|i_c|$ as a function of normalized radial position with elapsed time as a parameter and b)$i_a/|i_c|$ as functions of elapsed time at droplet center, droplet periphery and location at r/r_0=0.9

separable with anodic region near the droplet center and cathodic region near the droplet periphery. The peak value of current density was on the order of 0.5 and -0.5 nA/cm^2 at $t = 0.08$ years, 1 or -1.5 pA/cm^2 at $t = 3.5$ years and 0.1 or -0.2 $\pm$ 1 pA/cm^2 at $t = 5.6$ years. The radial distribution of total current density for slower oxygen decay is shown in Figure 4-9. At $t = 2.7 \times 10^{-3}$ years, both droplet center and periphery shows the anodic region with a maximum anodic current density of 3.6 nA/cm^2, and locations in between show the cathodic region with a maximum cathodic current density of -0.2 nA/cm^2. The current density for faster oxygen decay decreased faster as compared to slower oxygen decay. The peak value for anodic and cathodic current density was 0.4 or -0.7 nA/cm^2 at $t = 0.08$ years, 1 or -1.5 pA/cm^2 at $t = 0.18$ year and 0.1 or -0.2 pA/cm^2 at $t = 0.2$ years.

4.1.2 Gaseous Concentrations and pH

Normalized average gaseous concentrations $< c_i > / c_i(t = 0s)$ for O_2, CO_2 and H_2 are presented as functions of elapsed time for slower and faster oxygen decay in Figure 4-10. For both oxygen decays, $< c_i > / c_i(t = 0s)$ decreased from 1 to 0.22 for CO_2 and from 1 to 0.72 for H_2 in the 10-year simulation. For O_2, $< c_{O_2} > / c_{O_2}(t = 0s)$ decreased to 4×10^{-7} for slower oxygen decay, and decreased to a value smaller than one molecule per droplet concentration for faster oxygen concentration decay in 10 years. The decrease of gaseous concentrations was primarily influenced by the concentration supply at the droplet boundary. Due to the elevation of temperature, gaseous concentrations decreased as temperature increased, as shown in equation (3-79). Gaseous concentrations could also be affected by associated reaction, but the effect was relatively minimal as compared to the temperature influence since mass-transfer-limited behavior was not seen.

Water dissociation was included in the current model, and pH could be calculated using concentration of hydrogen ions. The value of neutral pH was 7 for systems at room temperature, and this value is strongly influenced by temperature. As shown in Figure 4-11, neutral pH decreased from 7.3 to 6.4 as temperature increased from 283 K to 346 K in the 10-year simulation. For slower oxygen decay in 10 years, the pH changed from the neutral condition with

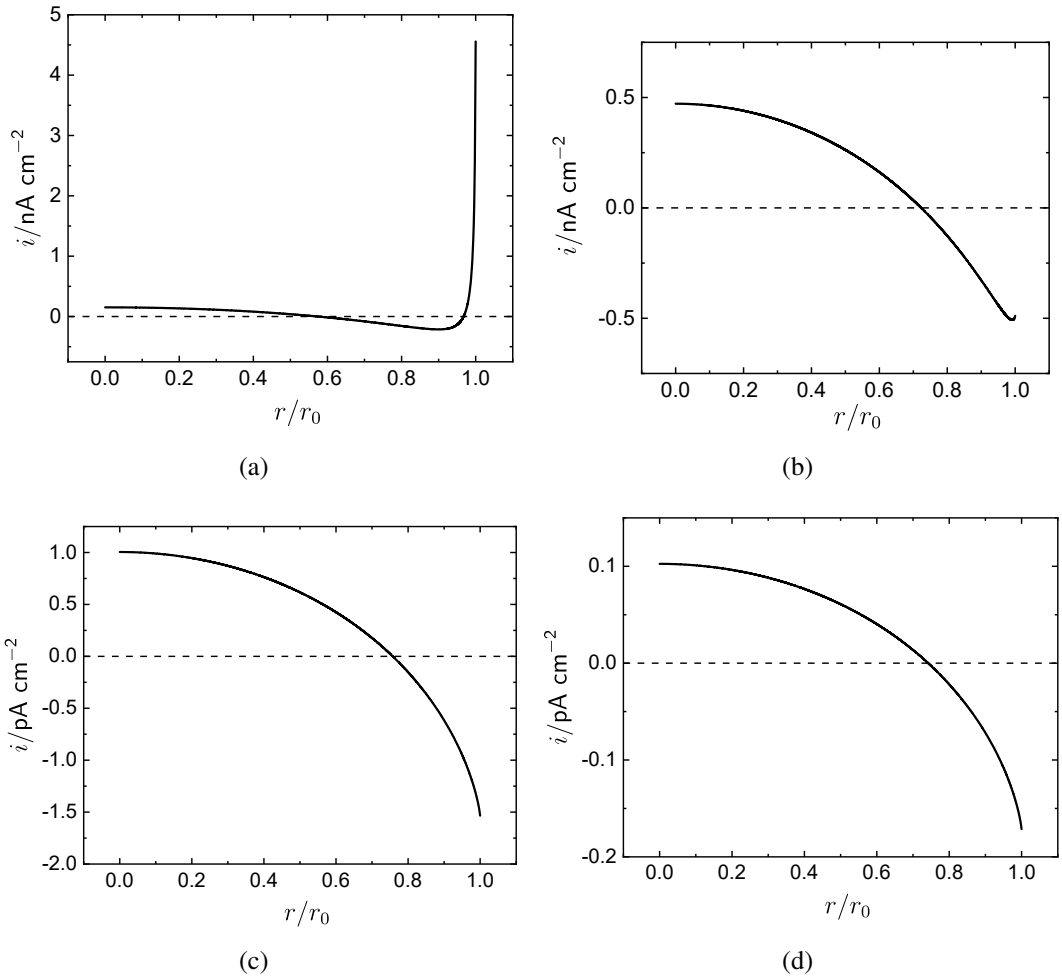

Figure 4-8. Total current density as a function of normalized radial position for slower oxygen decay with different elapsed time: a) $t = 2.7 \times 10^{-3}$ years ,b) $t = 0.08$ year, c) $t = 3.5$ years and d) $t = 5.6$ years

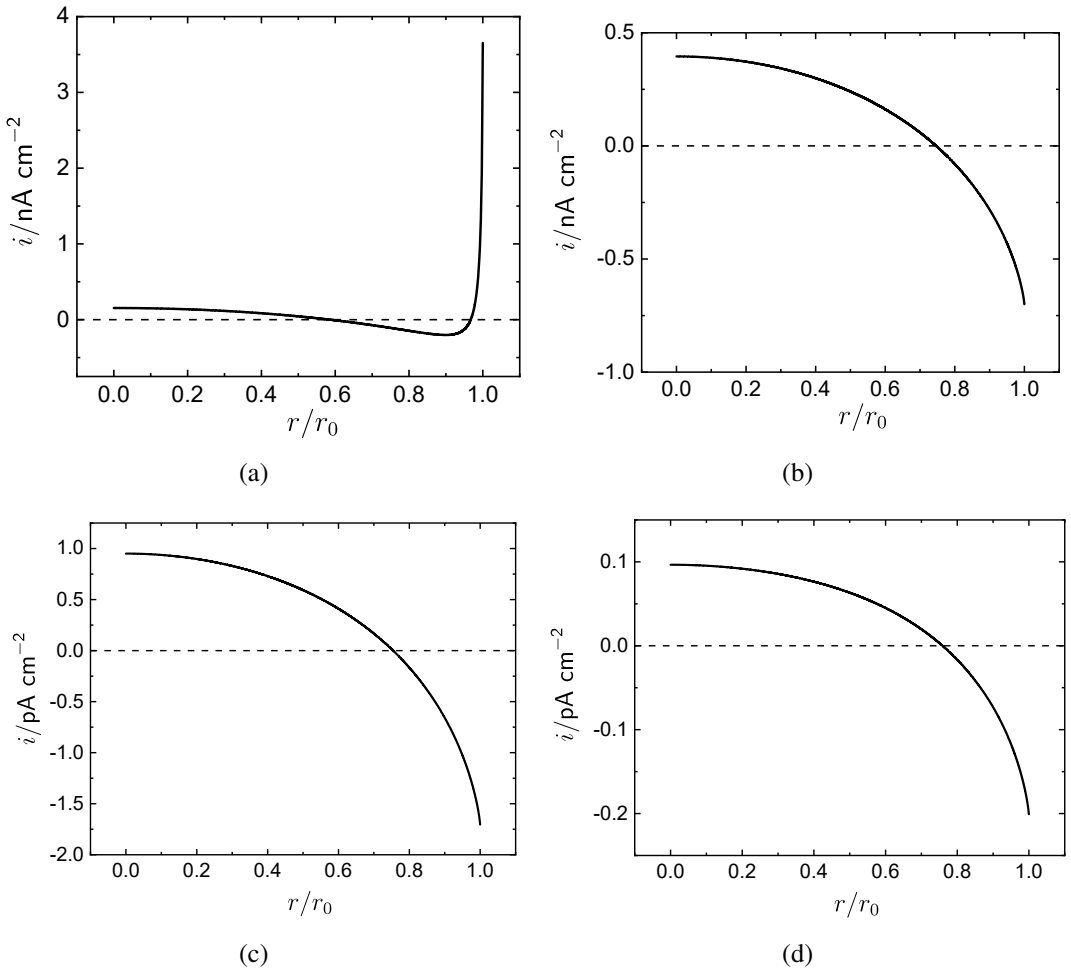

Figure 4-9. Total current density as a function of normalized radial position for faster oxygen decay with different elapsed time: a) $t = 2.7 \times 10^{-3}$ years, b) $t = 0.08$ years, c) $t = 0.18$ years and d) $t = 0.2$ years

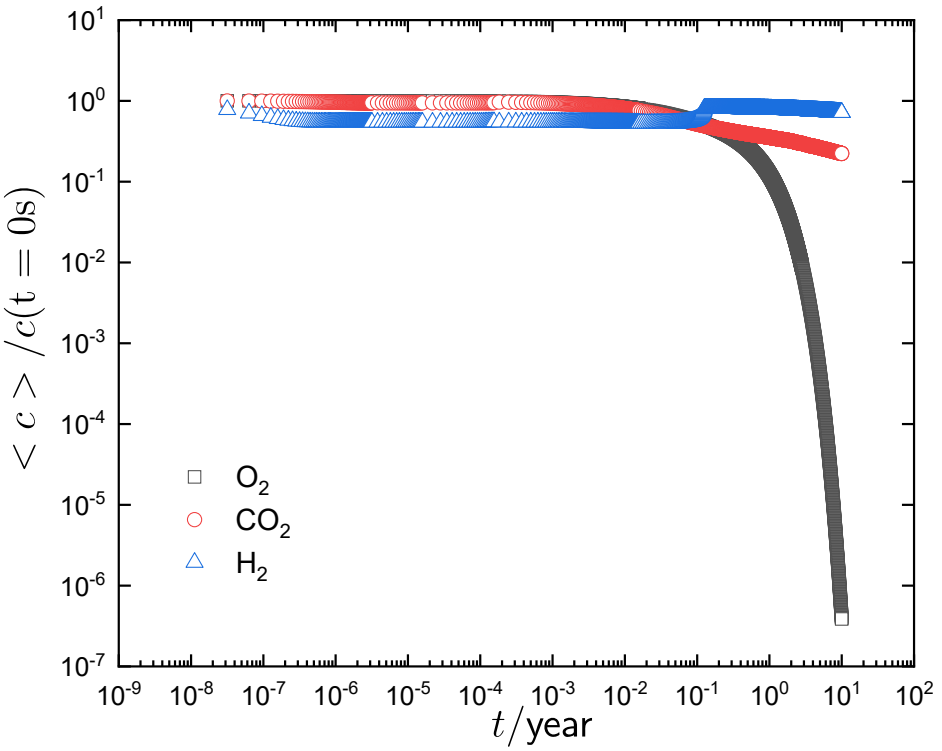

(a)

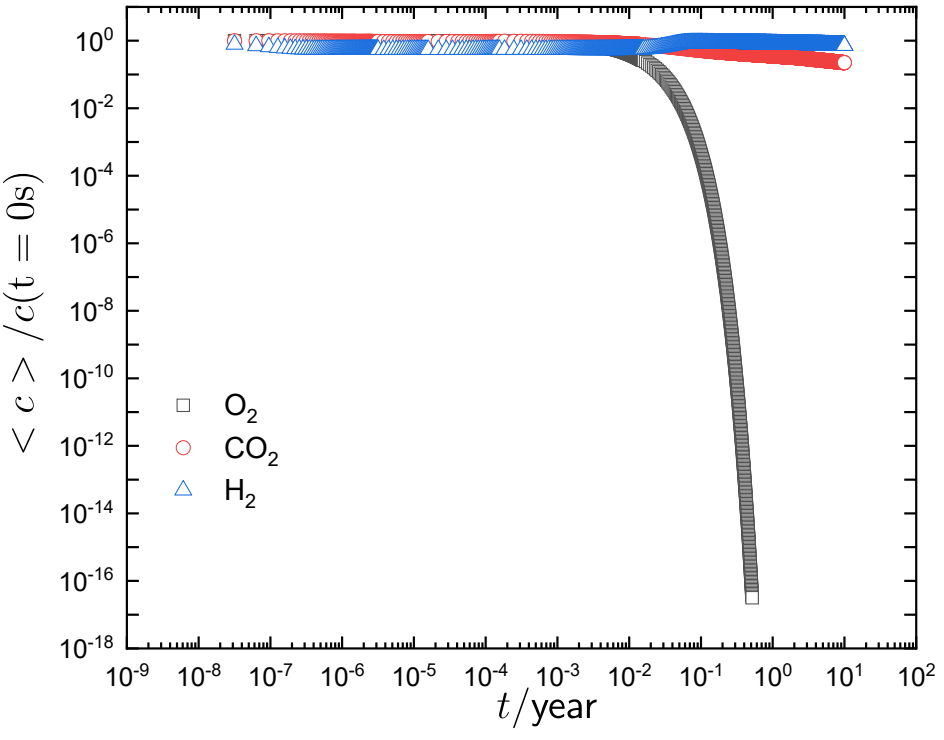

(b)

Figure 4-10. Normalized average gaseous concentrations as functions of elapsed time: a) slower oxygen decay with $t_{0.1\%} = 5$ years and b) faster oxygen decay with $t_{0.1\%} = 5$ weeks.

a value of 7.25 to a more alkaline condition with a value of 10.3, and it tended to increase in even longer elapsed time. For faster oxygen decay, the pH changed initially from the neutral condition with a value of 7.25 to a more alkaline condition with a peak value of 10.1 at $t = 3.56$ years. The pH then tended to decrease at $t = 10$ years.

4.1.3 Influence of CuCl and Cu_2O Films

Growth of nm-scale films was considered in the current model. Average surface coverages for films as functions of elapsed time are shown in Figure 4-12. For the average surface coverage of CuCl film $< \gamma_{CuCl} >$ shown in Figure 4-12(a), two curves were overlapped for slower and faster oxygen decay, indicating that growth of CuCl film is barely influenced by temperature or oxygen. The surface coverage γ_{CuCl} became larger than 1 monolayer thickness at $t = 1.84 \times 10^{-4}$ years and reached a plateau of 64 monolayer thickness in 10 years. For growth of Cu_2O film shown in Figure 4-12(b), the average surface coverage of Cu_2O film $< \gamma_{Cu_2O} >$ became larger than 1 monolayer thickness at $t = 0.36$ years for faster oxygen decay with $t_{0.1\%} = 5$ weeks and became larger than 1 monolayer thickness at $t = 0.13$ years for slower oxygen decay with $t_{0.1\%} = 5$ years. Average surface coverage of Cu_2O film $< \gamma_{Cu_2O} >$ increased to 1,593 monolayer thickness for slower oxygen decay and increased to 164 monolayer thickness for faster oxygen decay. Oxygen was shown to play an important role in accelerating the growth of Cu_2O film and increasing the surface coverage for Cu_2O film.

Radial distributions of the CuCl surface coverage at four elapsed times for both oxygen decays are shown in Figure 4-13. Four associated elapsed times were chosen when γ_{CuCl} reached around 1, 10, 31, and 64 monolayer thickness. Figure 4-13(a) is the summary of γ_{CuCl} for four elapsed times, and Figures 4-13(b), 4-13(c), 4-13(d) and 4-13(e) are γ_{CuCl} at each selected elapsed time. The surface coverage γ_{CuCl} was almost uniform on the copper metal surface with a slightly larger monolayer thickness at the droplet periphery and with a smaller monolayer thickness at the droplet center. For systems with faster oxygen decay, γ_{CuCl} followed a similar shape and had a smaller value as compared to systems with slower oxygen decay.

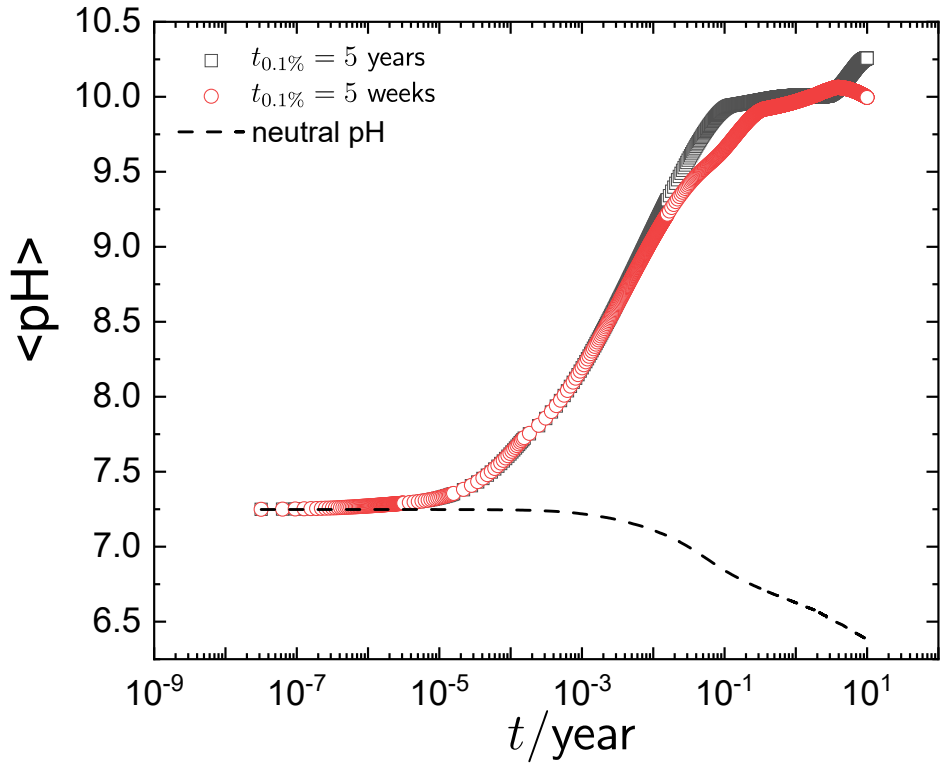

Figure 4-11. The average value of pH in the droplet as functions of elapsed time

Radial distributions of surface coverage for the Cu_2O film γ_{Cu_2O} are shown in Figure 4-14 for slower oxygen decay and are shown in Figure 4-15 for faster oxygen decay. Four elapsed times were chosen when γ_{Cu_2O} was around 1, 10, 100, and 1,717 monolayer thickness for slower oxygen decay, and four elapsed time were chosen when γ_{Cu_2O} was around 1, 10, 100, and 172 monolayer thickness for faster oxygen decay. Figures 4-14(a) and 4-15(a) shows the summary of γ_{Cu_2O} for four selected elapsed time. The surface coverage γ_{Cu_2O} is presented in Figures 4-14(b), 4-14(c),4-14(d), and 4-14(e) for selected elapsed times. The radial distribution of γ_{Cu_2O} was also relatively uniform with a slightly larger monolayer thickness near the droplet periphery and with a smaller monolayer thickness near the droplet center. After an elapsed time of 10 years, the maximum deviation of the coverage by Cu_2O was $1.5 \times 10^{-5}\%$ of the maximum value of the surface coverage for slower oxygen decay and $2.3 \times 10^{-6}\%$ for faster oxygen decay.

Potentials and oxygen concentration were adjusted to account for the presence of CuCl film that was treated as a thin diffusion barrier. Ratios of oxygen concentration on the electrode

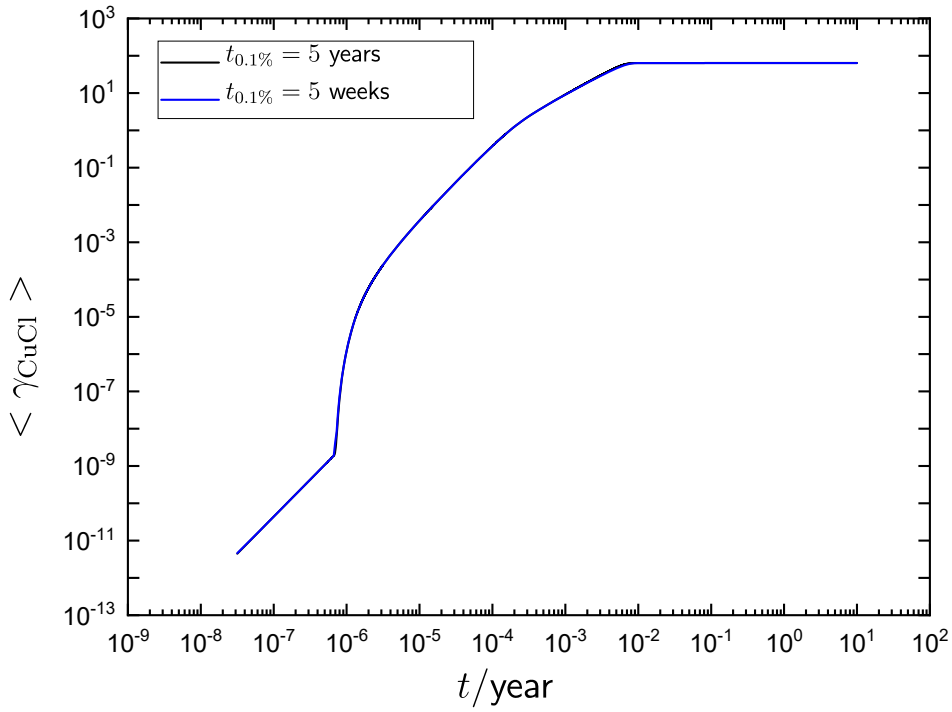

(a)

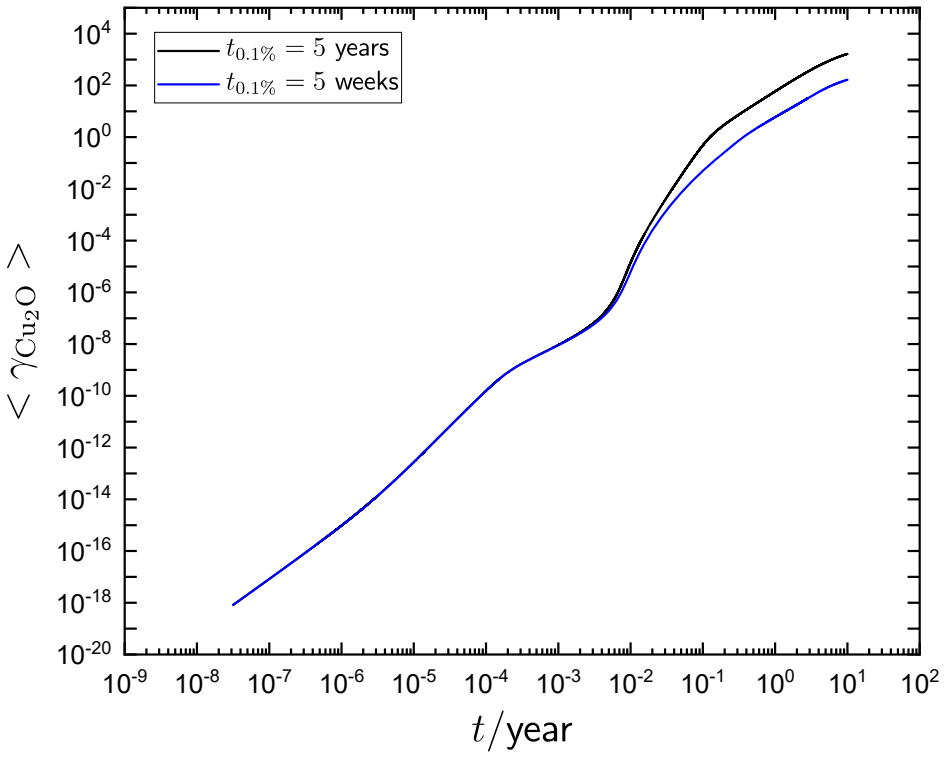

(b)

Figure 4-12. The average surface coverage as functions of elapsed time for CuCl and Cu_2O films: a) γ_{CuCl}, and b) γ_{Cu_2O}

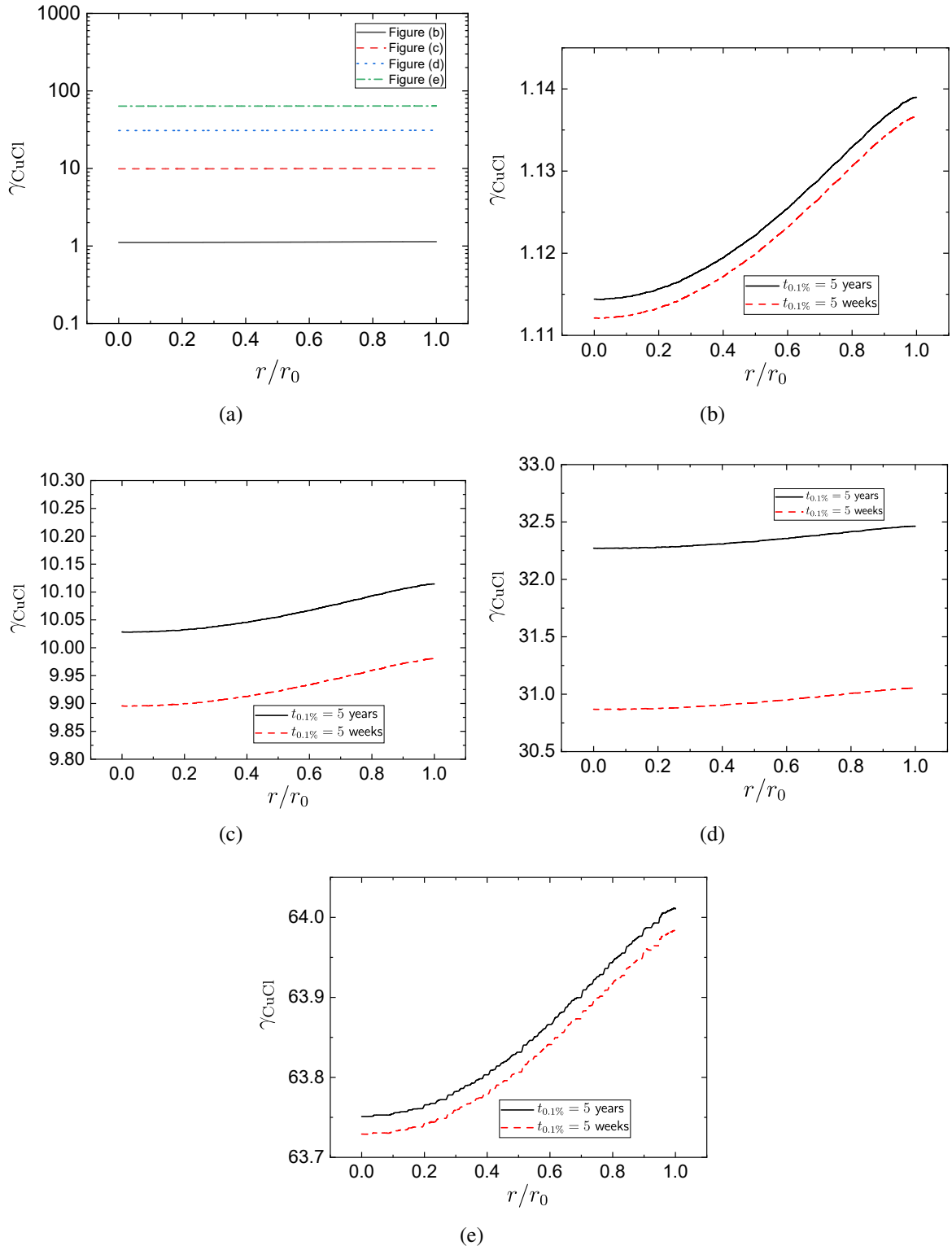

Figure 4-13. Radial distributions of CuCl surface coverage at different elapsed time: a)Summary of four elapsed times, b) $t = 1.84 \times 10^{-4}$ years c) $t = 1.07 \times 10^{-3}$ years d) $t = 3.22 \times 10^{-3}$ years e) 10 years

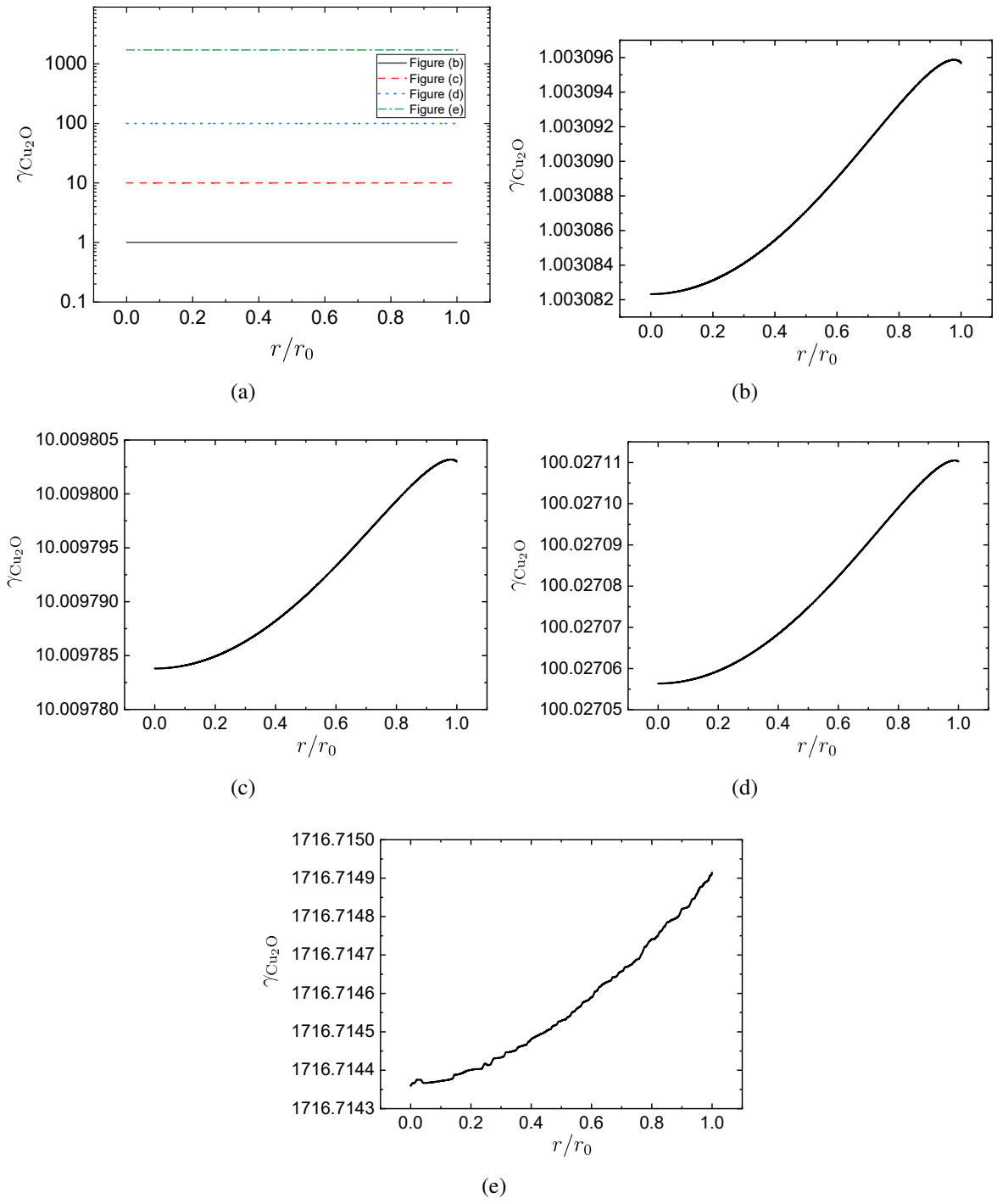

Figure 4-14. Radial distributions of Cu_2O surface coverage at different elapsed time for slower oxygen decay: a)Summary of four elapsed times, b) t= 0.12 years c) t=0.36 years d) t=1.34 years and e) 10 years

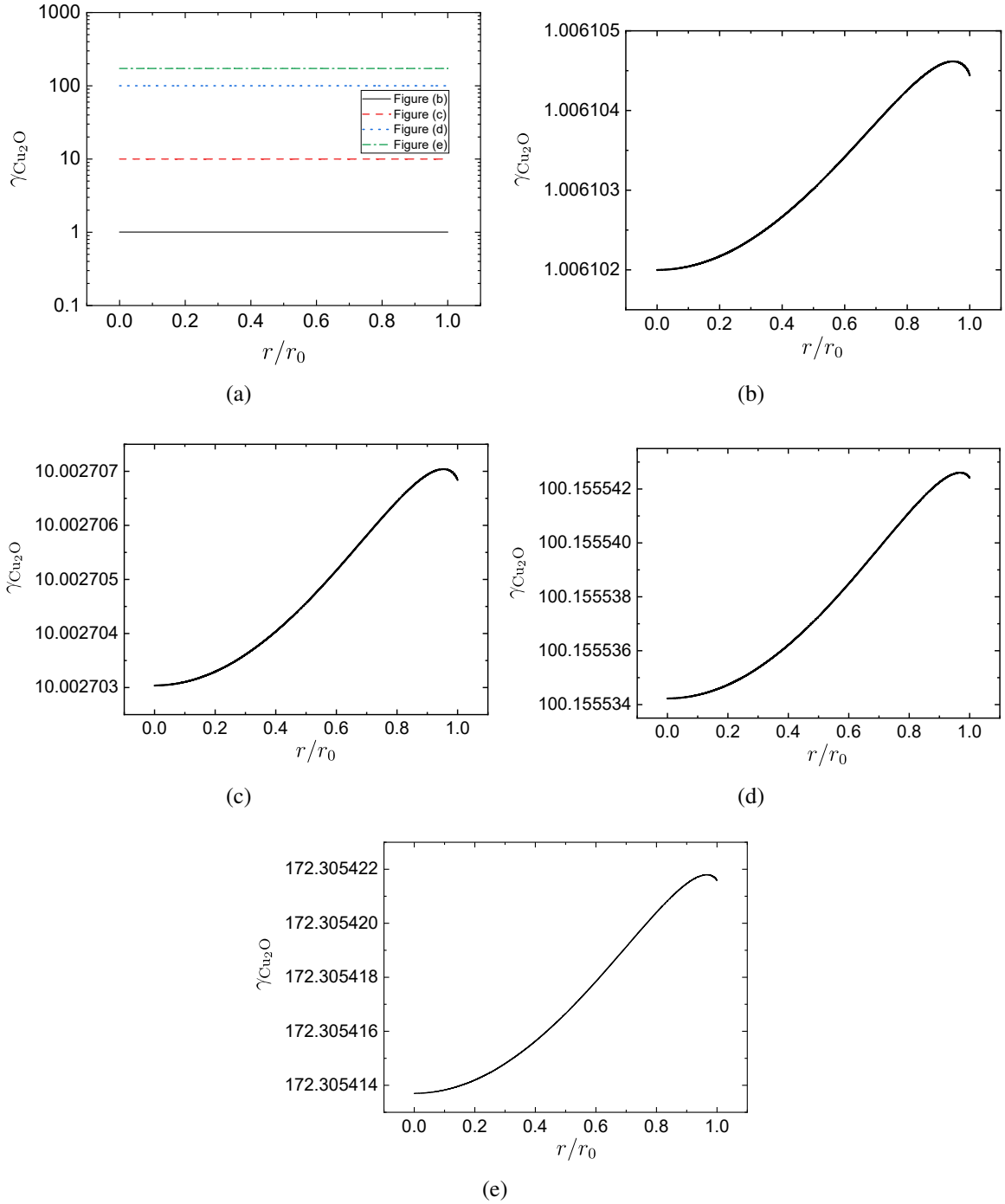

Figure 4-15. Radial distributions of Cu_2O surface coverage at different elapsed time for faster oxygen decay: a)Summary of four elapsed times, b) t= 0.35 years c) t=1.34 years d) t=5.92 years and e) 10 years

surface and outside the CuCl film $\lambda = c_{O_2}(0)/c_{O_2}(\text{CuCl})$ are presented in Figure 4-16 as functions of elapsed time for r/r_0=0, 0.5 and 1. Curves were overlapped for systems with the same oxygen decay time constant, indicating that the influence of oxygen yielded a uniform film thickness. In 10 years, λ decreased from 1 to 0.997 for slower oxygen decay, and it decreased from 1 to 0.954 for faster oxygen decay. Systems with slower or faster oxygen decays had the same surface coverage of CuCl film, and the smaller λ for slower oxygen decay was due to a more cathodic potential that was applied on electrochemical reactions.

Ratios of potential outside the diffuse part of the double layer and outside the CuCl film $\eta = \Phi_0/\Phi(\text{CuCl})$ are presented as functions of elapsed time for r/r_0=0, 0.5 and 1 in Figure 4-17. The CuCl film had a relative higher influence on potentials near the droplet periphery, but values of η were very close to 1 at all elapsed times for $t_{0.1\%} = 5$ years and 5 weeks. In 10 years, η initially increased to a value slightly hight than 1 due to the growth of CuCl film and η went back to 1 in longer elapsed time due to a huge decrease of total current density. Values of η smaller or larger than 1 were determined by the sign of total current density.

4.1.4 Localized Corrosion Rates and Depth

Corrosion rates and corrosion depths were controlled by the copper dissolution current density shown in equation (3-56). The spatially averaged instantaneous corrosion rates $< R_{\text{corr,local}} >$ are presented in Figure 4-18(b) as functions of elapsed time. The initial average local corrosion rate $< R_{\text{corr,local}} >$ was 6μm/year for both rates of oxygen decay and $< R_{\text{corr,local}} >$ decreased to 3 μm/year at $t = 1.84 \times 10^{-4}$ years, corresponding to $\gamma_{\text{CuCl}} > 1$. For slower oxygen decay with $t_{0.1\%} = 5$ years, $< R_{\text{corr,local}} >$ slightly increased to 4 μm/year at $t = 0.07$ years due to the elevation of temperature; then decreased to 0.2 μm/year at $t = 0.13$ years as $\gamma_{\text{Cu}_2\text{O}} > 1$ and decreased to 50 nm at 10 years. For faster oxygen decay with $t_{0.1\%} = 5$ weeks, $< R_{\text{corr,local}} >$ decreased to 0.14 nm/year as $\gamma_{\text{Cu}_2\text{O}} > 1$ and tended toward zero with a value of 6.7×10^{-3} nm/year at 10 years. The average corrosion depth $< L_{\text{corr,local}} >$, which is a radially dependent accumulated value, is shown in Figure 4-18(b). After an elapsed time of 10 years, $< L_{\text{corr,local}} >$ reached a value of 2 μm for slower oxygen decay. For the faster oxygen

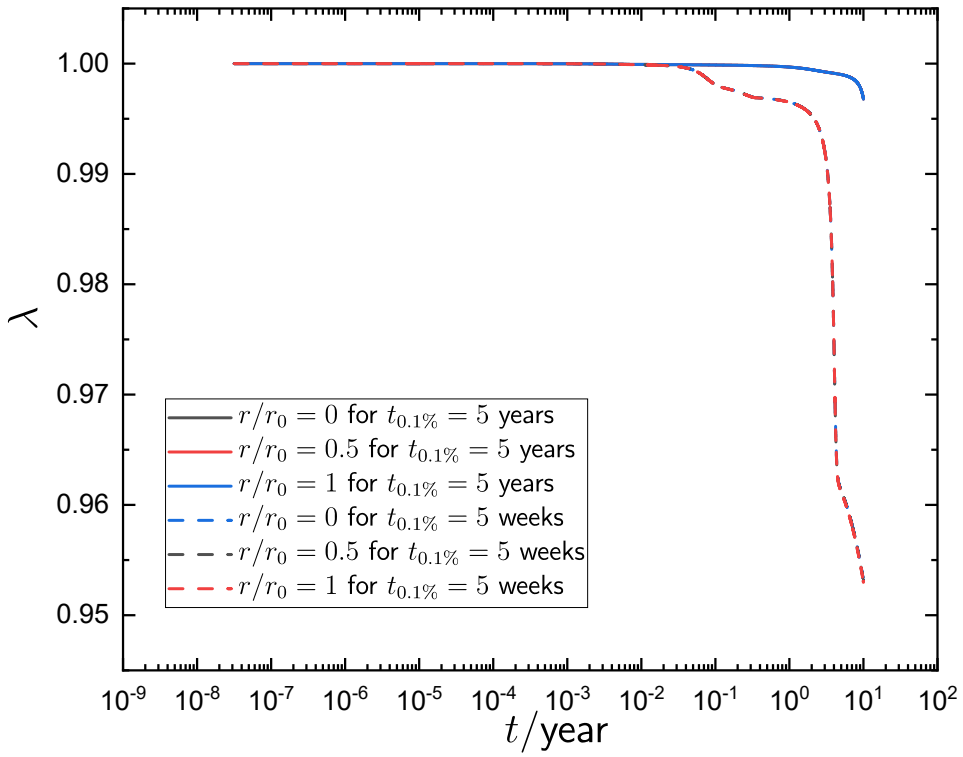

Figure 4-16. Ratios of oxygen concentration on the electrode surface and outside the CuCl film as functions of elapsed time for r/r_0=0, 0.5 and 1 for slower oxygen decay and faster oxygen decay.

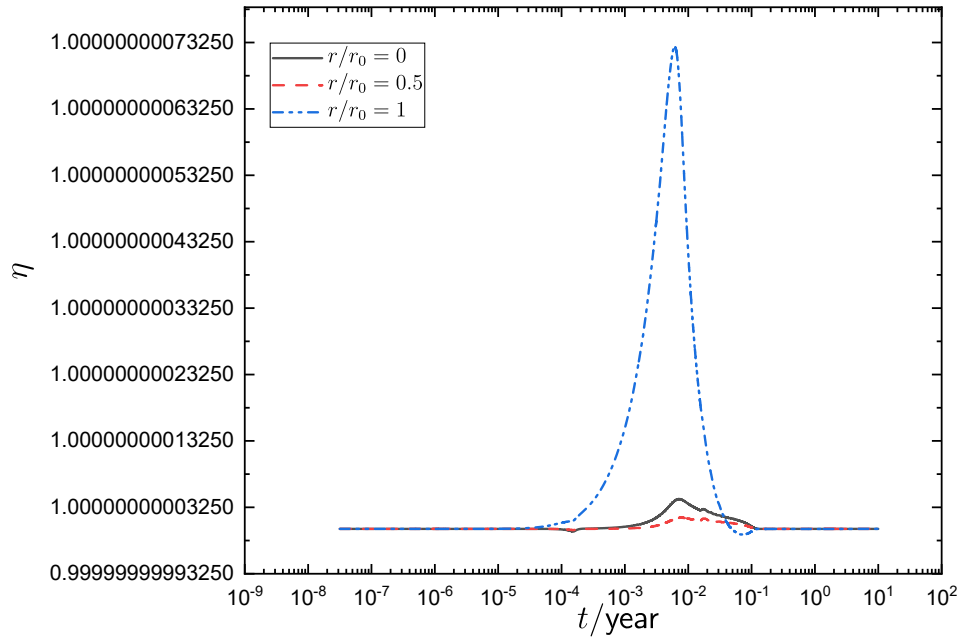

(a)

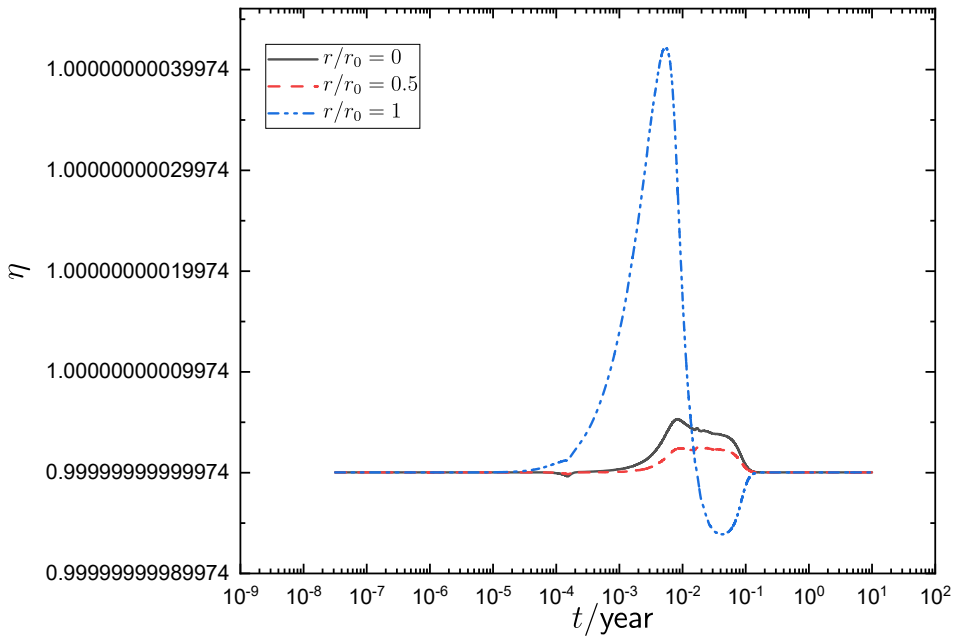

(b)

Figure 4-17. Ratios of potential outside the diffuse part of the double layer and outside the CuCl film as functions of elapsed time for r/r_0=0, 0.5 and 1: a) slower oxygen decay with $t_{0.1\%} = 5$ years and b) faster oxygen decay with $t_{0.1\%} = 5$ weeks.

decay, $< L_{corr,local} >$ reached a plateau with a value of 0.2 μm, which showed that oxygen played an important role in the corrosion of copper.

The radial distribution of local corrosion rate $R_{corr,local}$ for slower oxygen decay is shown in Figure 4-19. Four elapsed times were chosen when $R_{corr,local}$ have different orders of magnitude as shown in Figure 4-19(a). The radial distribution of local corrosion rate $R_{corr,local}$ is presented in Figures 4-19(b), 4-19(c), 4-19(d) and 4-19(e) for each selected elapsed time such that $R_{corr,local} = 5.10$ μm/year at $t = 1.42 \times 10^{-4}$ years, $R_{corr,local} = 1.03$ μm/year at t = 0.12 years, $R_{corr,local} = 0.1$ μm/year at t = 7.02 years, and $R_{corr,local} = 4.67 \times 10^{-2}$ μm/year at $t = 10$ years. For early elapsed times, a higher local corrosion rate is seen near the droplet center at $t = 1.42 \times 10^{-4}$ years, but a higher corrosion rate near the droplet periphery at t = 0.12 years. For longer elapsed times, the local corrosion rate was higher near the droplet periphery and was lower near the droplet center. The radial distribution of local corrosion rate is shown in Figure 4-20 for faster oxygen decay. Four elapsed times were chosen when $R_{corr,local}$ had different orders of magnitude such that $R_{corr,local} = 1.0076$ μm/year at $t = 0.046$ years, $R_{corr,local} = 5.19 \times 10^{-2}$ μm/year at t = 0.33 years, $R_{corr,local} = 1.072 \times 10^{-3}$ μm/year at t = 4.12 years, and $R_{corr,local}$ = -5.221 $\times 10^{-8}$ μm/year at $t = 10$ years. The local corrosion rate was slightly higher near the droplet periphery as compared to the droplet center for $t = 0.046$ years, t =0.33 years and t =4.12 years. $R_{corr,local}$ decreased to a much smaller value and became negative in 10 years, indicating that copper plating reaction dominated and copper stopped corroding. The local corrosion rate was almost uniform. The maximum deviation of the corrosion rate was 6.4×10^{-7}% of the maximum value of the corrosion rate for slower oxygen decay and 1.2×10^{-5}% for faster oxygen decay.

The radial distribution of local corrosion depth $L_{corr,local}$ for slower oxygen decay is shown in Figure 4-21. Four elapsed times were chosen when $L_{corr,local}$ had different orders of magnitude as shown in Figure 4-21(a). The radial distribution of local corrosion depth $L_{corr,local}$ is presented in Figures from 4-21(b), 4-21(c), 4-21(d) and 4-21(e) for each selected elapsed time with $L_{corr,local} = 10.01$ nm at $t = 2.91 \times 10^{-3}$ years, $L_{corr,local}$ =0.103 μm at t = 0.026 years,

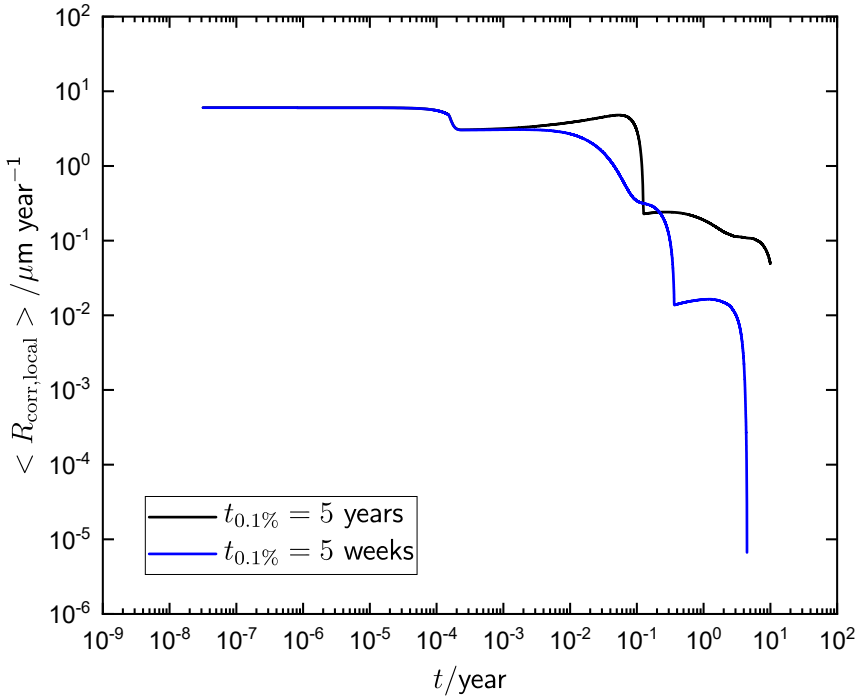

(a)

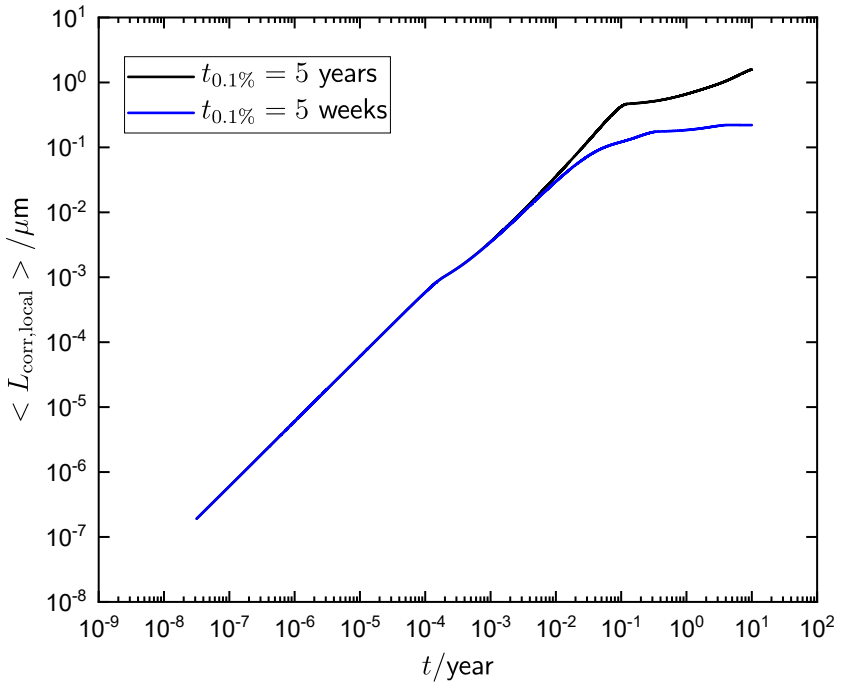

(b)

Figure 4-18. Simulated Corrosion results for two oxygen decays: a) average corrosion rates as functions of elapsed time and b) average corrosion depth as functions of elapsed time.

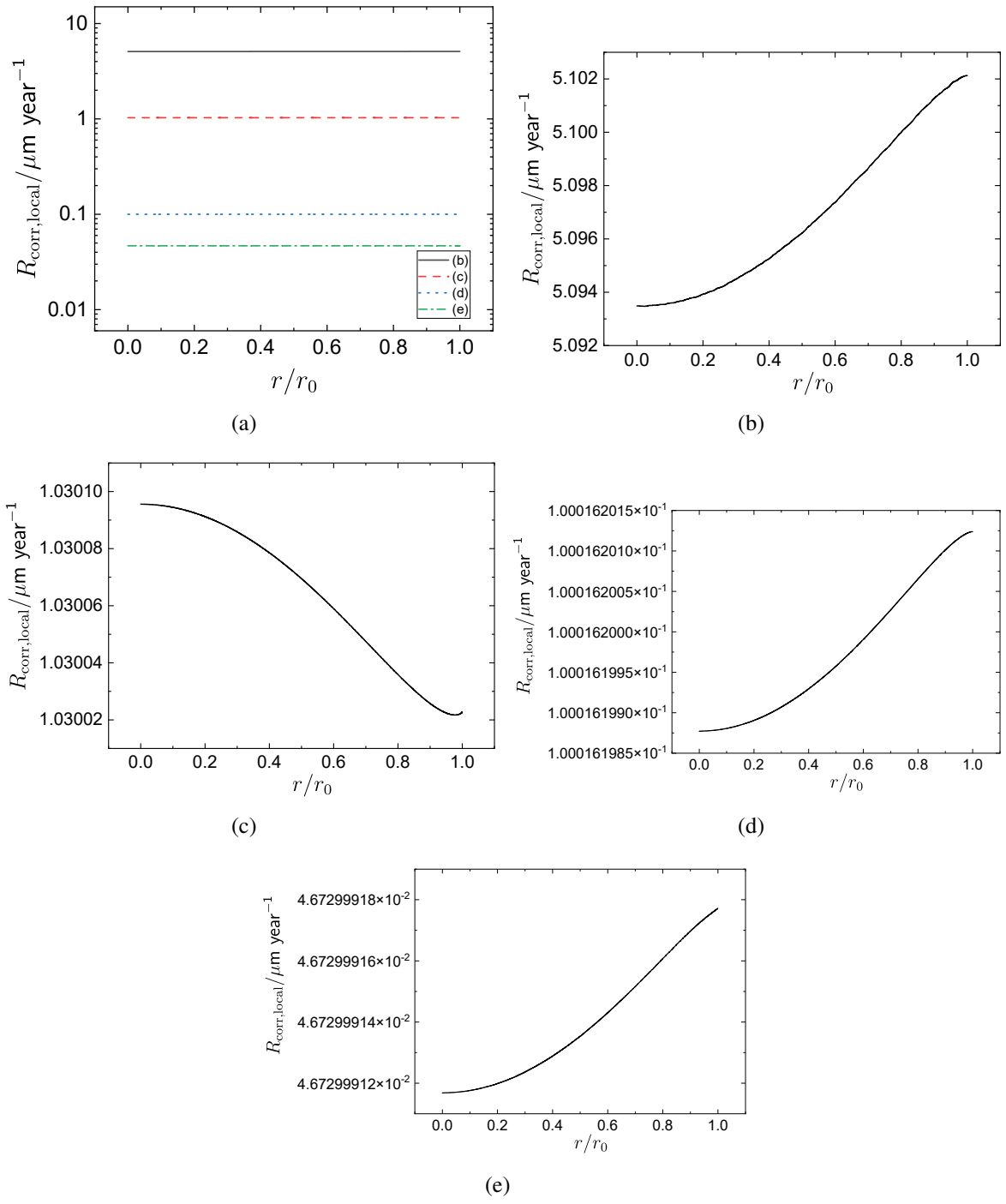

Figure 4-19. The radial distribution of local corrosion rate at different elapsed time for slower oxygen decay: a) summary of four elapsed times, b) $t = 1.42 \times 10^{-4}$ years, c) t = 0.12 years, d) t = 7.02 years, and e) t = 10 years.

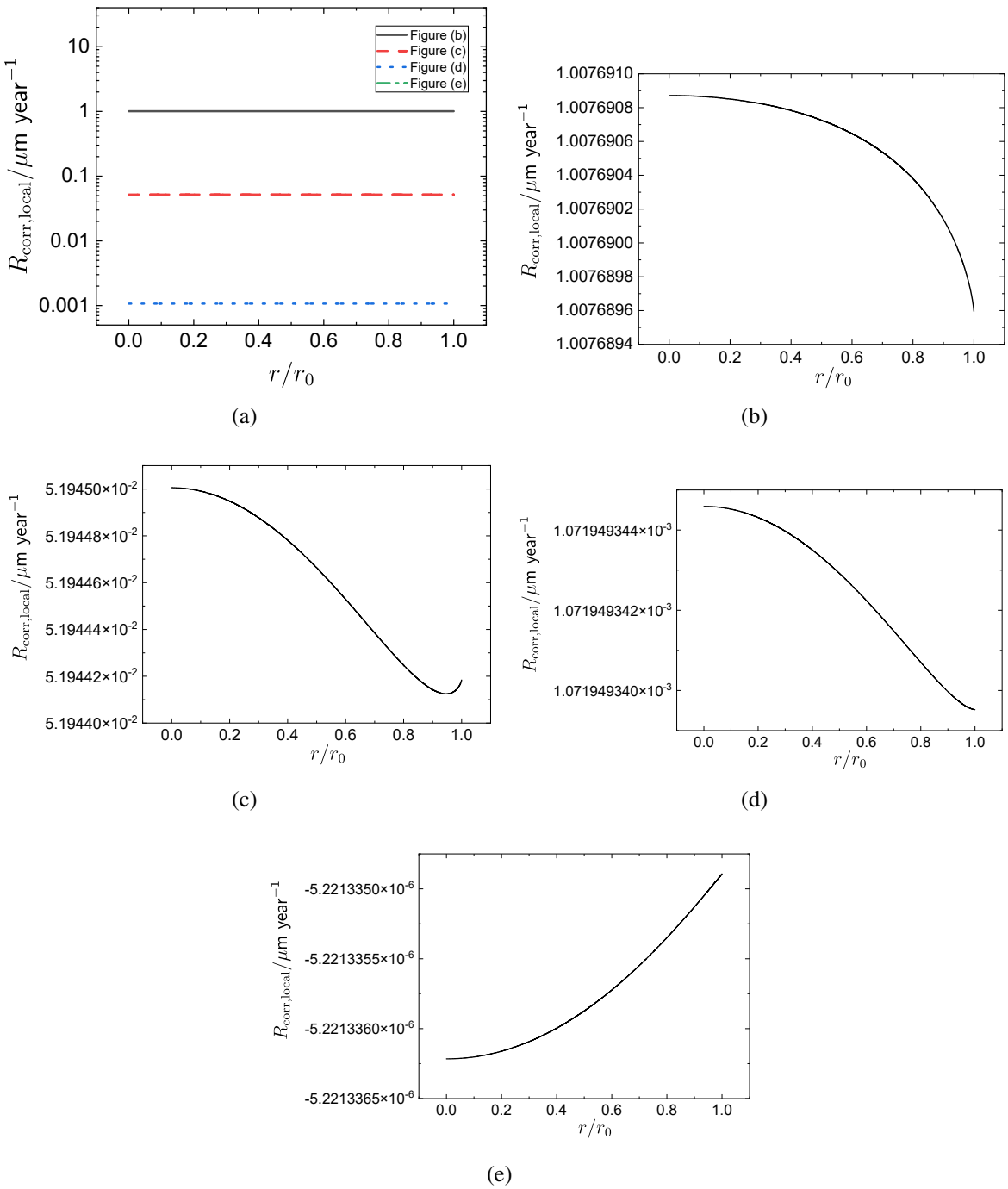

Figure 4-20. The radial distribution of local corrosion rate at different elapsed time for faster oxygen decay: a) summary of four elapsed times, b) t = 0.046 years, c) t=0.33 years, d) t = 4.12 years, and d) t = 10 years.

$L_{corr,local} = 1.001\ \mu m$ at t = 3.37 years, and $L_{corr,local} = 1.623\ \mu m$ at $t = 10$ years. For all four elapsed times, a lager local corrosion depth was observed near the droplet center as compared to that at the droplet periphery. The radial distribution of local corrosion depth is shown in Figure 4-22 for faster oxygen decay. Four elapsed times were chosen when $L_{corr,local}$ had different orders of magnitude such that $L_{corr,local} = 1.000$ nm at $t = 1.84 \times 10^{-4}$ years, $L_{corr,local}$ =10.1 nm at $t = 3.10 \times 10^{-3}$ years, $L_{corr,local} = 0.1010 \mu m$ at t = 0.026 years, and $L_{corr,local} = 0.225\ \mu m$ at $t =$ 10 years. The local corrosion depth was also slightly larger near the droplet center as compared to droplet periphery. The depth of corrosion was almost uniform over the elapsed time simulated, and the maximum deviation from the average corrosion depth was less than 0.0004% for slower oxygen decay and less than 0.002% for faster oxygen decay in 10 years.

Average concentrations of cuprous and cupric ions are shown in Figure 4-23 as functions of elapsed time for slower and faster oxygen decay cases. The initial condition for the model did not include Cu^+ or Cu^{2+} ions and they were generated by homogeneous and electrochemical reactions. For systems with faster or slower oxygen decay, concentration c_{Cu^+} was larger than $c_{Cu^{2+}}$ over 10 years. Concentrations c_{Cu^+} and $c_{Cu^{2+}}$ are larger in the system with faster oxygen decay. The simulation results from PHREEQC software for the system starting with 0.01 M NaCl solutions and 2.52 $\times 10^{-4}$ M oxygen showed that equilibrium values of concentrations for Cu^+ and Cu^{2+} were very close.[137] However, there are several reasons that could cause the discrepancy of Cu^+ and Cu^{2+} concentrations from two simulation results.

1. The current model considered more electrochemical reactions and homogeneous reactions involving Cu^+ and Cu^{2+}, such as reactions discussed in sections 3.2 and 3.3.

2. Simulation conditions in PHREEQC were at room temperature and pH is 7. In the current program, temperature changed as a function of time and pH was determined by H^+ concentrations.

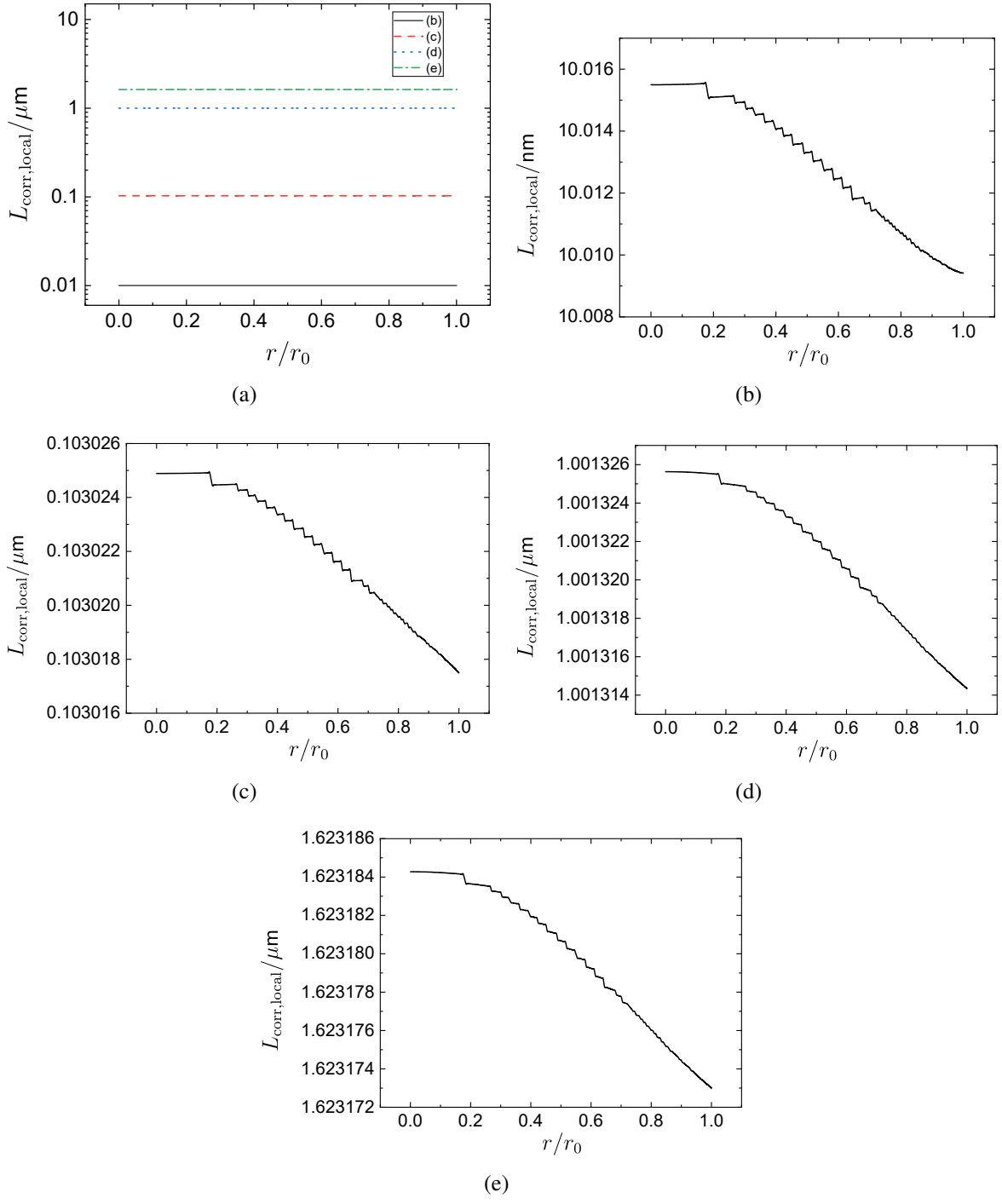

Figure 4-21. The radial distribution of local corrosion depth at different elapsed time for slower oxygen decay: a) summary of four elapsed times, b) $t = 2.91 \times 10^{-3}$ years, c) t = 0.026 years, d) t =3.37 years, and e) t = 10 years.

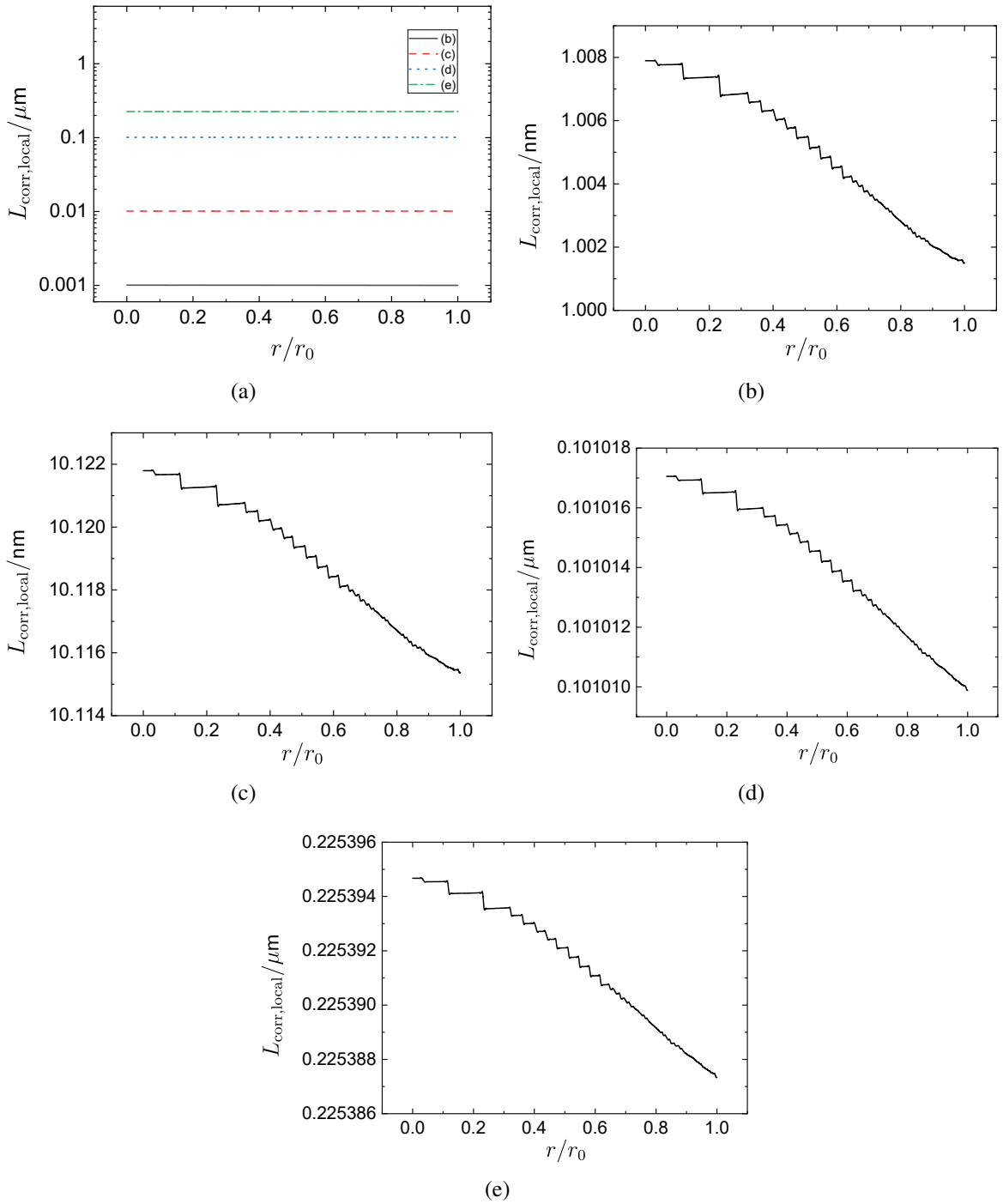

Figure 4-22. The radial distribution of local corrosion depth at different elapsed time for faster oxygen decay: a) summary of four elapsed times, b) $t = 1.84 \times 10^{-4}$ years, c) $t = 3.10 \times 10^{-3}$ years, d) t = 0.026 years and e) t = 10 years.

3. Simulations results from PHREEQC was under assumption that system has reached the equilibrium state, but the current program has not reached the equilibrium conditions in 10 years.

Each of above explanations may apply for the present system.

4.2 Comparison of Results between System with Constant Temperature and Transient Temperature

Simulation results were compared between systems having constant temperature and transient temperature in this section and elevated temperature was shown to play an important role on copper corrosion. The temperature was held at 284K for the constant temperature simulations, which is the initial temperature in the DGR environment. The temperature changed from 284K to 346K in 10 years' simulation with transient temperature.

4.2.1 Oxygen concentration and pH

The normalized average oxygen concentration is presented in Figure 4-24 as functions of elapsed time for calculations with constant temperature and transient temperature. In Figure 4-24, concentrations smaller than one molecule per droplet were set to zero. For slower oxygen decay, presented in Figure 4-24(a), the oxygen concentration deviated from its initial concentration faster with transient temperature, but there was more oxygen left in the droplet with constant temperature in 10 years. For faster oxygen decay, presented in Figure 4-24(b), the oxygen concentration deviated from its initial concentration slightly faster with transient temperature, and it decreased to zero at the same elapsed time t = 0.53 years.

The average pH is presented in Figure 4-25 as functions of elapsed time for systems with constant temperature and transient temperature. For slower oxygen decay with constant temperature, presented in Figure 4-25(a), $< \text{pH} >$ became alkaline more slowly and tended to increase with a smaller slope after 10 years as compared to the system with transient temperature. The average droplet $< \text{pH} >$ was 10.25 for transient temperature and 10.04 for constant temperature at the elapsed time t = 10 years. For faster oxygen decay with constant temperature, the average pH became alkaline more slowly and reached a plateau of 8.9 at an elapsed time t =

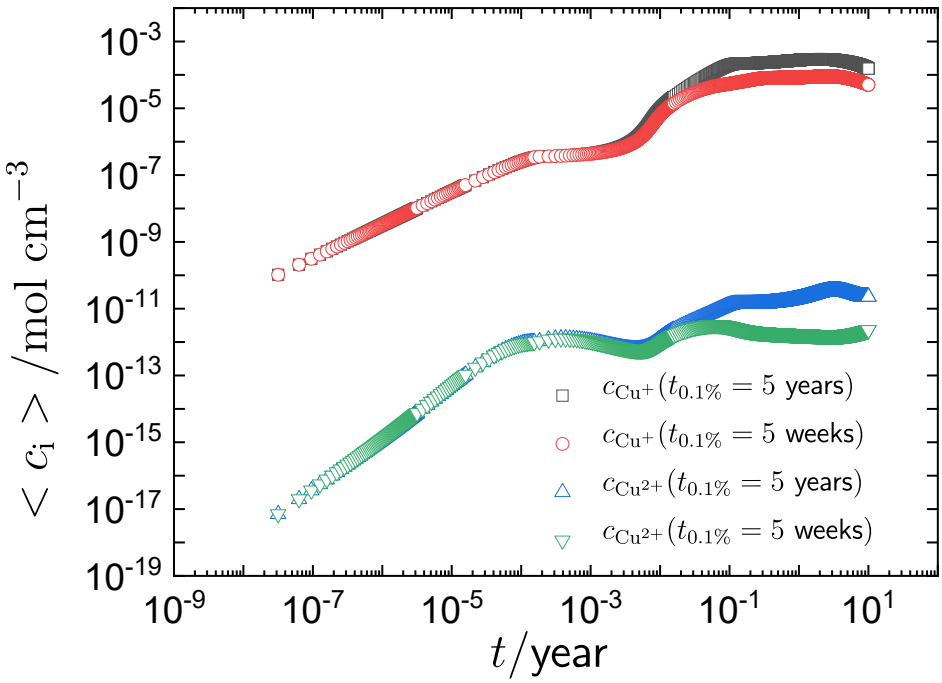

Figure 4-23. Average concentrations of Cu^+ and Cu^{2+} as functions of elapsed time for slower oxygen decay and faster oxygen decay.

2.6 years. For faster oxygen decay with transient temperature, presented in Figure 4-25(b), the average pH increased more rapidly and reached a peak value of 10.06 at elapsed time t= 4.5 years. Then the average pH decreased to 10.0 at an elapsed time t= 10 years.

4.2.2 Surface Coverage for Films

The average surface coverage of CuCl film presented in Figures 4-26 as functions of elapsed time for systems with constant temperature and transient temperature. For both oxygen decay cases, the average coverage $< \gamma_{CuCl} >$ increased to 63.9 monolayer thickness with transient and constant temperature. All curves overlapped, showing that temperature did not have an influence on the growth of CuCl film. The formation and dissolution of CuCl film are dynamic processes, and both processes are influenced by temperature such that the film thickness is unaffected by temperature excursions.

The average surface coverage for Cu_2O film is presented in Figures 4-27 as functions of elapsed time for systems with constant temperature and transient temperature. For slower oxygen

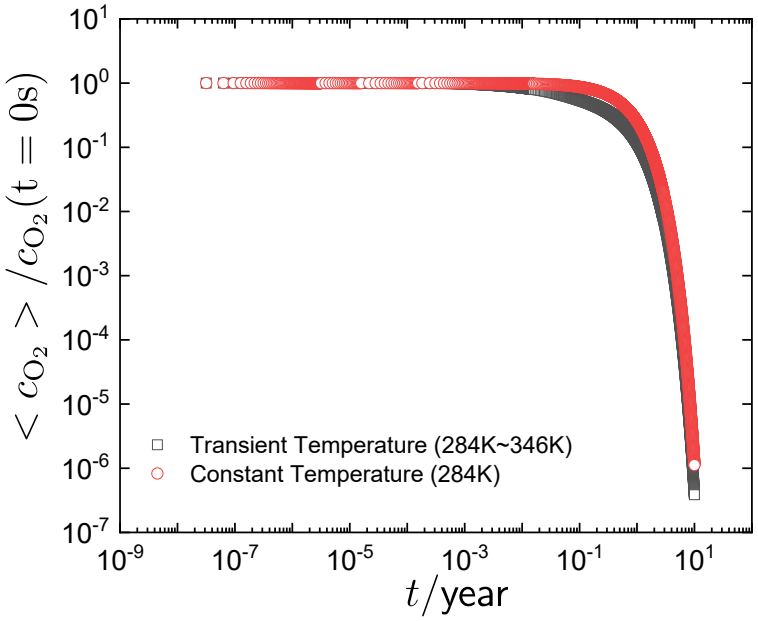

(a)

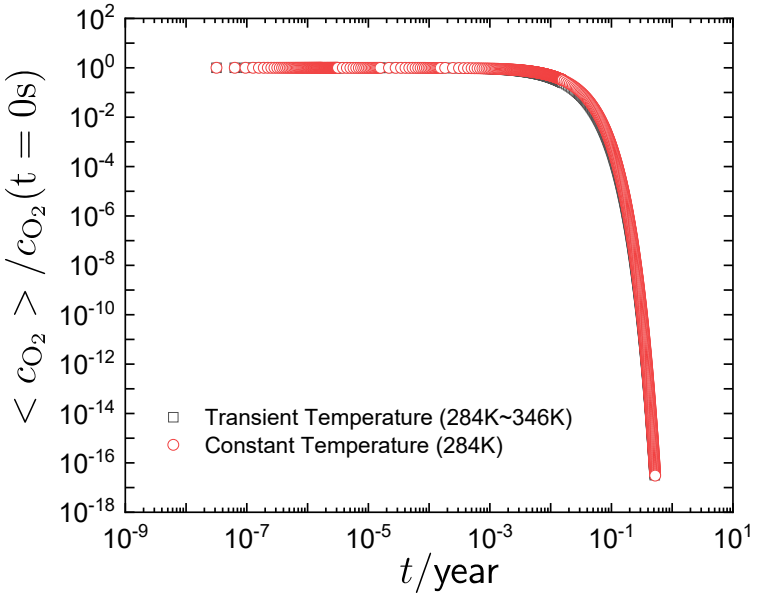

(b)

Figure 4-24. Comparison of normalized average oxygen concentrations as functions of elapsed time between systems with constant temperature and transient temperature: a) slower oxygen decay with $t_{0.1\%} = 5$ years and b) faster oxygen decay with $t_{0.1\%} = 5$ weeks.

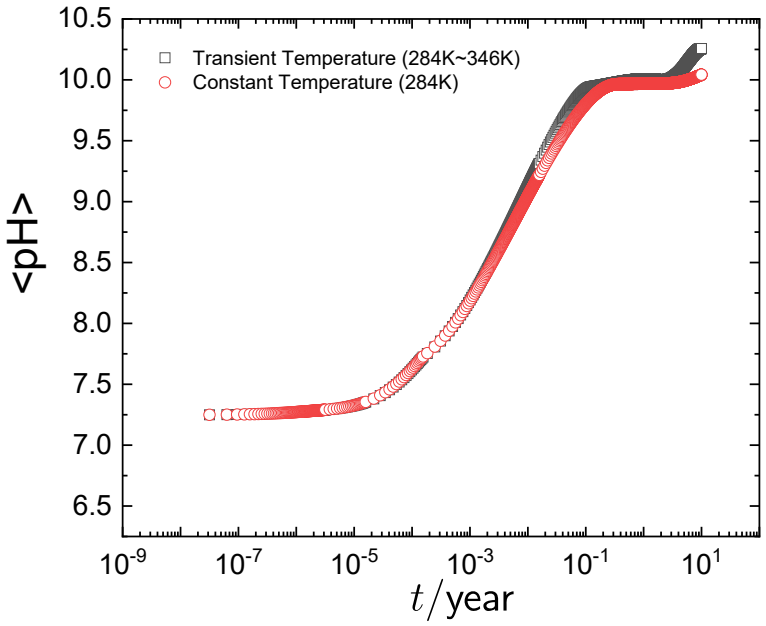

(a)

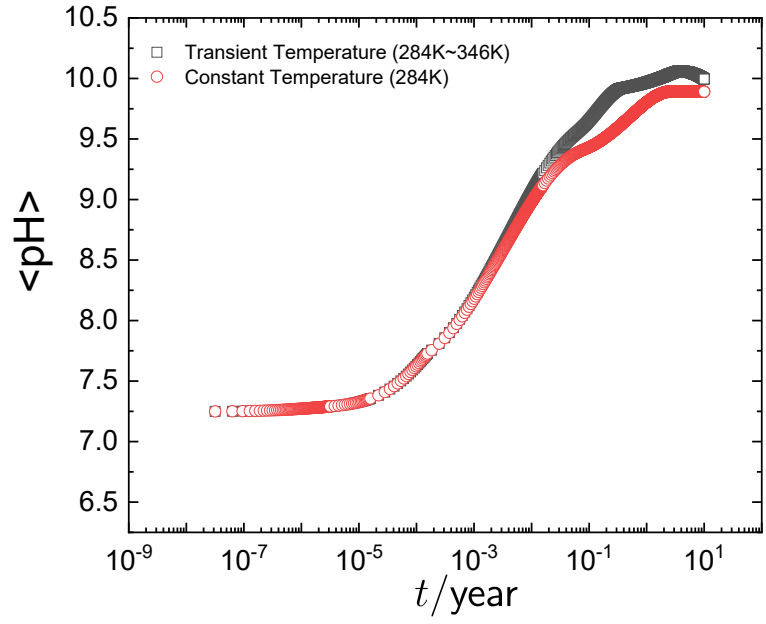

(b)

Figure 4-25. Comparison of the average pH as functions of elapsed time between systems with constant temperature and transient temperature: a) slower oxygen decay with $t_{0.1\%} = 5$ years and b) faster oxygen decay with $t_{0.1\%} = 5$ weeks.

decay, presented in Figure 4-26(a), the average surface coverage $< \gamma_{Cu_2O} >$ with transient and constant temperature followed the same trend at early elapsed time, but a discrepancy was observed as elapsed time increased. The average surface coverage for Cu_2O film increased to 1,647 monolayer thickness for transient temperature and increased to 66.6 monolayer thickness for constant temperature at the elapsed time t = 10 years. γ_{Cu_2O} tended to increase to larger values for both temperature cases at t = 10 years. For faster oxygen decay presented in Figure 4-26(b), $< \gamma_{Cu_2O} >$ increased to 165.5 monolayer thickness for transient temperature and increased to 3.1 monolayer thickness for constant temperature at elapsed time t = 10 years.

4.2.3 Local Corrosion Rate and Depth

The average local corrosion rates are presented in Figure 4-28 as functions of elapsed time for systems with constant temperature and transient temperature. For slower oxygen decay, presented in Figure 4-28(a), systems with both temperature have the same initial average local corrosion rate of 6.2 μm/year. The average corrosion rate $< R_{corr,local} >$ reached a second peak value of 4.8 μm/year for the transient temperature calculations due to the elevation of temperature; whereas, $< R_{corr,local} >$ continued to decrease from the initial value to a smaller value for the constant temperature case. In 10 years, $< R_{corr,local} >$ was 0.05 μm/year for transient temperature and $< R_{corr,local} >$ was 8.8 nm/year for constant temperature. For faster oxygen decay, presented in Figure 4-28(b), $< R_{corr,local} >$ decreased to 6.66 $\times 10^{-6}$ μm/year for transient temperature, and it decreased to 4.6 $\times 10^{-6}$ μm/year for constant temperature in 10 years.

The average local corrosion depth is presented in Figure 4-29 as functions of elapsed time for systems with constant temperature and transient temperature. For slower oxygen decay, presented in Figure 4-29(a), $< L_{corr,local} >$ increased to 1.59 μm for transient temperature in 10 years, and it increased to 0.85 μm for constant temperature. The average local corrosion depth $< L_{corr,local} >$ tended to increase for both temperature cases, but with a much larger slope for transient temperature. For faster oxygen decay presented in Figure 4-29(b), $< L_{corr,local} >$ reached a plateau of 0.22 μm for transient temperature and a plateau of 0.16 μm for constant temperature.

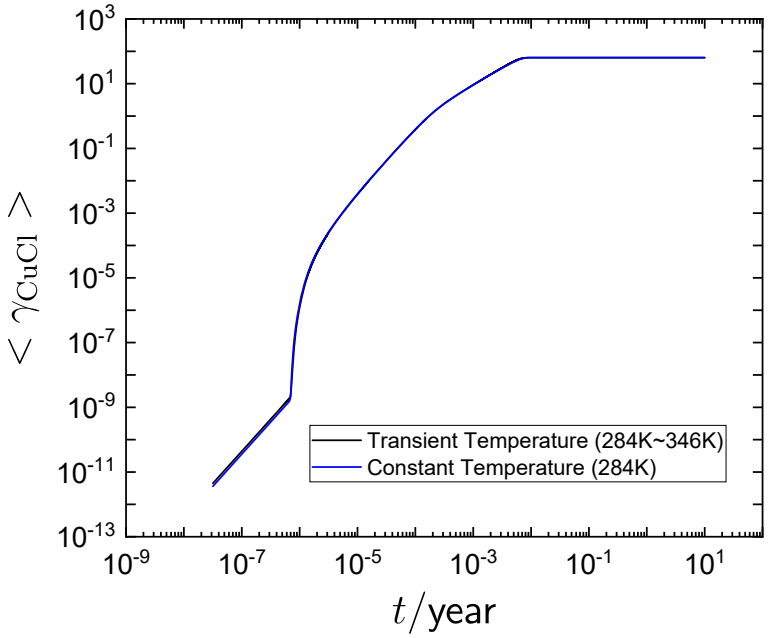

(a)

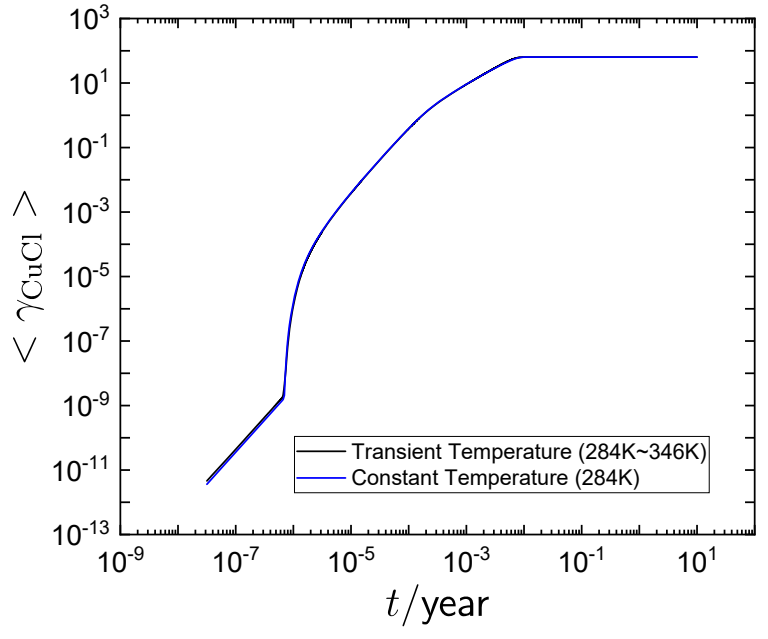

(b)

Figure 4-26. Comparison of the average surface coverage for CuCl film as functions of elapsed time between systems with constant temperature and transient temperature: a) slower oxygen decay with $t_{0.1\%} = 5$ years and b) faster oxygen decay with $t_{0.1\%} = 5$ weeks.

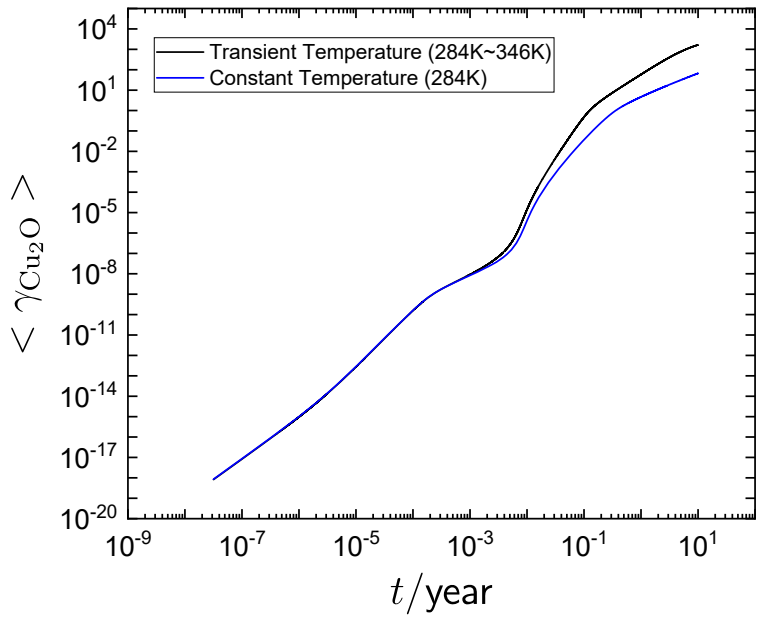

(a)

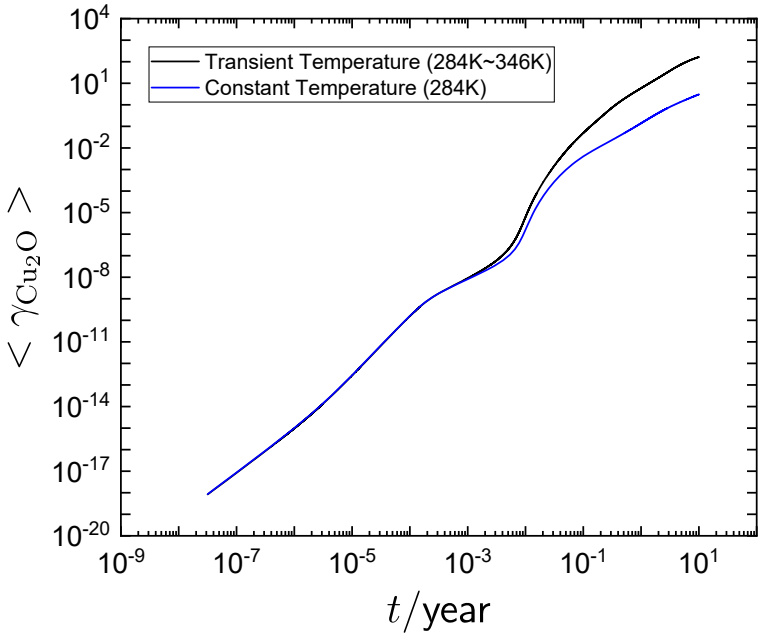

(b)

Figure 4-27. Comparison of the average surface coverage for Cu_2O film as functions of elapsed time for systems with constant temperature and transient temperature: a) slower oxygen decay with $t_{0.1\%} = 5$ years and b) faster oxygen decay with $t_{0.1\%} = 5$ weeks.

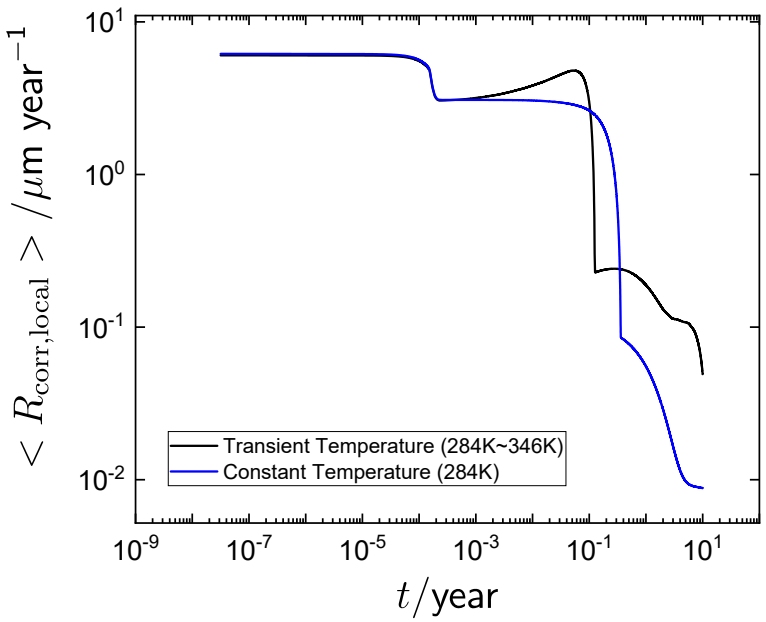

(a)

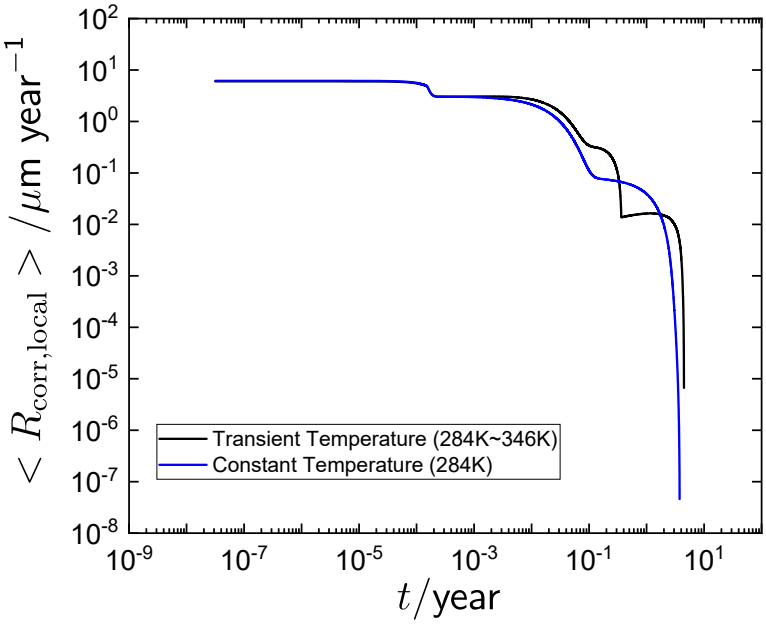

(b)

Figure 4-28. Comparison of average local corrosion rates as functions of elapsed time between systems with constant temperature and transient temperature: a) slower oxygen decay with $t_{0.1\%} = 5$ years and b) faster oxygen decay with $t_{0.1\%} = 5$ weeks.

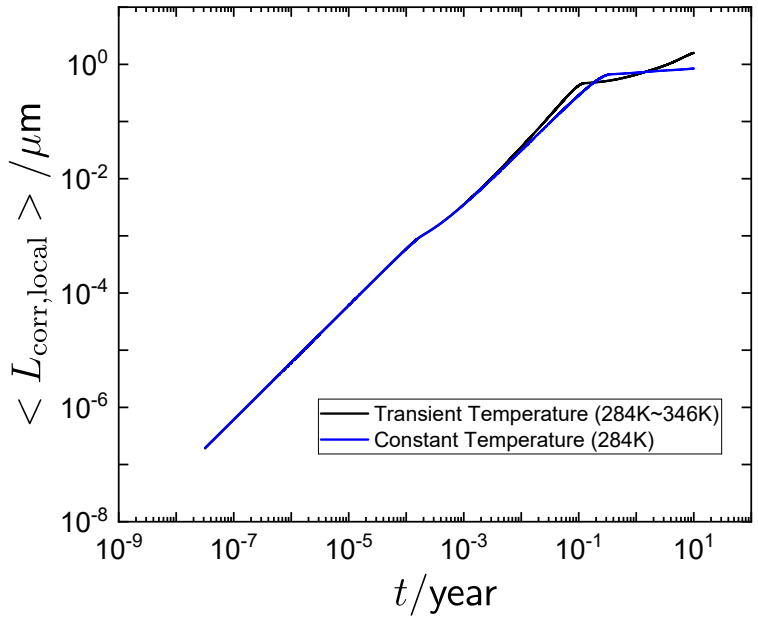

(a)

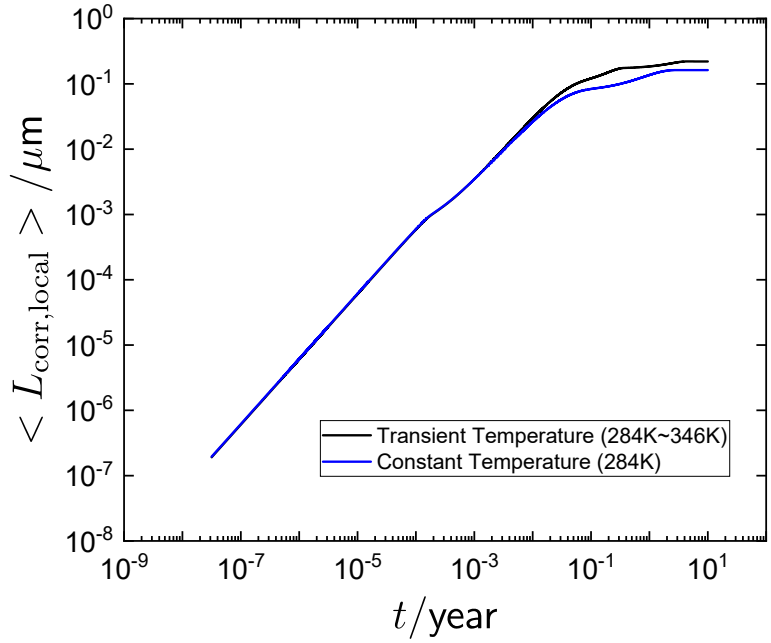

(b)

Figure 4-29. Comparison of the average local corrosion depth as functions of elapsed time between systems with constant temperature and transient temperature: a) slower oxygen decay with $t_{0.1\%} = 5$ years and b) faster oxygen decay with $t_{0.1\%} = 5$ weeks.

CHAPTER 5
IMPEDANCE MEASUREMENTS ON QLED DEVICES

Impedance measurements were performed on red and green QLED devices under current densities chosen to yield specified luminescence.* A circuit model was developed for the observed high-frequency loop in terms of the thickness, dielectric constant, and resistivity distribution of the hole-injection layer. dielectric constant and resistivity were extracted with a known layer thickness obtained from Scanning Electron Microscopy (SEM) analysis. Impedance measurements performed on hole-transport only devices were used to verify the interpretation of the high-frequency capacitive loop in terms of the properties of the hole-injection layer.

5.1 Methods

The red and green QLED devices were measured at different current density conditions chosen to yield specified luminescence. An interpretation model was developed to fit the impedance data. QLED devices in the present work were synthesized by NanoPhotonica Inc.

5.1.1 Materials

A schematic structure representation of the QLED devices is shown in Figure 5-1. The top aluminum layer is the cathode and the bottom indium tin oxide (ITO) layer is the anode, adjacent to a transparent substrate made of glass. After applying the potential, electrons are injected from the cathode and holes are injected from the anode through the hole-injection layer (HIL). The carriers move through the electron-transport layer (ETL) made of zinc oxide (ZnO), and hole transport layer (HTL), respectively. The quantum-dot emitting layer (EL) was made of cadmium-based core/shell-type colloidal quantum dots dispersed in octane. The EL is sandwiched between the ETL and HTL, where electrons and holes recombine to produce photons, and light is emitted from the EL through the transparent substrate. The emission wavelength was 633 nm with a full width at half maximum (FWHM) equal to 27 nm for the red quantum dots, and was 535 nm with a FWHM of 30 nm for the green quantum dots. The chemical compositions of the HIL and HTL are given in the caption of Figure 5-1.

*The work presented in the chapter is reprinted with permission from C. You, A. Titov, B. H. Kim, and M. E. Orazem, "Impedance Measurements on QLED Devices: Analysis of High-Frequency Loop in Terms of Material Properties," invited paper, Journal of Solid State Electrochemistry, 24 (2020), 3083-3090.[130]

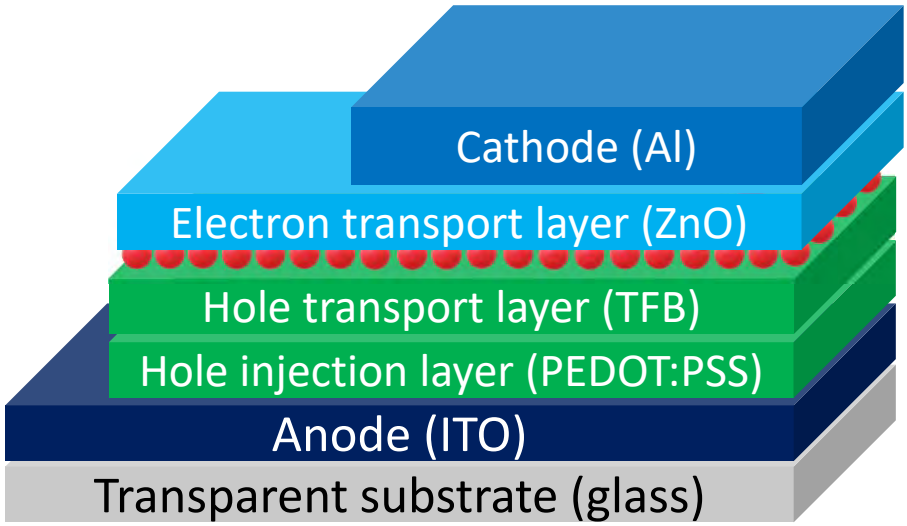

Figure 5-1. Schematic representation of a QLED device. The hole injection layer is poly (3,4-ethylenedioxythiophene) polystyrene sulfonate (PEDOT:PSS); the hole transport layer (HTL) is poly (9,9-dioctylfluorene-alt-N-(4-sec-butylphenyl)-diphenylamine) (TFB), and the electron-transport layer (ETL) is zinc oxide (ZnO). (Taken from You et al. [130])

The high-frequency loop was interpreted to be associated with the property of the hole-injection layer, and the low-frequency loop was associated with the slow degradation processes occurring during the device operation. Hole-transport-layer-only devices were fabricated to verify that the high-frequency loop of the impedance spectra could be associated with the property of the hole-injection layer. The electron-transport layer in red QLED devices shown in Figure 5-1 was replaced by a hole-transport layer made of N,N'-Di(1-naphthyl)-N,N'-diphenyl-(1,1'-biphenyl)-4,4'-diamine or (NPB).

5.1.2 Electrochemical Measurements

EIS measurements were performed on the red and green QLED devices using a Gamry Ref 3000 potentiostat at current densities chosen to yield different values of luminescence. The QLED device used had four duplicate sites patterned on four corners of a square, each with a nominal surface area of 0.04 cm^2. During the measurement, the device was fixed on a holder designed and 3-D printed by NanoPhotonica, and one of the sites was placed in contact with pin needles to ensure good electrical contact. A two-electrode setup was used in all the

measurements. The frequency range was from 1 MHz to 20 mHz for the red QLED devices, and from 100 kHz to 20 mHz for the green QLED devices. A sinusoidal perturbation of 10 mV was applied. Potentials were measured with reference to the open-circuit potential. The experimental device was placed inside a copper-wire-mesh Faraday cage to prevent interference caused by external fields. The stability and causality of the impedance response was checked through the Kramers–Kronig relations by using the measurement model,[1, 3] and the linearity was checked by monitoring the Lissajous plots.[170, 171]

5.1.3 Film Thickness

The film thickness was measured by use of a scanning electron microscope (SEM). Samples were prepared in cross-section by focused-ion beam.

5.1.4 Equivalent Circuit Model

The equivalent circuit model shown in Figure 5-2 was developed to fit the impedance data of the QLED devices. The corresponding impedance could be expressed as

$$Z = R_e + \frac{R_H}{1+(j\omega)^{\alpha_H} R_H Q_H} + \frac{R_L}{1+(j\omega)^{\alpha_L} R_L Q_L} \tag{5-1}$$

where R_e is the ohmic resistance, α_H and α_L the CPE exponents for the high-frequency and low-frequency loops, respectively, Q_H and Q_L are CPE coefficients for the high-frequency and low-frequency loops, respectively, R_H is the resistance associated with the high-frequency loop, and R_L is the resistance associated with the low-frequency loop. Complex non-linear regression was performed in Origin 2019® using Levenberg-Marquardt algorithm to extract the fitting parameters. Preliminary experiments suggested that the high-frequency loop was the property of

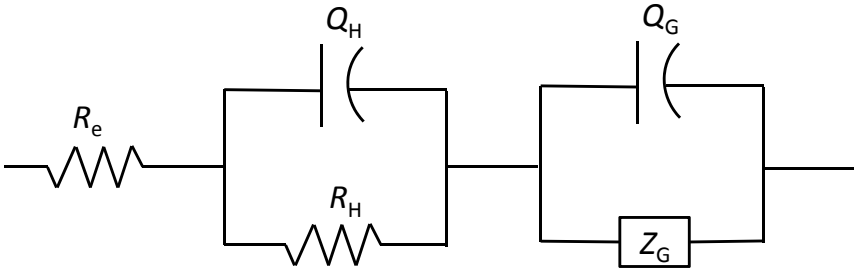

Figure 5-2. Equivalent circuit model for the QLED device. (Taken from You et al. [130])

the hole-injection layer, and the low-frequency loop could be associated with the kinetic degradation processes during the operation.

5.2 Experiment Results

A calibration curve of the red QLED devices is shown in Figure 5-3. As the applied potential increased, the current density and luminescence exponentially increased. The EIS measurements were performed for luminescence equal to 100 cd/m^2, 200 cd/m^2, 300 cd/m^2, 400 cd/m^2, and 500 cd/m^2. The Nyquist plots of the red and green QLED devices with the luminescence as a parameter are shown in Figures 5-4(a) and 5-4(b), respectively. The impedance data were checked by the measurement model,[1, 2, 3] and data inconsistent with the Kramers–Kronig relations were deleted.[49] Two depressed capacitive loops were observed for both red and green QLED devices. The characteristic frequency of the high-frequency loop increased for increased luminescence; whereas, the characteristic frequency decreased for the low-frequency loop. The sizes of the two loops decreased when increasing the luminescence.

Regression was performed to fit the equivalent circuit model shown in Figure 5-2 to the experimental data. As shown in Figures 5-4(a) and 5-4(b), the model provided an excellent fit to the experimental data. Regressed parameters for each luminescence condition are shown in Table 5-1, and all the regressed parameters were found to be statistically significant. For the red QLED devices, α_H ranged from 0.97 to 0.98 for the high-frequency loop, and α_L ranged from 0.49 to 0.51 for the low-frequency loop. For green QLED devices, α_H ranged from 0.96 to 0.97 for the high-frequency loop, and α_L ranged from 0.46 to 0.54 for the low-frequency loop. The normalized Nyquist plots by R_e and R_H are shown in Figures 5-4(c) and 5-4(d). The superposed impedance spectra suggest that the chemistry and physics are the same under each luminescence condition.

The impedance response of hole-transport-only devices, shown in Figure 5-5, showed a depressed capacitive loop at high frequency and a little tail at low frequency. The high-frequency loop was fitted by an equivalent circuit model including an ohmic resistance in series with a

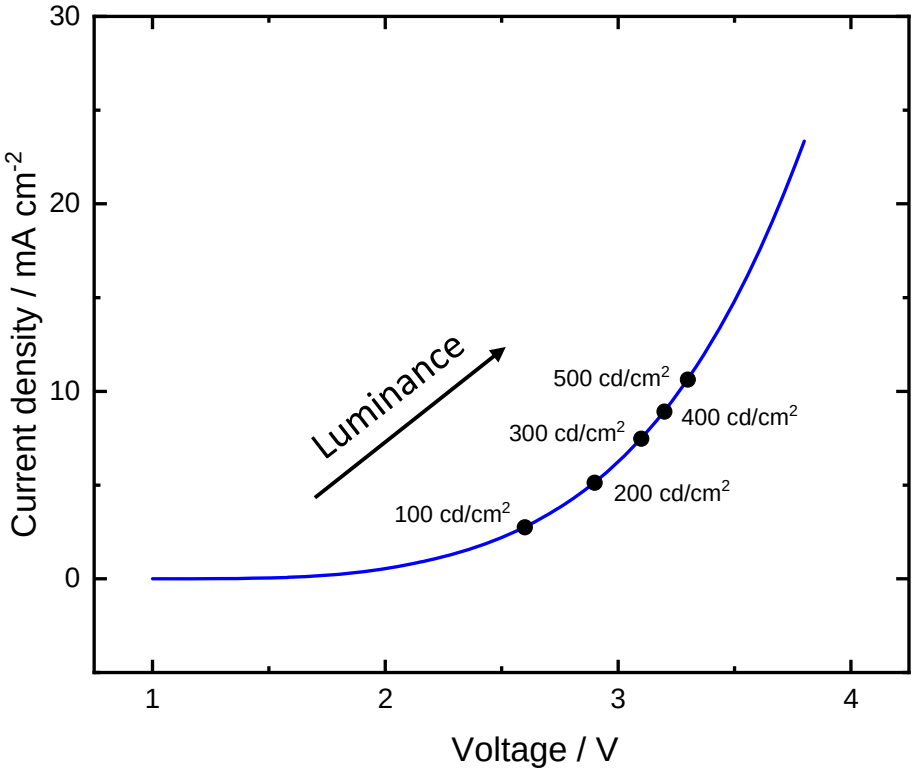

Figure 5-3. Calibration curve of red QLED devices: Current density and luminescence were plotted as a function of the potential. (Taken from You et al. [130])

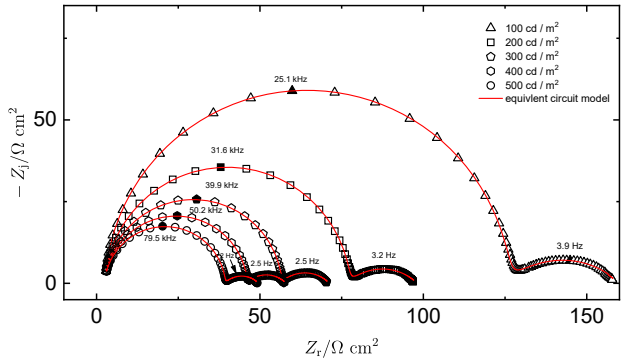

(a)

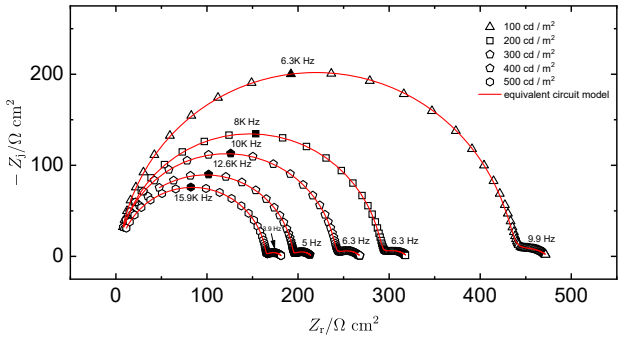

(b)

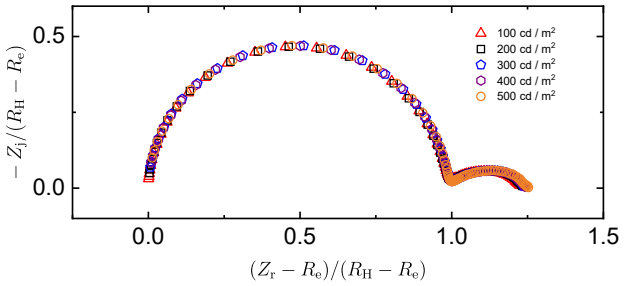

(c)

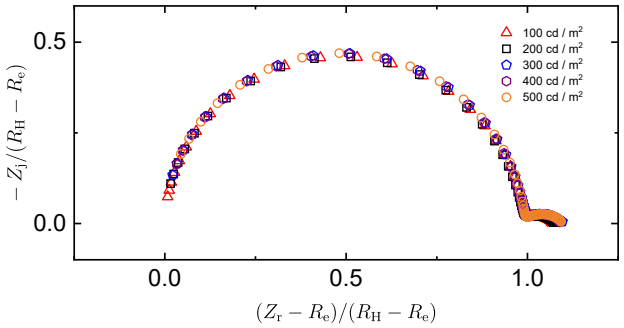

(d)

Figure 5-4. Regression of the equivalent circuit model shown in Figure 5-2 to the impedance data with the luminescence as a parameter: a) red and b) green. Normalized Nyquist plot of the QLED devices with the luminescence as a parameter: c) red and d) green. (Taken from You et al. [130])

Table 5-1. Parameters from regression of the equivalent circuit model to the experimental impedance data for red and green QLED devices.

red QLED devices							
L[1] (cd/m^2)	R_e (Ωcm^2)	Q_H ($\mu F/s^{(1-\alpha)}cm^2$)	α_H	R_H (Ωcm^2)	Q_L ($mF/s^{(1-\alpha)}cm^2$)	α_L	R_L (Ωcm^2)
100	2.575 ± 0.012	0.07383 ± 0.00078	0.977 ± 0.001	122.75 ± 0.17	5.88 ± 0.19	0.490 ± 0.009	34.78 ± 0.51
200	2.588 ± 0.009	0.07933 ± 0.00074	0.973 ± 0.001	74.34 ± 0.07	9.42 ± 0.19	0.498 ± 0.006	21.19 ± 0.16
300	2.521 ± 0.007	0.08073 ± 0.00068	0.972 ± 0.001	53.80 ± 0.04	12.26 ± 0.21	0.514 ± 0.004	14.93 ± 0.08
400	2.507 ± 0.009	0.08490 ± 0.00088	0.969 ± 0.001	43.37 ± 0.03	16.60 ± 0.30	0.510 ± 0.005	12.14 ± 0.08
500	2.508 ± 0.009	0.08731 ± 0.00103	0.967 ± 0.001	36.71 ± 0.03	19.71 ± 0.38	0.512 ± 0.005	10.36 ± 0.07
green QLED devices							
L (cd/m^2)	R_e (Ωcm^2)	Q_H ($\mu F/s^{(1-\alpha)}cm^2$)	α_H	R_H (Ωcm^2)	Q_L ($mF/s^{(1-\alpha)}cm^2$)	α_L	R_L (Ωcm^2)
100	3.005 ± 0.119	0.09977 ± 0.00013	0.963 ± 0.001	428.27 ± 1.16	3.68 ± 0.26	0.458 ± 0.026	43.24 ± 2.00
200	3.137 ± 0.054	0.1001 ± 0.0008	0.962 ± 0.001	286.52 ± 0.31	6.29 ± 0.23	0.479 ± 0.012	30.31 ± 0.57
300	2.029 ± 0.046	0.09025 ± 0.00061	0.970 ± 0.001	237.64 ± 0.19	6.52 ± 0.17	0.491 ± 0.008	28.91 ± 0.35
400	3.415 ± 0.038	0.09391 ± 0.00053	0.966 ± 0.001	189.99 ± 0.11	8.36 ± 0.17	0.528 ± 0.006	21.77 ± 0.18
500	3.518 ± 0.037	0.09372 ± 0.00065	0.967 ± 0.001	160.54 ± 0.10	10.17 ± 0.25	0.539 ± 0.008	18.19 ± 0.18

[1] L is the luminescence.

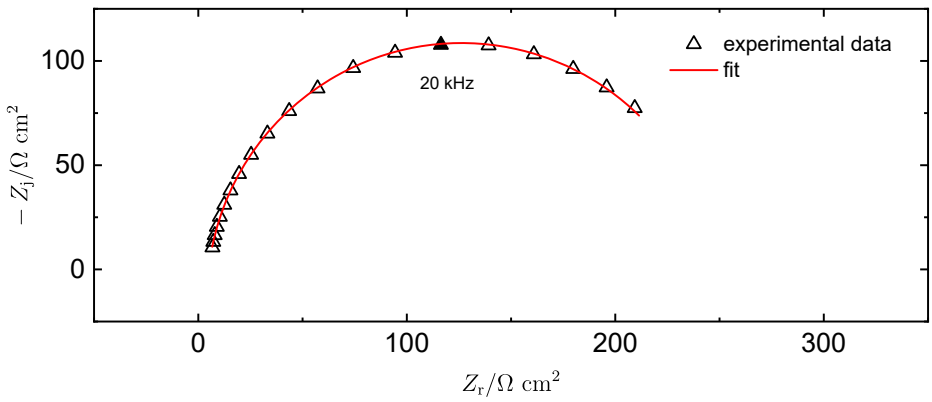

Figure 5-5. Regression of the equivalent circuit model to the high-frequency experimental impedance data for hole-transport only device. (Taken from You et al. [130])

parallel combination of a CPE and a resistance. As shown in Figure 5-5, the fitted curve was in good agreement with the experimental data with CPE exponent α equal to 0.96.

5.3 Regression Analysis

The CPE parameters obtained from regression of equation (5-1) are related to the device properties such as layer thickness and capacitance, but extraction of physical parameters requires a more refined analysis. Hirschorn et al. [42, 43] found that a CPE behavior can be related to a power-law distribution of resistivity within a film. The power-law model analysis is combined in the present work with ex-situ measurement of film thickness and estimation of capacitance by use of the measurement model[47] to identity the properties of the hole-injection layer.

The thickness of hole-injection layer was measured by SEM to be 71.3 nm. Values for capacitance $C_{\text{eff,M}}$, dielectric constant ε, and ρ_δ obtained using equations (2-19) and (2-25) are shown in Table 5-2. The standard deviation of ρ_δ and ε were obtained by 5000 Monte Carlo simulations under the assumption that the standard deviation of layer thickness was 10% of the measured value and the error was normally distributed. The capacitance obtained by the

Table 5-2. The value of $C_{\text{eff,M}}$, ε, and ρ_δ using equations (2-19) and (2-25) for red and green QLED devices.

	red QLED devices			green QLED devices		
Luminescence (cd/m^2)	$C_{\text{eff,M}}$ ($\mu\text{F/cm}^2$)	ε	$\log(\rho_\delta)$ ($\log(\Omega\text{cm})$)	$C_{\text{eff,M}}$ ($\mu\text{F/cm}^2$)	ε	$\log(\rho_\delta)$ ($\log(\Omega\text{cm})$)
100	0.0518 ± 0.0058	4.17 ± 0.89	5.80 ± 1.57	0.0608 ± 0.0057	4.89 ± 0.96	6.53 ± 0.86
200	0.0520 ± 0.0038	4.19 ± 0.73	5.56 ± 0.71	0.0608 ± 0.0052	4.90 ± 0.92	6.68 ± 0.67
300	0.0518 ± 0.0061	4.27 ± 0.92	5.57 ± 1.39	0.0597 ± 0.0035	4.81 ± 0.77	6.68 ± 0.49
400	0.0529 ± 0.0018	4.26 ± 0.57	5.77 ± 0.06	0.0609 ± 0.0038	4.90 ± 0.80	6.63 ± 0.56
500	0.0530 ± 0.0015	4.26 ± 0.55	5.74 ± 0.04	0.0608 ± 0.0027	4.90 ± 0.71	6.74 ± 0.26
Mean	0.0523 ± 0.0006	4.23 ± 0.05	5.69 ± 0.11	0.0606 ± 0.0005	4.88 ± 0.04	6.65 ± 0.08

measurement model approach can be compared to the value obtained by extrapolation of the complex capacitance,

$$C_\text{r} + \text{j}C_\text{j} = \frac{1}{\text{j}\omega(Z - R_\text{e})} \tag{5-2}$$

A sample result is presented in Figure 5-6 for red and green QLED devices with luminescence equal to 100 cd/m^2. The capacitance of the film can be obtained from the high-frequency limit of

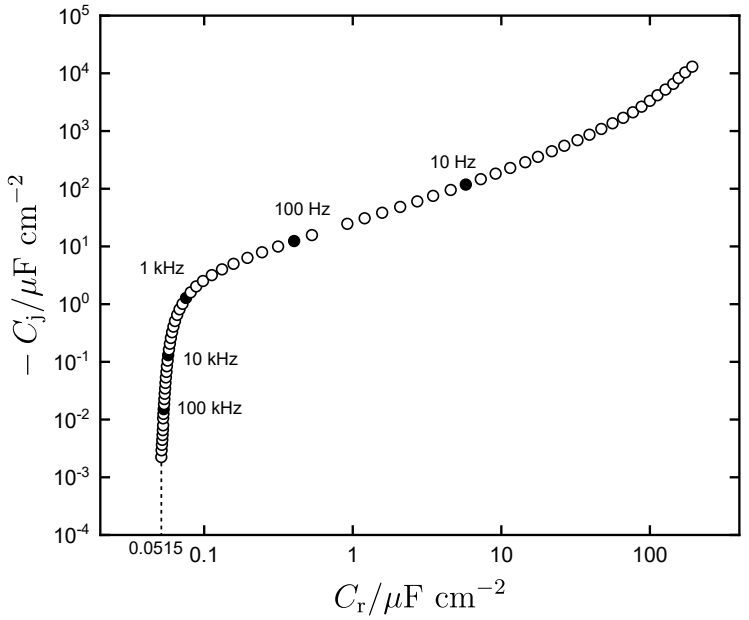

(a)

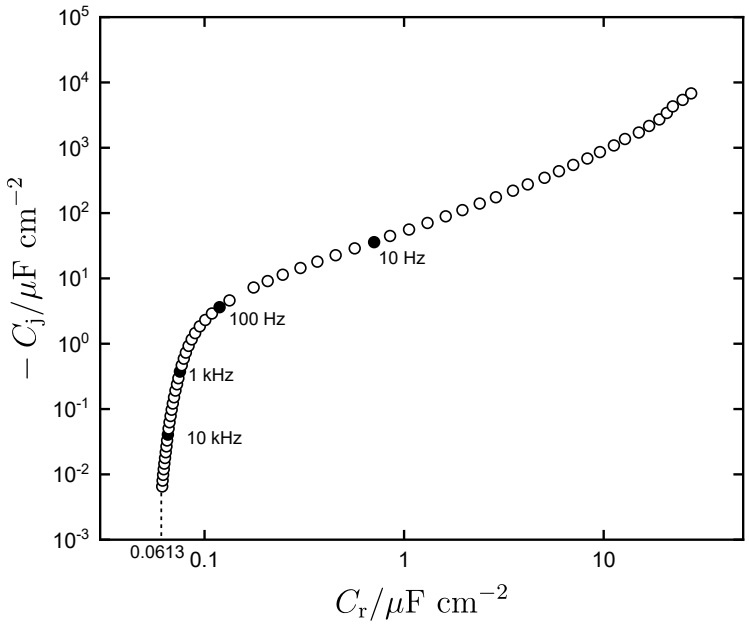

(b)

Figure 5-6. Complex-capacitance plots using equation (5-2) for the QLED devices when luminescence is equal to 100 cd/m^2: a) red and b) green. (Taken from You et al. [130])

the real part of the capacitance. The asymptotic value of the real part of the capacitance shown in Figure 5-6(a) is 0.0515 μF/cm^2 for the red QLED devices, and the corresponding value obtained by regression of the measurement model was 0.0518 ± 0.0058 μF/cm^2. The asymptotic value of the real part of the capacitance shown in Figure 5-6(b) is 0.0613 μF/cm^2 for the green QLED devices, and the corresponding value obtained by regression of the measurement model was 0.0608 ± 0.0057 μF/cm^2. These results suggest that the measurement model approach of estimating the effective capacitance is appropriate in the present system.

The mean value of capacitance for the red devices was 0.0523 ± 0.0006 μF/cm^2. The calculated value of ε ranged from 4.17 to 4.27 for the red QLED devices. The mean value of dielectric constant was 4.23 ± 0.05. For the resistivity at $y = \delta$, ρ_δ ranged from 0.365 MΩcm to 0.634 MΩcm under five different luminescence conditions. The mean value of ρ_δ was 0.488 MΩcm with a 95.4% confidence interval from 0.288 MΩcm to 0.825 MΩcm. For the green QLED devices, the mean value of capacitance was 0.0606 ± 0.00051 μF/cm^2. The mean value of ε was 4.880 ± 0.039, and the mean value of ρ_δ was 4.604 MΩcm with the 95.4% confidence interval from 3.125 MΩcm to 6.443 MΩcm.

The thickness of the hole-injection layer for the hole-transport-only device was measured to be 50 nm, and the capacitance determined from the measurement model was 0.0297 ± 0.0021 μF/cm^2. The dielectric constant was $\varepsilon = 4.06 \pm 0.68$, and the resistivity ρ_δ at $y = \delta$ was 0.294 MΩcm with a 95.4% confidence interval from 0.051 MΩcm to 1.549 MΩcm. The value of ε obtained from the power-law model for hole-transport-only devices was in good agreement with the value obtained from the red emitting devices and also agrees with the typical range of dielectric constant for the organic material. The values of ρ_δ are on the same order of magnitude as the red QLED devices, but smaller than the green QLED devices.

The uncertainty in ρ_δ is large because, as seen in equation (2-19),[46] the sensitivity to ρ_δ is small when α is close to unity. A sample distribution of $\log(\rho_\delta)$ and ε were obtained by 5000 Monte Carlo simulations for red QLED and green QLED devices shown in Figure 5-7 with luminescence equal to 200cd/m^2. The results were compared with the hole-transport-only device.

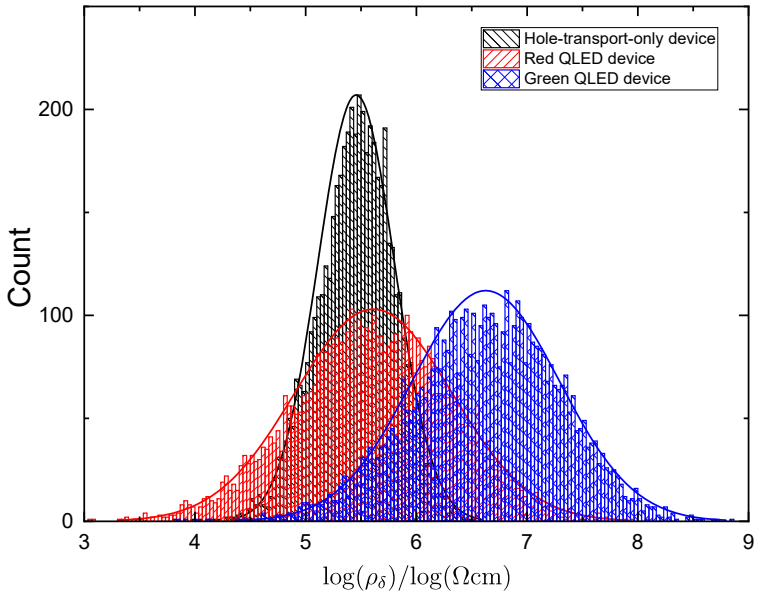

(a)

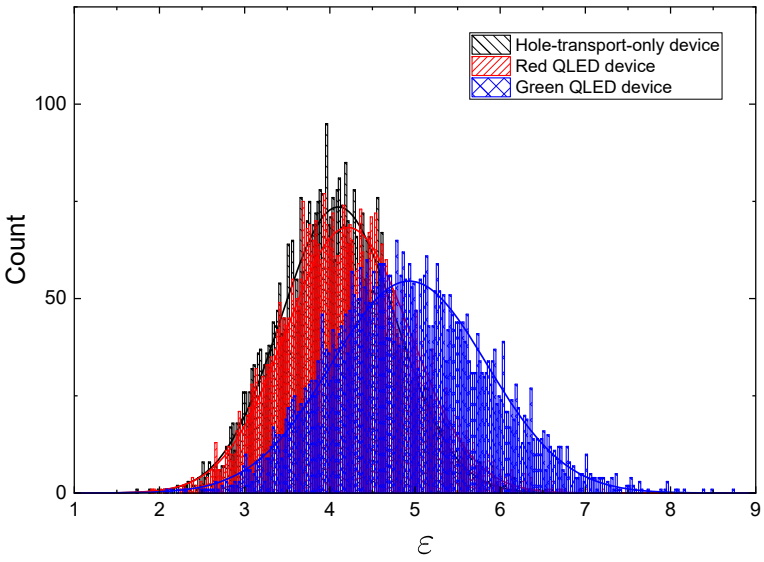

(b)

Figure 5-7. The distribution of $\log(\rho_\delta)$ and ε obtained by 5000 Monte Carlo simulations for red QLED, green QLED and hole-transport-only devices. The luminescence was equal to 200cd/m^2. The standard deviation of the layer thickness was assumed to be 10% of the measured value and the errors were assumed normally distributed. : a) Histograms of $\log(\rho_\delta)$ and b) Histograms of ε. (Taken from You et al. [130])

The value of ρ_δ was found to follow a log-normally distribution shown in Figure 5-7(a) and the overlapping part extended over two orders of magnitude. The value of ε was found to be normally distributed shown in Figure 5-7(b) and the majority part of three Histograms were found to be overlapped. Even though the results from Histograms of $\log(\rho_\delta)$and ε showed the uncertainty with a large standard deviation, the standard deviation from regression analysis were pretty tight supporting the argument that the high-frequency loop is associated with the properties of the hole-injection layer.

CHAPTER 6
APPLICATION OF KRAMERS-KRONIG RELATIONS TO MULTI-SINE IMPEDANCE MEASUREMENTS

The issue of whether the Kramers–Kronig relations may be used to validate multi-sine impedance data is not fully resolved. * Srinivasan et al. [105] state that the Kramers–Kronig relations may be used to identify multi-sine data affected by potential drift. Sacci et al. [106] used the Kramers–Kronig relations to validate dynamic electrochemical impedance spectroscopy data that employs a multi-sine technique. The results presented by Macdonald [107] suggest that multi-sine signals treated by fast Fourier and related transformations yield results that automatically satisfy the Kramers–Kronig relations. The objective of this work is to use experiments and numerical simulations to test for the compliance of the Kramers–Kronig relations to the non-stationary behaviors utilizing single-sine and multi-sine excitation signals.

6.1 Experimental and Numerical Method

The approach taken in the present work included application of the Kramers–Kronig relations to both experimental measurements and synthetic data.

6.1.1 Experimental Measurement of Non-Stationarity System

The MS-EIS measurements were performed on a Lithium Thionyl Chloride ($Li/SOCl_2$) primary D-size (13Ahr) battery using a Gamry Interface 1000E. The impedance results for such a system is discussed elsewhere [73] in which galvanostatic impedance measurement under discharge with a moderate direct current (DC) offset was shown to cause non-stationary behavior. Both multi-sine and single-sine impedance measurements were obtained for the same system with the same excitation amplitude and frequency range. The DC offset used for the measurement was 20mA with $\pm$10mA alternating current (AC) excitation signal. The frequency range was between 100Hz to 25mHz. The elapsed time for the single-sine measurement was 1983 seconds, and the elapsed time for the multi-sine measurement was 3403 seconds, which is 10 times the typical multisine EIS experiment in these frequencies and this timescale was increased for lower noise and enhanced non-stationarity effects.

*The work presented in the chapter is reprinted with permission from C. You, M. A. Zabara, M. E. Orazem, and B. Ulgut, "Application of the Kramers-Kronig Relations to Multi-Sine Electrochemical Impedance Measurements," Journal of the Electrochemical Society, 167 (2020), 020515 [128]

6.1.2 Kramers–Kronig Analysis

The simulated and measured impedance data were tested for compliance with the Kramers–Kronig relations using the measurement model method. The method to assess Kramers–Kronig consistency, developed by Agarwal et al., is based on fitting a measurement model of sequential Voigt elements shown in Figure 1 to either the real or imaginary component of impedance data and then predicting the other component of impedance from the extracted parameters [1, 2, 2]. As the circuit shown in Figure 2-8 satisfies the Kramers–Kronig relations, the ability to fit the measurement model to experimental data demonstrates consistency of the data to the Kramers–Kronig relations.

An important advantage of the measurement model approach is that it identifies a small set of model structures that are capable of representing a large variety of observed behaviors or responses. The inability to fit an impedance spectrum by a measurement model can be attributed to the failure of the data to conform to the assumptions of the Kramers–Kronig relations rather than to the failure of the model. The measurement model approach allows calculation of a confidence interval, providing a statistical rigor to the rejection of data due to failure to conform to the Kramers–Kronig relations. A disadvantage of the measurement model approach is that regression is strongly influenced by data outliers.

The experimentally measured impedance data were also tested for Kramers–Kronig compliance by linear measurement model approach developed by Boukamp [4] and implemented by Gamry Instruments. In this approach, the Voigt elements are fitted via linear equations to a selected region of the spectrum. Values of time constant $\tau_k = 1/R_k C_k$ are specified as the inverse of frequencies selected over the experimental range of frequencies. This yields a set of linear equations to be solved for values of the corresponding R_k. An advantage of the Boukamp approach is that it is less sensitive to outliers. A disadvantage is that confidence intervals are not provided for the resulting comparison between experiment and measurement model.

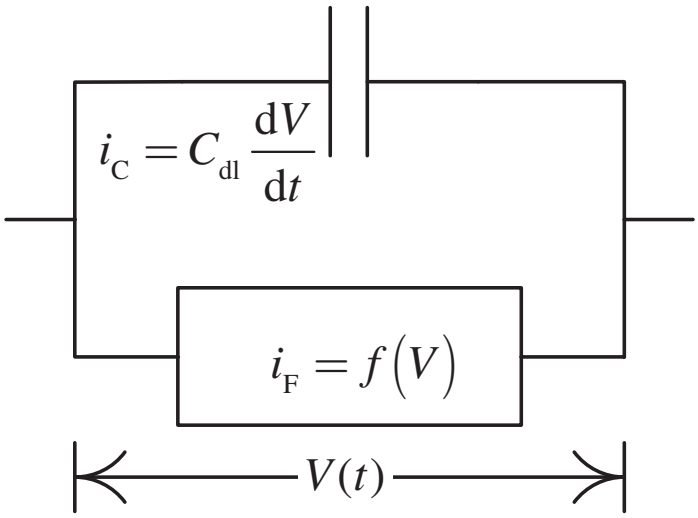

Figure 6-1. Circuit representation of the faradaic current and the double layer capacitor used in the simulation. (Taken from You et al. [128])

6.1.3 Model System Simulation

The non-stationarity was simulated on a system in which a charging current is added to a faradaic current given by a Tafel expression with a time-dependent rate constant as shown in Figure 2 [49]. The applied potential for the single sine case was a sinusoidal perturbation as

$$V = \Delta V \sin(2\pi f_i) \tag{6-1}$$

where ΔV is the input potential amplitude and f_i is the input frequency range of $f_i = 1\text{Hz}$ 1kHz with 10 points/decade. The applied potential for the multi-sine case was a sinusoidal perturbation as

$$V = \Delta V \sin(2\pi f_i + \varphi_i) \tag{6-2}$$

where φ_i is the phase shift and $N = 31$. The faradic current density and the charging current density were expressed as

$$i_F = k_a \exp(b_a V) - k_c \exp(-b_c V) \tag{6-3}$$

and

$$i_C = C_{dl} \frac{dV}{dt} \tag{6-4}$$

where b_a and b_c are the anodic and cathodic coefficients with $b_a = b_c = 19.5\ \mathrm{V}^{-1}$. The values of k_a, k_c were $k_a = k_b = 0.14 \times 10^{-3}$ mA/cm^2 and the double-layer capacitance was $C_{dl} = 31\mu$ F/cm^2. The impedance response was calculated by a Fourier analysis for the single-sine potential perturbation and by an FFT analysis for the multi-sine.

The simulation was performed with linear and exponential increases in the charge-transfer resistances which caused a decrease of the rate constant as a function of time. The behavior was expressed as

$$i_F = K_a(1-\gamma)\exp(b_a V) - K_c(1-\gamma)\exp(-b_c V) \tag{6-5}$$

where $\gamma = 0.01t$ for a linear decrease in active area, and $\gamma = 0.1(1-\exp(-t))$ for an exponential decrease in active area. The variation of γ used in the simulations is presented in Figure 6-2. The corresponding charge-transfer resistance increased from 183.2 Ω to 203.5 Ω within 10 s.

6.2 Experiment and Simulation Results

Results are presented for the single-sine and multi-sine impedance of a Li/$SOCl_2$ primary battery with a DC offset known to cause nonstationary behavior. Results are also presented for the single-sine and multi-sine impedance of synthetic data designed to represent a nonstationary system. Both the Boukamp [4] and the Agarwal et al. .

6.2.1 Experimental measurement: Li/$SOCl_2$ with DC offset

The experimentally measured single-sine and multi-sine impedance of the Li/$SOCl_2$ battery under nonstationary conditions are shown in Figure 6-3. The lines shown in Figure 6-3 are the result of the linear Kramers–Kronig analysis reported by Boukamp [4, 3] and implemented by Gamry. The superposition of the lines with the multi-sine data indicates that the multi-sine data satisfy the Kramers–Kronig relations; whereas, the single-sine data show deviation in the Kramers–Kronig compliance. The deviation is seen most readily in plots of the phase as shown in Figure 6-3(d). A more sensitive analysis can be obtained by use of the measurement model as developed by Agarwal et al. . [1, 2, 2] The results presented in Figure 6-4 reflect the results of a fit of the measurement model to the imaginary part of the impedance for the single-sine data and a complex fit for the multi-sine. For this system, the imaginary fit yielded more statistically

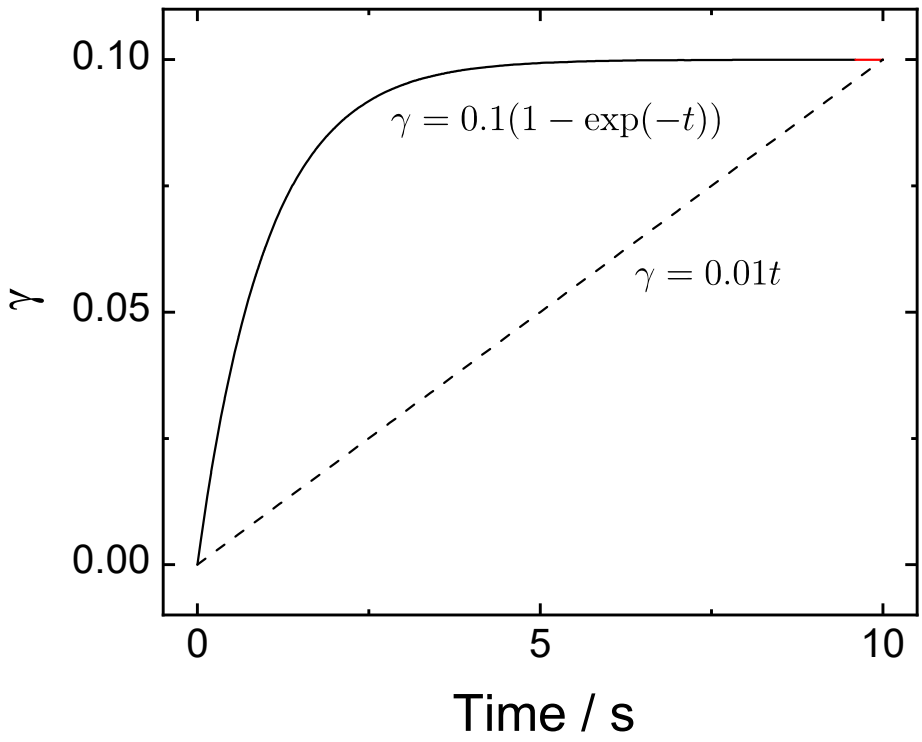

Figure 6-2. Behavior of the fraction of inactive area γ as a function of time for the calculation of the impedance of nonstationary systems. (Taken from You et al. [128])

significant parameters for the single-sine data than could be achieved by a complex fit; whereas, the complex fit yielded more statistically significant parameters for the multi-sine data than could be achieved by an imaginary fit. As shown in Nyquist format in Figure 6-4(a), the measurement model provided an adequate fit of the single-sine data only at higher frequencies; whereas, the measurement model provided an excellent fit to the multi-sine data over the complete measured range of frequencies. The measurement model provided an excellent fit to the imaginary part of the single-sine data, but the experimental data deviated from the predicted real part of the measurement, as shown in Figure 6-4(d). The complex fit of the measurement model yielded an excellent agreement to the imaginary (Figure 6-4(c)) and real (Figure 6-4(e)) parts of the measurement.

A more detailed analysis may be obtained by an examination of the residual errors shown in Figure 6-5. The residual errors for the regression to the imaginary part of the single-sine measurement are shown in Figure 6-5(a), and the errors in the prediction of the real part of the

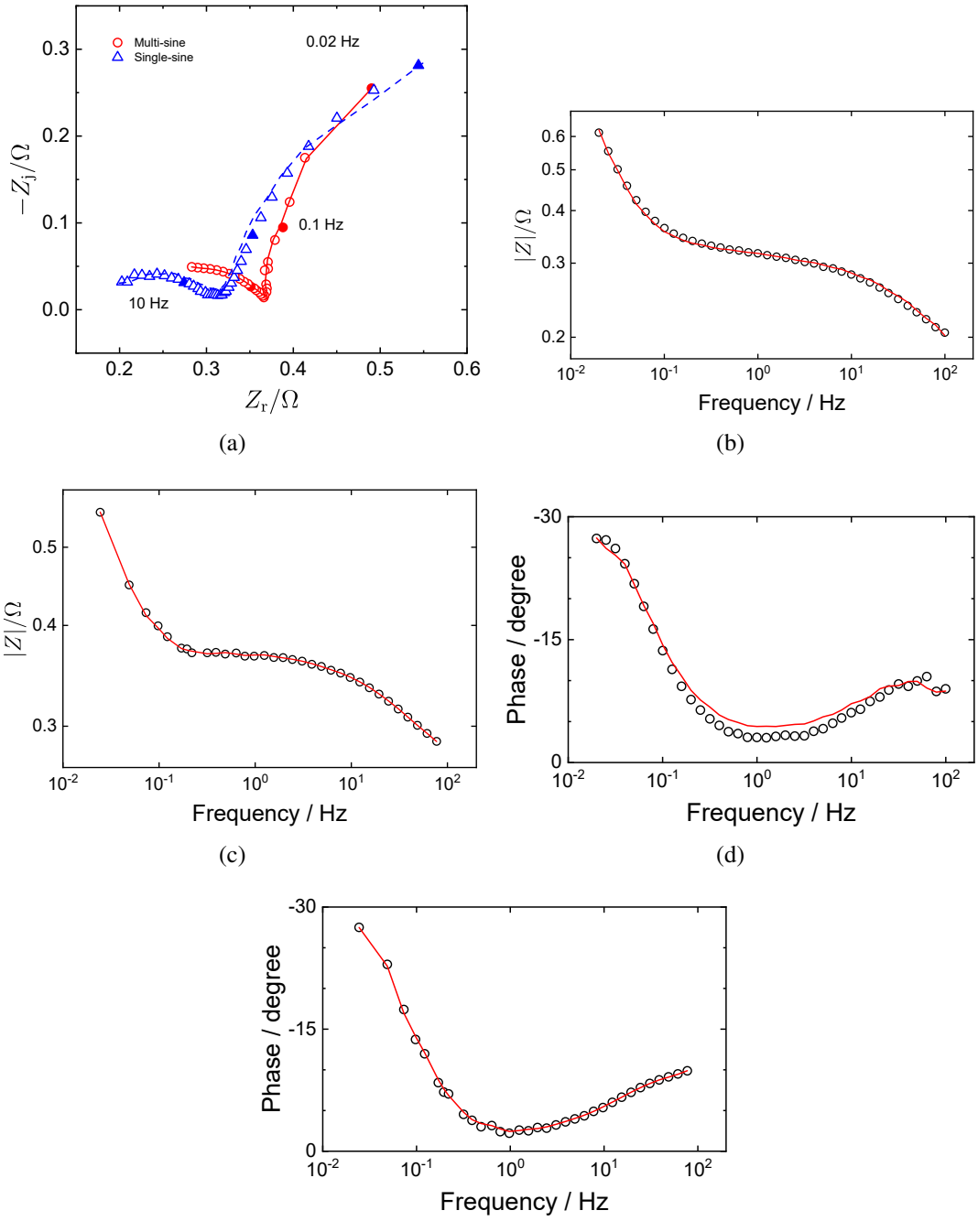

Figure 6-3. Single-sine and multi-sine impedance response for a Li/SOCl2 battery under nonstationary conditions: a) Nyquist; b) and c) magnitude for single-sine and multi-sine measurements, respectively; and d) and e) phase for single-sine and multi-sine measurements, respectively. Lines represent the results of a linear Kramers–Kronig analysis as implemented by the Gamry software. (Taken from You et al. [128])

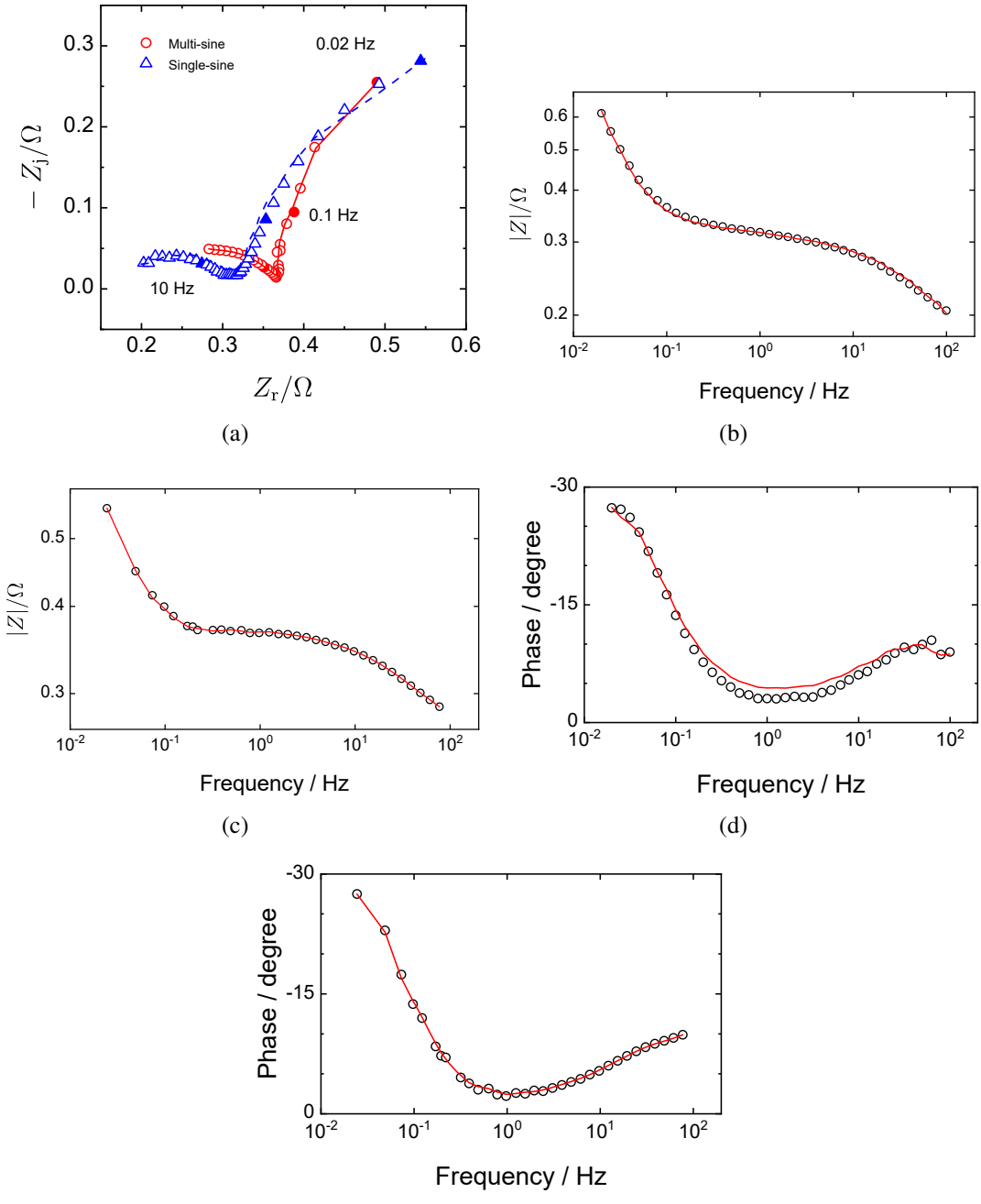

Figure 6-4. Results of the measurement model analysis of the data presented in Figure 6-3: a) Nyquist; b) and c) imaginary for single-sine and multi-sine measurements, respectively; and d) and e) real for single-sine and multi-sine measurements, respectively. Solid lines represent the results of a measurement model fit to the imaginary part of the spectrum for single-sine measurements and both real and imaginary parts of the spectrum for the multi-sine measurements. Dashed lines in b-e represent 95.4% confidence intervals for the model. (Taken from You et al. [128])

measurement is shown in Figure 6-5(b). The large errors at low frequency are consistent with the results presented in Figure 5a. In contrast, the residual errors for a complex fit to the multi-sine data shown in Figures 6-5(c) and d indicate that the measurement model provided a good fit to the data. The residual errors fall within the 95.4% confidence interval for the model; thus, the data may be considered to be consistent with the Kramers–Kronig relations. A complex fit to the single-sine data yielded residual errors that were outside the 95.4% confidence interval for the model. This work shows that the single-sine data did not satisfy the Kramers–Kronig relations. The experimental work presented in Figures 6-3-6-5 shows that multi-sine method yielded Kramers–Kronig-consistent impedance data for a nonstationary system for which a single-sine approach showed failure to conform to the Kramers–Kronig relations. The time allocated for the multi-sine measurement was 70% larger than the time allocated for the single-sine measurements; thus, the system had ample time to demonstrate nonstationary behavior. The issue is that the presence of nonstationary behavior for a multi-sine measurement could not be identified by application of the Kramers–Kronig relations. The results suggest also that the measurement model implementation by Agarwal et al. [1, 2, 2] was more sensitive to failures to satisfy the Kramers–Kronig relations than was the linear implementation by Boukamp [4].

6.2.2 Numerical Simulation: Linear Increase in Charge-Transfer Resistance

The single-sine and multi-sine calculations were designed such that the elapsed times for the simulated impedance measurements were identical. Thus, the level of nonstationarity experienced for the two calculations was the same. The perturbation amplitude for the single-sine calculations was 1 mV, and the perturbation amplitude for the multi-sine calculations was 0.5 mV. To minimize superposition, the phase angles of signals used to construct the multi-sine potential input were staggered. The effective maximum potential amplitude was 5 mV.

Results are presented in Figure 6-6 for the impedance calculated under the linear transient increase in charge-transfer resistance shown in Figure 6-2. The Nyquist plots shown in Figure 6-6(a) show that, while the single-sine calculations revealed a low-frequency tail corresponding to the increase in charge-transfer resistance, the multi-sine calculations produced a semicircle with a

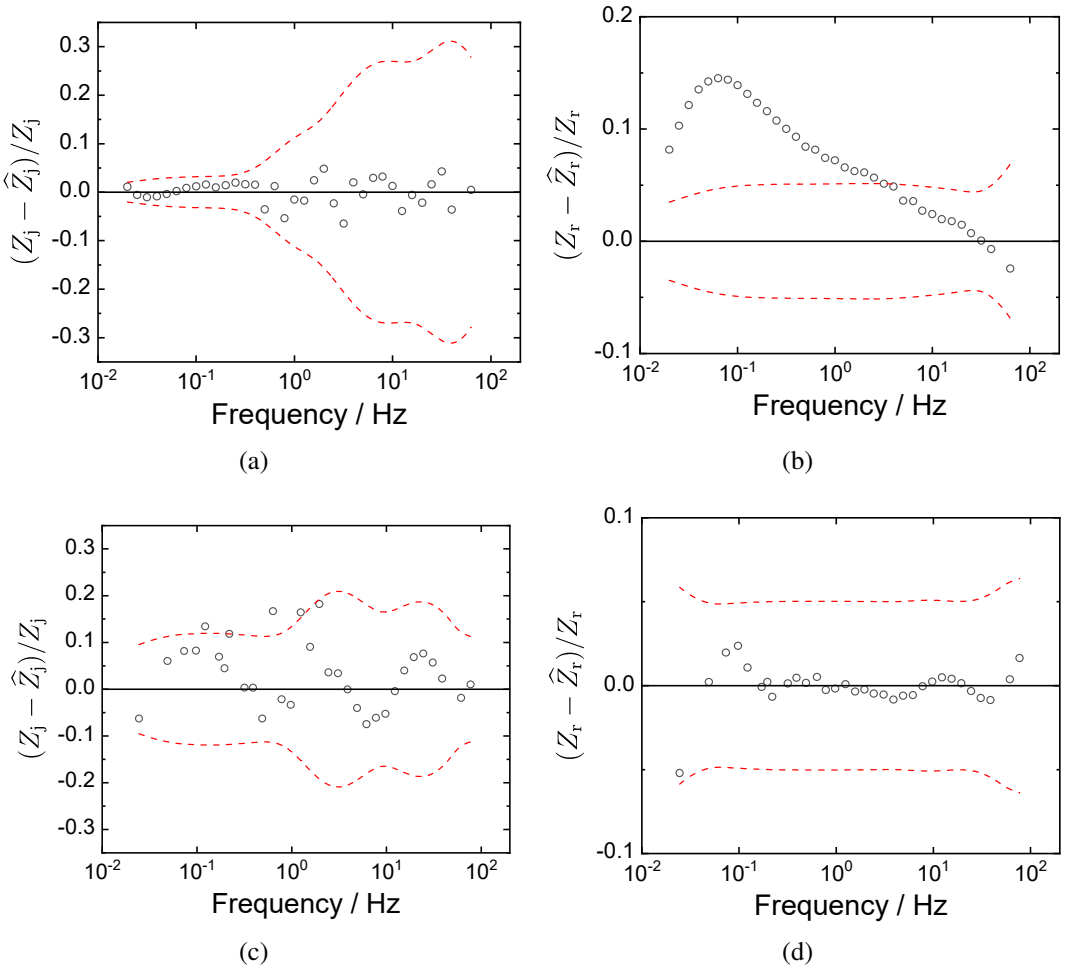

Figure 6-5. Normalized residual errors resulting from a measurement model fit to the data presented in Figure 6-3: a) results of a measurement model fit to the imaginary part of the spectrum for single-sine measurements and b) the resulting error in the prediction of the real part of the measurement; c) and d) imaginary and real residual errors for a complex fit to both real and imaginary parts of the spectrum for the multi-sine measurements. Dashed lines in represent 95.4% confidence intervals for the model. (Taken from You et al. [128])

radius between the initial and final charge-transfer resistance. Regression of the measurement model to the imaginary part of the single-sine impedance yielded the normalized residual error presented in Figure 6-6(b), indicating an excellent fit to the data. The normalized prediction errors for the real part of the measurement, shown in Figure 6-6(c), show that the low-frequency real part of the data was inconsistent with the imaginary part of the data. Thus, the Kramers–Kronig relations were not satisfied for the single-sine simulations.

The residual errors for a complex fit to the multi-sine simulations are presented in Figures 7d and e. These results could be fit by only a single RC element. The simulations yielded scatter at low frequency that could be diminished by increasing the elapsed time for the signals. In a purely numerical study, a similar result for synthetic calculations of multi-sine impedance was reported by Srinivasan et al. [105] and attributed to failure to satisfy the Kramers–Kronig relations. The Boukamp implementation of the Kramers–Kronig relations, however, showed these simulated data to be consistent. The multi-sine calculation of the impedance yielded a semicircle with scattered values at low frequency. The measurement model analysis reported the charge transfer resistance to be Rt = 193.2 Ω cm^2, which was the temporal average. The capacitance was obtained as C_{dl} = 31 μ F/cm^2, which was the same as the input.

6.2.3 Numerical Simulation: Exponential Increase In Charge-Transfer Resistance

Results are presented in Nyquist format in Figure 6-7(a) for the impedance calculated under the exponential transient increase in charge-transfer resistance shown in Figure 6-2. The charge-transfer resistance transient was characterized by a rapid increase in resistance at short times at which the singe-sine calculation yielded high-frequency values of the impedance. The shape of the single-sine results reveals that the charge-transfer resistance was almost constant for the calculation of lower frequencies. The single-sine calculations yielded a distorted semicircle; whereas, the multi-sine calculations produced a semicircle with a radius between the initial and final charge-transfer resistance. Regression of the measurement model to the imaginary part of the single-sine impedance yielded the normalized residual error presented in Figure 6-7(b), indicating an excellent fit to the data. The normalized prediction errors for the real part of the

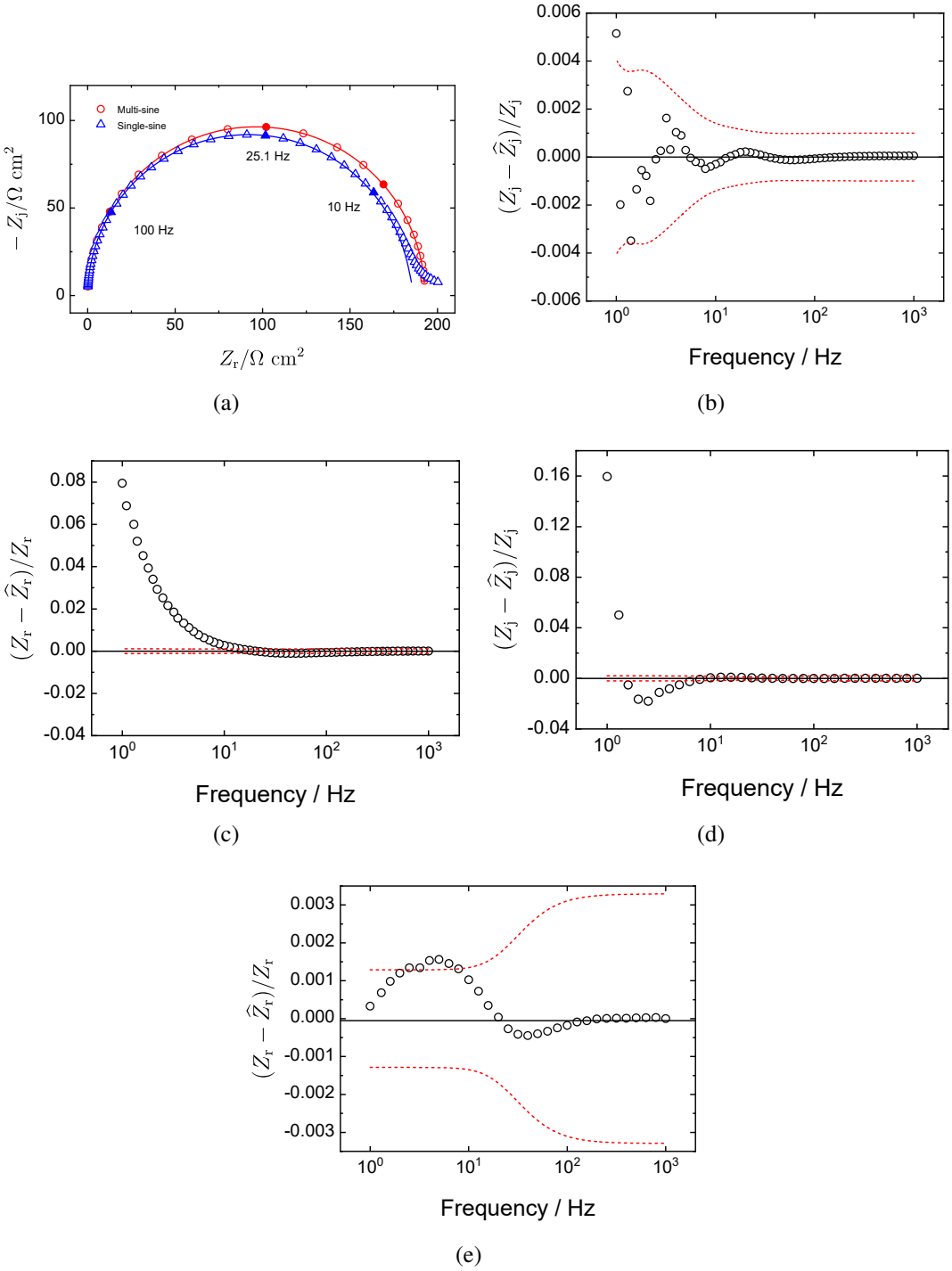

Figure 6-6. Calculated impedance for the linear increase of the charge-transfer resistance for single and multi-sine signals: a) Nyquist plot for single-sine and multi-sine results with lines representing the corresponding fit of the measurement model; b) and c) normalized residual and prediction errors respectively, for a measurement model fit to the imaginary part of the single-sine impedance; and d) and e) normalized residual errors for a complex measurement model fit to multi-sine impedance. Dashed lines in b-e represent 95.4% confidence intervals for the model. (Taken from You et al. [128])

measurement, shown in Figure 6-7(c), show that the data were inconsistent with the Kramers–Kronig relations over a broad frequency range. Again, the Kramers–Kronig relations were not satisfied for the single-sine simulations.

The residual errors for a complex fit to the multi-sine simulations, presented in Figures 6-7(d) and 6-7(e), were similar to those presented in Figures 6-6(d) and e for a linear increase in charge-transfer resistance. Again, these results could be fit by only a single RC element. The simulations yielded scatter at low frequency that could be diminished by increasing the elapsed time for the signals. The multi-sine calculation of the impedance yielded a semicircle with scattered values at low frequency. The measurement model analysis showed a value of charge transfer resistance of $R_t = 201.38\ \Omega\ cm^2$, which is the temporal average. The capacitance was found as $C_{dl} = 31\ \mu F/cm^2$ which is the same as the input.

6.3 Inspection of Non-Linearity and Non-Stationarity on Impedance Spectra

The experimental and simulation results in the present work demonstrate that the Kramers–Kronig relations do not provide a means of determining, for multi-sine measurements, whether the system has undergone a transient change during the course of the impedance measurement. The multi-sine technique provides a temporally averaged impedance diagram which satisfies automatically the Kramers–Kronig relations. In contrast, application of the Kramers–Kronig relations can reveal nonstationary behavior from single-sine measurements.

In principle, the coherence function

$$C_{xy}(\omega) = \frac{|P_{xy}(\omega)|^2}{P_{xx}(\omega)P_{yy}(\omega)} \tag{6-6}$$

can provide a means for assessing the quality of input signals used to assess the impedance. In equation (6-6), the coherence function C_{xy} is a real number between 0 and 1 that measures the correlation between the input signal $x(t)$ and the output signal $y(t)$. A value of unity means that the two signals are considered to correspond to each other perfectly at a given frequency. P_{xx} and P_{yy} are the power spectra of $x(t)$ and $y(t)$, respectively, and P_{xy} is the average cross-power spectrum of $x(t)$ and $y(t)$.

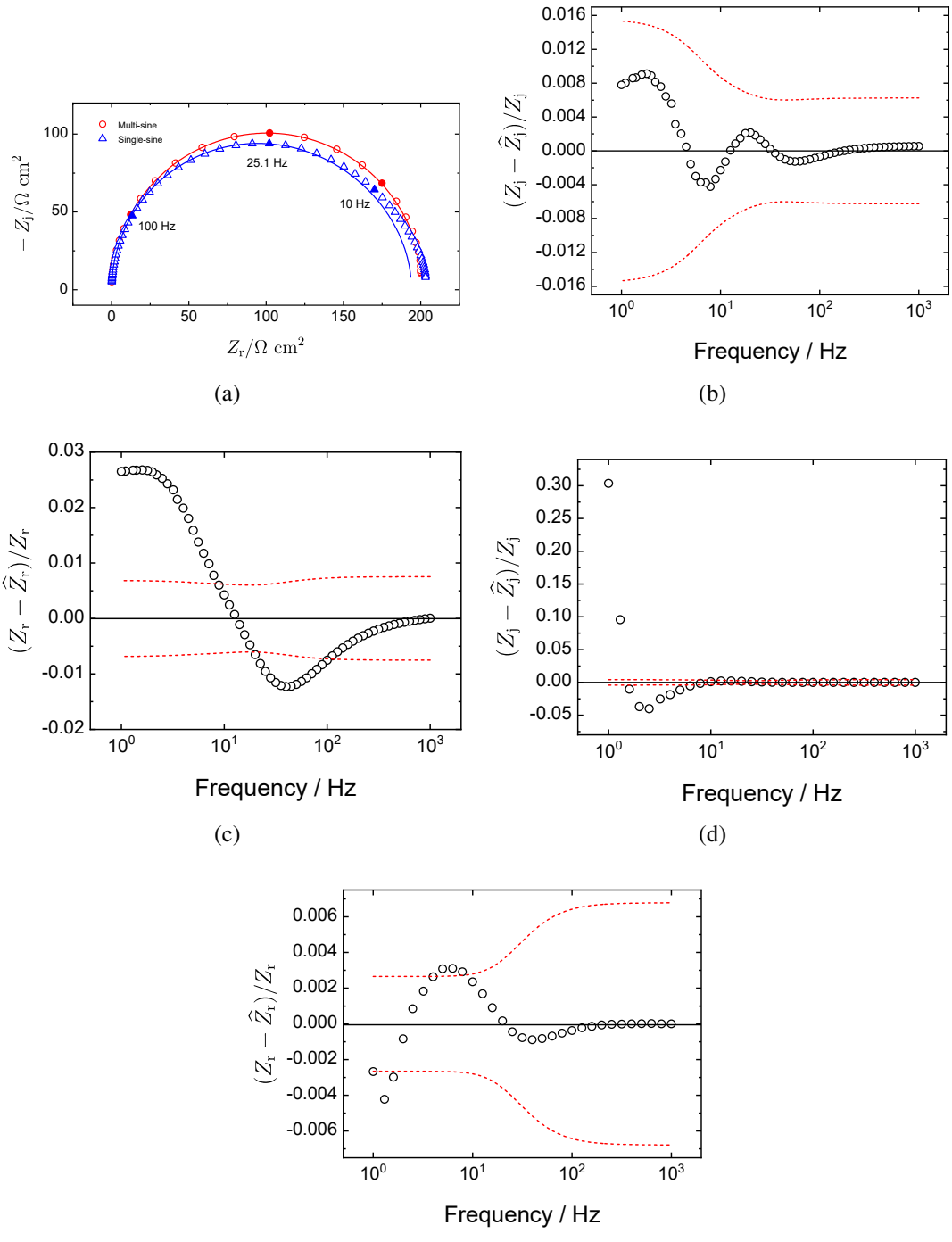

Figure 6-7. Calculated impedance for the exponential increase of the charge-transfer resistance for single and multi-sine signals: a) Nyquist plot for single-sine and multi-sine results with lines representing the corresponding fit of the measurement model; b) and c) normalized residual and prediction errors respectively, for a measurement model fit to the imaginary part of the single-sine impedance; and d) and e) normalized residual errors for a complex measurement model fit to multi-sine impedance. Dashed lines in b-e represent 95.4% confidence intervals for the model. (Taken from You et al. [128])

The coherence function calculated for the synthetic multi-sine impedance values presented in Figures 6-6 and 6-7 varied slightly from unity, as shown in Figure 6-8. The maximum variation was 0.3% for the linear variation of charge-transfer resistance and 0.02% for the exponential decaying variation of charge-transfer resistance. This level of variation would be masked by experimental artifacts in electrochemical measurements. Further, the coherence calculation suffers from sensitivity to window size and shape selection and artifacts due to timing inaccuracies. Therefore, the coherence function was not explored further for experimental data. On the other hand, inspecting the full Fourier space can be considered to be an alternative for inspecting non-linearity and non-stationarity in multi-sine impedance spectra. Figure 6-9(b) and 6-9(d) show the multi-sine current excitation and the resulting voltage in the frequency domain for two experiments done with galvanostatic control. These datasets can essentially be read in two parts: the signal and the noise. On the logarithmic y-scale, the points that are high are those frequencies that are excited by the applied signal and the corresponding measurement are the signal and the more crowded points that are much lower are the noise level of the applied signal for the excitation and the result of any nonlinearity and drift for the measured signal. The noise floor shown for the voltage signal on the graphs depend on the settings on the instrument, environment noise etc. As shown in Figure 6-9(b), non-stationarity can be observed in the unexcited frequencies in the frequency domain signal. Non-stationarity exhibits a signal that is below the noise level of the instrument at high frequencies, but gradually increases as the frequency gets lower. It eventually gets above the noise level and keeps rising until the lowest frequency. In contrast for a stationary system shown in Figure 6-9(d), such behavior is not observed. One way of quantifying the total power at the unexcited frequencies is the so-called “Total Harmonic Distortion (THD)” [172, 173, 174, 175, 176] which is the integral of power in the frequencies that are not excited by the excitation. Though THD provides no distinction between non-linearity and non-stationarity, it is a good parameter to check for both effects in bulk.

The present work provided the opportunity to explore the relative merits of two different implementations of the measurement model for assessing consistency with the Kramers–Kronig

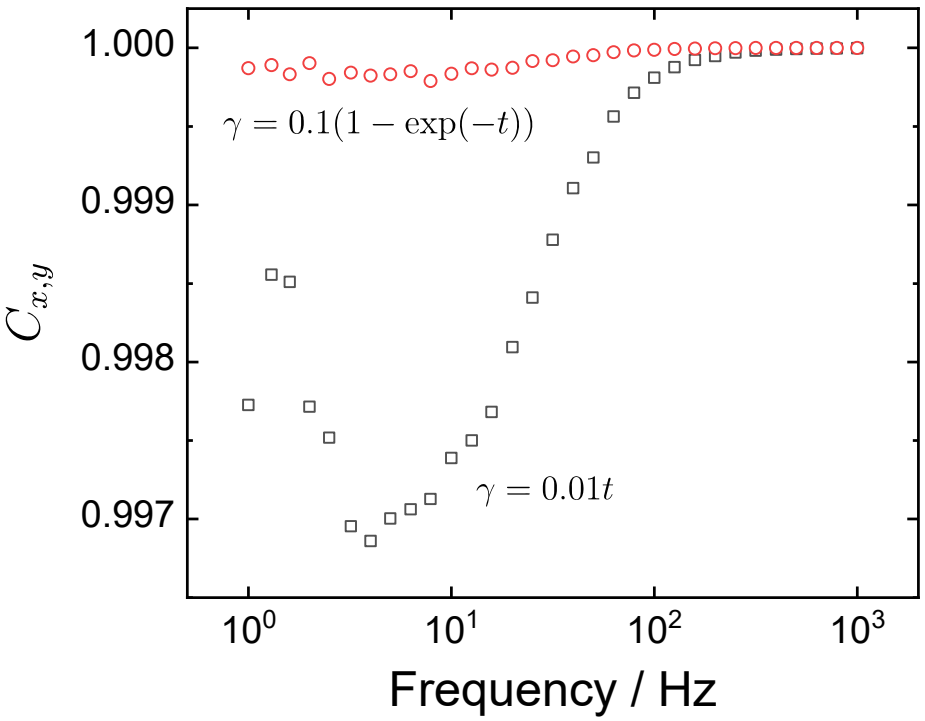

Figure 6-8. Coherence function calculated for the multi-sine simulations presented in Figures 6-6 and 6-7. (Taken from You et al. [128])

relations. The linear regression approach pioneered by Boukamp [46] allows specification of one time constant for every measured frequency, thus providing a point by point analysis that is insensitive to outliers. The point by point analysis is evident in the results for the multi-sine data presented in Figure 6-3(a). In contrast, the analysis pioneered by Agarwal et al. [1, 2, 2] relies on nonlinear regression and can resolve only a small number of parameters. As shown in Figures 6-4 and 6-5, the approach of Agarwal et al. [1, 2, 2] was very sensitive to the failure of the single-sine data to conform to the Kramers–Kronig relations and demonstrated unequivocally the extent to which the multi-sine data satisfied the Kramers–Kronig relations. A more subtle deviation is seen between model and single-sine data in Figure 6-3. The Boukamp approach is preferred for data, such as those with outliers, for which an adequate number of RC elements cannot be resolved.

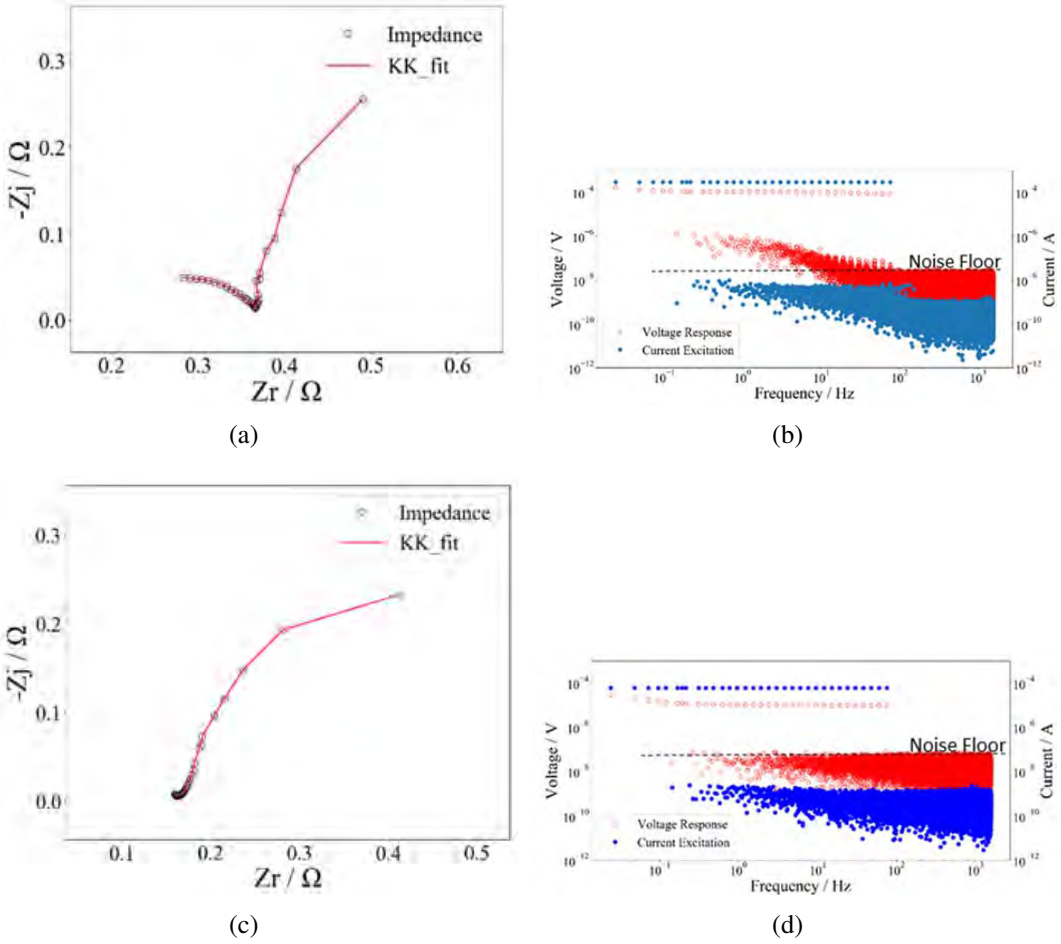

Figure 6-9. Multi-sine impedance response for a Li/$SOCl_2$ battery under nonstationary conditions: a) Nyquist; b) Frequency domain of the current excitation and the voltage signals. Multi-sine impedance response for a Dummy Cell in stationary conditions: c) Nyquist; d) Frequency domain of the current excitation and the voltage signals. (Taken from You et al. [128])

CHAPTER 7
EXPERIMENTAL OBSERVATION OF OHMIC IMPEDANCE

The objective of this work was to demonstrate the experimental determination of the ohmic impedance.* Experimental data were collected for the ferricyanide/ferrocyanide redox couple in a supported electrolyte. The regression results were supported by a series of finite-element calculations. Simulations performed for a disk electrode influenced by ohmic and kinetic effects provided an updated relationship for the normalized difference $R_{e,LF} - R_{e,HF}$ as a function of the parameter J. A second set of finite-element simulations showed that the updated relationship was unaffected by mass transfer. A third set of finite-element simulations demonstrated that the experimentally obtained results could be attributed to the presence of a film on the electrode surface. Such a step-by-step analysis provides a comprehensive description of the interfacial processes.

7.1 Simulation and Experimental Method

The present work represents a combination of experimental and numerical approaches.

7.1.1 Experimental

Experiments were performed for ferri/ferrocyanide redox species (10 mM each) in a 0.5 M KCl electrolyte using a Gamry Reference 600+ potentiostat. The working electrode consisted of a 5-mm-diameter gold disk rotating at 800 rpm. A Pt gauze (4 cm^2) was used as the counterelectrode, a saturated Ag/AgCl electrode was used as a reference electrode, and the temperature of double-walled electrochemical cell was held at 25 ± 0.1 °C. The frequency range was 500 kHz to 9.98 mHz with 10 measurements per decade, and the perturbation amplitude was 10 mV rms (or 28.3 mV peak-to-peak). The "low-noise" option was implemented, which imposes the largest minimum number of cycles for each frequency measured.

7.1.2 Numerical

Numerical simulations for the impedance response associated with primary and secondary current distributions were performed using COMSOL Multiphysics® 5.0. The hardware used was a 64-bit Dell™ Precision T7500 workstation with dual Intel® Xeon® E5620 2.4 GHz processors and 96 GB of RAM. The numerical simulations for the impedance response associated with

*The work presented in the chapter is reprinted with permission from C. You, A. Dizon, M. Gao, V. Vivier, and M. E. Orazem, "Experimental Observation of Ohmic Impedance," Electrochimica Acta, 413 (2022), 140177 [177]

convective diffusion of ferricyanide and ferrocyanide species employed COMSOL Multiplysics® 6.0 on a Dell precision workstation T7920 with dual Intel® Xeon® Gold 6242R 3.1GHz processors and 256 GB of RAM.

7.2 Mathematical Models

Numerical simulations were performed for the primary and secondary current distributions on a disk electrode for which Laplace's equation governed potential in the electrolyte. Simulations were also performed for a rotating disk electrode for which Laplace's equation was assumed to apply in conjunction with the convective diffusion equations for ferricyanide and ferrocyanide species.

7.2.1 Primary and Secondary Distributions

The 2-D axisymmetric solution to Laplace's equation for a secondary current and potential distribution was obtained numerically in cylindrical coordinates. A schematic representation (not to scale) of the disk geometry is presented in Figure 7-1 with boundaries identified as Γ_{WE} for the disk electrode, Γ_{CE} for the counterelectrode, and Γ_I for insulating surfaces. For the simulations, $R/r_0 = 2000$, and $r_0 = 0.5$ cm.

The governing equation for the potential phasor was

$$\frac{1}{r}\frac{\partial}{\partial r}\left(r\frac{\partial \widetilde{\Phi}}{\partial r}\right) + \frac{\partial^2 \widetilde{\Phi}}{\partial y^2} = 0 \tag{7-1}$$

where r is the radial coordinate and y is the distance normal to the electrode. Equation (7-1) was solved subject to boundary conditions

$$\widetilde{\Phi} = 0 \tag{7-2}$$

on the counterelectrode, Γ_{CE},

$$\mathbf{n}_{\Gamma_I} \cdot \nabla \widetilde{\Phi}\Big|_{\Gamma_I} = 0 \tag{7-3}$$

on insulating surfaces Γ_I, where $\mathbf{n}_{\Gamma_I}$ is the unit normal vector for insulating surfaces, and

$$-\left.\frac{\partial \widetilde{\Phi}}{\partial y}\right|_{y=0} = K\left(\widetilde{\Phi}_m - \widetilde{\Phi}_0\right) + J\left(\widetilde{\Phi}_m - \widetilde{\Phi}_0\right) \tag{7-4}$$

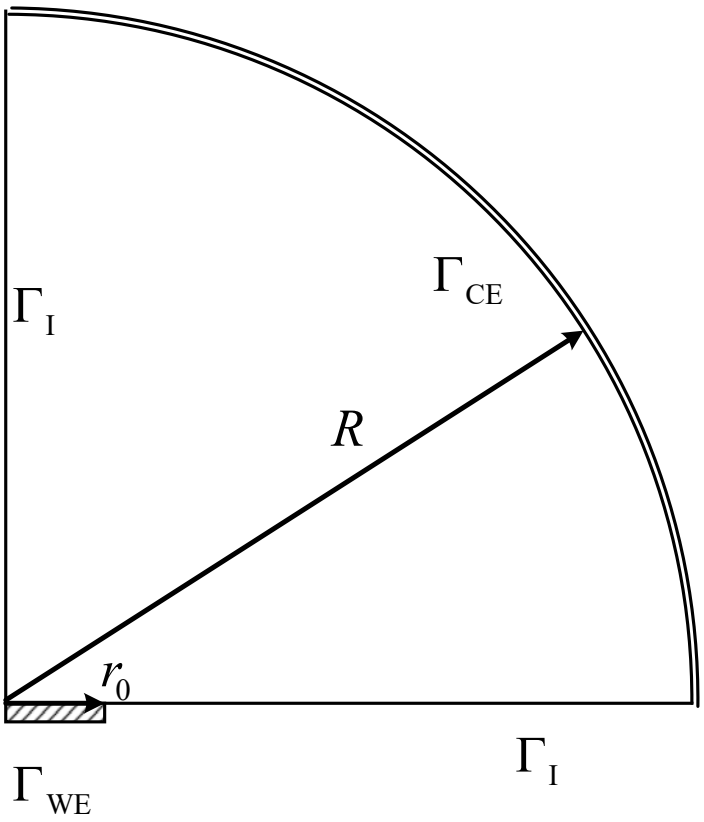

Figure 7-1. Schematic representation of the disk geometry with boundaries identified as Γ_{WE} for the disk electrode, Γ_{CE} for the counterelectrode, and Γ_I for insulating surfaces. Drawing is not to scale. For the simulations, $R/r_0 = 2000$, and $r_0 = 0.5$ cm. (Taken from You et al. [177])

at the disk electrode surface (Γ_{WE}), where $\widetilde{\Phi}_m$ is the potential phasor at the electrode surface, $\widetilde{\Phi}_0$ is the potential phasor just outside the diffuse part of the double layer, J is defined by equation (2-34), and

$$K = \frac{\omega C_0 r_0}{\kappa} \tag{7-5}$$

is the dimensionless frequency where r_0 is the radius of the disk electrode, C_0 is the capacity of the electrode-electrolyte interface, and κ is the electrolyte conductivity.

The numerical results were very sensitive to domain size and the meshing strategy. The methods discussed in Gharbi et al. [124] were used to adjust the simulation parameters to yield a high-frequency asymptote equal to the expression for the primary resistance,[108] i.e.,

$$R_{e,HF} = \frac{\pi r_0}{4\kappa} \tag{7-6}$$

The ohmic impedance was obtained as

$$Z_e = Z - Z_0 \tag{7-7}$$

where

$$Z = \left(\frac{2}{r_0^2} \int_0^{r_0} \frac{\widetilde{i}(r,0)}{\widetilde{\Phi}_m} r dr \right)^{-1} \tag{7-8}$$

and

$$Z_0 = \left(\frac{2}{r_0^2} \int_0^{r_0} \frac{\widetilde{i}(r,0)}{\widetilde{\Phi}_m - \widetilde{\Phi}_0} r dr \right)^{-1} \tag{7-9}$$

The results are presented in Figure 7-2 with $J = 4R_{e,HF}/\pi R_t$ as a parameter. The dimensionless frequency was defined in equation (7-5). At high frequencies ($K \to \infty$), the ohmic impedance approaches a real value $R_{e,HF}$, and at low frequencies ($K \to 0$), the ohmic impedance approaches a real value $R_{e,LF}$. The accuracy of the simulations is reflected in that the high-frequency asymptote is equal to the dimensionless primary resistance of $1/4$. As J increases, the difference between $R_{e,HF}$ and $R_{e,LF}$ is reduced.

The normalized difference between high- and low-frequency values of the ohmic resistance is presented in Figure 7-3 as a function of J. Symbols show the values taken from Newman[113]

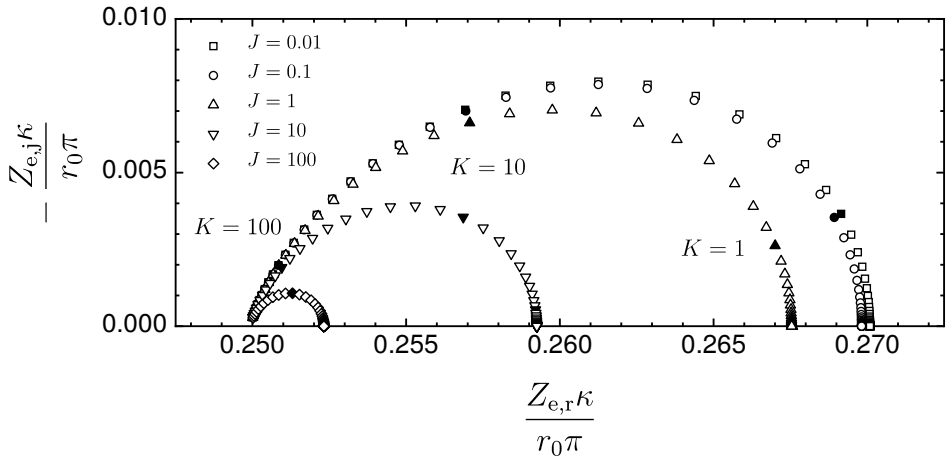

Figure 7-2. Calculated dimensionless ohmic impedance in Nyquist format with $J = 4R_{\mathrm{e,HF}}/\pi R_{\mathrm{t}}$ as a parameter. The dimensionless frequency K is defined in equation (7-5). The accuracy of the simulations is reflected in that the high-frequency asymptote is equal to the dimensionless primary resistance of $1/4$. (Taken from You et al. [177])

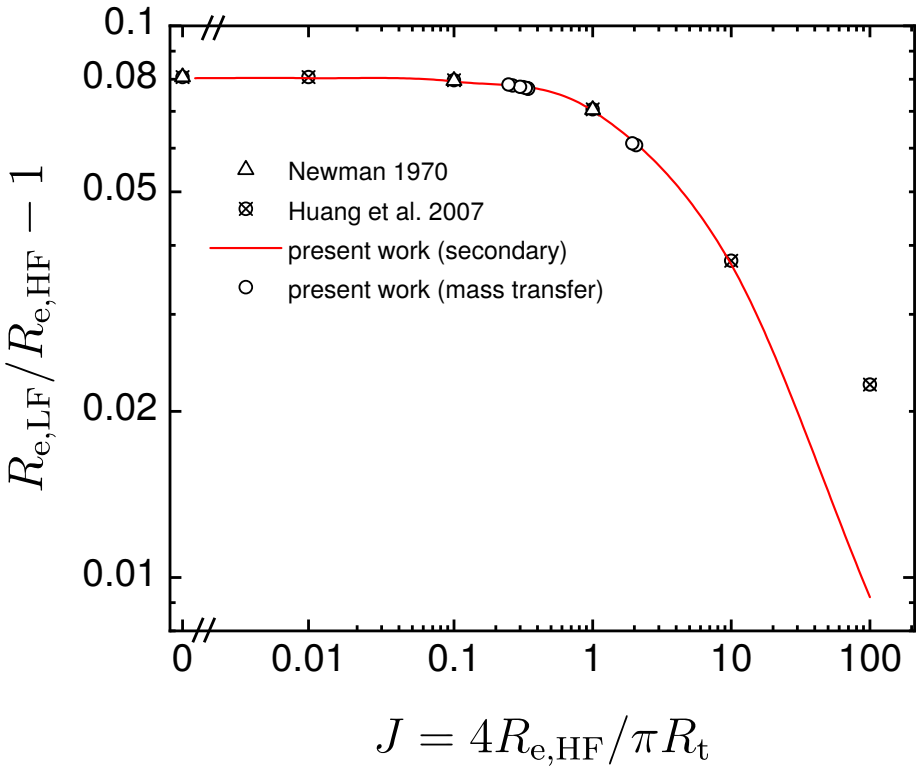

Figure 7-3. Normalized difference between high- and low-frequency values of the ohmic resistance as a function of $J = 4R_{\mathrm{e,HF}}/\pi R_{\mathrm{t}}$. Symbols show the values taken from Newman[113] and Huang et al. [114, 115]. (Taken from You et al. [177])

and Huang et al. [114, 115]. The maximum value of J reported by Newman was $J = 1$, and the maximum value of reported by Huang et al. was $J = 100$. The present results are in good agreement with the results obtained by Newman[113] and by Huang et al. [114, 115] for $J \leq 10$.

7.2.2 Disk Electrode with Mass Transfer

Finite-element simulations were performed to model the reversible oxidation of ferrocyanide to ferricyanide on a rotating disk electrode. The nonlinear set of coupled equations governing the steady-state were solved by the Newton–Raphson method, and synthetic impedance data were calculated by the direct linear solver. The domain comprised a volume bounded by an area defined by the working electrode Γ_{WE}, the insulator in which the electrode is embedded Γ_{I}, and the hemispherical counterelectrode Γ_{CE}.

The solution was obtained under the assumptions that homogeneous reactions were not present, and migration was neglected due to a strong supporting electrolyte. The governing equation for the mass transfer to a rotating disk electrode under steady-state conditions may be expressed as

$$v_{\mathrm{r}}\frac{\partial \bar{c}_{\mathrm{i}}}{\partial r} + v_{\mathrm{y}}\frac{\partial \bar{c}_{\mathrm{i}}}{\partial y} - D_{\mathrm{i}}\left(\frac{1}{r}\frac{\partial}{\partial r}\left(r\frac{\partial \bar{c}_{\mathrm{i}}}{\partial r}\right) + \frac{\partial^2 \bar{c}_{\mathrm{i}}}{\partial y^2}\right) = 0 \tag{7-10}$$

where D_{i} is the diffusion coefficient, $\bar{c}_{\mathrm{i}}$ is the steady-state concentration, and v_{r} and v_{y} are the radial and axial components of velocity.

The velocity profile was expressed as[178, 179]

$$v_{\mathrm{y}} = \sqrt{\nu\Omega}H(\zeta) \tag{7-11}$$

for the axial direction, and

$$v_{\mathrm{r}} = r\Omega F(\zeta) \tag{7-12}$$

for the radial direction where ν is the kinematic viscosity, Ω is the rotation speed of the electrode, $H(\zeta)$ is the dimensionless axial velocity, $F(\zeta)$ is the dimensionless radial velocity, and $\zeta = y\sqrt{\Omega/\nu}$ is the dimensionless axial distance from the disk. The velocity profile was written in

terms of a series expansion for distances near the electrode surface, i.e.,

$$H_0 = -\mathrm{a}\zeta^2 + \frac{1}{3}\zeta^3 + \frac{\mathrm{b}}{6}\zeta^4 + \ldots \tag{7-13}$$

and

$$F_0 = \mathrm{a}\zeta + \frac{1}{2}\zeta^2 - \frac{\mathrm{b}}{3}\zeta^3 + \ldots \tag{7-14}$$

where $\mathrm{a} = 0.510232618867$ and $\mathrm{b} = -0.615922014399$. For distances far away from the electrode, the dimensionless velocity can be expressed as

$$H_\infty = -\alpha + \frac{2\mathrm{A}}{\mathrm{C}}\exp(-\mathrm{C}\zeta) - \frac{\mathrm{A}^2 + \mathrm{B}^2}{2\mathrm{C}^3}\exp(-2\mathrm{C}\zeta) + \ldots \tag{7-15}$$

and

$$F_\infty = A\exp(-\mathrm{C}\zeta) - \frac{\mathrm{A}^2 + \mathrm{B}^2}{2\mathrm{C}^2}\exp(-2\mathrm{C}\zeta) + \frac{\mathrm{A}(\mathrm{A}^2 + \mathrm{B}^2)}{4\mathrm{C}^4}\exp(-3\mathrm{C}\zeta) + \ldots \tag{7-16}$$

where A=0.934, B=1.208, and $\mathrm{C} = 0.88447$.

The first three terms of the series expansion were applied in the present calculation. An interpolation formula introduced by Wu [180] was used to describe the velocity profile near the electrode and far away from the electrode, i.e.,

$$H = (1-f)H_0 + fH_\infty \tag{7-17}$$

and

$$F = (1-f)F_0 + fF_\infty \tag{7-18}$$

where f is the interpolation function given by

$$f = \frac{1}{1 + \mathrm{e}^{-\xi(\zeta - \zeta_0)}} \tag{7-19}$$

where $\zeta_0 = 1$ and $\xi = 25$.

In the region outside of a thin diffusion layer near the electrode, concentrations may be assumed uniform and potential is governed by Laplace's equation[181]

$$\frac{1}{r}\frac{\partial}{\partial r}\left(r\frac{\partial \overline{\Phi}}{\partial r}\right)+\frac{\partial^2 \overline{\Phi}}{\partial y^2}=0 \tag{7-20}$$

At the electrode surface, Γ_{WE}, the current given by Ohm's law was set equal to the faradaic current, i.e.,

$$\bar{i}_{\mathrm{F}}=-\kappa\left.\frac{\partial \overline{\Phi}}{\partial y}\right|_{y=0}=K_{\mathrm{a}}\bar{c}_4(0)\exp(b_{\mathrm{a}}(\overline{\Phi}_m-\overline{\Phi}_0))-K_{\mathrm{c}}\bar{c}_3(0)\exp(-b_{\mathrm{c}}(\overline{\Phi}_m-\overline{\Phi}_0)) \tag{7-21}$$

where K_{a} and K_{c} are the reaction rate constants, b_{a} and b_{c} are lumped parameters related to the apparent transfer coefficients, and $\bar{c}_4(0)$ and $\bar{c}_3(0)$ are the concentrations of ferrocyanide and ferricyanide, respectively, on the electrode surface. Equation (7-21) includes the contribution of both cathodic and anodic reactions. The fluxes of ionic species were related to the faradaic current by

$$D_{\mathrm{i}}\left.\frac{\partial \bar{c}_{\mathrm{i}}}{\partial y}\right|_{y=0}=\frac{s_{\mathrm{i}}}{n\mathrm{F}}\bar{i}_{\mathrm{F}} \tag{7-22}$$

where s_{i} is the stoichiometric coefficient, and $n=1$ is the number of electrons transferred in the electrochemical reaction. The stoichiometric coefficient is assigned a positive value for an anodic reactant, a negative value for an anodic product, and zero for a species that does not participate in the reaction.

The boundary conditions at the counterelectrode, Γ_{CE}, were

$$\overline{\Phi}=0 \tag{7-23}$$

and

$$\bar{c}_{\mathrm{i}}=c_{\mathrm{i}}(\infty) \tag{7-24}$$

At the insulating surfaces,

$$\mathbf{n}_{\Gamma_{\mathrm{I}}}\cdot\nabla\overline{\Phi}\big|_{\Gamma_{\mathrm{I}}}=0 \tag{7-25}$$

and

$$\mathbf{n}_{\Gamma_I} \cdot \nabla \overline{c}_i|_{\Gamma_I} = 0 \tag{7-26}$$

where $\mathbf{n}_{\Gamma_I}$ is the unit normal vector for the insulating surface Γ_I.

For calculation of the impedance, conservation equations were written in the phasor notation, i.e.,

$$j\omega\widetilde{c}_i = v_r\frac{\partial\widetilde{c}_i}{\partial r} + v_y\frac{\partial\widetilde{c}_i}{\partial y} - D_i\left(\frac{1}{r}\frac{\partial}{\partial r}\left(r\frac{\partial\widetilde{c}_i}{\partial r}\right) + \frac{\partial^2\widetilde{c}_i}{\partial y^2}\right) \tag{7-27}$$

and potential was governed by equation (7-1). Faradaic and charging current densities were assumed to be uncoupled, thus the boundary condition for potential at the electrode surface Γ_{WE} was

$$-\kappa\left.\frac{\partial\widetilde{\Phi}}{\partial y}\right|_{y=0} = j\omega C_{dl}(\widetilde{\Phi}_m - \widetilde{\Phi}_0) + \widetilde{i}_F \tag{7-28}$$

where

$$\begin{aligned}\widetilde{i}_F \;=\; & +K_a b_a \overline{c}_4(0)\exp(b_a(\overline{\Phi}_m - \overline{\Phi}_0))(\widetilde{\Phi}_m - \widetilde{\Phi}_0) + K_a\exp(b_a(\overline{\Phi}_m - \overline{\Phi}_0))\widetilde{c}_4(0) \\ & +K_c b_c \overline{c}_3(0)\exp(-b_c(\overline{\Phi}_m - \overline{\Phi}_0))(\widetilde{\Phi}_m - \widetilde{\Phi}_0) - K_c\exp(-b_c(\overline{\Phi}_m - \overline{\Phi}_0))\widetilde{c}_3(0)\end{aligned} \tag{7-29}$$

Equation (7-30) shows the coupling between steady-state and phasor variables.

The flux of individual ionic species on Γ_{WE} was given by

$$D_i\left.\frac{\partial\widetilde{c}_i}{\partial y}\right|_{y=0} = \frac{s_i}{nF}\widetilde{i}_F \tag{7-30}$$

The boundary conditions far away from the electrode, i.e., Γ_{CE}, were given by equation (7-2) for the potential phasor and

$$\widetilde{c}_i = 0 \tag{7-31}$$

for the concentration phasors. On insulating surfaces, equation (7-3) and

$$\mathbf{n}_{\Gamma_I} \cdot \nabla \widetilde{c}_i|_{\Gamma_I} = 0 \tag{7-32}$$

were employed.

The overall impedance was calculated as

$$Z = \left(\frac{2}{r_0^2} \int_0^{r_0} \frac{\widetilde{i}(r,0)}{\widetilde{\Phi}_m} r \mathrm{d}r \right)^{-1} \tag{7-33}$$

The results of the simulations provided synthetic data for subsequent regression analysis.

7.3 Regression Model Development

The model accounted for the faradaic impedance at any frequency, a look-up table implementation of the convective diffusion impedance for a rotating disk that accounted for a finite value of the Schmidt number, a local constant-phase-element behavior of the disk electrode, and the ohmic impedance that resulted from the frequency-dependent nonuniform current and potential distribution.

7.3.1 Faradaic Impedance

The reaction stoichiometry for reversible oxidation of ferrocyanide to ferricyanide can be expressed as

$$\mathrm{Fe(CN)}_6^{4-} \rightleftarrows \mathrm{Fe(CN)}_6^{3-} + \mathrm{e}^- \tag{7-34}$$

The associated faradaic current density is

$$i_\mathrm{F} = K_\mathrm{a} c_4(0) \exp(b_\mathrm{a} V) - K_\mathrm{c} c_3(0) \exp(-b_\mathrm{c} V) \tag{7-35}$$

where rate constants K_a and K_c and coefficients b_a and b_c represent lumped parameters. The terms $c_4(0)$ and $c_3(0)$ are respectively the concentrations of $\mathrm{Fe(CN)}_6^{4-}$ and $\mathrm{Fe(CN)}_6^{3-}$ evaluated at the electrode-electrolyte interface.

The current density may be expressed as

$$i_\mathrm{F} = \bar{i}_\mathrm{F} + \mathrm{Re}\left\{ \widetilde{i}_\mathrm{F} \exp(\mathrm{j}\omega t) \right\} \tag{7-36}$$

where $\bar{i}_\mathrm{F}$ is the steady-state current density and $\widetilde{i}_\mathrm{F}$ is the associated phasor. Similar expressions apply to potential and concentration variables. The current-density phasor may be obtained from

a Taylor series expansion as

$$\widetilde{i}_{\mathrm{F}} = \left(K_{\mathrm{a}} b_{\mathrm{a}} \overline{c}_4(0) \exp(b_{\mathrm{a}} \overline{V}) + K_{\mathrm{c}} b_{\mathrm{c}} \overline{c}_3(0) \exp(-b_{\mathrm{c}} \overline{V})\right) \widetilde{V} + K_{\mathrm{a}} \exp(b_{\mathrm{a}} \overline{V}) \widetilde{c}_4(0) - K_{\mathrm{c}} \exp(-b_{\mathrm{c}} \overline{V}) \widetilde{c}_3(0) \tag{7-37}$$

The current density may be related to the flux of species to and from the electrode by

$$i_{\mathrm{F}} = n\mathrm{F} D_4 \left.\frac{\partial c_4}{\partial t}\right|_{y=0} = -n\mathrm{F} D_3 \left.\frac{\partial c_3}{\partial t}\right|_{y=0} \tag{7-38}$$

where $n = 1$ is the number of electrons exchanged in reaction (7-34). Application of equation (7-36) yields

$$\widetilde{i}_{\mathrm{F}} = n\mathrm{F} D_4 \left.\frac{\mathrm{d}\widetilde{c}_4}{\mathrm{d}t}\right|_{y=0} = -n\mathrm{F} D_3 \left.\frac{\mathrm{d}\widetilde{c}_3}{\mathrm{d}t}\right|_{y=0} \tag{7-39}$$

Equation (7-37) may be expressed as

$$1 = \frac{1}{R_{\mathrm{t,eff}}} \frac{\widetilde{V}}{\widetilde{i}_{\mathrm{F}}} + K_{\mathrm{a}} \exp(b_{\mathrm{a}} \overline{V}) \frac{\widetilde{c}_4(0)}{\widetilde{i}_{\mathrm{F}}} - K_{\mathrm{c}} \exp(-b_{\mathrm{c}} \overline{V}) \frac{\widetilde{c}_3(0)}{\widetilde{i}_{\mathrm{F}}} \tag{7-40}$$

where

$$R_{\mathrm{t,eff}} = \frac{R_{\mathrm{t},4} R_{\mathrm{t},3}}{R_{\mathrm{t},4} + R_{\mathrm{t},3}} \tag{7-41}$$

$$R_{\mathrm{t},4} = \frac{1}{K_{\mathrm{a}} b_{\mathrm{a}} \overline{c}_4(0) \exp(b_{\mathrm{a}} \overline{V})} \tag{7-42}$$

and

$$R_{\mathrm{t},3} = \frac{1}{K_{\mathrm{c}} b_{\mathrm{c}} \overline{c}_3(0) \exp(-b_{\mathrm{c}} \overline{V})} \tag{7-43}$$

where the effective charge-transfer resistance $R_{\mathrm{t,eff}}$ accounts for contributions of anodic and cathodic reactions.

Introduction of equations (7-39) to equation (7-40) yields

$$Z_{\mathrm{F}} = R_{\mathrm{t,eff}} - \frac{K_{\mathrm{a}} \exp(b_{\mathrm{a}} \overline{V})}{n\mathrm{F} D_4} \frac{\widetilde{c}_4(0)}{\left.\frac{\mathrm{d}\widetilde{c}_4}{\mathrm{d}y}\right|_{y=0}} - \frac{K_{\mathrm{c}} \exp(-b_{\mathrm{c}} \overline{V})}{n\mathrm{F} D_3} \frac{\widetilde{c}_3(0)}{\left.\frac{\mathrm{d}\widetilde{c}_3}{\mathrm{d}y}\right|_{y=0}} \tag{7-44}$$

A general expression for the gradient of the concentration phasor is obtained under the definitions $\theta_4 = \widetilde{c}_4/\widetilde{c}_4(0)$, $\theta_3 = \widetilde{c}_3/\widetilde{c}_3(0)$, $\xi_4 = y/\delta_4$, and $\xi_3 = y/\delta_3$.

$$Z_F = R_{t,eff} + R_{t,eff}\frac{K_a \exp(b_a\overline{V})\delta_4}{nFD_4}\left(\frac{-1}{\theta_4'(0)}\right) + R_{t,eff}\frac{K_c \exp(-b_c\overline{V})\delta_3}{nFD_3}\left(\frac{-1}{\theta_3'(0)}\right) \tag{7-45}$$

Equation (7-45) may be written as

$$Z_F = R_{t,eff} + R_{d,eff}\left(\frac{-1}{\theta'(0)}\right) \tag{7-46}$$

where

$$R_{d,eff} = R_{t,eff}\left(\frac{K_a \exp(b_a\overline{V})\delta_4}{nFD_4} + \frac{K_c \exp(-b_c\overline{V})\delta_3}{nFD_3}\right) \tag{7-47}$$

and the dimensionless diffusion impedance was assumed to be the same for species 4 and 3, i.e.,

$$\left(\frac{-1}{\theta'(0)}\right) = \left(\frac{-1}{\theta_4'(0)}\right) = \left(\frac{-1}{\theta_3'(0)}\right) \tag{7-48}$$

Thus, the faradaic impedance was given as equation (7-46).

7.3.2 Diffusion Impedance

The convective-diffusion impedance for the rotating disk is obtained directly from

$$\frac{-1}{\theta_i'(0)} = Z_{(0)} + \frac{Z_{(1)}}{Sc_i^{1/3}} + \frac{Z_{(2)}}{Sc_i^{2/3}} + \ldots \tag{7-49}$$

where $-1/\theta_i'(0)$ is the dimensionless diffusion impedance, $Z_{(0)}$, $Z_{(1)}$, and $Z_{(2)}$ are the three complex solutions to the convective diffusion impedance corresponding to three terms in the series expansion for the axial velocity near the disk electrode, and the Schmidt number is expressed as $Sc = \nu/D_i$, where $\nu = \mu/\rho$ is the kinematic viscosity and D_i is the diffusion coefficient for the reacting species. A look-up table was implemented to enable evaluation of $Z_{(0)}$, $Z_{(1)}$, and $Z_{(2)}$ at a specified frequency. The mathematical foundation is given in Section 11.3.4 of Orazem and Tribollet[115] and is based on the work of Tribollet and Newman.[182]

7.3.3 Total Impedance

As suggested by Gharbi et al. [124], the ohmic impedance for the experimental data was modeled by the Havriliak-Negami equation,[183] expressed as equation (2-36). Thus, the

expression for the impedance was given as

$$Z = R_{\mathrm{e,HF}} + \frac{R_{\mathrm{e,LF}} - R_{\mathrm{e,HF}}}{(1 + (\mathrm{j}\omega\tau)^{\alpha})^{\beta}} + \frac{R_{\mathrm{t,eff}} + R_{\mathrm{d,eff}}\left(\frac{-1}{\theta'(0)}\right)}{1 + (\mathrm{j}\omega)^{\alpha} Q\left(R_{\mathrm{t,eff}} + R_{\mathrm{d,eff}}\left(\frac{-1}{\theta'(0)}\right)\right)} \tag{7-50}$$

where $-1/\theta'(0)$ was given by equation (7-49). The synthetic data generated in Section 7.2.2 did not incorporate a local CPE behavior. Thus, the Havriliak-Negami equation was replaced by the Cole–Davidson equation[184], i.e.,

$$Z = R_{\mathrm{e,HF}} + \frac{R_{\mathrm{e,LF}} - R_{\mathrm{e,HF}}}{(1 + (\mathrm{j}\omega\tau))^{\beta}} + \frac{R_{\mathrm{t,eff}} + R_{\mathrm{d,eff}}\left(\frac{-1}{\theta'(0)}\right)}{1 + \mathrm{j}\omega C\left(R_{\mathrm{t,eff}} + R_{\mathrm{d,eff}}\left(\frac{-1}{\theta'(0)}\right)\right)} \tag{7-51}$$

Figure 7-3 provided the basis for the comparison of regressed ohmic impedance parameters to theoretical values.

7.4 Regression Analysis on Simulations and Experimental Results

The regression was performed using an in-house program recently made available for non-commercial use.[185] A measurement-model analysis was performed to identify high-frequency artifacts, confirm consistency with the Kramers–Kronig relations at low frequency, and identify the error structure used to weight regression. Data within the frequency range of 99.8 kHz to 9.98 mHz were found to be free of artifacts.

The nonlinear complex regression was performed using a weighted Levenberg–Marquardt algorithm that implemented the python package *lmfit*, a wrapper/extension of the *leastsq* function of scipy. In turn, the scipy function *leastsq* is described as a wrapper around MINPACK's *lmdif* and *lmder* algorithms.[186] MINPACK is a set of solvers/minimizers written in Fortran at the Argonne National Laboratory.

7.4.1 Results from Simulations and Experiment

Regression of equation (7-51) was performed for synthetic data generated by the methods presented in Section 7.2.2. Regression of equation (7-50) was performed for the experimental data collected as described in Section 7.1.1.

7.4.1.1 Synthetic data

Synthetic data were generated for ferri/ferrocyanide redox species (10 mM each) in a supported electrolyte at a disk rotation speed of 800 rpm. Normally distributed noise, with $\sigma = 0.0001|Z|$ Ωcm^2, was added to the synthetic data, i.e.,

$$Z_\mathrm{r} = Z_\mathrm{r,model} + N_\mathrm{r}(\mu, \sigma^2) \tag{7-52}$$

and

$$Z_\mathrm{j} = Z_\mathrm{j,model} + N_\mathrm{j}(\mu, \sigma^2) \tag{7-53}$$

where the means of independent normal distributions N_r and N_j had value $\mu = 0$. The regressions were weighted by the inverse of the variance of the assumed stochastic error structure.[47] The added noise was smaller than values found experimentally, but larger than the errors expected for the numerical simulations.

Two sets of kinetic parameters were considered, shown in Figure 7-1, and the corresponding polarization curves are shown in Figure 7-4. Symbols mark the potentials at which impedance was calculated and subjected to regression analysis. The potential is referenced to an electrode of the same kind such that the open-circuit potential is equal to zero. The values of J were obtained from the regression analysis.

Regression results are presented in Table 7-2 for small values of J at open-circuit and anodic potentials, in Table 7-3 for small values of J at cathodic potentials, and in Table 7-4 for

Table 7-1. Parameters used in the simulation for the disk electrode with mass transfer. Results shown in Figure 7-4 and Tables 7-2–7-4.

Parameter	J = 0.25 - 0.34	J = 1.9 - 2.1
K_3 and K_4, A/cm mol	500	2250
b_3 and b_4, V^{-1}	19.5	19.5
C_0, μF/cm^2	20	20
ν, cm^2/s	0.01	0.01
D_3, cm^2/s	8.96×10^{-6}	8.96×10^{-6}
D_4, cm$^2/s$	7.39×10^{-6}	7.39×10^{-6}
ρ, Ωcm	3.52	7.04
Ω, rpm	800	800

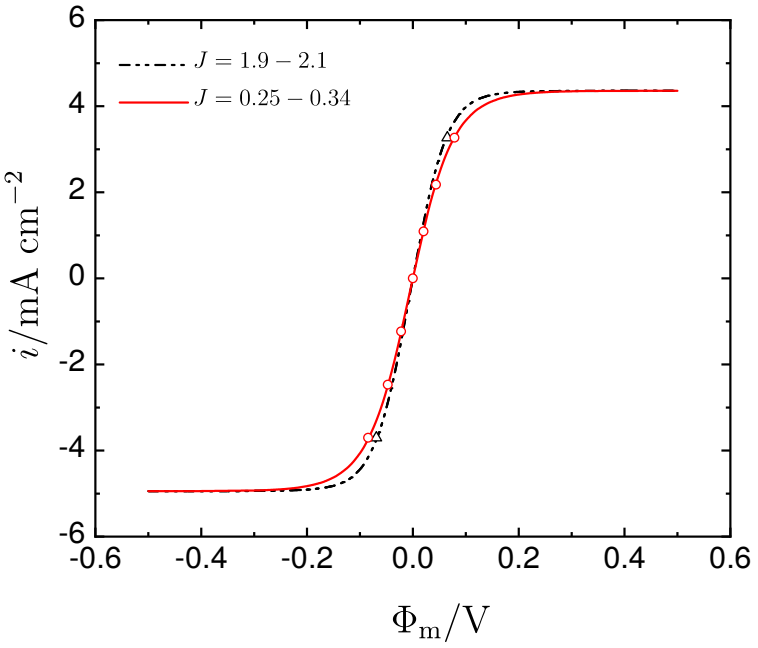

Figure 7-4. Calculated polarization curve generated for ferri/ferrocyanide redox species (10 mM each) in a supported electrolyte at a disk rotation speed of 800 rpm with J as a parameter. Symbols mark the potentials at which impedance was calculated and subjected to regression analysis. Potential is referenced to an electrode of the same kind such that the open-circuit potential is equal to zero. (Taken from You et al. [177])

Table 7-2. Parameter estimates from regression of equation (7-51) to synthetic impedance data with $J = 0.25$ to 0.34 for open-circuit and anodic potentials. The notation A 1/4 signifies anodic potential with $i = i_\mathrm{lim}/4$. The potential is referenced to an electrode of the same kind, such that the potential at open-circuit is equal to zero.

Parameter	OC (0 V)	A 1/4 (0.0202 V)	A 1/2 (0.0439 V)	A 3/4 (0.787 V)
Sc	1209.2 ± 1.7	1260.0 ± 1.6	1321.6 ± 1.3	1389.8 ± 0.93
$R_\mathrm{e,HF}$, $\Omega\mathrm{cm}^2$	1.38020 ± 0.00018	1.38010 ± 0.00017	1.38010 ± 0.00015	1.38000 ± 0.00013
C, $\mu\mathrm{F/cm}^2$	19.9920 ± 0.0060	19.9920 ± 0.0054	19.9920 ± 0.0044	19.9960 ± 0.0034
R_d, $\Omega\mathrm{cm}^2$	10.6910 ± 0.0013	12.1260 ± 0.0013	17.0390 ± 0.0015	35.261 ± 0.0024
R_t, $\Omega\mathrm{cm}^2$	5.13240 ± 0.00066	5.33340 ± 0.00063	5.86760 ± 0.00061	7.10670 ± 0.00070
$R_\mathrm{e,LF}$, $\Omega\mathrm{cm}^2$	1.4863 ± 0.00041	1.48660 ± 0.00039	1.48710 ± 0.00033	1.48800 ± 0.00028
τ, ms	7.17 ± 0.10	7.201 ± 0.098	7.256 ± 0.086	7.402 ± 0.075
β	0.6385 ± 0.0051	0.6384 ± 0.0047	0.6380 ± 0.0041	0.6350 ± 0.0036
χ^2/ν	13.0	11.1	7.9	7.0
Calculated Results				
$R_\mathrm{e,LF}/R_\mathrm{e,HF} - 1$	0.0769	0.0771	0.0775	0.0783
J	0.342	0.329	0.299	0.247

Table 7-3. Parameter estimates from regression of equation (7-51) to synthetic impedance data with $J = 0.26$ to 0.34 for cathodic potentials. The notation C 1/4 signifies cathodic potential with $i = i_{\text{lim}}/4$. The potential is referenced to an electrode of the same kind, such that the potential at open-circuit is equal to zero.

Parameter	C 1/4 (-0.0221 V)	C 1/2 (-0.0473 V)	C 3/4 (-0.0844 V)
Sc	1175.0 ± 1.6	1155.3 ± 1.3	1169.5 ± 0.86
$R_{e,HF}$, Ωcm^2	1.38010 ± 0.00018	1.38010 ± 0.00017	1.38000 ± 0.00013
C, $\mu F/cm^2$	19.9910 ± 0.0059	19.9920 ± 0.0050	19.9930 ± 0.0035
R_d, Ωcm^2	11.1270 ± 0.0014	15.4540 ± 0.0015	32.0740 ± 0.0021
R_t, Ωcm^2	5.16156 ± 0.00066	5.5840 ± 0.00064	6.6431 ± 0.00065
$R_{e,LF}$, Ωcm^2	1.48640 ± 0.00042	1.48690 ± 0.00037	1.48760 ± 0.00028
τ, ms	7.17 ± 0.11	7.269 ± 0.095	7.358 ± 0.075
β	0.6387 ± 0.0050	0.6358 ± 0.0045	0.6353 ± 0.0036
χ^2/ν	12.7	10.5	7.0
Calculated Results			
$R_{e,LF}/R_{e,HF} - 1$	0.0770	0.0774	0.0780
J	0.340	0.315	0.264

larger values of J. The corresponding values of $R_{e,LF}/R_{e,HF} - 1$ and J are presented as open circles in Figure 7-3. The results show that reactions influenced by mass transfer yield the same result as was found for the secondary current distributions for which reactions are independent of mass transfer.

7.4.1.2 Experimental data

The polarization curve is presented in Figure 7-5 for a gold electrode rotating at 800 rpm in an electrolyte containing a ferri/ferrocyanide redox species (10 mM each) in a 0.5 M KCl electrolyte. The potential at which impedance measurements were collected is represented by a dashed line. The impedance measurements were collected after the polarization curves were obtained for different rotation speeds, after an elapsed time of about 4 hours. The impedance analysis was performed in two parts: The measurement model was used to identify the error structure of the data, and equation (7-50) was then regressed to the portion of the measurement found to be consistent with the Kramers–Kronig relations using the stochastic error structure to weight the regressions.

Table 7-4. Parameter estimates from regression of equation (7-51) to synthetic impedance data with $J = 1.9 - 2.1$. The notation A 3/4 signifies anodic potential with $i = 3i_{\text{lim}}/4$. The potential is referenced to an electrode of the same kind, such that the potential at open-circuit is equal to zero. Regression could be achieved only for C held fixed at the input value.

Parameter	C 3/4 (-0.116 V)	A 3/4 (0.109 V)
Sc	1245.1 ± 2.3	1444.3 ± 2.1
$R_{\text{e,HF}}$, Ωcm^2	2.7618 ± 0.00069	2.7618 ± 0.00062
C, $\mu\text{F/cm}^2$	20	20
R_{d}, Ωcm^2	25.9340 ± 0.0047	29.367 ± 0.0046
R_{t}, Ωcm^2	1.7074 ± 0.0016	1.8169 ± 0.0015
$R_{\text{e,LF}}$, Ωcm^2	2.9296 ± 0.0012	2.9309 ± 0.0010
τ, ms	9.03 ± 0.30	9.09 ± 0.27
β	0.681 ± 0.014	0.682 ± 0.012
χ^2/ν	59.0	46.8
Calculated Results		
$R_{\text{e,LF}}/R_{\text{e,HF}} - 1$	0.061	0.061
J	2.06	1.93

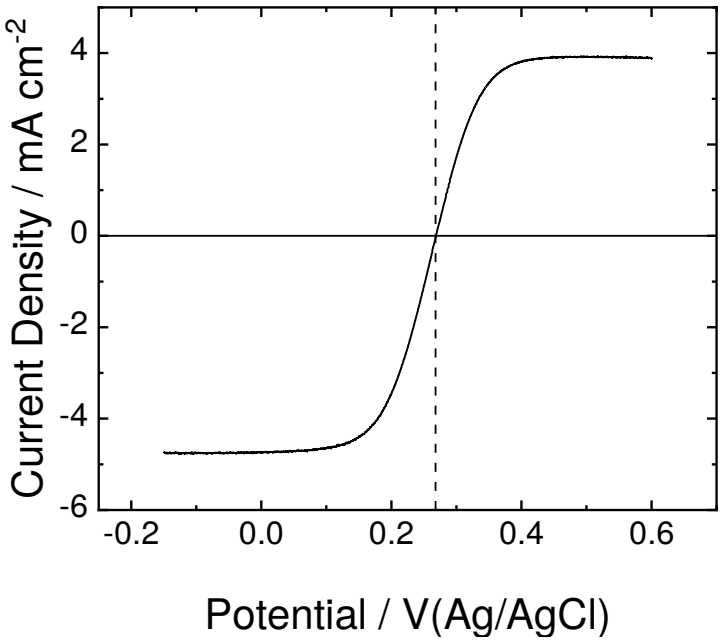

Figure 7-5. Polarization curve for a rotation speed of 800 rpm. The dashed line is the potential at which impedance measurements were collected. (Taken from You et al. [177])

7.4.2 Measurement Model Analysis

The approach developed by Agarwal et al. [187, 188, 189] was used to show that data within the 99.8 kHz to 9.98 mHz frequency range were consistent with the Kramers–Kronig relations. The measurement model was used to filter minor lack of replication between the five repeated measurements, and the resulting estimates of the standard deviations of the stochastic part of the measurement are presented in Figure 7-6(a) as a function of frequency. The results showed that, while scattered, the standard deviations for the real and imaginary parts of the impedance were equal, in agreement with expectations for Kramers–Kronig -consistent data.

A model was fit to the results shown in Figure 7-6(a) and found to be

$$\sigma_r = \sigma_j = \sigma = 0.01193 \pm 0.00053 \tag{7-54}$$

Equation (7-54) is presented as a dashed line in Figure 7-6(a). The standard deviations of impedance measurements made under potentiostatic modulation are generally assumed to be roughly proportional to the modulus of the impedance measurement, but equation (7-54) and Figure 7-6(a) suggest that, instead, the standard deviations of the present impedance measurements are independent of impedance. The standard deviations normalized by the modulus, presented in Figure 7-6(b), demonstrate the nonsuitability of using modulus weighting to regress the present data. Equation (7-54) is represented by a dashed line in Figure 7-6(b).

The error structure depends greatly on the algorithms employed by the manufacturers of the impedance instrumentation. The results shown in Figure 7-6 illustrate the importance of using a tool such as the measurement model program to assess the experimental error structure.

7.4.3 Process Model Analysis

Equation (7-50) was regressed to the impedance spectra collected at the open-circuit potential for a gold disk rotation at 800 rpm. The error structure given as equation (7-54) was used to weight the Levenberg–Marquardt regression. The data and the resulting fit are presented in Figure 7-7.

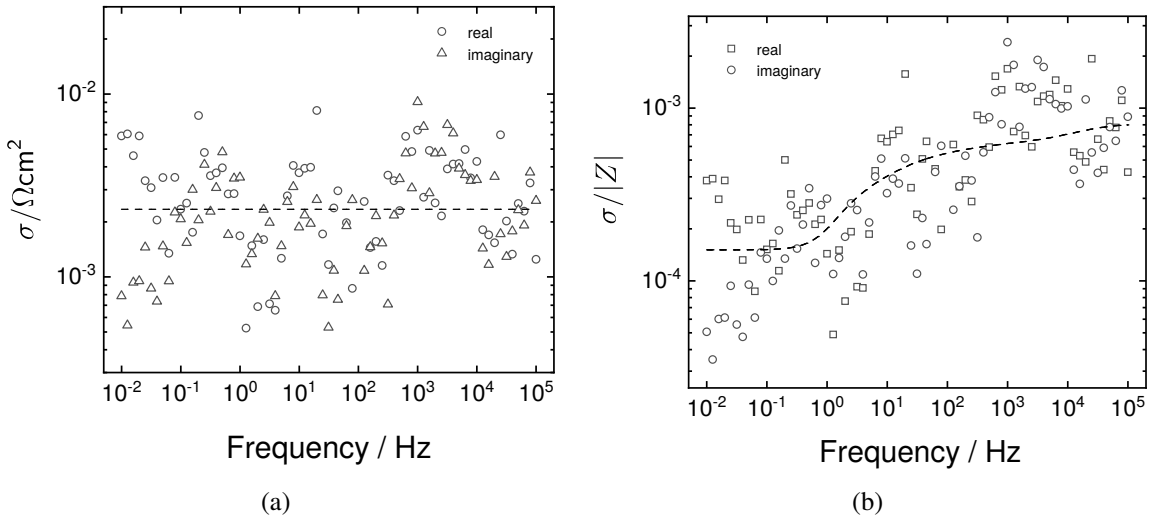

Figure 7-6. Stochastic error structure for the impedance measurements: a) standard deviations for real and imaginary parts of the impedance and b) standard deviations for real and imaginary parts of the impedance normalized by the magnitude of the impedance. The dashed line is the model for the error structure given by equation (7-54). (Taken from You et al. [177])

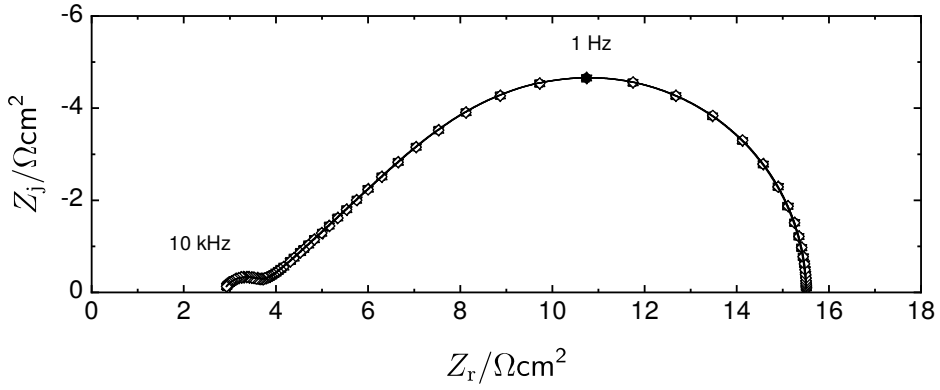

Figure 7-7. Replicated impedance data in Nyquist format. The line represents the fit of equation (7-50) to the impedance spectra. (Taken from You et al. [177])

The model comprised nine parameters, of which three can be attributed to incorporation of the Havriliak-Negami equation. Regression with all nine parameters resulted in some parameters with confidence intervals that included zero. To achieve a regression with statistically significant parameter estimations, β was fixed to 0.7, a value close to that obtained by regression of the Havriliak–Negami equation to synthetic impedance data.[124] The results are presented in Table 7-5. The ξ^2/ν statistic has values on the order of 5. Nominally, a good fit should have a value

$$\frac{\chi^2}{\nu} = 1 + \sqrt{\frac{2}{\nu}} \tag{7-55}$$

where ν is the degree of freedom for the regression. In the present case, $\nu = 132$, and the values reported in Table 7-5 can be compared to $1 + \sqrt{2/\nu} = 1.12$.

7.5 Insight from Synthetic and Experimental Data

Both synthetic and experimental data provide insight into the role of the complex ohmic impedance for electrochemical studies.

7.5.1 Synthetic Data

The ohmic impedance associated with primary and secondary current distributions was obtained by subtraction of the calculated interfacial impedance from the calculated impedance, following equations (7-7)–(7-9). The results, given in Figure 7-2, show that the high-frequency asymptote approaches the expected value of $1/4$[108] for all values of J. The relationship for scaled difference between high- and low-frequency ohmic impedance as a function of J, calculated in the present work, extends the analysis of Newman[113] by two orders of magnitude and extends the analysis of Huang et al. [114, 115] by one order of magnitude. The error in the value of $R_{e,LF}/R_{e,HF} - 1$ for $J = 100$ by Huang et al. [114, 115] can be attributed to use of a mesh size that is too large.

The synthetic data for the ferri/ferrocyanide system were subjected to the same regression analysis as used for experimental data. The Schmidt number for ferricyanide is on the order of 1120, and the Schmidt number for ferrocyanide is on the order of 1350. The Schmidt number reported in Tables 7-2 and 7-4 is 1390–1444 at $i/i_{lim} = 3/4$ under anodic potentials, for which

Table 7-5. Parameter estimates from regression of equation (7-50) to the impedance data shown in Figure 7-7.

Parameter	1	2	3	4	5
Sc	1198.2±4.0	1204.2±2.9	1206.4±2.9	1209.4±3.2	1211.0±2.8
$R_{e,HF}$, Ωcm^2	2.8496±0.0044	2.8537±0.0034	2.8590±0.0036	2.8573±0.0041	2.8577±0.0038
Q, $\mu F/cm^2 s^{1-\alpha}$	228±15	201.4±9.9	180.9±9.5	172±10	155.7±8.8
R_d, Ωcm^2	11.3688±0.0047	11.3680±0.0038	11.3718±0.0040	11.3735±0.0043	11.3834±0.0037
R_t, Ωcm^2	0.8266±0.0076	0.8412±0.0058	0.8425±0.0060	0.8415±0.0069	0.8311±0.0064
α	0.7690±0.0064	0.7775±0.0049	0.7858±0.0052	0.7887±0.0059	0.7961±0.0055
ΔR_e, Ωcm^2	0.1202±0.0046	0.1137±0.0036	0.1109±0.0038	0.1119±0.0041	0.1093±0.0036
β	0.7	0.7	0.7	0.7	0.7
τ, ms	6.29±0.87	7.14±0.80	7.44±0.89	6.56±0.85	5.71±0.67
χ^2/ν	6.6	4.0	4.5	5.6	4.8
Calculated Results					
$R_{e,LF}/R_{e,HF} - 1$	0.0422± 0.0016	0.0399±0.0013	0.0389±0.0014	0.0392±0.0015	0.0383±0.0013
J	4.391±0.041	4.321±0.030	4.32±0.032	4.325±0.036	4.379±0.034
C_{eff}, $\mu F/cm^2$	29.4	29.1	29.1	28.5	28.0

oxidation of ferrocyanide is expected to dominate. The Schmidt number reported in Tables 7-3 and 7-4 is 1170–1245 at $i/i_{\text{lim}} = 3/4$ under cathodic potentials, for which reduction of ferricyanide is expected to dominate. The Schmidt number reported in Table 7-2 at open circuit is 1209. Regressed values for R_{t} and R_{d} increase as the magnitude of the potential increases in both anodic and cathodic directions, in agreement with equations (7-41) and (7-47) and with experimental observation.[142] The most important observation for the present work is that the values of $R_{\text{e,LF}}/R_{\text{e,HF}} - 1$ fall on the same curve (Figure 7-3) as was calculated for the secondary current distribution.

7.5.2 Experimental Data

The values reported in Table 7-5 are on the order of 1200, a value that is, as expected, between the values for ferricyanide and ferrocyanide. The capacitance was estimated using the formula derived by Brug et al. [190], i.e.,

$$C_{\text{eff}} = Q^{1/\alpha} \left(\frac{R_{\text{e,HF}} R_{\text{t}}}{R_{\text{e,HF}} + R_{\text{t}}} \right)^{(1-\alpha)/\alpha} \tag{7-56}$$

The values between 28 and 29 μF/cm^2 are typical of those expected for a double-layer capacitance.

The value of $J = 4R_{\text{e,HF}}/\pi R_{\text{t}}$ was found to be about 4.3, and the confidence interval reported was obtained from Monte Carlo calculations. The value of $\Delta R_{\text{e}}/R_{\text{e,HF}}$ or $R_{\text{e,LF}}/R_{\text{e,HF}} - 1$ was found to be smaller than that expected for $J = 4.3$ in Figure 7-3. As suggested by Orazem et al. [191] and by Wang et al. [192], the value of the Schmidt number obtained by regression is influenced by elapsed time, suggesting formation of a film on the electrode surface.

The simulations presented in Section 7.2 were repeated with a film on the electrode surface of thickness $\delta = 1$ μm and with uniform resistivity. The results of the simulation and the results form the regression analysis are presented in Figure 7-8. The film thickness of 1 μm was chosen because it could be resolved by finite-element calculations. While the film thickness for the present system is expected to be much smaller than 1 μm, other calculations for different film

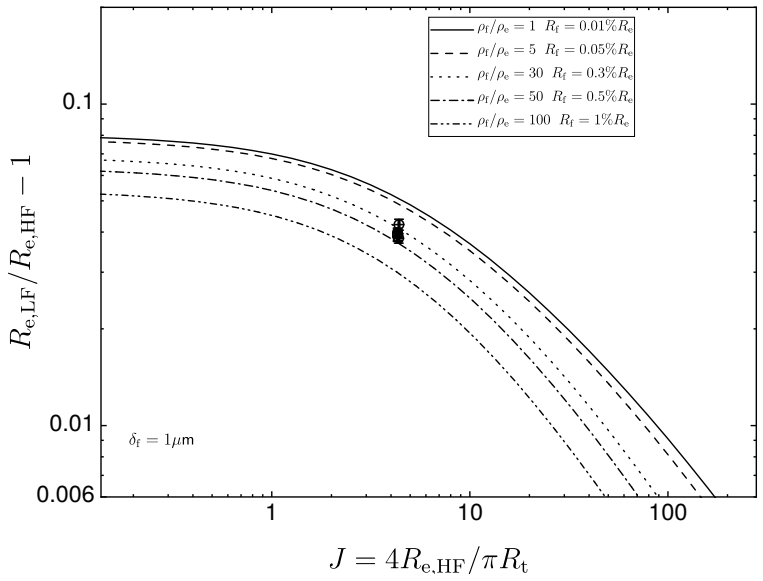

Figure 7-8. Normalized difference between high- and -low frequency values of the ohmic resistance for a disk electrode covered by a film of uniform resistivity and a thickness of 1 μm as a function of $J = 4R_{e,HF}/\pi R_t$. Symbols show the values obtained from the regression of the spectra shown in Figure 7-7. (Taken from You et al. [177])

thicknesses for which $\delta\rho_f$ was fixed yielded almost identical results. The relevant quantity is $R_f/R_{e,HF}$, also shown in Figure 7-8.

As shown in Table 7-5, the Schmidt number increased with elapsed time. This behavior is similar to that reported by Orazem et al. [191] and by Wang et al. [192] and was attributed to formation of a film. The value of $R_{e,LF}/R_{e,HF} - 1$ decreased with elapsed time, and, as shown in Figure 7-8, an increase in film resistance causes a reduction of $R_{e,LF}/R_{e,HF} - 1$.

Experiments were performed immediately after the electrode was polished, but, for these measurements, regression analysis did not yield statistically significant values for Havriliak-Negami parameters. The ohmic impedance cannot be resolved for all impedance measurements. For cases where the ohmic impedance parameters cannot be obtained by regression, the best alternative is to truncate the data at frequencies above the characteristic frequency given by equation (2-35). This will eliminate the effect of the ohmic impedance, as discussed by Huang et al. [123] and by Wang et al. [192]. For the present work, the values reported in Table 7-5 yield a characteristic frequency for ohmic impedance on the order of

1.9 kHz. The corresponding value for the faradaic reaction is 6.6 kHz, suggesting that the ohmic impedance plays a discernable role throughout the faradaic loop shown in Figure 7-7. The overlap of ohmic and faradaic impedance loops is consistent with the observed value of J, given by equation (2-34), that is larger than unity.

The significance of the present work is that it shows, for the first time, that the ohmic impedance predicted by Huang et al. [122, 114, 123] could be resolved experimentally. A similar conclusion was presented by Gharbi et al. [124], but that work employed a simplex regression routine which is subject to over fitting. Subsequent efforts to employ Levenberg–Marquardt algorithms to regress the data reported in Gharbi et al. [124] were unsuccessful, suggesting that the ohmic impedance parameters obtained were not statistically significant. In the present work, the ohmic impedance parameters both have statistical significance and are in full agreement with simulations that account for the influence of a film on the electrode surface.

CHAPTER 8
OHMIC IMPEDANCE DATA INTERPRETED BY MEASUREMENT MODEL

The objective of the present work in this Chapter was to use the measurement model to interpret the impedance data complicated by the ohmic impedance without using the process model. The measurement model analysis was used to extract capacitance and ohmic resistance for different electrochemical systems having the ohmic impedance with the influence of the mass transfer. Process models accounting for the ohmic impedance were also discussed as alternatives to interpret impedance data and confirm the results from measurement model analysis. The measurement model could provide a insight to estimate characteristic frequency above which the electrode geometry distorted the impedance spectra.

8.1 Simulation and Experimental Method

The present work represents a combination of experimental and numerical approaches.

8.1.1 Simulation

Finite-element simulation was used to study the current and potential distribution associated with the mass transfer on the rotating disk electrode. This work was performed using COMSOL Multiplysics® 5.2. Governing equations for the steady state were solved by the full-coupled approach utilizing Newton–Raphson method, and the governing equations for the impedance calculations were solved by the direct linear solver. The COMSOL Multiplysics® software was running on a Dell precision workstation T7400 with two E5410 2.33GHz Intel® Xeon® processors and 32 GB of RAM.

The development of mathematical model was very similar as described in section 7.2.2. The current model solved for the same form of governing equations with the same boundary conditions. In this system, only one cathodic reaction was considered on the electrode surface and system accounts for both the pure capacitance and CPE behavior. At the steady state, the contribution of the charging current density was equal to zero and boundary conditions at the electrode surface was expressed as

$$i = \bar{i}_{\mathrm{F}} = -K_{\mathrm{c}}\bar{c}_{\mathrm{i}}(0)\exp(-b_{\mathrm{c}}\overline{V}) \tag{8-1}$$

and

$$\overline{\mathbf{N}}_i = -\frac{s_\mathrm{i}}{n\mathrm{F}}\bar{i}_\mathrm{F} \tag{8-2}$$

where K_c is the reaction rate constant, b_c is the cathodic coefficient, s_i is the stoichiometric coefficient, and n is the number of electrons transferred in the electrochemical reaction. Equation (8-1) assumed that the cathodic reaction dominated and the anodic reaction could be neglected. The boundary conditions far away from the electrode were given by

$$\overline{\Phi} = 0 \tag{8-3}$$

and

$$\bar{c}_\mathrm{i} = c_\mathrm{i}(\infty) \tag{8-4}$$

In the frequency domain, boundary conditions for the current density at the electrode surface were given by

$$\widetilde{i} = K_\mathrm{c} b_\mathrm{c} \bar{c}_\mathrm{i}(0)\exp(-b_\mathrm{c}(\overline{\Phi}_m - \overline{\Phi}_0))(\widetilde{\Phi}_m - \widetilde{\Phi}_0) - K_\mathrm{c}\exp(-b_\mathrm{c}(\overline{\Phi}_m - \overline{\Phi}_0))\widetilde{c}_\mathrm{i}(0) + \mathrm{j}\omega C_\mathrm{dl}(\widetilde{\Phi}_m - \widetilde{\Phi}_0) \tag{8-5}$$

for a system with a capacitance, or

$$\widetilde{i} = K_\mathrm{c} b_\mathrm{c} \bar{c}_\mathrm{i}(0)\exp(-b_\mathrm{c}(\overline{\Phi}_m - \overline{\Phi}_0))(\widetilde{\Phi}_m - \widetilde{\Phi}_0) - K_\mathrm{c}\exp(-b_\mathrm{c}(\overline{\Phi}_m - \overline{\Phi}_0))\widetilde{c}_\mathrm{i}(0) + (\mathrm{j}\omega)^\alpha Q(\widetilde{\Phi}_m - \widetilde{\Phi}_0) \tag{8-6}$$

for a system with a CPE behavior. The boundary condition for the net flux at the electrode surface were given by

$$\widetilde{\mathbf{N}}_i = -\frac{s_\mathrm{i}}{n\mathrm{F}}\widetilde{i}_\mathrm{F} \tag{8-7}$$

Thus, the overall impedance was calculated by The overall impedance was calculated as

$$Z = \left(\frac{2}{r_0^2}\int_0^{r_0} \frac{\widetilde{i}(r,0)}{\widetilde{\Phi}_m} r\mathrm{d}r\right)^{-1} \tag{8-8}$$

For a disk electrode, frequency dispersion could be found due to the non-uniform potential and current distribution.[49] The characteristic frequency caused by the disk geometry could be

expressed as

$$f_c = \frac{1}{2\pi r_0 \rho C_{dl}} \tag{8-9}$$

or

$$f_c = \frac{1}{2\pi}\left(\frac{1}{Q r_0 \rho}\right)^{1/\alpha} \tag{8-10}$$

where r_0 is the radius of the disk and ρ is the resistivity of the electrolyte. Equations (8-9) could be used for the system with a capacitance and (8-10) could be used for the system having a CPE behavior associated with the surface distribution. The characteristic frequency associated with the faradic reaction could be expressed as

$$f_{R_t} = \frac{1}{2\pi R_t C_{eff}} \tag{8-11}$$

where R_t is the charge-transfer resistance. The effective capacitance C_{eff} was equal to C_{dl} for the system with a capacitance. For the system with a CPE behavior associated with a surface distribution, the effective capacitance developed by Brug et al. [190] could be expressed as

$$C_{eff} = Q^{1/\alpha}\left(\frac{R_e R_t}{R_e + R_t}\right)^{(1-\alpha)/\alpha} \tag{8-12}$$

8.1.2 Experimental Method

The impedance data was measured on a 5 mm diameter platinum disk electrode with a rotation speed of 120 rpm. The disk was immersed in 1M KCl solution with 0.01M $K_3Fe(CN)_6$ and 0.01M $K_4Fe(CN)_6$ as supporting electrolyte. The impedance data was collected by Solatron 1286 potentiostat and 1250 frequency-response analyzer (FRA). Matched two-channel Kemo VBF8 48 low-pass Butterworth analog filter was used in the experiment and Long (1% closure error) auto-integration option of the FRA was used on the current channel. The potentiostatic modulation was 10 mV peak-to-peak and the measurements were performed at 1/4 of the mass-transfer-limited current density condition. The frequency range was between 0.02 Hz to 4.61 kHz and the elapsed time for the measurement was over 10 hours.

8.2 Regression of Measurement Model to Experimental and Simulation Results

The measurement model was regressed to the impedance calculations from the numerical simulation, and to the impedance data from the experimental measurements for a rotating disk electrode. Process models accounting for the ohmic impedance were also regressed to the impedance data as alternatives to extract the value of the capacitance and ohmic resistance. Complex non-linear Levenberg-Marquardt regression was used in the regression. The weighting method was the modulus weighting assuming 0.2% normally distributed errors for the synthetic data, and the stochastic error structure weighting for the experimental data. In the present work, the regression was performed in a Python-based program [185] and available for noncommercial use under the terms of the GNU General Public License, version 3.

8.2.1 Numerical Simulation with a Capacitance

Two different ratios of f_c/f_{R_t} were chosen under half-limiting current density condition in the present work. For case I, f_c/f_{R_t} is equal to 492, in which two characteristic frequencies were far away from each other. The synthetic data for this case with $\Omega = 120$ rpm, $r_0 = 0.1$ cm, $\nu = 0.01$ cm^2/s, $\rho = 10$ Ωm, $K_c = 11$ A/cm^2, $b_c = 19.9$ V^{-1}, $D_i = 2 \times 10^{-5}$ cm^2/s, $c_i(\infty) = 2$ mol/cm^3, and $C_{dl} = 20$ μF/cm^2 is presented in Figure 8-1(a). It reveals two loops., in which the high-frequency loop was associated with the faradic reaction, and the low-frequency loop was caused by the mass transfer. The geometry-induced frequency dispersion at high-frequency zoom-in region is shown in Figure 8-1(b) and the characteristic frequency calculated by (8-9) was $f_c = 7.9$ kHz.

The value of capacitance obtained by regression of equation (2-23) to the full impedance spectrum was $C_{dl} = 12.31 \pm 0.81$ μF/cm^2, which was smaller than the input value of $C_{dl} = 20$ μF/cm^2. The value of high-frequency ohmic resistance was $R_{e,H} = 0.7881 \pm 0.0007$ Ω/cm^2 in good agreement with the value of 0.7854 Ω/cm^2 calculated from the Ohmic resistance for a disk electrode, which was defined as

$$R_{e,H} = \frac{\pi r_0 \rho}{4} \tag{8-13}$$

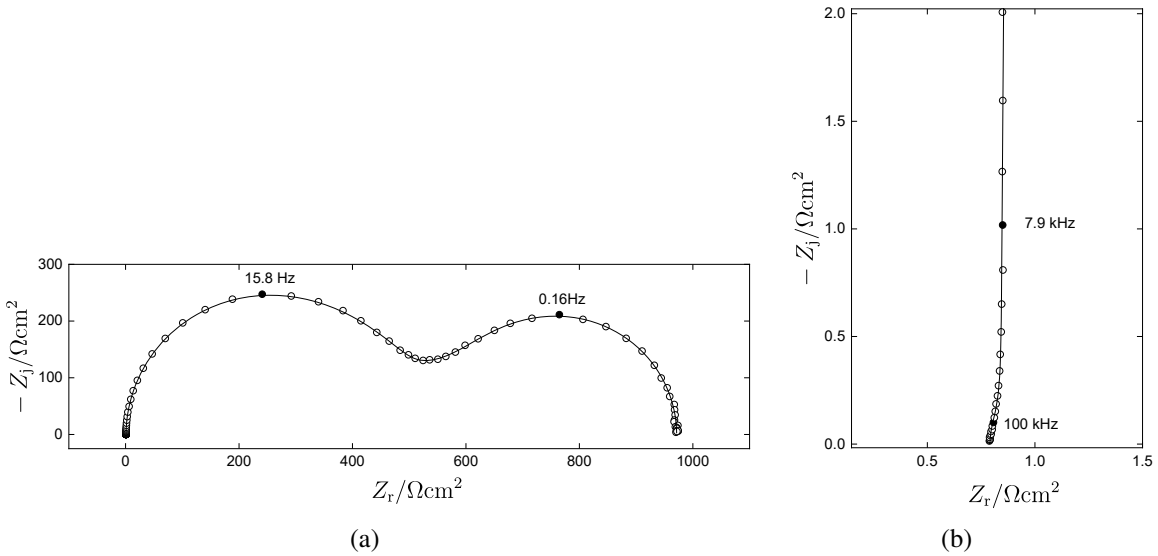

Figure 8-1. Impedance calculations in Nyquist format for the system having a capacitance on a rotating disk electrode with $\Omega = 120$ rpm, $r_0 = 0.1$ cm, $\nu = 0.01$ cm^2/s, $\rho = 10$ Ωm, $K_{\rm c} = 11$ A/cm^2, $b_{\rm c} = 19.9$ V^{-1}, $D_{\rm i} = 2 \times 10^{-5}$ cm^2/s, $c_{\rm i}(\infty) = 2$ mol/cm^3, and $C_{\rm dl} = 20$ μF/cm^2. The ratio of the dispersion frequency and the characteristic frequency associated with the charge transfer is 492. The frequency range was 1 mHz to 1 MHz, and $\chi^2/\upsilon = 0.93$. A normally distributed error of 0.2% was added to the synthetic data. The line represents the complex fit of the measurement model to the data using modulus weighting: a) full impedance spectrum and b) high-frequency zoom-in region of the impedance spectrum.

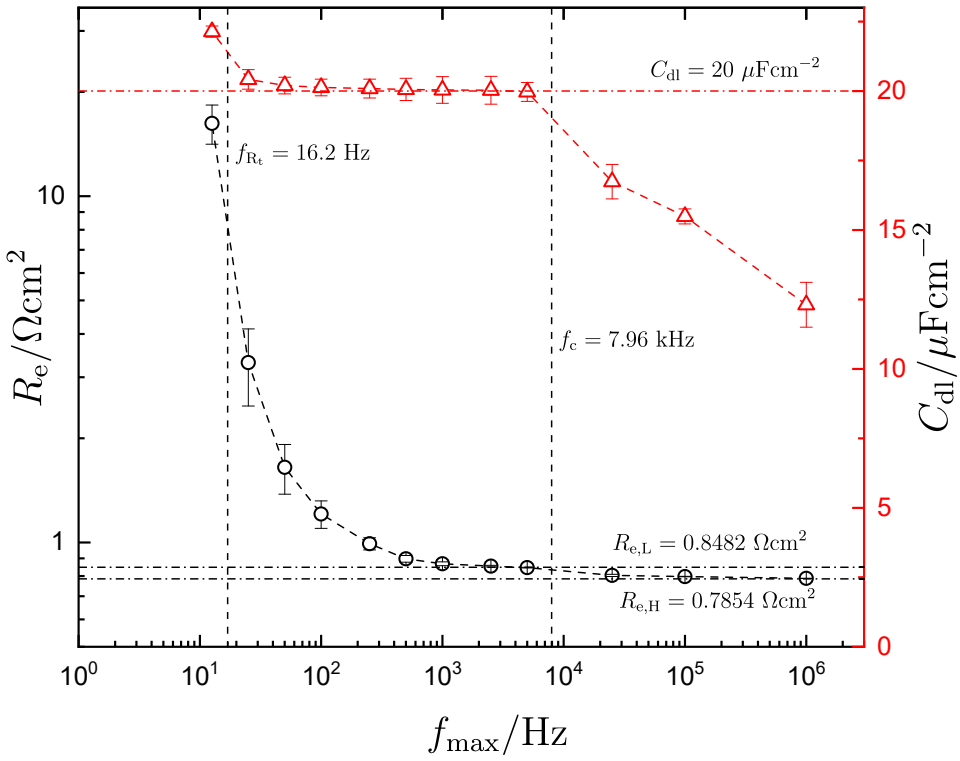

Figure 8-2. Capacitance and ohmic resistance obtained by regression of the measurement model to the complex impedance shown in Figure 8-1(a) for truncated frequency ranges as functions of the maximum regressed frequencies.

8 Viogt elements were added to the regression. Values of capacitance and ohmic resistance as functions of maximum regressed frequencies obtained by regression of the measurement model to truncated impedance data are shown in Figure 8-2. The value of the extracted capacitance was close to the correct value when the maximum regressed frequencies were between f_c and f_{R_t}. The value of the ohmic resistance was close to the low-frequency Ohmic resistance $R_{e,L} = 0.8482$. The ratio of $R_{e,L}/R_{e,H} = 1.08$ agreed with the Figure 13.13 showed by Orazem and Tribollet [49] for $J = 4R_e/\pi R_t = 0.002$. The correct value of the capacitance and ohmic resistance could not be obtained from the measurement model when the maximum regressed frequency is lower than f_{R_t} due to the effect from the mass transfer.

For case II, f_c/f_{R_t} is equal to 4.9, in which two characteristic frequencies were close and the synthetic data of this case is presented in Figure 8-3(a). The simulated data with $\Omega = 120$ rpm, $r_0 = 0.1$ cm, $\nu = 0.01$ cm^2/s, $\rho = 1000$ Ωm, $K_c = 13$ A/cm^2, $b_c = 19.9$ V^{-1}, $D_i = 2 \times 10^{-5}$ cm^2/s, $c_i(\infty) = 2$ mol/cm^3, and $C_{dl} = 20$ μF/cm^2 is shown in Figure 8-3(a). The geometry-induced frequency dispersion at high-frequency zoom-in region is shown in Figure 8-3(b) and the characteristic frequency was $f_c = 79.4$ Hz. The value of capacitance obtained by regression of the measurement model with 9 Viogt elements to the full impedance spectrum was $C_{dl} = 10.33 \pm 1.06$ μF/cm^2, and the ohmic resistance was $R_{e,H} = 78.56 \pm 0.03$ Ω/cm^2. As shown in Figure 8-4, the extracted values of the capacitance and the low-frequency ohmic resistance are close to the input value of $C_{dl} = 20$ μF/cm^2 and $R_{e,L} = 84.82$ only if the maximum regressed frequencies were between f_c and f_{R_t}.

The percent error $\left|(C_{dl,regressed} - C_{dl,input})/C_{dl,input}\right|$ between the regressed value and input value for capacitance as a function of the maximum frequency of the regressed data is shown in Figure 8-5. $\left|(C_{dl,regressed} - C_{dl,input})/C_{dl,input}\right|$ has a maximum value of 62 % for $f_c/f_{R_t} = 492$ and has a maximum value of 94% for $f_c/f_{R_t} = 4.9$ when $f_{max} = 10^6$HZ. For frequencies between f_c and f_{R_t}, $\left|(C_{dl,regressed} - C_{dl,input})/C_{dl,input}\right|$ is approaching 0%, which indicates that measurement model could yield correct values for capacitance. As frequencies become lower than f_{R_t}, $\left|(C_{dl,regressed} - C_{dl,input})/C_{dl,input}\right|$ started to deviate from 0%

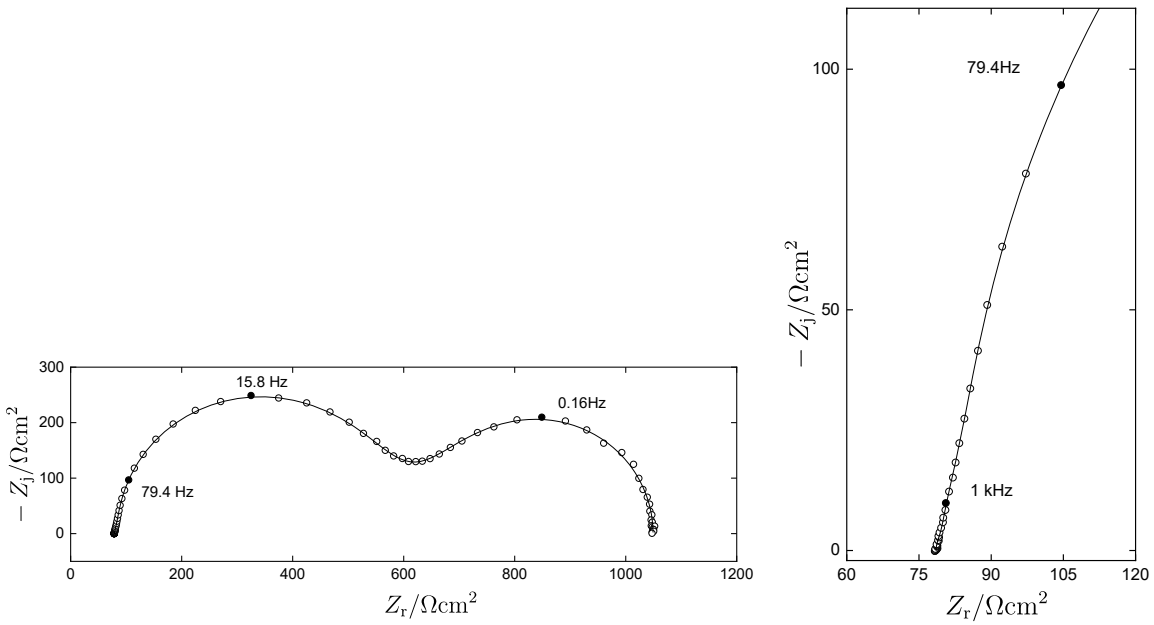

(a) (b)

Figure 8-3. Impedance calculations in Nyquist format for the system having a capacitance on a rotating disk electrode with $\Omega = 120$ rpm, $r_0 = 0.1$ cm, $\nu = 0.01$ cm^2/s, $\rho = 1000$ Ωm, $K_c = 13$ A/cm^2, $b_c = 19.9$ V^{-1}, $D_i = 2 \times 10^{-5}$ cm^2/s, $c_i(\infty) = 2$ mol/cm^3, and $C_{dl} = 20$ μF/cm^2. The ratio of the dispersion frequency and the characteristic frequency associated with the charge transfer is 4.9. The frequency range was 1 mHz to 1 MHz, and $\chi^2/\upsilon = 0.91$. A normally distributed error of 0.2% was added to the synthetic data. The line represents the complex fit of the measurement model to the data using modulus weighting: a) full impedance spectrum and b) high-frequency zoom-in region of the impedance spectrum.

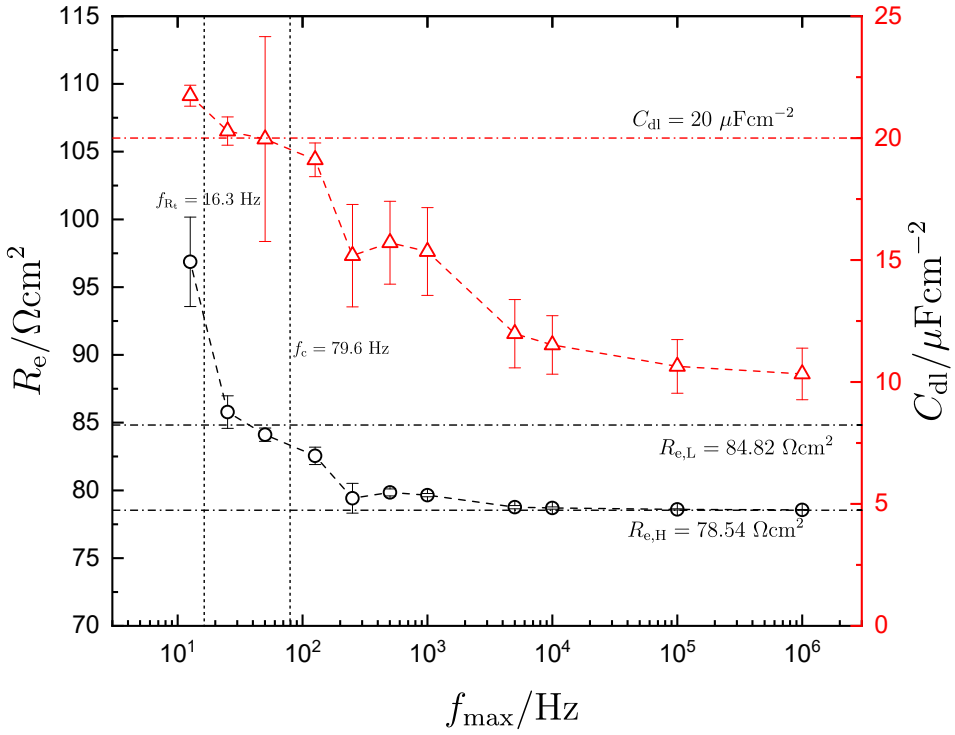

Figure 8-4. Capacitance and ohmic resistance obtained by regression of the measurement model to the complex impedance shown in Figure 8-3(a) for truncated frequency ranges as functions of the maximum frequency of the regressed data.

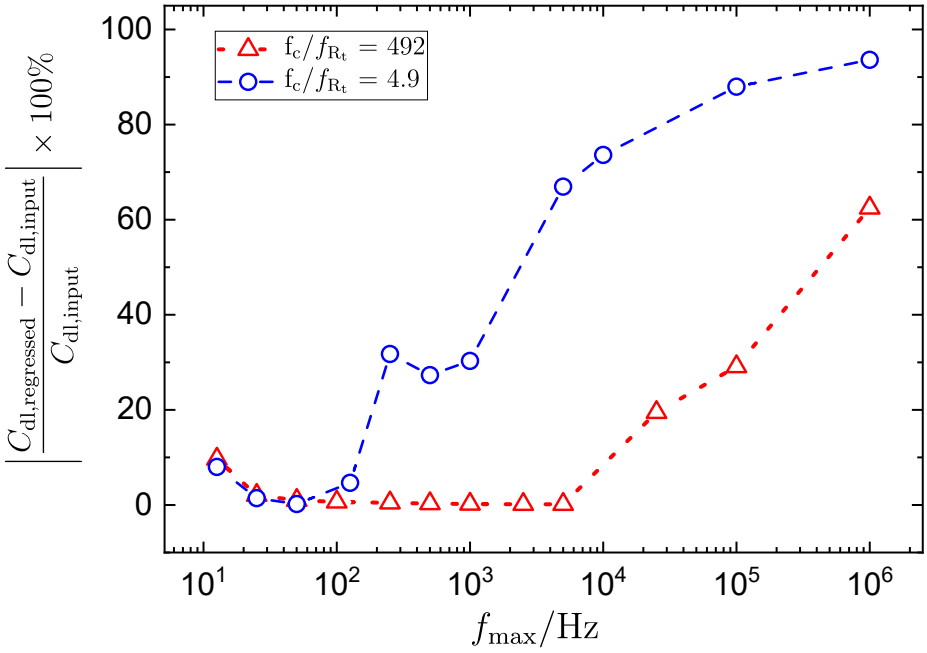

Figure 8-5. Percent error between regressed value and input value for capacitance as a function of the maximum frequency of the regressed data for $f_{\mathrm{c}}/f_{\mathrm{R_t}} = 4.9$ and $f_{\mathrm{c}}/f_{\mathrm{R_t}} = 492$.

The correct value of the capacitance and the ohmic resistance could also be obtained by regression of the process model including the Cole-Davidson expression to impedance data, which could be expressed as

$$Z = R_{e,H} + \frac{R_{e,L} - R_{e,H}}{(1 + j\omega\tau)^{\beta}} + \frac{R_t + R_d Z_{dim}}{1 + j\omega C_{dl}(R_t + R_d Z_{dim})} \tag{8-14}$$

where β and τ are parameters associated with the distribution of time constant, R_d is the diffusion resistance, and Z_{dim} is the dimensionless diffusion impedance, which can be obtained by using a look-up table of the solution from the convective-diffusion impedance without the homogeneous reaction. [49, 193] Regression of equation (8-14) to the impedance calculations for cases I and II were presented in Figure 8-6. As shown in Figures 8-6(a) and 8-6(b), fitting curve were overlapped with the impedance data, which represented the model provided a good fit to the synthetic data. The value of regressed parameters and percentage error compared with the input parameters were shown in Table 8-1. All the regressed parameters were found to be statistically significant. The value of C_{dl} = 20.001±0.008 μFcm^{-2} for case I and C_{dl} = 19.996±0.022 μFcm^{-2} for case II, which were in good agreement with the input value of C_{dl} = 20 μFcm^{-2}.

8.2.2 Numerical Simulation with CPE

Impedance calculations for the system having CPE behavior on a rotating disk electrode with $\Omega = 120$ rpm, $r_0 = 0.1$ cm, $\nu = 0.1$ cm^2/s, $\rho = 10$ Ωm, $K_c = 11$ A/cm^2, $b_c = 19.9$ V^{-1}, $D_i = 2 \times 10^{-5}$ cm^2/s, $c_i(\infty) = 2$ mol/cm^3, $\alpha = 0.9$, and $Q = 60.45$ μF/s$^{(1-\alpha)}$cm^2 is presented in Figure 8-7. The characteristic frequency associated with frequency dispersion calculated by equation (8-10) was $f_c = 7.75$ kHz and the characteristic frequency associated with the faradic reaction calculated by equation (8-11) was $f_{R_t} = 137.6$ Hz. The ratio of f_c/f_{R_t} was 56, which two characteristic frequencies were far away from each other. The value of capacitance obtained by regression of the measurement model with 11 Viogt elements to the full impedance spectrum was $C_{eff} = 8.32 \pm 0.74$ μF/cm^2, and the ohmic resistance was $R_{e,H} = 0.7905 \pm 0.0010$ Ω/cm^2. As shown in Figure 8-8, the extracted values of the capacitance and ohmic resistance kept increasing when the maximum regressed frequencies decreased. The value of the capacitance did not stay

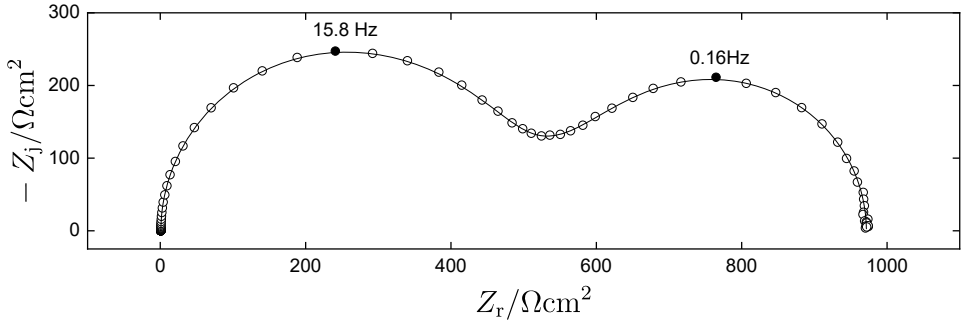

(a)

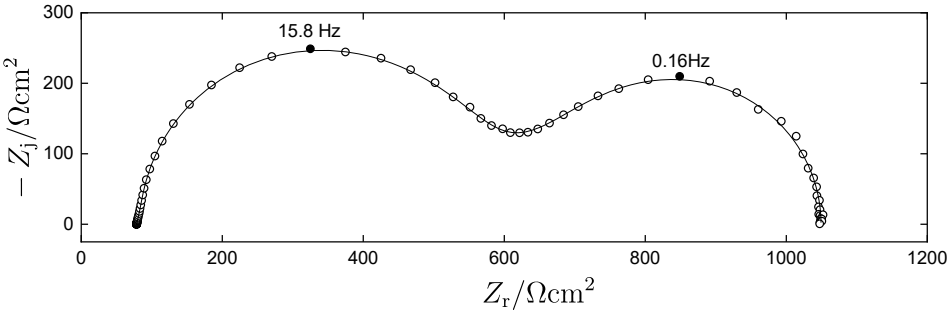

(b)

Figure 8-6. Regression of equation (8-14) to the impedance calculations. A normally distributed error of 0.2% was added to the synthetic data. The line represents the complex fit to the data using modulus weighting: a) $f_c/f_{R_t} = 492$ with $\chi^2/\upsilon = 0.94$, and b) $f_c/f_{R_t} = 4.9$ with $\chi^2/\upsilon = 0.90$.

Table 8-1. Parameters from regression of equation (8-14) to the impedance calculations for the system with a capacitance.

	Case I		Case II	
Parameter	Value	% Error	Value	% Error
Sc	1027±11	2.70	985±12	-1.52
$R_{e,H}$ / Ωcm^2	0.783±0.001	-0.31	78.44±0.04	-0.13
$R_{e,L}$ / Ωcm^2	0.850±0.001	-0.15	84.64±0.11	-0.21
R_t / Ωcm^2	469.24±0.31	-0.03	470.95±0.36	0.13
R_d / Ωcm^2	486.37±0.08	-0.23	478.69±0.56	-0.96
C_{dl} / μFcm^{-2}	20.001±0.008	0.01	19.996±0.022	-0.02
τ / μs	5.32±0.42		439.66±30.00	
β	0.582±0.036		0.632±0.022	

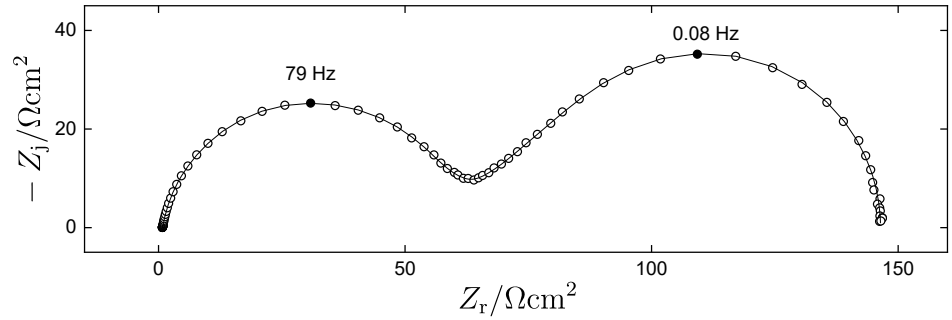

Figure 8-7. Impedance calculations in Nyquist format for the system having CPE behavior on a rotating disk electrode with $\Omega = 120$ rpm, $r_0 = 0.1$ cm, $\nu = 0.1$ cm^2/s, $\rho = 10$ Ωm, $K_c = 11$ A/cm^2, $b_c = 19.9$ V^{-1}, $D_i = 2 \times 10^{-5}$ cm^2/s, $c_i(\infty) = 2$ mol/cm^3, $\alpha = 0.9$, and $Q = 60.45$ μF/s$^{(1-\alpha)}$cm^2. The ratio of the dispersion frequency and the characteristic frequency associated with the charge transfer is 56. The frequency range was 1 mHz to 1 MHz, and $\chi^2/\upsilon = 0.96$. A normally distributed error of 0.2% was added to the synthetic data. The line represents the complex fit of the measurement model to the data using modulus weighting.

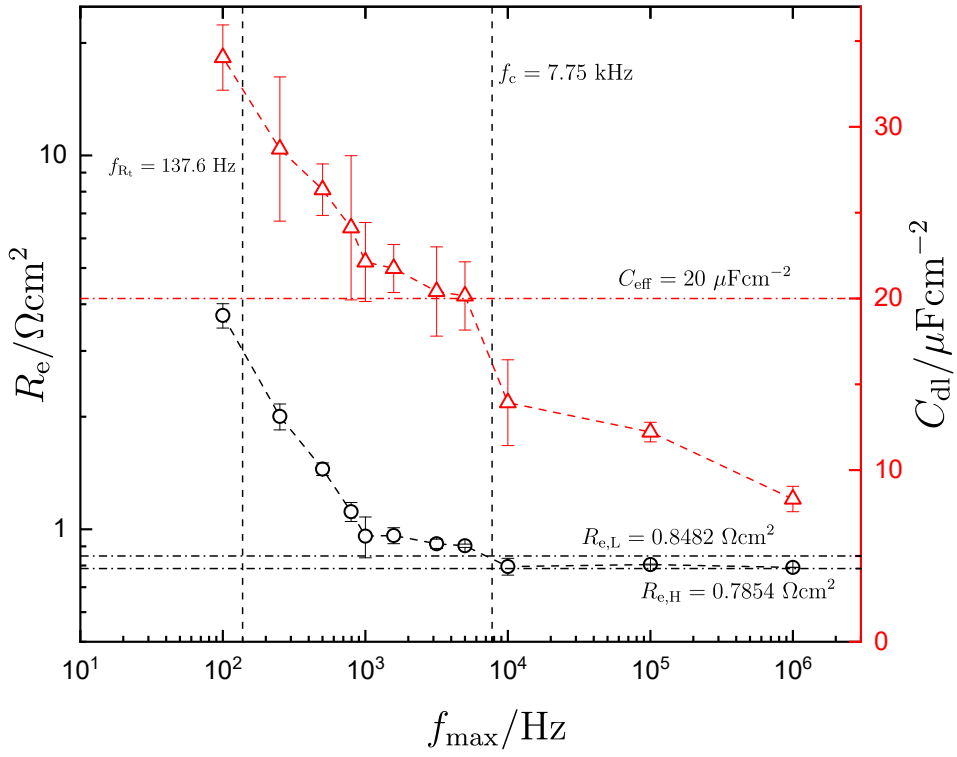

Figure 8-8. Capacitance and ohmic resistance obtained by regression of the measurement model to the complex impedance shown in Figure 8-7 for truncated frequency ranges as functions of the maximum frequency of the regressed data.

constant between f_c and f_{R_t} . The measurement model may not be able to extract the capacitance for the system having the CPE behavior. This could be explained in a system with a pure CPE and the impedance could be expressed as

$$Z = \frac{1}{(j\omega)^{\alpha} Q} \tag{8-15}$$

Impedance given by equation (8-15) for the system having a pure CPE with $\alpha = 0.9$, and $Q = 60$ $\mu F/s^{(1-\alpha)}cm^2$ is shown in Figure 8-9. The value of capacitance obtained by regression of the measurement model with 13 Viogt elements to the full impedance spectrum was $C_{eff} = 9.93 \pm 0.27$ $\mu F/cm^2$. Values of capacitance as functions of maximum regressed frequencies obtained by regression of the measurement model to truncated impedance data are shown in Figure 8-10. The value of the capacitance increased as the maximum regressed frequency decreased. In this case, the measurement model could not give the correct value of the capacitance. However, the correct value of the capacitance and ohmic resistance could be obtained by regression of the process model including the Havriliak-Negami equation [183] to impedance data, which could be expressed as

$$Z = R_{e,H} + \frac{R_{e,L} - R_{e,H}}{(1 + (j\omega\tau)^{\alpha})^{\beta}} + \frac{R_t + R_d Z_{dim}}{1 + (j\omega)^{\alpha} Q (R_t + R_d Z_{dim})} \tag{8-16}$$

Regression of equation (8-16) to the impedance calculations was shown in Figure 8-11 and the model provided an excellent fit to the impedance data. The regressed parameters were shown in Table 8-2 and all the regressed parameters were found to be statistically significant. The value of $C_{eff} = 19.86 \pm 0.14$ $\mu F/cm^2$ were calculated from equation (8-12) and the standard deviation were obtained by 5000 Monte Carlo simulations assuming normally distributed errors.

8.2.3 Experimental Measurement

The impedance response for a reduction of ferricyanide on a Pt disk at rotation speed of 120 rpm was shown in Figure 8-12 and the impedance data was checked by the measurement model error structure analysis with 10 Voigt elements to identify the frequency range that may be considered to be consistent with the Kramers-Kronig relations. The value of capacitance obtained by regression of equation (2-23) was $C_{dl} = 2.5 \pm 0.5$ $\mu F/cm^2$, and ohmic resistance was 1.223 ± 0.038 Ωcm^2. The value of the ohmic resistance may be considered $R_{e,H}$ due to a

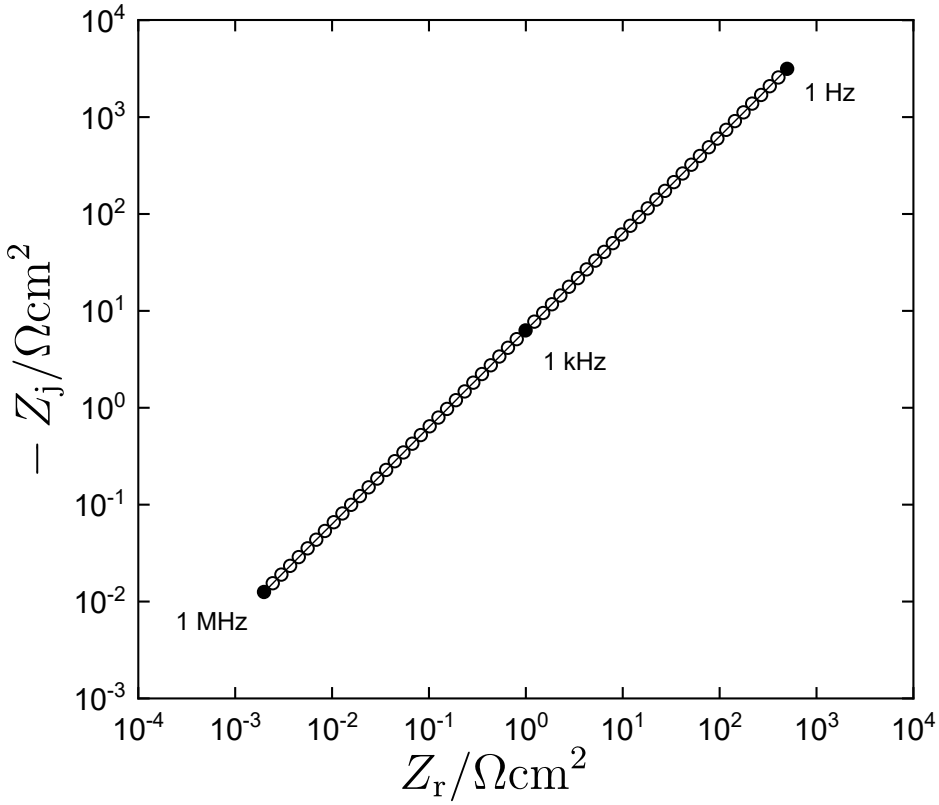

Figure 8-9. Impedance given by equation (8-15) in Nyquist format for the system having a pure CPE with $\alpha = 0.9$, and $Q = 60\ \mu\mathrm{F/s}^{(1-\alpha)}\mathrm{cm}^2$. A normally distributed error of 0.2% was added to the synthetic data. The line represents the complex fit of the measurement model to the data using modulus weighting. The frequency range was 1 Hz to 1 MHz, and $\chi^2/\upsilon = 0.03$.

Table 8-2. Parameters from regression of equation (8-16) to the impedance calculations for the system with CPE.

Parameter	Value	% Error
Sc	10231±79	2.31
$R_{e,H}$ / $\Omega\mathrm{cm}^2$	0.7846±0.0010	-0.11
$R_{e,L}$ / $\Omega\mathrm{cm}^2$	0.8442±0.0014	-0.47
R_t / $\Omega\mathrm{cm}^2$	57.90±0.03	0.13
R_d / $\Omega\mathrm{cm}^2$	86.52±0.08	-0.64
τ / μs	3.661±0.134	
β	0.637±0.064	
α	0.8982±0.0003	-0.20
Q / $\mu\mathrm{Fs}^{(\alpha-1)}\mathrm{cm}^{-2}$	61.35±0.16	1.48
C_{eff} / $\mu\mathrm{Fcm}^{-2}$	19.86±0.14	-0.72

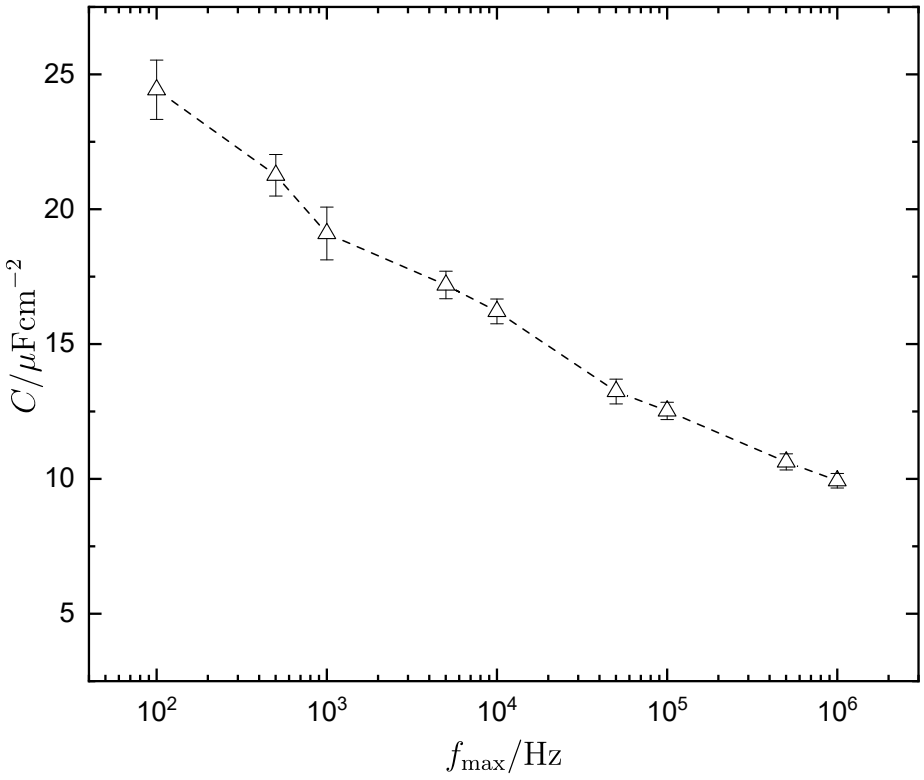

Figure 8-10. Capacitance obtained by regression of the measurement model to the complex impedance shown in Figure 8-9 for truncated frequency ranges as functions of the maximum frequency of the regressed data.

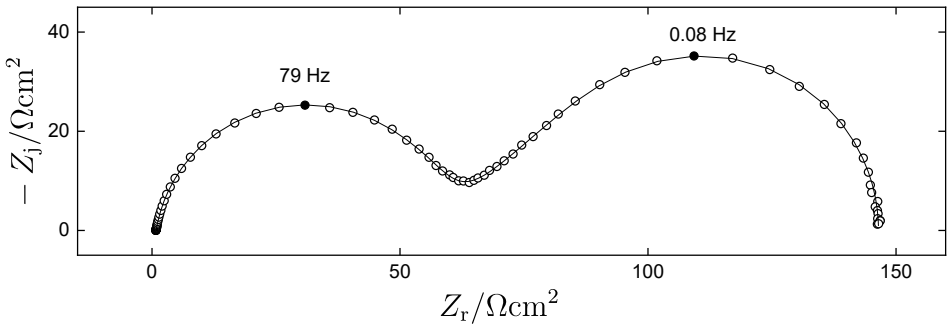

Figure 8-11. Regression of equation (8-16) to the impedance calculations. A normally distributed error of 0.2% was added to the synthetic data. The line represents the complex fit to the data using modulus weighting. $\chi^2/\upsilon = 0.99$.

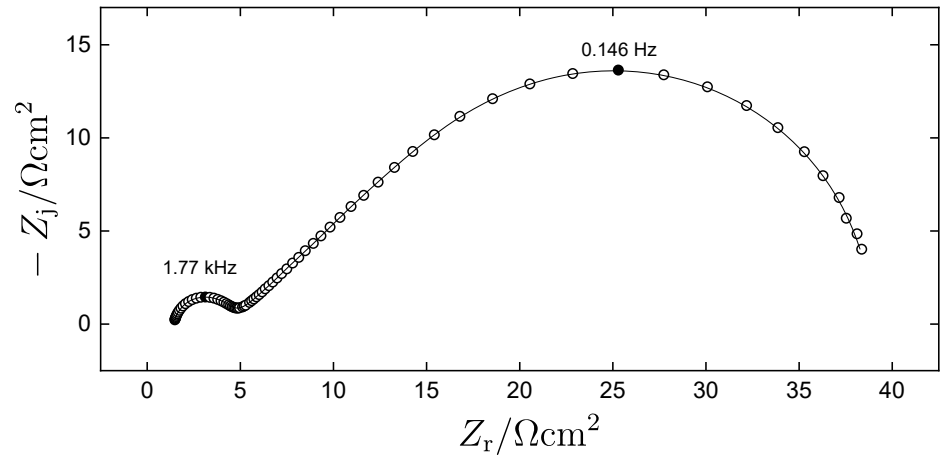

Figure 8-12. Impedance calculations in Nyquist format for a reduction of ferricyanide on a Pt disk at a rotation speed of 120 rpm. The line represents the complex fit of the measurement model to the data using stochastic error structure weighting. The stochastic error was expressed as $\sigma = \alpha|Z_j| + \gamma|Z|^2$ with $\alpha = 0.00088 \pm 0.00015$ and $\gamma = (3.18 \pm 0.19) \times 10^{-5}\ \Omega^{-1}\text{cm}^{-1}$. The frequency range was 1 mHz to 1 MHz, and $\chi^2/\upsilon = 2.43$.

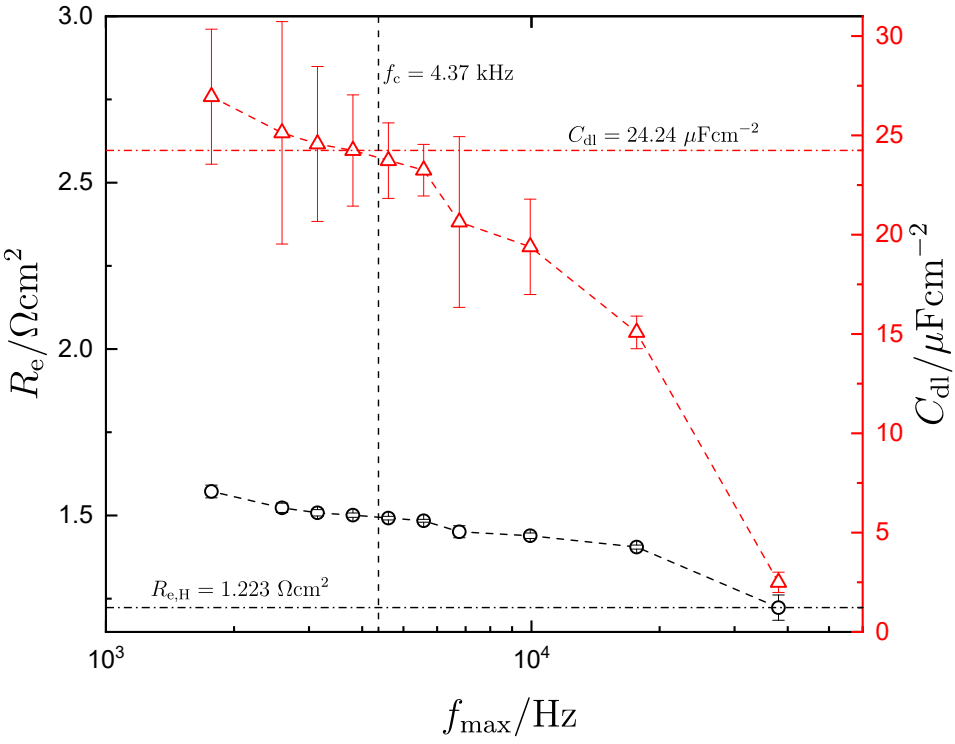

Figure 8-13. Capacitance and ohmic resistance obtained by regression of the measurement model to the complex impedance shown in Figure 8-12 for truncated frequency ranges as functions of the maximum frequency of the regressed data.

non-uniform current and potential distribution. The characteristic frequency was calculated from equation (8-9) to be 52.12 kHz. A sequential procedure was followed. A regression was performed in the frequency range of 21.54 mHz to 17.66 kHz that yielded a new value for the capacitance of 15.1±0.8 μF/cm^2 that was then used to estimate the characteristic frequency. The results are presented in Table 8-3 and in Figure 8-12. The sequential procedure may be considered successful if the characteristic frequency calculated from equation (2-23) was larger than the maximum regressed frequency, as is highlighted in Table 8-3. The analysis suggested that $R_{e,H} =$ 1.223±0.038 Ωcm^2, $R_{e,L} =$ 1.501±0.007 Ωcm^2, $C =$ 24.2±2.8 μ/Fcm^2, and $f_c =$ 4.37 kHz.

The value of the capacitance and ohmic resistance may also be obtained by regression of the process model, which can be expressed as

$$Z = R_e + \frac{R_t + R_d Z_{dim}}{1 + (j\omega)^{\alpha} Q(R_t + R_d Z_{dim})} \tag{8-17}$$

Results for regression of equation (8-17) are shown in Figure 8-14 and regressed parameters are shown in Table 8-4. The impedance data set was truncated to frequencies below the characteristic frequency $f_c =$ 4.37 kHz and the contribution of the ohmic impedance can be eliminated. The model provided an excellent fit to the impedance data and all the regressed parameters were found to be statistically significant. The value of $C_{eff} = 2.08 \pm 0.36$ μF/cm^2 were calculated from equation (8-12) and the standard deviation were obtained by 5000 Monte Carlo simulations assuming normally distributed errors. Sample Histograms for C_{eff} calculated by equations (2-23) and (8-12) with 5000 Monte Carlo simulations assuming normally distributed errors are shown in Figure 8-15. Overlapped histograms suggests that the capacitance obtained by use of the Brug formula and the measurement model differed slightly.

Table 8-3. Results for the sequential regression of the measurement model to the data presented in Figure 8-12 over a frequency ranging from f_{max} to 21.54 mHz.

f_{max}/ Hz	R_e/ Ωcm^2	C /μFcm^{-2}	$f_{c,est}$/ Hz
38,051	1.223±0.038	2.5±0.5	52,116
17,662	1.405±0.006	15.1±0.8	7,511
9,932	1.439±0.008	19.4±2.4	5,704
6,767	1.451±0.018	20.6±4.3	5,314
5,581	1.484±0.004	23.3±1.3	4,612
4,610	1.439±0.005	23.7±1.9	4,495
3,805	1.501±0.007	24.2±2.8	4,374
3,141	1.508±0.010	24.6±3.9	4,295
2,592	1.523±0.014	25.1±5.6	4,158
1,766	1.572±0.019	26.95±3.4	3,757

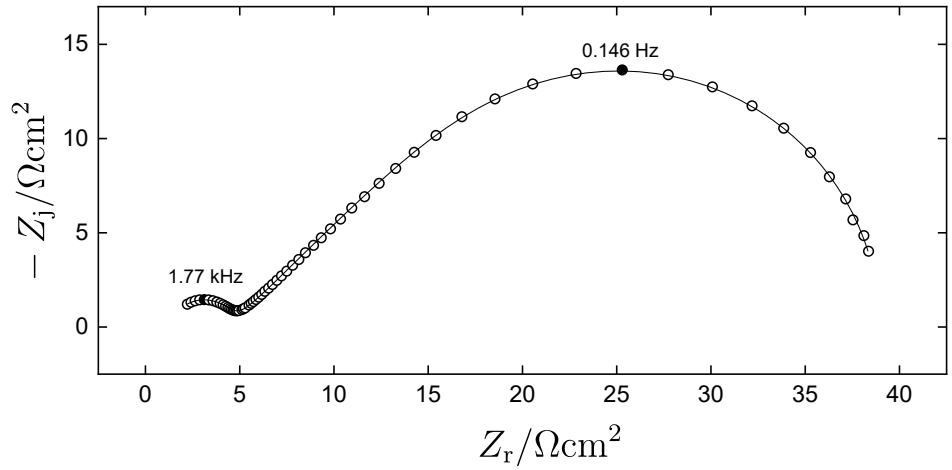

Figure 8-14. Regression of equation (8-17) to the measured impedance data over a frequency ranging from 21.54 mHz to 3.81 kHz. The line represents the complex fit to the data using stochastic error structure weighting. The stochastic error was expressed as $\sigma = \alpha|Z_j| + \gamma|Z|^2$ with $\alpha = 0.00088 \pm 0.00015$ and $\gamma = (3.18\pm0.19)\times 10^{-5}$ Ω^{-1}cm^{-1}. $\chi^2/\upsilon = 99.98$.

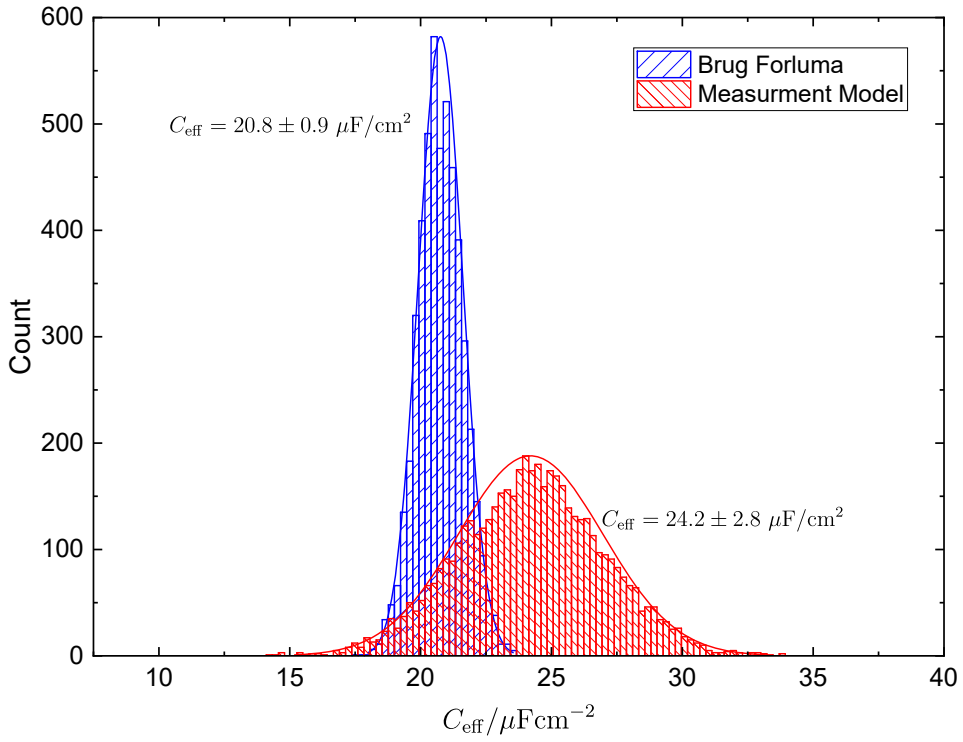

Figure 8-15. The distribution of C_{eff} obtained by 5000 Monte Carlo simulations for the experiment measurements and the errors were assumed normally distributed.

Table 8-4. Parameters from regression of equation (8-17) to the measured impedance data over a frequency ranging from 21.54 mHz to 3.81 kHz.

Parameter	Value
Sc	1240.7±7.0
R_e / Ωcm^2	1.358±0.014
R_t / Ωcm^2	3.204±0.016
R_d / Ωcm^2	33.416±0.016
α	0.8999±0.0029
Q / $\mu\text{Fs}^{(\alpha-1)}\text{cm}^{-2}$	61.35±1.20
C_{eff} / μFcm^{-2}	20.8±0.36

CHAPTER 9
CONCLUSIONS

Several projects were conducted to solve for problems on different electrochemical systems and conclusions were drawn based on each individual work. The first project was to develop a mathematical model for localized corrosion of copper used in Canadian used nuclear fuel containers. The second project was to use impedance measurements to understand physics and chemistries behind QLED devices. Three projects solved different fundamental problems on impedance spectroscopy.

9.1 Mathematics Model for Localized Corrosion of Copper

The model included coupled, nonlinear, diffusion equations for ionic species, which included the contribution of migration, local electroneutrality, and homogeneous reactions. The anodic and cathodic regions were not predefined but, instead, were determined by values of local concentration and potential from the simulation results. The growth of nm-scale films was calculated implicitly without using finite-element meshing and surface coverage was expressed in terms of the thickness in units of monolayers. The model also accounted for the effect of porous CuCl film thickness on the surface oxygen concentration and potential applied on electrochemical reactions. The influence of temperature was included on model parameters such as equilibrium rate constant, diffusion coefficient, Henry's law constant, solubility product constant and kinetic parameters associated with electrochemical reactions. Transient droplet temperature was described by interpolating results from a one-million-year simulation for the temperature change on the used fuel container surface. A total of 28 dependent spatial-temporal variables including species' concentrations, potentials and local corrosion rate were solved in this model.

In the current version of model, two extreme conditions were chosen such that droplet boundary has a faster or slower rate of oxygen decay for an initially air-saturated droplet. The model showed a 10-year time-dependent radial distribution of anodic and cathodic current density, surface coverage of CuCl film and Cu_2O film, and localized corrosion rates and depths. It also showed a distribution of pH, potential, and concentrations of dissolved gaseous and ionic species through the entire droplet. Temperature and oxygen concentration were shown to have a strong contribution to the simulation results. The model showed formation of Cu_2O film and

pitting corrosion is possible as a perforation of the cuprous oxide film. Simulations showed that the depth of corrosion was almost uniform over the elapsed time simulated and the maximum deviation from the average corrosion depth was less than 0.0004% for slower oxygen decay and less than 0.002% for faster oxygen decay in 10 years. The model could be used to explore the influence of different parameters on the localized corrosion rate and depth, film thickness and growth, and each individual current profiles. The parameters could be adjusted to conform to the DGR environment.

9.2 Impedance Measurements on QLED Devices

Impedance measurements were performed on red and green QLED devices. The impedance spectra was characterized by a high-frequency capacitive loop that was interpreted in terms of the physical properties of the hole-injection layer. The CPE parameters Q and α is related to layer thickness, dielectric constant, and a parameter ρ_δ related to the power-law distribution of resistivity in the layer. Independent measurement of layer thickness, capacitance obtained using a Voigt measurement model, and the formula derived under assumption of a power-law resistivity distribution was used to obtain dielectric constant and ρ_δ for the hole-injection layer. The present work demonstrates a way to extract useful parameters, which can be used to the characterize the properties of the QLED devices.

9.3 Application of The Kramers-Kronig Relations to Multi-Sine Electrochemical Impedance Measurements

Impedance measurements and model system simulations with single-sine and multi-sine excitations were performed for non-stationary systems. The obtained impedance results were tested for the compliance with Kramers–Kronig relations with measurement model methods. The non-stationary experimental measurements were performed on a Li/$SOCl_2$ primary battery with moderated DC offset. Both nonlinear measurement model and linear measurement model methods showed that the obtained impedance spectra with single-sine excitation were inconsistent with Kramers–Kronig relation; whereas, the multi-sine spectra were consistent with the Kramers–Kronig relations. The non-stationarity was simulated with linear and exponential increase in the charge transfer resistance. In both cases the calculated impedance spectra with

single-sine signals were found to be inconsistent with the Kramers–Kronig relation. On the other hand, the calculated impedance spectra with multi-sine signals were found to be consistent with the Kramers–Kronig relations.

The present work demonstrates that the validity of multi-sine impedance spectra cannot be assessed by use of the Kramers–Kronig relations. The coherence function, used primarily to detect issues with nonlinear responses, is only modestly sensitive to nonstationarity during the course of a multi-sine measurement.

Though the $Li/SOCl_2$ battery was used as the sample, the results obtained are universal and the conclusions are relevant well-beyond this sample. In any measurement involving a sample that is not stationary within the timescale of the measurement, a multisine EIS experiment will exhibit data that is compatible with the Kramers-Kronig relations. Therefore, a full Fourier domain analysis is necessary for evaluation using the non-excited frequencies.

9.4 Experimental Observation of Ohmic Impedance

A regression analysis of impedance data showed that parameters associated with the ohmic impedance could be resolved with statistical significance. The regression analysis was preceded by a measurement model analysis which restricted the frequency range to that which was consistent with the Kramers–Kronig relations and yielded a mode for the stochastic error structure, subsequently employed to weight the regression analysis. The standard deviation was not proportional to the modulus of the impedance, as is usually assumed. This surprising result demonstrates the importance of the measurement model as a tool for experimental determination of error structure.

The presence of ohmic impedance, predicted by numerical simulations, was confirmed by experimental observation. Numerical simulations showed that the dependence of regressed ohmic impedance parameters $R_{e,LF}$ and $R_{e,HF}$ on J was consistent with the formation of a film on the electrode surface. The Havriliak–Negami equation used to fit the ohmic impedance employs four parameters; whereas, an ohmic resistance requires only one parameter. As the ohmic impedance makes only a small contribution to the overall impedance, it can therefore be difficult to resolve

the ohmic impedance. Even if unresolved, the presence of an ohmic impedance can confound interpretation of impedance spectra by regression analysis. Thus, the best practice, if the ohmic impedance parameters cannot be regressed, is to truncate the data above the characteristic frequency for the ohmic impedance given by equation (2-35). As shown by Liao et al. [47], the measurement model employed in Section 7.4.2 can be used to estimate the parameters needed to calculate the characteristic frequency.

9.5 Measurement Model Interpretation of The Impedance Data Complicated by Ohmic Impedance

Measurement model was shown to give the correct value of the capacitance for the system with a capacitance, but a wrong value for the system having a local CPE behavior. Ohmic impedance could also be fitted by the process model including the Cole-Davidson or Havriliak-Negami equation. The value of the effective capacitance for the system with a CPE could be calculated by the Brug formula using regressed parameters. Even the measurement model could not give the correct value of the interface capacitance in case of local CPE, it could be used to identify which portion of the data was affected by the ohmic impedance and to calculate the effective capacitance by eliminating the frequencies above the geometry-induced dispersion frequency.

CHAPTER 10
FUTURE WORK

Future work for the mathematic model for localized corrosion of copper is discussed in section 10.1. Future work for the development of a 1-D mathematic model for N-type semi-conductor is discussed in section 10.2, which could be extended to a mathematic model for QLED devices.

10.1 Mathematical Model for Localized Corrosion of Copper

Several future works are proposed for the Mathematical Model for Localized Corrosion of Copper, including modification of droplet size and shape, sensitivity analysis, exploration of influence of predefined pits, and adding other Possible Reaction Mechanisms.

10.1.1 Modify Droplet Size And Shape

A fixed dimension of the droplet was used to study the localized corrosion of copper in the current version of program, but the environment in the Canadian deep geological repository will go from dry and warm to wet and cold conditions. Humanity will also change accordingly and droplet size will be affected. Many studied showed that the size of the droplet could affect the corrosion. Xiao et al. [194, 195] studied effect of droplet size on electrochemical distributions and local corrosion kinetics for pure iron under a saline droplet. The simulation results suggested that initiation and development of localized corrosion are likely to be found at Evans droplet with a symmetric electrochemical corrosion distribution. Different droplet sizes could result in significant differences in the control mechanisms of local corrosion kinetics between different locations under the droplets. Li et al. [196] studied the atmospheric corrosion of carbon steel under NaCl droplet. The experiment results showed that mass-transfer current density for oxygen reduction increased as droplet size decreased. Different droplet height and radius in the current model could be chosen to explore the influence of droplet size on corrosion copper. Reasonable ranges of droplet size could be determined by the humidity in the Canadian deep geological repository. The current version of model was built in the 2-D axisymmetric geometry. To account for the influence of droplet shape on corrosion of copper, the model could also be extended to a 3-D geometry using a hemispherical shape with different contact angles. The results from the 3-D geometry could be compared to the results from 2-D geometry.

10.1.2 Perform Sensitivity Analysis Of The Mathematic Model

The current version of program has a large number of parameters as shown in Table 4-1. Some parameters are from literature, some are selected to yield good results, and some are arbitrary. The parameters labelled with $\star$ were adjusted from literature to increase the stability of model. While the number of parameters is very large, the impact of each parameter is constrained by the model. A parametric study may be used to identify reasonable ranges of values. These studies may be informed by experimental results, thermodynamic calculations, and the best available information taken from the literature. The simulation results also showed that oxygen and temperature have a large contribution on corrosion of copper. Besides having two different oxygen decays at the droplet boundary, the oxygen boundary conditions could be chosen such that the droplet boundary could either has an infinite supply of oxygen or it could have no external supply of oxygen for an initially air-saturated droplet. The current model runs 10 year time-dependent simulations. Temperature interpolated from Guo's data [144] showed that temperature still elev ates after 10 years. The simulated elapsed time in the model could be increased to more than 10 years to explore the influence of higher temperature on corrosion of copper. The completed model will have greatest utility as a tool to evaluate possible scenarios in the Canadian deep geological repository.

10.1.3 Explore Influence Of Predefined Pits In The Corrosion Model

Cavities or holes may be produced in the copper caused by the pitting corrosion. Pitting is normally initiated by the localized damage to the oxide film or protective coatings. The Current model shows almost uniform corrosion and formation of cuprous oxide film. Surface coverage for cuprous oxide film has reached 1634 monolayer thickness (1.634 μm) for slower oxygen decay and 160 monolayer thickness (0.16 μm) for faster oxygen decay. Pitting corrosion is possible as a perforation of the cuprous oxide film and a predefined pit could be added to the current geometry and the normal depth of the pit could be from a few microns to 50 μm. [197] Results of corrosion depth and rate for model with predefined pit could be compared with the simulation results for model with initially bare copper metal under a droplet.

10.1.4 Add Other Possible Reaction Mechanisms

The current model accounts for a large amount of reactions including 6 electrochemical reactions, 3 homogeneous reactions involving films formation and other 15 homogeneous reactions involving copper chloride complex, copper hydroxide complex, copper carbonate complex and superoxide species. As discussed in section2.1.2, nitric acid could be produced through γ radiation in the humid air at the early stage after placement of used nuclear fuel container. Hall et al. [13] showed that maximum corrosion depth caused by oxygen for the used fuel container in the Canadian generic DGR environment was estimated to be 80 μm and maximum corrosion depth caused by radiation was estimated to be 9.4 μm. Even thought corrosion depth affected by oxygen was estimated to be dominant, it's still necessary to account for the influence of radiation on the corrosion of copper. At the later stage after placement of used nuclear fuel container, sulphate was likely to be produced microbiologically or by minerals that contains sulphate, which could cause copper corrosion. However, the current model runs the 10-year simulation at the initial stage after the used fuel container placement. It's worthwhile to introduce corrosion mechanisms related to sulphate when simulations extends to longer elapsed time.

10.2 One-Dimensional Model for N-Type Semi-Conductor

A one-dimensional mechanistic model including the QLED multi-layer structure could be developed to better understand the degradation mechanism. The initial stage of development of 1-D model for N-type semi-conductor is described in this section.

10.2.1 Mathematical Development

A one-dimensional model for N-type semi-conductor was developed in the FORTRAN language, accounting for the mass transfer of electrons and holes, and the kinetic process of the recombination reaction. The preliminary single-layer model could be developed further that includes multi-layer structure. The schematic representation of the single electron-transport layer was shown in Figure 10-1. The thickness δ_n of the electron-transport layer was equal to 20 Debye

lengths, which can be defined as

$$\lambda = \left[\frac{\varepsilon\varepsilon_0 \mathrm{RT}}{2\mathrm{F}^2\left(N_\mathrm{d} - N_\mathrm{a}\right)}\right]^{1/2} \tag{10-1}$$

where F is Faraday's constant, R is the universal gas constant, T is the temperature, ε is the dielectric constant of the material, ε_0 is the permittivity in vacuum, and $(N_\mathrm{d} - N_\mathrm{a})$ is the doping level, which is positive for an n-type material and negative for a p-type material. A multi-layer model, including the quantum-dots layer and the hole-transport layer, will be developed step by step. The nonlinear set of differential equations for the steady-state condition was solved by Newton-Raphson iteration. The results were incorporated into the impedance calculations, which were linearized under the assumption that the perturbation amplitude was small. The finite-difference equations for both steady-state and impedance calculations were solved by use of Newman's BAND algorithm. [131]

10.2.1.1 Governing equation

The material balance equation of species i can be expressed as

$$\frac{\partial c_\mathrm{i}}{\partial t} = -\nabla \cdot \mathbf{N}_\mathrm{i} + R_\mathrm{i} \tag{10-2}$$

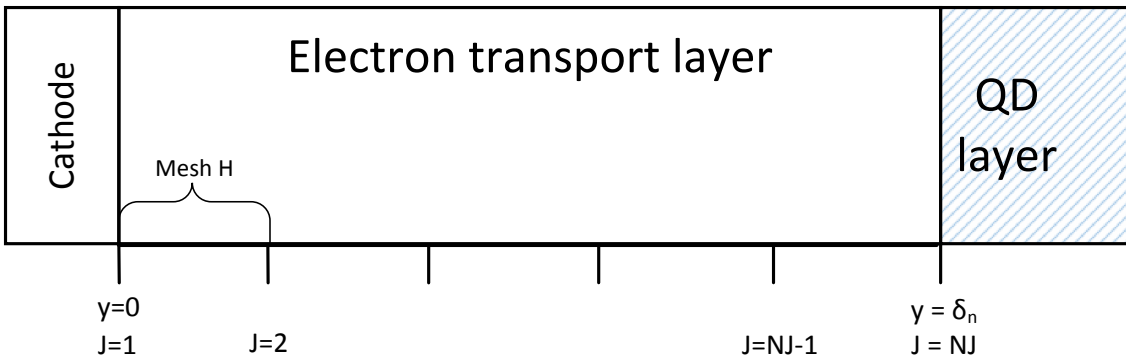

Figure 10-1. The schematic representation of the single electron-transport layer with the mesh size

where c_i is the concentration of species i, N_i is the flux of species i, and R_i is the reaction rate of species i in the homogeneous reaction, which can be expressed as

$$R_i = -k_r \left(c_n c_p - n_i^2 \right) \tag{10-3}$$

where k_r is the reaction rate constant of the electron and hole recombination reaction, n_i is the intrinsic concentration, c_n is the concentration of electrons, and c_p is the concentration of holes. The left-hand-side term of equation (10-2) represents the accumulation, which is the concentration change with respect to the time. The first term on the right-hand side of equation (10-2) represents the net convergence of species i. The second term on the right-hand side of equation (10-2) represents the production by the homogeneous chemical reaction. In this case, the convection was ignored due to a solid-state device.

The flux of each species in the system is given by

$$\mathbf{N}_i = -z_i u_i \mathrm{F} c_i \nabla \Phi - D_i \nabla c_i \tag{10-4}$$

where Φ is the potential, z_i represents charge associated with species i, D_i is diffusion coefficient of species i, and u_i is the mobility of the species of species i, which can be expressed as

$$D_i = \mathrm{RT} u_i \tag{10-5}$$

The first term in equation (10-4) represents the migration of the species i and the second term represents the diffusion of the species i.

The Poisson's equation, which relates the concentration of the charged species and potential distribution through the multi-layer devices, can be expressed as

$$\frac{\partial^2 \Phi}{\partial^2 y} = -\frac{\mathrm{F}}{\varepsilon \varepsilon_0} \rho \tag{10-6}$$

where ρ is the charge density, which can be expressed as

$$\rho = \mathrm{F} \left[c_p - c_n + (N_d - N_a) \right] \tag{10-7}$$

The current density can be expressed as a function of carrier fluxes and shown as

$$\mathbf{i} = \mathrm{F}\sum_{\mathrm{i}} z_{\mathrm{i}}\mathbf{N}_{\mathrm{i}} \tag{10-8}$$

10.2.1.2 Boundary conditions

At the electrode surface, the current was assumed to be injected by the electron fluxes. Thus, the boundary conditions for fluxes were expressed as

$$\mathbf{N}_{\mathrm{n}}(0) = \frac{\mathbf{i}}{z_{\mathrm{n}}\mathrm{F}} \tag{10-9}$$

and

$$\mathbf{N}_{\mathrm{p}}(0) = 0 \tag{10-10}$$

The boundary conditions for two species of electrons and holes at the cathode surface were expressed as

$$\mathbf{c}_{\mathrm{i}} = \mathbf{c}_{\mathrm{i}}(0) \tag{10-11}$$

where the value of $\mathbf{c}_{\mathrm{i}}(0)$ was obtained by solving equation (10-12)and (10-13) as

$$\mathbf{c}_{\mathrm{n}}(0) - \mathbf{c}_{\mathrm{p}}(0) + (N_{\mathrm{d}} - N_{\mathrm{a}}) = 0 \tag{10-12}$$

and

$$\mathbf{c}_{\mathrm{n}}(0)\mathbf{c}_{\mathrm{p}}(0) = n_{\mathrm{i}}^2 \tag{10-13}$$

under equilibrium conditions. The boundary conditions for potential were expressed as

$$\Phi(0) = 0 \tag{10-14}$$

and

$$\frac{\partial \Phi}{\partial y}(\delta_{\mathrm{n}}) = \frac{q}{\varepsilon\varepsilon_0} \tag{10-15}$$

where q is the surface charge density located at the interface between the electron-transport layer and quantum-dots layer.

10.2.1.3 Impedance calculations

All the variables in the governing equations can be written in phasor notation as

$$X = \overline{X} + \mathrm{Re}\left\{\widetilde{X}\exp\left(\mathrm{j}\omega t\right)\right\} \tag{10-16}$$

where the $\overline{X}$ is the steady-state value of variable X, j is the imaginary number, ω is the angular frequency and $\widetilde{X}$ is the phasor, which can be expressed in terms of the complex format as

$$\widetilde{X} = \widetilde{X}_{\mathrm{r}} + \mathrm{j}\widetilde{X}_{\mathrm{j}} \tag{10-17}$$

where $\widetilde{X}_{\mathrm{r}}$ and $\widetilde{X}_{\mathrm{j}}$ are the real and imaginary parts of the variable X. Similarly, equation (10-2) can be expressed as

$$0 = -\nabla\cdot\overline{\mathbf{N}}_{\mathrm{i}} + \overline{R}_{\mathrm{i}} \tag{10-18}$$

and

$$\mathrm{j}\omega\widetilde{c_{\mathrm{i}}} = -\nabla\cdot\widetilde{\mathbf{N}}_{\mathrm{i}} + \widetilde{R}_{\mathrm{i}} \tag{10-19}$$

After solving the governing equations simultaneously, the overall impedance could be calculated as

$$Z = \frac{\widetilde{\Phi}(\delta_{\mathrm{n}}) - \widetilde{\Phi}(0)}{\widetilde{\mathbf{i}}} \tag{10-20}$$

10.2.2 Simulation of Single Electron-Transport Layer

Table 10-1. Parameter values used for the simulations of 1-D N-type semi-conductor.

Parameter	Value	Units
Doping level, $N_{\mathrm{d}} - N_{\mathrm{a}}$	1×10^{-9}	$\mathrm{mol/cm^3}$
Intrinsic concentration, n_{i}	1×10^{-14}	$\mathrm{mol/cm^3}$
Dielectric constant, ε	11.3	unity
Electron-transport layer thickness, δ_{n},	24	μm
Diffusion coefficient of electrons, D_{n}	25	$\mathrm{cm^2/s}$
Diffusion coefficient of holes, D_{p}	8	$\mathrm{cm^2/s}$
Surface charge density, q	-5×10^{-9}	$\mathrm{C/cm^2}$
Recombination reaction rate constant, k_{r}	10^{15}	$\mathrm{cm^3/mol\ s}$
Temperature, T	300	K

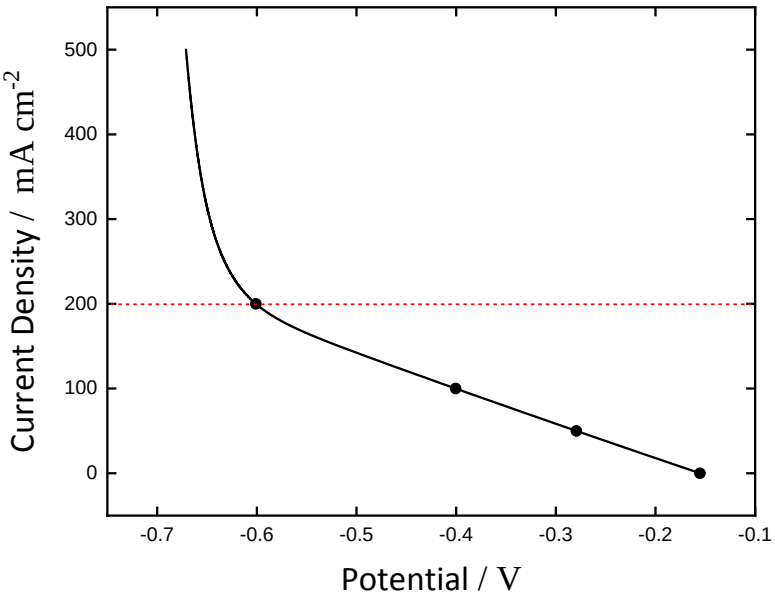

Figure 10-2. The polarization curve calculated for parameters presented in Table 10-1. Labeled current density corresponds to the steady-state calculations shown in Figure 10-3 and the dashed line represents the maximum current density for steady-state calculation with physical meanings.

The polarization curve calculated for parameters in Table 10-1 is shown in Figure 10-2. The potential increases as the current density increases and the dashed line represents a maximum current density of 200 mA/cm^2 for steady-state calculations. The current density higher than the dashed line will yield non-physical results, such as the electrical field higher than 100 V/cm and concentration of electrons/holes 100 times larger than the doping level. Thus, the steady-state profiles were calculated under conditions of current densities below 200 mA/cm^2. The steady-state calculations as a function of the position with the current density as a parameter are shown in Figure 10-3. The electron transport layer could be divided into two regions: the charge-neutral region for $y \rightarrow 0$, and the space charge region for $y \rightarrow \delta_n$. The normalized concentrations of electrons and holes by doping level are presented in Figure 10-3(a) and 10-3(b). Under the open-circuit condition, the concentration of electrons and holes stays constant in the charge-neutral region, in which the concentration of electrons is equal to the doping level and the concentration of holes is equal to 10^{-19} mol/cm^3. The concentration of electrons decreases when approaching the space-charge region, whereas the concentration of holes increases. As the current

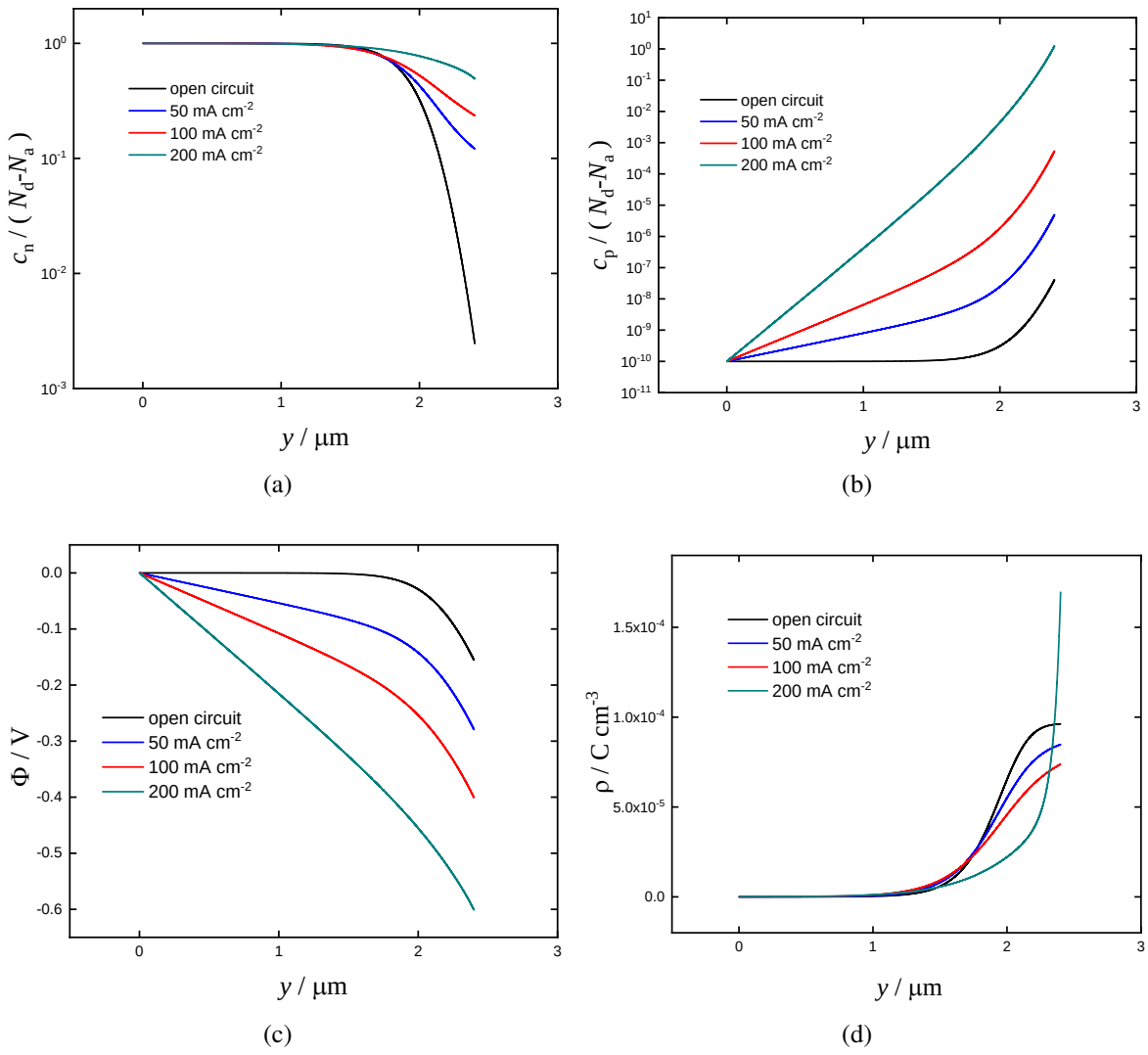

Figure 10-3. Steady-state calculations as a function of the position with the current density as a parameter a) Normalized concentration of electrons, b) normalized concentration of holes, c) potential, d) charge density.

density increases, fewer electrons are consumed in the space charge region and more holes are generated to balance the charge. As shown in Figure 10-3(c), the potential decreases and higher current density yields a larger potential drop across the electron-transport layer. The distribution of the charge density calculated by equation (10-7) is shown in Figure 10-3(d).

The calculated impedance corresponding to the steady-state results presented in Figure 10-3 is shown in Figure 10-4. The frequency is from 0.1 mHz to 0.1 GHz. For all current densities, the shape of the impedance is a semi circle, which is a capacitive loop. As the current density increases, the size of the loop decreases and the characteristic frequency increases. The calculated impedance could be fitted by the circuit model including a single RC element in series with an ohmic resistance. The ohmic resistance is associated with resistance contributed by the electrons and holes in the charge-neutral region and this is evident in Figure 10-3(c) that the potential drops linearly due to the ohmic loss. The capacitance and the charge-transfer resistance are associated with the space-charge region.

Parallel development of the numerical simulations and experimental work could be used to study the degradation mechanisms of QLED devices. For the numerical simulation, a one-dimensional model including the QLED multi-layer structure can be developed. Steady-state profiles and impedance response could calculated under different operating conditions. Deep-level state reactions and corresponding degradation reactions could be added to the numerical simulation. Parameter variation study will also be performed to better understand the physics and chemistry in the QLED devices, such as the diffusion coefficients of electrons, the homogeneous reaction rate constant, and the dielectric constant of the layer material. For the experiments, EIS measurements could be measured on new devices not only including the full-emitting devices with different colors but also single-layer and double-layer devices. Hypotheses for performance degradation could be developed and experimental methods could be designed to confirm proposed explanations for performance degradation.

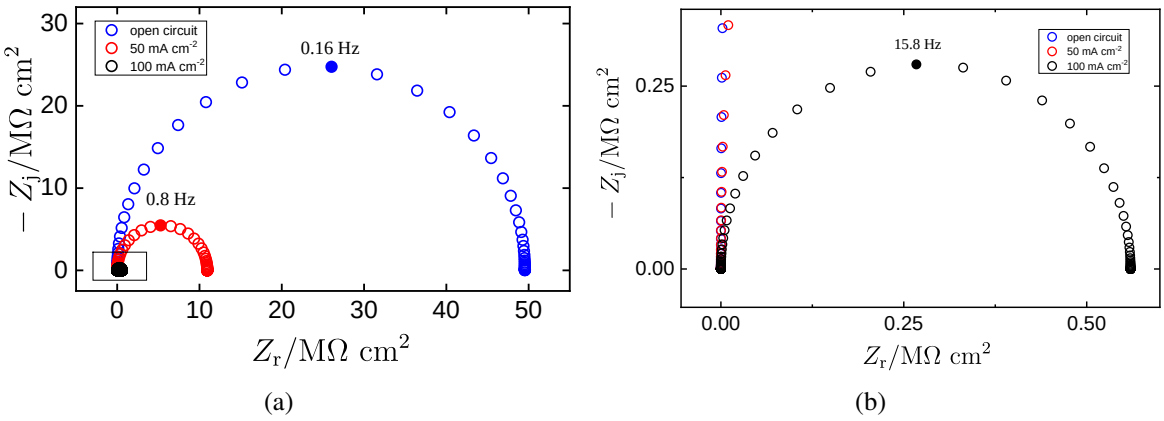

Figure 10-4. Impedance calculations with applied current density as a parameter: a)the overall impedance, defined by equation (5-1), for different values of the current densities. b) The overall impedance corresponding to the box in (a).

APPENDIX A
CODE FOR SINGLE-SINE AND MULTI-SINE IMPEDANCE CALCULATIONS

In Chapter 6, the synthetic impedance response data calculated by a Fourier analysis for the single-sine potential perturbation and by an FFT analysis for the multi-sine. MATLAB code used to calculate the single-sine impedance is show in Appendix A.1 and to calculate the multi-sine impedance is shown in Appendix A.2. MATLAB code used to calculation coherence function for the synthetic multi-sine impedance is shown in Appendix A.3.

Listing A.1. MATLAB Code to Calculate the Signle-Sine Impedance

```
clc; close all;clear all;
%Chen You
global Vbar
syms t
Cdl=31*1E-6; % F/cm2
ba=19.5; %V^-1
bc=19.5; %V^-1
Vbar=0;%V
N=61; %Frequemcy points
C=3; %Cycle number
nfka=0.14*1E-3;
nfkc=0.14*1E-3;
% time =(0:fpoints-1)*T;%total time
deltaV=[1e-3,2E-2,4E-2];
f=zeros(1,N);
for fspan=1:N
    f(fspan)=round(10^(3-0.05*(fspan-1)),1);
    time(fspan)=1./f(fspan);
end
time_total=sum(time);
for fspan=1:N
    T(fspan)=1./round(10^(3-0.05*(fspan-1)),1);
    %real part potential
    A=cumsum(T);
    TK=A-T;
% Ka(fspan)=(1-(0.1*(1-exp(-(t+TK(1,fspan))))));  expnonational
%  Ka(fspan)=(1-(0.01*(t+TK(1,fspan))));  linear
Ka(fspan)=(1-(0.1*(1-exp(-(t+TK(1,fspan))))));
Kc(fspan)=(1-(0.1*(1-exp(-(t+TK(1,fspan))))));
%  K(fspan)=1;
    pr1 = @(t)(Vbar+deltaV(1,1)*cos(2*pi.*f(1,fspan)*t)).*...
        cos(2*pi.*f(1,fspan).*t)/T(1,fspan);
Vr1(fspan) = integral(pr1,0,T(1,fspan),'ArrayValued',true);

%imaginary part potential
    pim1 = @(t)-(Vbar+deltaV(1,1)*cos(2*pi.*f(1,fspan)*t)).*...
        sin(2*pi.*f(1,fspan).*t)/T(1,fspan);
Vim1(fspan) = integral(pim1,0,T(1,fspan),'ArrayValued',true);

%real part current
cr1 = @(t)(nfka*(1-(0.1*(1-exp(-(t+TK(1,fspan))))))*exp(ba*(Vbar+...
        deltaV(1,1)*cos(2*pi.*f(1,fspan)*t))-...
        nfkc*(1-(0.1*(1-exp(-(t+TK(1,fspan))))))*exp(-bc*(Vbar+...
        deltaV(1,1)*cos(2*pi.*f(1,fspan)*t)))+...
       (-2*pi*Cdl.*f(1,fspan).*deltaV(1,1)*sin(2*pi.*f(1,fspan)*t))).*...
       cos(2*pi.*f(1,fspan).*t)/T(1,fspan);
ir1(fspan) = integral(cr1,0,T(1,fspan),'ArrayValued',true);

%imaginary part current
   cim1 = @(t)-(nfka*(1-(0.1*(1-exp(-(t+TK(1,fspan))))))*exp(ba*...
   (Vbar+deltaV(1,1)*cos(2*pi.*f(1,fspan)*t))-...
      nfkc*(1-(0.1*(1-exp(-(t+TK(1,fspan))))))*exp(-bc*(Vbar+...
      deltaV(1,1)*cos(2*pi.*f(1,fspan).*t)))+...
      (-2*pi*Cdl.*f(1,fspan).*deltaV(1,1)*sin(2*pi.*f(1,fspan)*t))).*...
      sin(2*pi.*f(1,fspan)*t)/T(1,fspan);
iim1(fspan) = integral(cim1,0,T(1,fspan),'ArrayValued',true);
V(fspan)=((Vr1(fspan))^2+(Vim1(fspan))^2)^0.5;
```

```
I(fspan)=((ir1(fspan))^2+(iim1(fspan))^2)^0.5;
end
figure(7)
plot(V(1),I(1))

%First cycle
V1=complex(Vr1,Vim1);
I1=complex(ir1,iim1);
Z1=V1./I1;
Zr1=real(Z1);
Zj1=imag(Z1);

%model
Rt=1/(ba*nfka*exp(ba*Vbar)+bc*nfkc*exp(-bc*Vbar));
for fspan=1:N
    f(fspan)=round(10^(3-0.05*(fspan-1)),1);
Z(fspan)=Rt/(1+2*pi.*f(1,fspan)*Cdl*1i*Rt);
Zr(fspan)=real(Z(1,fspan));
Zj(fspan)=imag(Z(1,fspan));

end

%real part of the impedance as a function of frequency
Zr1Rt=Zr1;
ZrRt=Zr;

%imaginary part of the impedance as a function of frequency
Zjab=abs(Zj);
Zj1ab=abs(Zj1);

impedance=zeros(N,2);
impedance(:,1)=Zr1;
impedance(:,2)=Zj1;

impedance_m=zeros(N,2);
impedance_m(:,1)=Zr;
impedance_m(:,2)=Zj;

frequency=zeros(N,1);
frequency(:,1)=f;


figure(1)
scatter(Zr1,-Zj1)
hold on
plot(Zr,-Zj)
legend('1 mV');
xlabel('$Z_\mathrm{r} / \Omega \mathrm{cm^{2}}$',...
    'interpreter','latex')
ylabel('$Z_\mathrm{j} / \Omega \mathrm{cm^{2}}$',...
    'interpreter','latex')
hold on;
axis equal

figure(2)
scatter(f,Zr1)
hold on
plot(f,Zr)
```

```
116 legend('1 mV');
117 xlabel('Frequency / Hz')
118 ylabel('$Z_\mathrm{r}$',...
119     'interpreter','latex')
120 set(gca, 'XScale', 'log')
121
122 figure(3)
123 scatter(f,-Zj1)
124 hold on;
125 plot(f,-Zj)
126 legend('1 mV');
127 xlabel('Frequency / Hz')
128 ylabel('$|Z_\mathrm{j}|$',...
129     'interpreter','latex')
130 set(gca, 'XScale', 'log')
```

Listing A.2. MATLAB Code to Calculate the Multi-Sine Impedance

```
clc; close all;clear all;
syms t
Cdl=31E-6;
b=19.5;
Fs=50; %sampling frequency
T=1/Fs; %sampling period
fpoints=200; %length of the signal
%Frequency
f1=1; %Hz
f2=5; %HZ
f3=7; %HZ

nfka=0.14*1E-3;
nfkc=0.14*1E-3;
Vbar=0;%V
deltaV=1E-3;
time = (0:fpoints-1)*T;
%Potential
V1=deltaV*sin(2*pi*f1*t);
V2=deltaV*sin(2*pi*f2*t+0.2);
V3=deltaV*sin(2*pi*f3*t+0.3);
V = Vbar+V1+V2+V3;
%Current
Ich1=diff(V1)*Cdl;
Ifa1=nfka*exp(b*V1)-nfkc*exp(-b*V1);
Itotal1=Ich1+Ifa1;
Ich2=diff(V2)*Cdl;
Ifa2=nfka*exp(b*V2)-nfkc*exp(-b*V2);
Itotal2=Ich2+Ifa2;
Ich3=diff(V3)*Cdl;
Ifa3=nfka*exp(b*V3)-nfkc*exp(-b*V3);
Itotal3=Ich3+Ifa3;
Ich=diff(V)*Cdl;
Ifa=nfka*exp(b*V)-nfkc*exp(-b*V);
Itotal=Ich+Ifa;
%Calcalate the potential/Current with a giveb value
for fspan=1:fpoints
    Vval(fspan)=eval((subs(V1,t,time(1,fspan))));
end
for fspan=1:fpoints
    Vva2(fspan)=eval((subs(V2,t,time(1,fspan))));
end
for fspan=1:fpoints
      Vva3(fspan)=eval((subs(V3,t,time(1,fspan))));
end
for fspan=1:fpoints
    Vva(fspan)=eval((subs(V,t,time(1,fspan))));
end
for fspan=1:fpoints
    Iva(fspan)=eval((subs(Itotal,t,time(1,fspan))));
end
for fspan=1:fpoints
    Iva1(fspan)=eval((subs(Itotal1,t,time(1,fspan))));

end
for fspan=1:fpoints
  Iva2(fspan)=eval((subs(Itotal2,t,time(1,fspan))));
```

```
58
59 end
60 for fspan=1:fpoints
61   Iva3(fspan)=eval((subs(Itotal3 ,t,time(1,fspan))));
62 end
63 %FFT for the current/potential
64 Vfft = fft(Vva);
65 Ifft = fft(Iva);
66 fv = Fs*(0:(fpoints)-1)/fpoints;
67 %Potential input singal as a function of the time
68 figure(1)
69 plot(time,Vva)
70  title('Potential input singal as a function of the time')
71 % Magnitude of the potential input
72  figure(2)
73  plot(fv,abs(Vfft)/length(Vfft)*2)
74  title('Magnitude of the potential input')
75
76 % Magnitude of the current input
77  figure(3)
78  plot(fv,abs(Ifft)/length(Ifft)*2)
79  title('Magnitude of the current input')
80 % Individual signal of the potential input
81 figure(4)
82 plot(time,Vva1)
83 hold on;
84 plot(time,Vva2)
85 plot(time,Vva3)
86 legend('1 Hz','5 Hz','10 Hz');
87 title('Individual signal of the potential input')
88
89 %Current input singal as a function of the time
90 figure(5)
91 plot(time,Iva)
92 title('Current input singal as a function of the time')
93
94 % Individual signal of the current input
95 figure(6)
96 plot(time,Iva1)
97 hold on;
98 plot(time,Iva2)
99 plot(time,Iva3)
100 legend('1 Hz','5 Hz','10 Hz');
101 title('Individual signal of the current input')
102
103 % Z100=Vfft((100/Fs*fpoints)+1)./Ifft((100/Fs*fpoints)+1)
104 % Z10=Vfft((10/Fs*fpoints)+1)./Ifft((10/Fs*fpoints)+1)
105 % Z1=Vfft((1/Fs*fpoints)+1)./Ifft((1/Fs*fpoints)+1)
```

Listing A.3. MATLAB Code for the Coherence Function Calculation

```
clc; close all;clear all;

M1=dlmread('Time_voltage_current.txt');
Time=M1(:,1);
Voltage=M1(:,2);
Current=M1(:,3);
M2=dlmread('freq.txt');
F=M2;
Fs=length(Time)/Time(length(Time),1);
[Cxy,FF] = mscohere(detrend(Voltage),detrend(Current),[],[],F,Fs);
[Cxy2,FF2] = mscohere(Voltage,Current,[],[],F,Fs);
Coherence=zeros(length(F),3);
Coherence(:,1)=M2;
Coherence(:,2)=Cxy;
Coherence(:,3)=Cxy2;
figure(1)
plot(FF,Cxy)
title('Magnitude-Squared Coherence')
xlabel('Frequency (Hz)')
grid
hold on;
plot(FF,Cxy2)
```

APPENDIX B
CODE FOR ONE-DIMENSIONAL MODEL FOR N-TYPE SEMI-CONDUCTOR

The finite-difference equations for both steady state and impedance calculations in the system for the N-type semi-conductor were solved by use of Newman's BAND algorithm in FORTRAN. Input file shown in Appendix B.1 is corresponding to the parameters shown in Table 10-1. [131] Fortran code used to calculate the steady-state profile is shown in Appendix B.2 and to calculate impedance is shown in Appendix B.3. For both steady-state and impedance calculations, the code file started with a program called QDETL, which was used for listing the model variables and creating calling files for the input and output files. Three subroutines called BC1, ETL and BCNJ were used to list the governing equations and associated boundary conditions. Subroutines BC1 and BCNJ are used to set up boundary condition at electrode surface and the interface between the electron-transport layer and quantum-dots layer. Subroutine ETL is used to set up non-linear governing equations. Subroutines called MATINV and BAND were used to solve the non-linear differential equations.

Listing B.1. Input Files for the Parameters Used in the N-Type Semi-Conductor Model

```
9
3001
2.4E-4
300.0
96487
8.314
0.0
1.E-9
1.E-12
-5.E-9
1.E15
1.E-14
1.E-12
0
25  -1.0 E-  1.E-9
8.02  +1.0 H+  1.E-19
C      line 1 is the number of species
C      line 2 is NJ
C      line 3 is the layer thickness,cm(50nm)
C      line 4 is the temperstaure K
C      line 5 is the farady constant
C      line 6 is the universal gas constant J/mol K
C      line 7 is the Potenial at Ohmic contact
C      line 8 is the dopping level
C      line 9 is the permitivity farad/cm
C      line 10 is the charge density at the ETL C/cm2
C      line 11 is the recombination rate constant
C      line 12 is the intrinsic concentration mol/cm3
C      line 13 is the error allowed for the BIGs
C      line 14-15 is the diffusion coefficient cm^2/s,stoichiometric
    coefficient and concentration profile cm^-3
```

Listing B.2. FORTRAN Code to Calculate the Steady-State Profile for N-Type Semi-Conductor

```
C     Electron transport layer and QD emissive layer
C     2 species system
C     SPECIES 1 = electron, SPECIES 2 = holes
C     This is the steady state solution only
C     It should be ran prior to Quantum_dots_os.for
C     The input file is the same for both
C     Copy and paste the appropriate lines to create the execuitable
C     cd C:\Chen\FORTRAN2019\ETL_IM
C     gfortran -static QuantumF_ss_HOMO_IG.for -o QuantumF_ss_HOMO_IG.exe
      PROGRAM QDETL
      IMPLICIT DOUBLE PRECISION (A-H, O-Z)
      COMMON/BAB/ A(9,9),B(9,9),C(9,1000001),D(9,19),G(9),X(9,9),Y(9,9)
      COMMON/NSN/ N,NJ
      COMMON/VAR/ FLUX(2,1000001),CURRENT(1000001)
      COMMON/DVAR/ DCONC(2,1000001),DPOT(1000001),DRHO(1000001)
      COMMON/VARR/ H,EBIG,Y1,JCOUNT,LCT
      COMMON/CONSTANT/ F,DIFF(2),Z(2)
      COMMON/CONCENRATION/ DCBULK(2,1000001),R,DPBULK,DRHOBULK
      COMMON/DCOMCENTRATION/ CBULK(2),PBULK,RHOBULK
      COMMON/SURF/ CSURF,ATEM,DOP,ELE
      COMMON/REFERENCE/ REF(3)
      COMMON/CHARGE/ DQCHARGE,QCHARGE,CHARCOE
      COMMON/CONSTRAIN/ CONCU,CONCD
      COMMON/REACTION/ RXN(2,1000001)
      COMMON/REARATE/ RATEE,CONCIN
      COMMON/GUESS/ NCOUNTMAX

      CHARACTER REF*8

  102 FORMAT (/30H THE NEXT RUN DID NOT CONVERGE)
  103 FORMAT ('Error=',E16.6/(1X,'NE at J=1',E12.5,2X,'NE atJ=N',E12.5))
  104 FORMAT (1X,'Ce- at J=1',E12.5,2X,'Ce- at J=N',E12.5)
  105 FORMAT (1X,'DPOT at J=1',E12.5,2X,'DPOT at J=N',E12.5)
  106 FORMAT (1X,'DRHO at J=1',E12.5,2X,'DRHO at J=N',E12.5)
  107 FORMAT (1X,'Nh+ at J=1',E12.5,2X,'Nh+ at J=N',E12.5)
  108 FORMAT (1X,'Ch+ at J=1',E12.5,2X,'Ch+ at J=N',E12.5)
  109 FORMAT (1X,'Current at J=1',E12.5,2X,'Current at J=N',E12.5)
  333 FORMAT (4x,'E-',12x,'H+',12x,'RXN')
  300 FORMAT (20x,'G(1)'14x,'G(2)'14x,'G(3)'14x,'G(4)',14x,
     1         'G(5)',14x,'G(6)',14x,'G(7)',14x,'G(8)',14x,'G(9)')
  302 FORMAT ('Iteration='I4)
  334 FORMAT (9(E16.10,5X))
  301 FORMAT (5x,'J=' I5, 9E18.9)
  866 FORMAT (5x,'J=' I5, 6E18.9)
  886 FORMAT (20x,'B(1,1)'10x,'B(2.2)'10x,'B(3,1)'10x,'B(3,3)',14x,
     1         'B(3,5)',14x,'B(4,2)',14x,'B(4,4)',14x,'B(4,5)',14x
     2         'B(5,5)',10x,'B(5,6)',10x,'B(6,3)',10x,'B(6,4)',10x,
     3        'B(6,5)',14x,'B(6,6)')

      open(11,file='Current_in.txt',status='old')
      read(11,*) CSURF

      OPEN(13, FILE='cdh_out.txt')
      CLOSE(13, STATUS='DELETE')
      OPEN(13, FILE='cdh_out.txt')

      OPEN(12,FILE='cdh_G_out.txt')
```

```
58        CLOSE(12, STATUS='DELETE')
59        OPEN(12, FILE='cdh_G_out.txt')
60        WRITE(12,300)
61
62        OPEN(44,FILE='cdh_G_NOEBIG.txt')
63        CLOSE(44, STATUS='DELETE')
64        OPEN(44, FILE='cdh_G_NOEBIG.txt')
65        WRITE(44,300)
66
67        OPEN(88,FILE='B_VALUE.txt')
68        CLOSE(88, STATUS='DELETE')
69        OPEN(88, FILE='B_VALUE.txt')
70        WRITE(88,886)
71
72        open(14,file='QDLED_HOMO_in.txt',status='old')
73        read(14,*) N,NJ,Y1,ATEM,F,R,PBULK,DOP,ELE,QCHARGE
74        read(14,*) RATEE,CONCIN,EBIG,NCOUNTMAX
75        read(14,*) (DIFF(I),Z(I),REF(I),CBULK(I),I=1,(N-7))
76
77        PRINT *, 'dopping level=', DOP
78        PRINT *, 'surface charge=', QCHARGE
79        PRINT *, 'PERMITIVITY=', ELE
80        PRINT *, 'Intrinsic concentration=', CONCIN
81        PRINT *, 'RateE', RATEE
82        PRINT *, 'Temperature=', ATEM
83        PRINT *, 'Bulk concentration of electrons=', CBULK(1)
84        PRINT *, 'Bulk concentration of holes=', CBULK(2)
85
86        OPEN(16,FILE='cdh_values_out.txt')
87        CLOSE(16, STATUS='DELETE')
88        OPEN(16, FILE='cdh_values_out.txt')
89
90 C    337 FORMAT (I2/I5/E15.8/E15.8/E15.8/E15.8/E15.8/E15.8/E15.8/E15.8/
91 C       1          E15.8/E15.8/E15.8/E15.8/
92 C       2          E15.8/E15.8/E15.8/E15.8)
93 C         write (16,337) N,NJ,H,CSURF,ATEM,F,R,PBULK,DOP,ELE,QCHARGE,RATEE,
94 C       1                CONCIN,EBIG,DIFF(1),DIFF(2),CBULK(1),CBULK(2)
95
96
97
98 C        PRINT *, 'current=', CSURF
99 C     Constants
100
101       DPBULK=PBULK*F/R/ATEM
102       PRINT *, 'DPBULK=', DPBULK
103
104 C        DCBULK(1)=CBULK(1)*EXP(Z(1)*EXP(-8.8))
105 C        PRINT *, 'DCBULK(1)=', DCBULK(1)
106
107 C        DCBULK(2)=CBULK(2)*EXP(Z(2)*EXP(-8.8))
108 C        PRINT *, 'DCBULK(2)', DCBULK(2)
109
110 C        RHOBULK=F*(Z*DCBULK*EXP(-Z*DPBULK)+DOP)
111 C        PRINT *, 'RHOBULK=', RHOBULK
112
113 C        DRHOBULK=RHOBULK*F/R/ATEM
114 C        PRINT *, 'DRHOBULK=', DRHOBULK
115
```

```
116       PRINT *, 'Y1=', Y1
117       H=Y1/(NJ-1)
118       PRINT *, 'H=', H
119
120 C     Coefficient for the charge density
121       CHARCOE=F**2/(8.314*ATEM)
122       PRINT *, 'charge Coefficient', CHARCOE
123
124 C    SURFACE CHARGE
125       DQCHARGE=QCHARGE*F/(8.314*ATEM)
126       PRINT *, 'SURFACE CHARGE', DQCHARGE
127
128 C    Number of the Current Density points-NCOUNTMAX
129   337 FORMAT (I2/I7/E15.8/E15.8/E15.8/E15.8/E15.8/I7)
130       write (16,337) N,NJ,H,DOP,ELE,Z(1),Z(2),NCOUNTMAX
131
132       NCOUNT=0
133
134     5  NCOUNT=NCOUNT+1
135
136
137       PRINT *, 'NCOUNT', NCOUNT
138
139       IF (NCOUNT.GE.2) GO TO 10
140
141       LCT=0
142       DO 28 J=1,NJ
143       DO 28 I=1,N
144
145       C(I,J)=0.0
146       FLUX(1,J)=CSURF/(F*Z(1))
147       FLUX(2,J)=0.0
148       DPOT(J)=0.155*(1.0-EXP(-LCT*H))
149 C        DPOT(J)=1.0
150 C        DPOT(J)=32.0153700899657*(EXP(-LCT*H))
151 C        DPOT(J)=0.0
152       DRHO(J)=F*(CBULK(2)-CBULK(1)+DOP)*F/(ATEM*8.314)
153
154       DCBULK(1,J)=CBULK(1)*EXP(Z(1)*DPOT(J))
155       DCBULK(2,J)=CBULK(2)*EXP(Z(2)*DPOT(J))
156 C        DCBULK(1,J)=CBULK(1)
157 C        DCBULK(2,J)=CBULK(2)
158       DCONC(1,J)=DCBULK(1,J)
159       DCONC(2,J)=DCBULK(2,J)
160       LCT=LCT+1
161    28 CURRENT(J)=CSURF
162
163       DO 28 J=1,NJ
164       DO 28 I=1,N
165       C(I,J)=0.0
166       FLUX(1,J)=0.0
167       FLUX(2,J)=0.0
168       DPOT(J)=0.0
169       DRHO(J)=0.0
170       DCONC(1,J)=0.0
171       DCONC(2,J)=0.0
172    28 CURRENT(J)=0.0
173     Read steady state values from previous condition
```

```
174
175       2    READ(13,334) (FLUXIG(1,J),FLUXIG(2,J),DCONCIG(1,J),DCONCIG(2,J),
176      1                  DPOTIG(J),DRHOIG(J),CURRENTIG(J),RXNIG(1,J),
177      2                  RXNIG(2,J),J=1,NJ)
178         DO 3 J=1,NJ
179         DO 3 I=1,N
180         C(I,J)=0.0
181         FLUX(1,J)=FLUXIG(1,J)
182         FLUX(2,J)=FLUXIG(2,J)
183         DCONC(1,J)=DCONCIG(1,J)
184         DCONC(2,J)=DCONCIG(2,J)
185         DPOT(J)=DPOTIG(J)
186         DRHO(J)=DRHOIG(J)
187       3 CURRENT(J)=CURRENTIG(J)
188
189      10 JCOUNT=0
190         TOL=1.E-12
191 C         TOL=1.E-10*N*NJ/1.E6
192         PRINT *, 'TOL=', TOL
193      22 JCOUNT=JCOUNT+1
194         AMP=0.0
195         J=0
196         DO 23 I=1,N
197         DO 23 K=1,N
198         Y(I,K)=0.0
199      23 X(I,K)=0.0
200      24 J=J+1
201         DO 25 I=1,N
202         G(I)=0.0
203         DO 25 K=1,N
204         A(I,K)=0.0
205         B(I,K)=0.0
206      25 D(I,K)=0.0
207
208         IF (J.EQ.1) CALL BC1(J)
209         IF (J.GT.1 .AND. J.LT.NJ) CALL ETL(J)
210         IF (J.EQ.NJ) CALL BCNJ(J)
211         CALL BAND(J)
212
213         AMP=AMP+DABS(G(1))+DABS(G(2))+DABS(G(3))+DABS(G(4))
214        1          +DABS(G(5))+DABS(G(6))+DABS(G(7))+DABS(G(8))
215        2          +DABS(G(9))
216
217         IF (J.LT.NJ)  GO TO 24
218
219         PRINT *, 'ERROR=', AMP
220
221         CONCU=EXP(5.0)-1.0
222         CONCD=1.0-EXP(-5.0)
223         DO 16 K=1,NJ
224 C         IF (C(1,K).LT.-CONCD*FLUX(1,K)) C(1,K)=-CONCD*FLUX(1,K)
225 C         IF (C(1,K).GT. CONCU*FLUX(1,K)) C(1,K)= CONCU*FLUX(1,K)
226         FLUX(1,K)=FLUX(1,K)+C(1,K)
227         FLUX(2,K)=FLUX(2,K)+C(2,K)
228         IF (C(3,K).LT.-CONCD*DCONC(1,K)) C(3,K)=-CONCD*DCONC(1,K)
229         IF (C(3,K).GT. CONCU*DCONC(1,K)) C(3,K)= CONCU*DCONC(1,K)
230         DCONC(1,K)=DCONC(1,K)+C(3,K)
231
```

```
232         IF (C(4,K).LT.-CONCD*DCONC(2,K)) C(4,K)=-CONCD*DCONC(2,K)
233         IF (C(4,K).GT. CONCU*DCONC(2,K)) C(4,K)= CONCU*DCONC(2,K)
234         DCONC(2,K)=DCONC(2,K)+C(4,K)
235         IF (C(5,K).LT.-40.) C(5,K)= -40.
236         IF (C(5,K).GT. 40.) C(5,K)= 40.
237         DPOT(K)=DPOT(K)+C(5,K)
238         DRHO(K)=DRHO(K)+C(6,K)
239         CURRENT(K)=CURRENT(K)+C(7,K)
240         RXN(1,K)=RXN(1,K)+C(8,K)
241         RXN(2,K)=RXN(2,K)+C(9,K)
242      16  CONTINUE
243
244         WRITE(12,302) (JCOUNT)
245
246 C     If the error is less then the tolerance, finish program
247         IF (DABS(AMP).LT.DABS(TOL)) GO TO  15
248
249 C       If the error is greater then tolerance, do another iteration
250      33  IF (JCOUNT.LE.19) GO TO 22
251         PRINT 102
252
253     15  PRINT 103, AMP,FLUX(1,1),FLUX(1,NJ)
254     37  PRINT 107, FLUX(2,1),FLUX(2,NJ)
255     27  PRINT 104, DCONC(1,1),DCONC(1,NJ)
256     38  PRINT 108, DCONC(2,1),DCONC(2,NJ)
257     30  PRINT 105, DPOT(1),DPOT(NJ)
258     36  PRINT 106, DRHO(1),DRHO(NJ)
259     39  PRINT 109, CURRENT(1),CURRENT(NJ)
260         PRINT *,'JCOUNT=',JCOUNT
261
262         DO 21 J=1,NJ
263         BIG=FLUX(1,J)
264         BIG2=1.0E-20
265      21 IF (ABS(BIG).LE.BIG2) FLUX(1,J)=0.0
266
267       DO 40 J=1,NJ
268         BIG=FLUX(2,J)
269         BIG2=1.0E-20
270      40 IF (ABS(BIG).LE.BIG2) FLUX(2,J)=0.0
271
272         DO 19 J=1,NJ
273         BIG=DCONC(1,J)
274         BIG2=1.0E-9
275      19 IF (ABS(BIG).LE.BIG2) DCONC(1,J)=0.0
276
277         DO 41 J=1,NJ
278         BIG=DCONC(2,J)
279         BIG2=1.0E-20
280      41 IF (ABS(BIG).LE.BIG2) DCONC(2,J)=0.0
281
282         DO 26 J=1,NJ
283         BIG=DPOT(J)
284         BIG2=1.0E-20
285      26 IF (ABS(BIG).LE.BIG2) DPOT(J)=0.0
286
287         DO 35 J=1,NJ
288         BIG=DRHO(J)
289         BIG2=1.0E-20
```

```
290     35  IF (ABS(BIG).LE.BIG2) DRHO(J)=0.0
291
292         DO 42 J=1,NJ
293         BIG=CURRENT(J)
294         BIG2=1.0E-20
295     42  IF (ABS(BIG).LE.BIG2) CURRENT(J)=0.0
296
297         DO 43 J=1,NJ
298         DO 43 I=1,2
299         BIG=RXN(I,J)
300         BIG2=1.0E-20
301     43  IF (ABS(BIG).LE.BIG2) RXN(I,J)=0.0
302
303         WRITE(13,334) (FLUX(1,J),FLUX(2,J),DCONC(1,J),DCONC(2,J),
304        1                DPOT(J),DRHO(J),CURRENT(J),RXN(1,J),RXN(2,J),
305        2                  J=1,NJ)
306 C         CLOSE(13, STATUS='delete')
307         CSURF=CSURF+2.0
308         IF (NCOUNT.GT.NCOUNTMAX) GO TO 6
309
310     4   IF (NCOUNT.LE.NCOUNTMAX) GO TO 5
311
312     6    END PROGRAM QDETL
313
314
315
316 c       SUBROUTINE BC1(J)
317         SUBROUTINE BC1(J)
318         IMPLICIT DOUBLE PRECISION (A-H, O-Z)
319         COMMON/BAB/ A(9,9),B(9,9),C(9,1000001),D(9,19),G(9),X(9,9),Y(9,9)
320         COMMON/NSN/ N,NJ
321         COMMON/VAR/ FLUX(2,1000001),CURRENT(1000001)
322         COMMON/DVAR/ DCONC(2,1000001),DPOT(1000001),DRHO(1000001)
323         COMMON/VARR/ H,EBIG,Y1,JCOUNT,LCT
324         COMMON/CONSTANT/ F,DIFF(2),Z(2)
325         COMMON/CONCENRATION/ DCBULK(2,1000001),R,DPBULK,DRHOBULK
326         COMMON/DCOMCENTRATION/ CBULK(2),PBULK,RHOBULK
327         COMMON/SURF/ CSURF,ATEM,DOP,ELE
328         COMMON/REFERENCE/ REF(3)
329         COMMON/CHARGE/ DQCHARGE,QCHARGE,CHARCOE
330         COMMON/CONSTRAIN/ CONCU,CONCD
331         COMMON/REACTION/ RXN(2,1000001)
332         COMMON/REARATE/ RATEE,CONCIN
333    301  FORMAT (5x,'J=' I5, 9E18.9)
334
335 C     FOR ELECTRON-MEB
336
337
338         G(1)=FLUX(1,J)-CSURF/(F*Z(1))
339         B(1,1)=-1.0
340         BIG=ABS(FLUX(1,J))
341         BIG2=ABS(CSURF/(F*Z(1)))
342         IF (BIG2.GT.BIG) BIG=BIG2
343         IF (ABS(G(1)).LT.BIG*EBIG) G(1)=0
344
345 C C       FOR HOLE-MEB
346         G(2)=FLUX(2,J)
347         B(2,2)=-1.0
```

```
348         BIG=ABS(FLUX(2,J))
349         IF (ABS(G(2)).LT.BIG*EBIG) G(2)=0
350
351 c     FOR ELECTRON-FLUX
352
353         G(3)=DCONC(1,J)-DCBULK(1,J)
354         B(3,3)=-1.0
355
356         BIG=ABS(DCONC(1,J))
357         BIG2=ABS(DCBULK(1,J))
358         IF (BIG2.GT.BIG) BIG=BIG2
359         IF (ABS(G(3)).LT.BIG*EBIG) G(3)=0
360
361 C       FOR HOLE-FLUX
362
363         G(4)=DCONC(2,J)-DCBULK(2,J)
364         B(4,4)=-1.0
365
366         BIG=ABS(DCONC(2,J))
367         BIG2=ABS(DCBULK(2,J))
368         IF (BIG2.GT.BIG) BIG=BIG2
369         IF (ABS(G(4)).LT.BIG*EBIG) G(4)=0
370
371
372 C     FOR POISSON'S EQUATION
373
374         G(5)=DPOT(J)
375         B(5,5)=-1.0
376         BIG=ABS(DPOT(J))
377         IF (ABS(G(5)).LT.BIG*EBIG) G(5)=0
378
379 C       FOR CHARGE DENSITY
380
381         G(6)=CHARCOE*(Z(1)*DCONC(1,J)*EXP(-Z(1)*DPOT(J))
382        1            +Z(2)*DCONC(2,J)*EXP(-Z(2)*DPOT(J))+DOP)
383        2            -DRHO(J)
384         B(6,3)=-CHARCOE*Z(1)*EXP(-Z(1)*DPOT(J))
385         B(6,4)=-CHARCOE*Z(2)*EXP(-Z(2)*DPOT(J))
386         B(6,5)=(Z(1)**2)*CHARCOE*DCONC(1,J)*EXP(-Z(1)*DPOT(J))
387        1            +(Z(2)**2)*CHARCOE*DCONC(2,J)*EXP(-Z(2)*DPOT(J))
388         B(6,6)=+1.0
389         BIG=ABS(CHARCOE*Z(1)*DCONC(1,J)*EXP(-Z(1)*DPOT(J)))
390         BIG2=ABS(CHARCOE*Z(2)*DCONC(2,J)*EXP(-Z(2)*DPOT(J)))
391         IF (BIG2.GT.BIG) BIG=BIG2
392         BIG3=ABS(DRHO(J))
393         IF (BIG3.GT.BIG) BIG=BIG3
394         BIG4=ABS(CHARCOE*DOP)
395         IF (BIG4.GT.BIG) BIG=BIG4
396         IF (ABS(G(6)).LT.BIG*EBIG) G(6)=0
397 C       For current density
398         G(7)=F*(Z(1)*FLUX(1,J)+Z(2)*FLUX(2,J))-CURRENT(J)
399         B(7,1)=-F*Z(1)
400         B(7,2)=-F*Z(2)
401         B(7,7)=+1.0
402         BIG=ABS(F*Z(1)*FLUX(1,J))
403         BIG2=ABS(F*Z(2)*FLUX(2,J))
404         IF (BIG2.GT.BIG) BIG=BIG2
405         BIG3=ABS(CURRENT(J))
```

```
406         IF (BIG3.GT.BIG) BIG=BIG3
407         IF (ABS(G(7)).LT.BIG*EBIG) G(7)=0
408 C       For homogeneous reaction of electrons
409         G(8)=-RATEE*(DCONC(1,J)*DCONC(2,J)-CONCIN**2)-RXN(1,J)
410         B(8,3)=RATEE*DCONC(2,J)
411         B(8,4)=RATEE*DCONC(1,J)
412         B(8,8)=1.0
413         BIG=ABS(RATEE*DCONC(1,J)*DCONC(2,J))
414         BIG2=ABS(RATEE*CONCIN**2)
415         IF (BIG2.GT.BIG) BIG=BIG2
416         BIG3=ABS(RXN(1,J))
417         IF (BIG3.GT.BIG) BIG=BIG3
418         IF (ABS(G(8)).LT.BIG*EBIG) G(8)=0
419 C       For homogeneous reaction of holes
420         G(9)=-RATEE*(DCONC(1,J)*DCONC(2,J)-CONCIN**2)-RXN(2,J)
421         B(9,3)=RATEE*DCONC(2,J)
422         B(9,4)=RATEE*DCONC(1,J)
423         B(9,9)=1.0
424         BIG=ABS(-RATEE*DCONC(1,J)*DCONC(2,J))
425         BIG2=ABS(RATEE*CONCIN**2)
426         IF (BIG2.GT.BIG) BIG=BIG2
427         BIG3=ABS(RXN(2,J))
428         IF (BIG3.GT.BIG) BIG=BIG3
429         IF (ABS(G(9)).LT.BIG*EBIG) G(9)=0
430         CONTINUE
431
432   212   WRITE(12,301) J, (G(K),K=1,N)
433
434         RETURN
435         END
436 c       SUBROUTINE ETL(J)
437         SUBROUTINE ETL(J)
438         IMPLICIT DOUBLE PRECISION (A-H, O-Z)
439         COMMON/BAB/ A(9,9),B(9,9),C(9,1000001),D(9,19),G(9),X(9,9),Y(9,9)
440         COMMON/NSN/ N,NJ
441         COMMON/VAR/ FLUX(2,1000001),CURRENT(1000001)
442         COMMON/DVAR/ DCONC(2,1000001),DPOT(1000001),DRHO(1000001)
443         COMMON/VARR/ H,EBIG,Y1,JCOUNT,LCT
444         COMMON/CONSTANT/ F,DIFF(2),Z(2)
445         COMMON/CONCENRATION/ DCBULK(2,1000001),R,DPBULK,DRHOBULK
446         COMMON/DCOMCENTRATION/ CBULK(2),PBULK,RHOBULK
447         COMMON/SURF/ CSURF,ATEM,DOP,ELE
448         COMMON/REFERENCE/ REF(3)
449         COMMON/CHARGE/ DQCHARGE,QCHARGE,CHARCOE
450         COMMON/CONSTRAIN/ CONCU,CONCD
451         COMMON/REACTION/ RXN(2,1000001)
452         COMMON/REARATE/ RATEE,CONCIN
453
454   301   FORMAT (5x,'J=' I5,  9E18.9)
455   866   FORMAT (5x,'J=' I5, 36E18.9)
456 C C       FOR ELECTRON-MEB
457         G(1)=(FLUX(1,J)-FLUX(1,J-1))/H-RXN(1,J-1)
458         A(1,1)=+1./H
459         B(1,1)=-1./H
460         A(1,8)=+1.0
461         BIG=ABS(FLUX(1,J)/(H))
462         BIG2=ABS(-FLUX(1,J-1)/(H))
463         IF (BIG2.GT.BIG) BIG=BIG2
```

```
464         BIG3=ABS(RXN(1,J-1))
465         IF (BIG3.GT.BIG) BIG=BIG3
466         IF (ABS(G(1)).LT.BIG*EBIG) G(1)=0
467
468
469 C       FOR HOLES-MEB
470
471         G(2)=(FLUX(2,J)-FLUX(2,J-1))/H-RXN(2,J-1)
472         A(2,2)=+1./H
473         B(2,2)=-1./H
474         A(2,9)=+1.0
475         BIG=ABS(FLUX(2,J)/H)
476         BIG2=ABS(-FLUX(2,J-1)/H)
477         IF (BIG2.GT.BIG) BIG=BIG2
478         BIG3=ABS(RXN(2,J-1))
479         IF (BIG3.GT.BIG) BIG=BIG3
480         IF (ABS(G(2)).LT.BIG*EBIG) G(2)=0
481
482 C       FOR ELECTRON-FLUX
483
484         G(3)=DIFF(1)*(DCONC(1,J)
485        1        -DCONC(1,J-1))/H*EXP(-0.5*Z(1)*(DPOT(J)+DPOT(J-1)))
486        2        +FLUX(1,J)
487         A(3,3)=+DIFF(1)/H*EXP(-0.5*Z(1)*(DPOT(J)+DPOT(J-1)))
488         B(3,3)=-DIFF(1)/H*EXP(-0.5*Z(1)*(DPOT(J)+DPOT(J-1)))
489         A(3,5)=+0.5*Z(1)*DIFF(1)*(DCONC(1,J)
490        1          -DCONC(1,J-1))/H*EXP(-0.5*Z(1)*(DPOT(J)+DPOT(J-1)))
491         B(3,5)=+0.5*Z(1)*DIFF(1)*(DCONC(1,J)
492        1          -DCONC(1,J-1))/H*EXP(-0.5*Z(1)*(DPOT(J)+DPOT(J-1)))
493         B(3,1)=-1.0
494
495         BIG=ABS(DIFF(1)*DCONC(1,J-1)/H*EXP(-0.5*Z(1)*(DPOT(J)+DPOT(J-1))))
496         BIG2=ABS(DIFF(1)*DCONC(1,J)/H*EXP(-0.5*Z(1)*(DPOT(J)+DPOT(J-1))))
497         IF (BIG2.GT.BIG) BIG=BIG2
498         BIG3=ABS(FLUX(1,J))
499         IF (BIG3.GT.BIG) BIG=BIG3
500         IF (ABS(G(3)).LT.BIG*EBIG) G(3)=0
501 C       FOR HOLES-FLUX
502         G(4)=DIFF(2)*(DCONC(2,J)
503        1        -DCONC(2,J-1))/H*EXP(-0.5*Z(2)*(DPOT(J)+DPOT(J-1)))
504        2        +FLUX(2,J)
505         A(4,4)=+DIFF(2)/H*EXP(-0.5*Z(2)*(DPOT(J)+DPOT(J-1)))
506         B(4,4)=-DIFF(2)/H*EXP(-0.5*Z(2)*(DPOT(J)+DPOT(J-1)))
507         A(4,5)=+0.5*Z(2)*DIFF(2)*(DCONC(2,J)
508        1          -DCONC(2,J-1))/H*EXP(-0.5*Z(2)*(DPOT(J)+DPOT(J-1)))
509         B(4,5)=+0.5*Z(2)*DIFF(2)*(DCONC(2,J)
510        1          -DCONC(2,J-1))/H*EXP(-0.5*Z(2)*(DPOT(J)+DPOT(J-1)))
511         B(4,2)=-1.0
512
513         BIG=ABS(DIFF(2)*DCONC(2,J-1)/H*EXP(-0.5*Z(2)*(DPOT(J)+DPOT(J-1))))
514         BIG2=ABS(DIFF(2)*DCONC(2,J)/H*EXP(-0.5*Z(2)*(DPOT(J)+DPOT(J-1))))
515         IF (BIG2.GT.BIG) BIG=BIG2
516         BIG3=ABS(FLUX(2,J))
517         IF (BIG3.GT.BIG) BIG=BIG3
518         IF (ABS(G(4)).LT.BIG*EBIG) G(4)=0
519
520 C       FOR POISSON'S Equation
521         G(5)=(DPOT(J+1)-2.*DPOT(J)+DPOT(J-1))/H**2+DRHO(J)/ELE
```

```
522         A(5,5)=-1./H**2
523         B(5,5)=+2./H**2
524         D(5,5)=-1./H**2
525         B(5,6)=-1./ELE
526         BIG=ABS(DPOT(J+1)/H**2)
527         BIG2=ABS(2.*DPOT(J)/H**2)
528         IF (BIG2.GT.BIG) BIG=BIG2
529         BIG3=ABS(DPOT(J-1)/H**2)
530         IF (BIG3.GT.BIG) BIG=BIG3
531         BIG4=ABS(DRHO(J)/ELE)
532         IF (BIG4.GT.BIG) BIG=BIG4
533         IF (ABS(G(5)).LT.BIG*EBIG) G(5)=0
534
535 C       FOR CHARGE DENSITY
536
537         G(6)=CHARCOE*(Z(1)*DCONC(1,J)*EXP(-Z(1)*DPOT(J))
538        1            +Z(2)*DCONC(2,J)*EXP(-Z(2)*DPOT(J))+DOP)
539        2            -DRHO(J)
540         B(6,3)=-CHARCOE*Z(1)*EXP(-Z(1)*DPOT(J))
541         B(6,4)=-CHARCOE*Z(2)*EXP(-Z(2)*DPOT(J))
542         B(6,5)=(Z(1)**2)*CHARCOE*DCONC(1,J)*EXP(-Z(1)*DPOT(J))
543        1            +(Z(2)**2)*CHARCOE*DCONC(2,J)*EXP(-Z(2)*DPOT(J))
544         B(6,6)=+1.0
545         BIG=ABS(CHARCOE*Z(1)*DCONC(1,J)*EXP(-Z(1)*DPOT(J)))
546         BIG2=ABS(CHARCOE*Z(2)*DCONC(2,J)*EXP(-Z(2)*DPOT(J)))
547         IF (BIG2.GT.BIG) BIG=BIG2
548         BIG3=ABS(DRHO(J))
549         IF (BIG3.GT.BIG) BIG=BIG3
550         BIG4=ABS(CHARCOE*DOP)
551         IF (BIG4.GT.BIG) BIG=BIG4
552         IF (ABS(G(6)).LT.BIG*EBIG) G(6)=0
553 C       For current density
554         G(7)=F*(Z(1)*FLUX(1,J)+Z(2)*FLUX(2,J))-CURRENT(J)
555         B(7,1)=-F*Z(1)
556         B(7,2)=-F*Z(2)
557         B(7,7)=+1.0
558         BIG=ABS(F*Z(1)*FLUX(1,J))
559         BIG2=ABS(F*Z(2)*FLUX(2,J))
560         IF (BIG2.GT.BIG) BIG=BIG2
561         BIG3=ABS(CURRENT(J))
562         IF (BIG3.GT.BIG) BIG=BIG3
563         IF (ABS(G(7)).LT.BIG*EBIG) G(7)=0
564 C       For homogeneous reaction of electrons
565         G(8)=-RATEE*(DCONC(1,J)*DCONC(2,J)-CONCIN**2)-RXN(1,J)
566         B(8,3)=RATEE*DCONC(2,J)
567         B(8,4)=RATEE*DCONC(1,J)
568         B(8,8)=1.0
569         BIG=ABS(RATEE*DCONC(1,J)*DCONC(2,J))
570         BIG2=ABS(RATEE*CONCIN**2)
571         IF (BIG2.GT.BIG) BIG=BIG2
572         BIG3=ABS(RXN(1,J))
573         IF (BIG3.GT.BIG) BIG=BIG3
574         IF (ABS(G(8)).LT.BIG*EBIG) G(8)=0
575 C       For homogeneous reaction of holes
576         G(9)=-RATEE*(DCONC(1,J)*DCONC(2,J)-CONCIN**2)-RXN(2,J)
577         B(9,3)=RATEE*DCONC(2,J)
578         B(9,4)=RATEE*DCONC(1,J)
579         B(9,9)=1.0
```

```
580         BIG=ABS(-RATEE*DCONC(1,J)*DCONC(2,J))
581         BIG2=ABS(RATEE*CONCIN**2)
582         IF (BIG2.GT.BIG) BIG=BIG2
583         BIG3=ABS(RXN(2,J))
584         IF (BIG3.GT.BIG) BIG=BIG3
585         IF (ABS(G(9)).LT.BIG*EBIG) G(9)=0
586 
587         CONTINUE
588 C     SAVE G OUT DATA
589   212 DO 11 I=2,NJ-1
590    11 If (I.EQ.J) WRITE(12,301) J, (G(K),K=1,N)
591 
592   888 if (J.EQ.2) WRITE(88,866) J,(B(1,1)),(B(2,2)),(B(3,1)),(B(3,3)),
593      1             (B(3,5)),(B(4,2)),(B(4,4)),(B(4,5)),(B(5,5)),(B(5,6)),
594      2             (B(6,3)),(B(6,4)),(B(6,5)),(B(6,6))
595         RETURN
596         END
597 c       SUBROUTINE BCNJ(J)
598         SUBROUTINE BCNJ(J)
599         IMPLICIT DOUBLE PRECISION (A-H, O-Z)
600         COMMON/BAB/ A(9,9),B(9,9),C(9,1000001),D(9,19),G(9),X(9,9),Y(9,9)
601         COMMON/NSN/ N,NJ
602         COMMON/VAR/ FLUX(2,1000001),CURRENT(1000001)
603         COMMON/DVAR/ DCONC(2,1000001),DPOT(1000001),DRHO(1000001)
604         COMMON/VARR/ H,EBIG,Y1,JCOUNT,LCT
605         COMMON/CONSTANT/ F,DIFF(2),Z(2)
606         COMMON/CONCENRATION/ DCBULK(2,1000001),R,DPBULK,DRHOBULK
607         COMMON/DCOMCENTRATION/ CBULK(2),PBULK,RHOBULK
608         COMMON/SURF/ CSURF,ATEM,DOP,ELE
609         COMMON/REFERENCE/ REF(3)
610         COMMON/CHARGE/ DQCHARGE,QCHARGE,CHARCOE
611         COMMON/CONSTRAIN/ CONCU,CONCD
612         COMMON/REACTION/ RXN(2,1000001)
613         COMMON/REARATE/ RATEE,CONCIN
614 
615 
616   301 FORMAT (5x,'J=' I5,  9E18.9)
617   866 FORMAT (5x,'J=' I5, 36E18.9)
618 C C       FOR ELECTRON-MEB
619 
620         G(1)=(FLUX(1,J)-FLUX(1,J-1))/H-RXN(1,J-1)
621         A(1,1)=+1./H
622         B(1,1)=-1./H
623         A(1,8)=+1.0
624         BIG=ABS(FLUX(1,J)/(H))
625         BIG2=ABS(-FLUX(1,J-1)/(H))
626         IF (BIG2.GT.BIG) BIG=BIG2
627         BIG3=ABS(RXN(1,J-1))
628         IF (BIG3.GT.BIG) BIG=BIG3
629         IF (ABS(G(1)).LT.BIG*EBIG) G(1)=0
630 
631 
632 
633 C C       FOR HOLE-MEB
634 
635         G(2)=(FLUX(2,J)-FLUX(2,J-1))/H-RXN(2,J-1)
636         A(2,2)=+1./H
637         B(2,2)=-1./H
```

```
      A(2,9)=+1.0
      BIG=ABS(FLUX(2,J)/H)
      BIG2=ABS(FLUX(2,J-1)/H)
      IF (BIG2.GT.BIG) BIG=BIG2
      BIG3=ABS(RXN(2,J-1))
      IF (BIG3.GT.BIG) BIG=BIG3
      IF (ABS(G(2)).LT.BIG*EBIG) G(2)=0

C     FOR ELECTON-FLUX
      G(3)=DIFF(1)*(DCONC(1,J)
     1     -DCONC(1,J-1))/H*EXP(-0.5*Z(1)*(DPOT(J)+DPOT(J-1)))
     2     +FLUX(1,J)
      A(3,3)=+DIFF(1)/H*EXP(-0.5*Z(1)*(DPOT(J)+DPOT(J-1)))
      B(3,3)=-DIFF(1)/H*EXP(-0.5*Z(1)*(DPOT(J)+DPOT(J-1)))
      A(3,5)=+0.5*Z(1)*DIFF(1)*(DCONC(1,J)
     1       -DCONC(1,J-1))/H*EXP(-0.5*Z(1)*(DPOT(J)+DPOT(J-1)))
      B(3,5)=+0.5*Z(1)*DIFF(1)*(DCONC(1,J)
     1       -DCONC(1,J-1))/H*EXP(-0.5*Z(1)*(DPOT(J)+DPOT(J-1)))
      B(3,1)=-1.0

      BIG=ABS(DIFF(1)*DCONC(1,J-1)/H*EXP(-0.5*Z(1)*(DPOT(J)+DPOT(J-1))))
      BIG2=ABS(DIFF(1)*DCONC(1,J)/H*EXP(-0.5*Z(1)*(DPOT(J)+DPOT(J-1))))
      IF (BIG2.GT.BIG) BIG=BIG2
      BIG3=ABS(FLUX(1,J))
      IF (BIG3.GT.BIG) BIG=BIG3
      IF (ABS(G(3)).LT.BIG*EBIG) G(3)=0

C     FOR HOLE-FLUX
      G(4)=DIFF(2)*(DCONC(2,J)
     1     -DCONC(2,J-1))/H*EXP(-0.5*Z(2)*(DPOT(J)+DPOT(J-1)))
     2     +FLUX(2,J)
      A(4,4)=+DIFF(2)/H*EXP(-0.5*Z(2)*(DPOT(J)+DPOT(J-1)))
      B(4,4)=-DIFF(2)/H*EXP(-0.5*Z(2)*(DPOT(J)+DPOT(J-1)))
      A(4,5)=+0.5*Z(2)*DIFF(2)*(DCONC(2,J)
     1       -DCONC(2,J-1))/H*EXP(-0.5*Z(2)*(DPOT(J)+DPOT(J-1)))
      B(4,5)=+0.5*Z(2)*DIFF(2)*(DCONC(2,J)
     1       -DCONC(2,J-1))/H*EXP(-0.5*Z(2)*(DPOT(J)+DPOT(J-1)))
      B(4,2)=-1.0

      BIG=ABS(DIFF(2)*DCONC(2,J-1)/H*EXP(-0.5*Z(2)*(DPOT(J)+DPOT(J-1))))
      BIG2=ABS(DIFF(2)*DCONC(2,J)/H*EXP(-0.5*Z(2)*(DPOT(J)+DPOT(J-1))))
      IF (BIG2.GT.BIG) BIG=BIG2
      BIG3=ABS(FLUX(2,J))
      IF (BIG3.GT.BIG) BIG=BIG3
      IF (ABS(G(4)).LT.BIG*EBIG) G(4)=0


C     FOR POSSON'S EQUATION

      G(5)=2.*DQCHARGE/(ELE*H)-2.*(DPOT(J)-DPOT(J-1))/H**2
     1     +(3.*DRHO(J)+DRHO(J-1))/(4.*ELE)
      B(5,5)=+2./H**2
      A(5,5)=-2./H**2
      A(5,6)=-0.25/ELE
      B(5,6)=-0.75/ELE
      BIG=ABS(2.*DPOT(J-1)/H**2)
      BIG2=ABS(2.*DPOT(J)/H**2)
      IF (BIG2.GT.BIG) BIG=BIG2
```

```
696         BIG3=ABS(3.*DRHO(J)/(4.*ELE))
697         IF (BIG3.GT.BIG) BIG=BIG3
698         BIG4=ABS(DRHO(J-1)/(4.*ELE))
699         IF (BIG4.GT.BIG) BIG=BIG4
700         BIG5=ABS(2.*DQCHARGE/(ELE*H))
701         IF (BIG5.GT.BIG) BIG=BIG5
702         IF (ABS(G(5)).LT.BIG*EBIG) G(5)=0
703
704 C       FOR CHARGE DENSITY
705         G(6)=CHARCOE*(Z(1)*DCONC(1,J)*EXP(-Z(1)*DPOT(J))
706        1            +Z(2)*DCONC(2,J)*EXP(-Z(2)*DPOT(J))+DOP)
707        2            -DRHO(J)
708         B(6,3)=-CHARCOE*Z(1)*EXP(-Z(1)*DPOT(J))
709         B(6,4)=-CHARCOE*Z(2)*EXP(-Z(2)*DPOT(J))
710         B(6,5)=(Z(1)**2)*CHARCOE*DCONC(1,J)*EXP(-Z(1)*DPOT(J))
711        1            +(Z(2)**2)*CHARCOE*DCONC(2,J)*EXP(-Z(2)*DPOT(J))
712         B(6,6)=+1.0
713         BIG=ABS(CHARCOE*Z(1)*DCONC(1,J)*EXP(-Z(1)*DPOT(J)))
714         BIG2=ABS(CHARCOE*Z(2)*DCONC(2,J)*EXP(-Z(2)*DPOT(J)))
715         IF (BIG2.GT.BIG) BIG=BIG2
716         BIG3=ABS(DRHO(J))
717         IF (BIG3.GT.BIG) BIG=BIG3
718         BIG4=ABS(CHARCOE*DOP)
719         IF (BIG4.GT.BIG) BIG=BIG4
720         IF (ABS(G(6)).LT.BIG*EBIG) G(6)=0
721
722 C       For Current density
723         G(7)=F*(Z(1)*FLUX(1,J)+Z(2)*FLUX(2,J))-CURRENT(J)
724         B(7,1)=-F*Z(1)
725         B(7,2)=-F*Z(2)
726         B(7,7)=+1.0
727         BIG=ABS(F*Z(1)*FLUX(1,J))
728         BIG2=ABS(F*Z(2)*FLUX(2,J))
729         IF (BIG2.GT.BIG) BIG=BIG2
730         BIG3=ABS(CURRENT(J))
731         IF (BIG3.GT.BIG) BIG=BIG3
732         IF (ABS(G(7)).LT.BIG*EBIG) G(7)=0
733 C       For homogeneous reaction of electrons
734         G(8)=-RATEE*(DCONC(1,J)*DCONC(2,J)-CONCIN**2)-RXN(1,J)
735         B(8,3)=RATEE*DCONC(2,J)
736         B(8,4)=RATEE*DCONC(1,J)
737         B(8,8)=1.0
738         BIG=ABS(RATEE*DCONC(1,J)*DCONC(2,J))
739         BIG2=ABS(RATEE*CONCIN**2)
740         IF (BIG2.GT.BIG) BIG=BIG2
741         BIG3=ABS(RXN(1,J))
742         IF (BIG3.GT.BIG) BIG=BIG3
743         IF (ABS(G(8)).LT.BIG*EBIG) G(8)=0
744 C       For homogeneous reaction of holes
745         G(9)=-RATEE*(DCONC(1,J)*DCONC(2,J)-CONCIN**2)-RXN(2,J)
746         B(9,3)=RATEE*DCONC(2,J)
747         B(9,4)=RATEE*DCONC(1,J)
748         B(9,9)=1.0
749         BIG=ABS(-RATEE*DCONC(1,J)*DCONC(2,J))
750         BIG2=ABS(RATEE*CONCIN**2)
751         IF (BIG2.GT.BIG) BIG=BIG2
752         BIG3=ABS(RXN(2,J))
753         IF (BIG3.GT.BIG) BIG=BIG3
```

```
      IF (ABS(G(9)).LT.BIG*EBIG) G(9)=0
      CONTINUE

  206 WRITE(12,301) J, (G(K),K=1,N)
C       WRITE(44,301) 1, (G(K),K=1,N)
      WRITE(44,301) 5001, (G(K),K=1,N)
C   209 IF (J.EQ.1) THEN
C       WRITE(44,301) J, (G(K),K=1,N)
C       END IF

  888 WRITE(88,866) J, (B(1,1)),(B(2,2)),(B(3,1)),(B(3,3)),(B(3,5)),
     1 (B(4,2)),(B(4,4)),(B(4,5)),(B(5,5)),(B(5,6)),(B(6,3)),(B(6,4)),
     2 (B(6,5)),(B(6,6))

      PRINT *, 'ITERATION=', JCOUNT
      RETURN
      END

C     SUBROUTINE MATINV
      SUBROUTINE MATINV(N,M,DETERM)
      IMPLICIT DOUBLE PRECISION (A-H,O-Z)
      COMMON/BAB/ A(9,9),B(9,9),C(9,1000001),D(9,19),G(9),X(9,9),Y(9,9)
      COMMON/NSN/ NTEMP, NJ
      DIMENSION ID(9)
      DETERM=1.01
      DO 1 I=1,N
    1 ID(I)=0
      DO 18 NN=1,N
      BMAX=1.1
      DO 6 I=1,N
      IF(ID(I).NE.0) GO TO 6
      BNEXT=0.0
      BTRY=0.0
      DO 5 J=1,N
      IF (ID(J).NE.0) GO TO 5
      IF (DABS(B(I,J)).LE.BNEXT) GO TO 5
      BNEXT=DABS(B(I,J))
      IF (BNEXT.LE.BTRY) GO TO 5
      BNEXT=BTRY
      BTRY=DABS(B(I,J))
      JC=J
    5 CONTINUE
      IF(BNEXT.GE.BMAX*BTRY) GO TO 6
      BMAX=BNEXT/BTRY
      IROW=I
      JCOL=JC
    6 CONTINUE
      IF (ID(JC).EQ.0) GO TO 8
      DETERM=0.0
      RETURN
    8 ID(JCOL)=1
      IF (JCOL.EQ.IROW) GO TO 12
      DO 10 J=1,N
      SAVE=B(IROW,J)
      B(IROW,J)=B(JCOL,J)
   10 B(JCOL,J)=SAVE
      DO 11 K=1,M
      SAVE=D(IROW,K)
```

```
812         D(IROW,K)=D(JCOL,K)
813    11   D(JCOL,K)=SAVE
814    12   F=1.0/B(JCOL,JCOL)
815         DO 13 J=1,N
816    13   B(JCOL,J)=B(JCOL,J)*F
817         DO 14 K=1,M
818    14   D(JCOL,K)=D(JCOL,K)*F
819         DO 18 I=1,N
820         IF (I.EQ.JCOL) GO TO 18
821         F=B(I,JCOL)
822         DO 16 J=1,N
823    16   B(I,J)=B(I,J)-F*B(JCOL,J)
824         DO 17 K=1,M
825    17   D(I,K)=D(I,K)-F*D(JCOL,K)
826    18   CONTINUE
827         RETURN
828         END
829
830 C       SUBROUTINE BAND(J)
831         SUBROUTINE BAND(J)
832         IMPLICIT DOUBLE PRECISION (A-H,O-Z)
833         DIMENSION E(9,10,1000001)
834         COMMON/BAB/ A(9,9),B(9,9),C(9,1000001),D(9,19),G(9),X(9,9),Y(9,9)
835         COMMON/NSN/ N,NJ
836         SAVE E, NP1
837   101   FORMAT(15H DETERM=0 AT J=,I4)
838         IF (J-2) 1,6,8
839     1   NP1=N+1
840         DO 2 I=1,N
841         D(I,2*N+1)=G(I)
842         DO 2 L=1,N
843         LPN=L+N
844     2   D(I,LPN)=X(I,L)
845         CALL MATINV(N, 2*N+1,DETERM)
846         IF (DETERM) 4,3,4
847     3   PRINT 101,J
848     4   DO 5 K=1,N
849         E(K,NP1,1)=D(K,2*N+1)
850         DO 5 L=1,N
851         E(K,L,1)=-D(K,L)
852         LPN=L+N
853     5   X(K,L)=-D(K,LPN)
854         RETURN
855     6   DO 7 I=1,N
856         DO 7 K=1,N
857         DO 7 L=1,N
858     7   D(I,K)=D(I,K)+A(I,L)*X(L,K)
859     8   IF (J-NJ) 11,9,9
860     9   DO 10 I=1,N
861         DO 10 L=1,N
862         G(I)=G(I)-Y(I,L)*E(L,NP1,J-2)
863         DO 10 M=1,N
864    10   A(I,L)=A(I,L)+Y(I,M)*E(M,L,J-2)
865    11   DO 12 I=1,N
866         D(I,NP1)=-G(I)
867         DO 12 L=1,N
868         D(I,NP1)=D(I,NP1)+A(I,L)*E(L,NP1,J-1)
869         DO 12 K=1,N
```

```
   12   B(I,K)=B(I,K)+A(I,L)*E(L,K,J-1)
        CALL MATINV(N,NP1,DETERM)
        IF (DETERM) 14, 13, 14
   13   PRINT 101,J
   14   DO 15 K=1,N
        DO 15 M=1,NP1
   15   E(K,M,J)=-D(K,M)
        IF (J-NJ) 20,16,16
   16   DO 17 K=1,N
   17   C(K,J)=E(K,NP1,J)
        DO 18 JJ=2,NJ
        M=NJ-JJ+1
        DO 18 K=1,N
        C(K,M)=E(K,NP1,M)
        DO 18 L=1,N
   18   C(K,M)=C(K,M)+E(K,L,M)*C(L,M+1)
        DO 19 L=1,N
        DO 19 K=1,N
   19   C(K,1)=C(K,1)+X(K,L)*C(L,3)
   20   RETURN
        END
```

Listing B.3. FORTRAN Code to Calculate the Impedance Profile for N-Type Semi-Conductor

```
C      Electron transport layer and QD emissive layer
C      2 species system
C      SPECIES 1 = electron, SPECIES 2 = holes
C      This is the steady state solution only
C      It should be ran prior to Quantum_dots_os.for
C      The input file is the same for both
C      Copy and paste the appropriate lines to create the execuitable
C      cd C:\Chen\FORTRAN2019\ETL_IM
C      gfortran -static QuantumF_os_HOMOA2.for -o QuantumF_os_HOMOA2.exe
       PROGRAM QDETL
       IMPLICIT DOUBLE PRECISION (A-H, O-Z)
       COMMON/BAB/ A(18,18),B(18,18),C(18,100001),D(18,37),G(18)
      1           ,X(18,18),Y(18,18)
       COMMON/NSN/ N,NJ
       COMMON/NSNP/ NPTS
       COMMON/VAR/ FLUXOS(4,100001),CURRENTOS(2,100001)
       COMMON/DVAR/ CONCOS(4,100001),POTOS(2,100001),RHOOS(2,100001)
       COMMON/VARR/ H,EBIG,Y1,JCOUNT
       COMMON/CONSTANT/ F,R,DPBULK,DRHOBULK,CURRPER,AMOBH,AMOBE
       COMMON/CONCENRATION/ DCBULK(2),CBULK(2)
       COMMON/VARSSA/ DCONCSS(2,1000001),DPOTSS(1000001),DRHOSS(1000001)
       COMMON/VARSSB/ FLUXSS(2,1000001),CURRENTSS(1000001)
       COMMON/DCOMCENTRATION/ PBULK,RHOBULK
       COMMON/SURF/ CSURF,ATEM,DOP,ELE
       COMMON/REFERENCE/ REF(3),DIFF(2),Z(2)
       COMMON/CHARGE/ DQCHARGE,QCHARGE,CHARCOE
       COMMON/CONSTRAIN/ CONCU,CONCD
       COMMON/REACTION/ RXNSS(2,1000001),RXNOS(4,100001)
       COMMON/REARATE/ RATEE,RATEF,CONCIN
       COMMON/FRE/ FREQ(100001),omega
       COMMON/POTFRE/DPOTII(1000,10001),CURNTII(1000,10001)
       COMMON/CONCRE/CONCEII(1000,10001)
       COMMON/OLDVARA/ FNS(100001),FPS(100001),CNS(100001),CPS(100001)
       COMMON/OLDVARB/ POTS(100001),RHOS(100001),CURS(100001)
       COMMON/OLDVARC/ RNS(100001),RPS(100001)
       COMMON/GUESS/ NCOUNTMAX
C  FNS(J),FPS(J),FPS(J),CNS(J),CPS(J)
C  POTS(J),RHOS(J),CURS(J),RNS(J),RPS(J)
       CHARACTER REF*8

  102 FORMAT (/30H THE NEXT RUN DID NOT CONVERGE)
  103 FORMAT ('Error=',E16.6/(1X,'NE at J=1',E12.5,2X,'NE atJ=N',E12.5))
  104 FORMAT (1X,'Ce- at J=1',E12.5,2X,'Ce- at J=N',E12.5)
  105 FORMAT (1X,'DPOT at J=1',E12.5,2X,'DPOT at J=N',E12.5)
  106 FORMAT (1X,'DRHO at J=1',E12.5,2X,'DRHO at J=N',E12.5)
  107 FORMAT (1X,'Nh+ at J=1',E12.5,2X,'Nh+ at J=N',E12.5)
  108 FORMAT (1X,'Ch+ at J=1',E12.5,2X,'Ch+ at J=N',E12.5)
  333 FORMAT (4x,'E-',12x,'H+',12x,'RXN')
  300 FORMAT (20x,'G(1)'14x,'G(2)'14x,'G(3)'14x,'G(4)',14x,
     1         'G(5)',14x,'G(6)',14x,'G(7)',14x,'G(8)',14x,'G(9)')
  302 FORMAT ('Iteration='I4)
  334 FORMAT (9(E16.10,5X))
  335 FORMAT (18(E16.10,5X))
  666 FORMAT (4(E16.10,5X))
  301 FORMAT (5x,'J=' I5, 18E18.9)
C   866 FORMAT (5x,'J=' I5, 6E18.9)
C   886 FORMAT (20x,'B(1,1)'10x,'B(2.2)'10x,'B(3,1)'10x,'B(3,3)'14x,
```

```
C      1         'B(3,5)' 14x,'B(4,2)' 14x,'B(4,4)'14x,'B(4,5)'14x,
C      2         'B(5,5)' 10x,'B(5,6)' 10x,'B(6,3)' 10x,'B(6,4)' 10x,
C      3        'B(6,5)'14x,'B(6,6)')
  336 FORMAT (1000(E25.15,1X))
  339 FORMAT (1000(E25.15,1X))

C     Read input values used in steady state
      open(10,file='QDLED_HOMO_in.txt',status='old')
      read(10,*) N,NJ,Y1,ATEM,F,R,PBULK,DOP,ELE,QCHARGE
      read(10,*) RATEE,CONCIN,EBIG,NCOUNTMAX
      read(10,*) (DIFF(I),Z(I),REF(I),CBULK(I),I=1,(N-7))
C     Read steady state values from previous file
      OPEN(UNIT=11, FILE='cdh_out.txt')
      DO 3 I=1,NJ*NCOUNTMAX
    3 READ(11,334)

      READ(11,334) (FLUXSS(1,J),FLUXSS(2,J),DCONCSS(1,J),DCONCSS(2,J),
     1               DPOTSS(J),DRHOSS(J),CURRENTSS(J),RXNSS(1,J),
     2               RXNSS(2,J),J=1,NJ)

      PRINT *, 'SS POTENTIAL',DPOTSS(2001)
      PRINT *, 'SS Electron_concentration',DCONCSS(1,NJ)
      PRINT *, 'SS Reaction_rate',RXNSS(1,NJ)
      PRINT *, 'Farady_constant',F


      OPEN(UNIT=13, FILE='cdh_os_out.txt')
      CLOSE(UNIT=13, STATUS='DELETE')
      OPEN(UNIT=13, FILE='cdh_os_out.txt')

      OPEN(12,FILE='cdh_G_os_out.txt')
      CLOSE(12, STATUS='DELETE')
      OPEN(12, FILE='cdh_G_os_out.txt')

      OPEN(15,FILE='cdh_P_out.txt')
      CLOSE(15, STATUS='DELETE')
      OPEN(15, FILE='cdh_P_out.txt')

      OPEN(20,FILE='cdh_CE_out.txt')
      CLOSE(20, STATUS='DELETE')
      OPEN(20, FILE='cdh_CE_out.txt')

      OPEN(30,FILE='cdh_Current_out.txt')
      CLOSE(30, STATUS='DELETE')
      OPEN(30, FILE='cdh_Current_out.txt')

      OPEN(16,FILE='cdh_values_out.txt')
      CLOSE(16, STATUS='DELETE')
      OPEN(16, FILE='cdh_values_out.txt')

      OPEN(19,FILE='Frequency_out.txt')
      CLOSE(19, STATUS='DELETE')
      OPEN(19, FILE='Frequency_out.txt')

      OPEN(51,FILE='cdh_old_ss.txt')
      CLOSE(51, STATUS='DELETE')
      OPEN(51, FILE='cdh_old_ss.txt')

```

```
116       open(50,file='Currentos_in.txt',status='old')
117       read(50,*) CURRPER
118 C       PRINT *, 'current=', CSURF
119 C     Constants
120 C     Current amplitude
121       PRINT *, 'Current amplitude', CURRPER
122 
123       PRINT *, 'Y1=', Y1
124       H=Y1/(NJ-1)
125       PRINT *, 'H=', H
126 
127       N=2*N
128       PRINT *, 'N=', N
129   337 FORMAT (I2/I7/E15.8/E15.8/E15.8/E15.8/E15.8/I7)
130       write (16,337) N,NJ,H,DOP,ELE,Z(1),Z(2),NCOUNTMAX
131 
132 C     Coefficient for the charge density
133       CHARCOE=F**2./(8.314*ATEM)
134       PRINT *, 'charge Coefficient', CHARCOE
135 C     Coefficient for the old variables
136       OLDCOE=8.314*ATEM/F
137       PRINT *, 'OldVaribles Coefficient', OLDCOE
138 C     MOBILITY OF ELECRONS AND HOLES
139       AMOBE=DIFF(1)/(8.314*ATEM)
140       AMOBH=DIFF(2)/(8.314*ATEM)
141 C     SURFACE CHARGE
142       DQCHARGE=QCHARGE*F/(8.314*ATEM)
143       PRINT *, 'SURFACE CHARGE', DQCHARGE
144 
145 C     SURFACE CHARGE
146       PRINT *, 'relative permitivity', ELE
147 
148 C     The number of points for frequency
149       NPTS=121
150       PRINT *, 'NPTS=', NPTS
151 
152 C     Create range for the dimensionless frequency
153       DO 261 I=1,NPTS
154       FREQ(I)=10.**(-5+0.1*(I-1.))
155   261 WRITE (19,339) FREQ(I)
156 C     Calculate the old varibles
157 
158       DO 444 J=1,NJ
159       FNS(J)=FLUXSS(1,J)
160       FPS(J)=FLUXSS(2,J)
161       CNS(J)=DCONCSS(1,J)*EXP(-Z(1)*DPOTSS(J))
162       CPS(J)=DCONCSS(2,J)*EXP(-Z(2)*DPOTSS(J))
163       POTS(J)=DPOTSS(J)*OLDCOE
164       RHOS(J)=DRHOSS(J)*OLDCOE
165       CURS(J)=CURRENTSS(J)
166       RNS(J)=RXNSS(1,J)
167   444 RPS(J)=RXNSS(2,J)
168 
169       write (51,334) (FNS(J),FPS(J),CNS(J),CPS(J),POTS(J),
170      1                RHOS(J),CURS(J),RNS(J),RPS(J), J=1,NJ)
171 
172       DO 17 nf=1,NPTS
173       PRINT *, 'FREQ(NF)=', FREQ(NF)
```

```
174         omega=2.*3.141592653589793*FREQ(NF)
175         PRINT *, 'omega=', omega
176
177       340 FORMAT (E12.6)
178         write (19,340) omega
179
180 C     Start actual code
181         DO 20 J=1,NJ
182         DO 20 I=1,N
183        20 C(I,J)=0.0
184         DO 21 J=1,NJ
185         DO 21 K=1,2
186         DO 21 L=1,4
187         FLUXOS(L,J)=0.0
188         CONCOS(L,J)=0.0
189         RXNOS(L,J)=0.0
190         POTOS(K,J)=0.0
191         CURRENTOS(K,J)=0.0
192        21 RHOOS(K,J)=0.0
193
194
195 C         DO 21 J=1,NJ
196 C        21 CURRENTOS(1,J)=CURRPER
197         JCOUNT=0
198         TOL=1.E-10*N*NJ
199 C         TOL=1.E-12
200 C         TOL=1.E-10
201         PRINT *, 'TOL=', TOL
202        22 JCOUNT=JCOUNT+1
203         AMP=0.0
204         J=0
205         DO 23 I=1,N
206         DO 23 K=1,N
207         Y(I,K)=0.0
208        23 X(I,K)=0.0
209        24 J=J+1
210         DO 25  I=1,N
211         G(I)=0.0
212         DO 25 K=1,N
213         A(I,K)=0.0
214         B(I,K)=0.0
215        25 D(I,K)=0.0
216
217         IF (J.EQ.1) CALL BC1(J)
218         IF (J.GT.1 .AND. J.LT.NJ) CALL ETL(J)
219         IF (J.EQ.NJ) CALL BCNJ(J)
220         CALL BAND(J)
221
222         AMP=DABS(G(1))+DABS(G(2))+DABS(G(3))+DABS(G(4))
223        1          +DABS(G(5))+DABS(G(6))+DABS(G(7))+DABS(G(8))
224        2          +DABS(G(9))+DABS(G(10))+DABS(G(11))+DABS(G(12))
225        3          +DABS(G(13))+DABS(G(14))+DABS(G(15))+DABS(G(16))
226        4          +DABS(G(17))+DABS(G(18))
227 C         PRINT *, 'ERROR1=', AMP
228         IF (J.LT.NJ)  GO TO 24
229
230 C         PRINT *, 'ERROR=', AMP
231
```

```
232       DO 16 K=1,NJ
233       DO 16 I=1,2
234       DO 16 L=1,4
235       FLUXOS(L,K)=FLUXOS(L,K)+C(L,K)
236       CONCOS(L,K)=CONCOS(L,K)+C(L+4,K)
237       POTOS(I,K)=POTOS(I,K)+C(I+8,K)
238       RHOOS(I,K)=RHOOS(I,K)+C(I+10,K)
239       CURRENTOS(I,K)=CURRENTOS(I,K)+C(I+12,K)
240       RXNOS(L,K)=RXNOS(L,K)+C(L+14,K)
241    16 CONTINUE
242
243       WRITE(12,302) (JCOUNT)
244
245 C     If the error is less then the tolerance, finish program
246       IF (DABS(AMP).LT.DABS(TOL)) GO TO 15
247
248 C     If the error is greater then tolerance, do another iteration
249       IF (JCOUNT.LE.4) GO TO 22
250       PRINT 102
251    15 CONTINUE
252       PRINT *,'JCOUNT=',JCOUNT
253       PRINT *, 'nf1=', nf
254
255 C       DO 18 I=1,2
256 C       DO 18 J=1,NJ
257 C       BIG=POTOS(I,J)
258 C       BIG2=1.0E-40
259 C    18 IF (ABS(BIG).LE.BIG2) POTOS(I,J)=0.0
260
261       WRITE(13,335) (FLUXOS(1,J),FLUXOS(2,J),FLUXOS(3,J),FLUXOS(4,J),
262      1       CONCOS(1,J),CONCOS(2,J),CONCOS(3,J),CONCOS(4,J),
263      2       POTOS(1,J),POTOS(2,J),RHOOS(1,J),RHOOS(2,J),
264      3       CURRENTOS(1,J),CURRENTOS(2,J),RXNOS(1,J),RXNOS(2,J),
265      4       RXNOS(3,J),RXNOS(4,J), J=1,NJ)
266
267       DO 17 J=1,NJ
268       CONCEII(2*nf-1,J)=CONCOS(1,J)
269       CONCEII(2*nf,J)=CONCOS(2,J)
270       DPOTII(2*nf-1,J)=POTOS(1,J)
271       DPOTII(2*nf,J)=POTOS(2,J)
272       CURNTII(2*nf-1,J)=CURRENTOS(1,J)
273    17 CURNTII(2*nf,J)=CURRENTOS(2,J)
274
275
276 c     for some reason nf is one greater then necessary
277       PRINT *, 'nf2=', nf
278
279 C      DO 17 I=1,2*nf-2
280       nf=nf-1
281     DO 39 J=1,NJ
282       WRITE(20,336) (CONCEII(I,J), I=1,2*nf)
283       WRITE(30,336) (CURNTII(I,J), I=1,2*nf)
284    39 WRITE(15,336) (DPOTII(I,J), I=1,2*nf)
285
286   338 FORMAT (I5)
287       write (16,338) nf
288
289
```

```
      END PROGRAM QDOSC

c     SUBROUTINE BC1(J)
      SUBROUTINE BC1(J)
      IMPLICIT DOUBLE PRECISION (A-H, O-Z)
      COMMON/BAB/ A(18,18),B(18,18),C(18,100001),D(18,37),G(18)
     1           ,X(18,18),Y(18,18)
      COMMON/NSN/ N,NJ
      COMMON/NSNP/ NPTS
      COMMON/VAR/ FLUXOS(4,100001),CURRENTOS(2,100001)
      COMMON/DVAR/ CONCOS(4,100001),POTOS(2,100001),RHOOS(2,100001)
      COMMON/VARR/ H,EBIG,Y1,JCOUNT
      COMMON/CONSTANT/ F,R,DPBULK,DRHOBULK,CURRPER,AMOBH,AMOBE
      COMMON/CONCENRATION/ DCBULK(2),CBULK(2)
      COMMON/VARSSA/ DCONCSS(2,1000001),DPOTSS(1000001),DRHOSS(1000001)
      COMMON/VARSSB/ FLUXSS(2,1000001),CURRENTSS(1000001)
      COMMON/DCOMCENTRATION/ PBULK,RHOBULK
      COMMON/SURF/ CSURF,ATEM,DOP,ELE
      COMMON/REFERENCE/ REF(3),DIFF(2),Z(2)
      COMMON/CHARGE/ DQCHARGE,QCHARGE,CHARCOE
      COMMON/CONSTRAIN/ CONCU,CONCD
      COMMON/REACTION/ RXNSS(2,1000001),RXNOS(4,100001)
      COMMON/REARATE/ RATEE,RATEF,CONCIN
      COMMON/FRE/ FREQ(100001),omega
      COMMON/POTFRE/DPOTII(1000,10001),CURNTII(1000,10001)
      COMMON/CONCRE/CONCEII(1000,10001)
      COMMON/OLDVARA/ FNS(100001),FPS(100001),CNS(100001),CPS(100001)
      COMMON/OLDVARB/ POTS(100001),RHOS(100001),CURS(100001)
      COMMON/OLDVARC/ RNS(100001),RPS(100001)
      COMMON/GUESS/ NCOUNTMAX
  301 FORMAT (5x,'J=' I5, 18E18.9)


C     FOR ELECTRON-MEB-Real

      G(1)=(FLUXOS(1,J+1)-FLUXOS(1,J))/H
     1        -0.5*(RXNOS(1,J+1)+RXNOS(1,J))
     2        -0.5*omega*(CONCOS(2,J+1)+CONCOS(2,J))
      B(1,1)=+1./H
      D(1,1)=-1./H
      B(1,15)=+0.5
      D(1,15)=+0.5
      B(1,6)=+0.5*omega
      D(1,6)=+0.5*omega


C     FOR ELECTRON-MEB-Imaginary

      G(2)=(FLUXOS(2,J+1)-FLUXOS(2,J))/H
     1        -0.5*(RXNOS(2,J+1)+RXNOS(2,J))
     2        +0.5*omega*(CONCOS(1,J+1)+CONCOS(1,J))
      B(2,2)=+1./H
      D(2,2)=-1./H
      B(2,16)=+0.5
      D(2,16)=+0.5
      B(2,5)=-0.5*omega
      D(2,5)=-0.5*omega

```

```
C     FOR HOLE-MEB-REAL


        G(3)=FLUXOS(3,J)
        B(3,3)=-1.0

C       FOR HOLE-MEB-Imaginary

        G(4)=FLUXOS(4,J)
        B(4,4)=-1.0

C     FOR ELECTRON-FLUX-Real


        G(5)=CONCOS(1,J)
        B(5,5)=-1.0

C     FOR ELECTRON-FLUX-Imaginary


        G(6)=CONCOS(2,J)
        B(6,6)=-1.0

C       FOR HOLE-FLUX-Real


        G(7)=CONCOS(3,J)
        B(7,7)=-1.0

C       FOR HOLE-FLUX-Imaginary

        G(8)=CONCOS(4,J)
        B(8,8)=-1.0

C    FOR POISSON'S EQUATION-real

        G(9)=POTOS(1,J)
        B(9,9)=-1.0


C    FOR POISSON'S EQUATION-Imaginary

        G(10)=POTOS(2,J)
        B(10,10)=-1.0


C       FOR CHARGE DENSITY-Real

        G(11)=F*(Z(1)*CONCOS(1,J)+Z(2)*CONCOS(3,J))-RHOOS(1,J)
        B(11,5)=-F*Z(1)
        B(11,7)=-F*Z(2)
        B(11,11)=+1.0

C       FOR CHARGE DENSITY-Imaginary

        G(12)=F*(Z(1)*CONCOS(2,J)+Z(2)*CONCOS(4,J))-RHOOS(2,J)
        B(12,6)=-F*Z(1)
```

```
406         B(12,8)=-F*Z(2)
407         B(12,12)=+1.0
408
409
410 C       For current density-Real
411
412         G(13)=F*(Z(1)*FLUXOS(1,J)+Z(2)*FLUXOS(3,J))-CURRENTOS(1,J)
413         B(13,1)=-F*Z(1)
414         B(13,3)=-F*Z(2)
415         B(13,13)=+1.0
416
417 C       For current density-Imaginary
418
419
420         G(14)=F*(Z(1)*FLUXOS(2,J)+Z(2)*FLUXOS(4,J))-CURRENTOS(2,J)
421         B(14,2)=-F*Z(1)
422         B(14,4)=-F*Z(2)
423         B(14,14)=+1.0
424
425
426 C       For homogeneous reaction of electrons-real
427
428         G(15)=-RATEE*(CNS(J)*CONCOS(3,J)+CPS(J)*CONCOS(1,J))
429        1        -RXNOS(1,J)
430         B(15,7)=RATEE*CNS(J)
431         B(15,5)=RATEE*CPS(J)
432         B(15,15)=+1.0
433
434 C       For homogeneous reaction of electrons-Imaginary
435
436         G(16)=-RATEE*(CNS(J)*CONCOS(4,J)+CPS(J)*CONCOS(2,J))
437        1        -RXNOS(2,J)
438         B(16,8)=RATEE*CNS(J)
439         B(16,6)=RATEE*CPS(J)
440         B(16,16)=+1.0
441
442 C       For homogeneous reaction of holes-real
443
444         G(17)=-RATEE*(CNS(J)*CONCOS(3,J)+CPS(J)*CONCOS(1,J))
445        1        -RXNOS(3,J)
446         B(17,7)=RATEE*CNS(J)
447         B(17,5)=RATEE*CPS(J)
448         B(17,17)=+1.0
449
450 C       For homogeneous reaction of holes-Imaginary
451
452         G(18)=-RATEE*(CNS(J)*CONCOS(4,J)+CPS(J)*CONCOS(2,J))
453        1        -RXNOS(4,J)
454         B(18,8)=RATEE*CNS(J)
455         B(18,6)=RATEE*CPS(J)
456         B(18,18)=+1.0
457
458         CONTINUE
459
460   212   WRITE(12,301) J, (G(K),K=1,N)
461
462         RETURN
463         END
```

```
c       SUBROUTINE ETL(J)
        SUBROUTINE ETL(J)
        IMPLICIT DOUBLE PRECISION (A-H, O-Z)
        COMMON/BAB/ A(18,18),B(18,18),C(18,100001),D(18,37),G(18)
       1                  ,X(18,18),Y(18,18)
        COMMON/NSN/ N,NJ
        COMMON/NSNP/ NPTS
        COMMON/VAR/ FLUXOS(4,100001),CURRENTOS(2,100001)
        COMMON/DVAR/ CONCOS(4,100001),POTOS(2,100001),RHOOS(2,100001)
        COMMON/VARR/ H,EBIG,Y1,JCOUNT
        COMMON/CONSTANT/ F,R,DPBULK,DRHOBULK,CURRPER,AMOBH,AMOBE
        COMMON/CONCENRATION/ DCBULK(2),CBULK(2)
        COMMON/VARSSA/ DCONCSS(2,1000001),DPOTSS(1000001),DRHOSS(1000001)
        COMMON/VARSSB/ FLUXSS(2,1000001),CURRENTSS(1000001)
        COMMON/DCOMCENTRATION/ PBULK,RHOBULK
        COMMON/SURF/ CSURF,ATEM,DOP,ELE
        COMMON/REFERENCE/ REF(3),DIFF(2),Z(2)
        COMMON/CHARGE/ DQCHARGE,QCHARGE,CHARCOE
        COMMON/CONSTRAIN/ CONCU,CONCD
        COMMON/REACTION/ RXNSS(2,1000001),RXNOS(4,100001)
        COMMON/REARATE/ RATEE,RATEF,CONCIN
        COMMON/FRE/ FREQ(100001),omega
        COMMON/POTFRE/DPOTII(1000,10001),CURNTII(1000,10001)
        COMMON/CONCRE/CONCEII(1000,10001)
        COMMON/OLDVARA/ FNS(100001),FPS(100001),CNS(100001),CPS(100001)
        COMMON/OLDVARB/ POTS(100001),RHOS(100001),CURS(100001)
        COMMON/OLDVARC/ RNS(100001),RPS(100001)
        COMMON/GUESS/ NCOUNTMAX

  301   FORMAT (5x,'J=' I5, 18E18.9)
C     866 FORMAT (5x,'J=' I5, 36E18.9)

C       FOR ELECTRON-MEB-Real

        G(1)=(FLUXOS(1,J+1)-FLUXOS(1,J-1))/(2.*H)
       1        -RXNOS(1,J)-omega*CONCOS(2,J)
        A(1,1)=+1./(2.*H)
        D(1,1)=-1./(2.*H)
        B(1,15)=+1.0
        B(1,6)=omega


C       FOR ELECTRON-MEB-Imaginary
        G(2)=(FLUXOS(2,J+1)-FLUXOS(2,J-1))/(2.*H)
       1        -RXNOS(2,J)+omega*CONCOS(1,J)
        A(2,2)=+1./(2.*H)
        D(2,2)=-1./(2.*H)
        B(2,16)=+1.0
        B(2,5)=-omega

C       FOR HOLES-MEB-Real

        G(3)=(FLUXOS(3,J+1)-FLUXOS(3,J-1))/(2.*H)
       1         -RXNOS(3,J)-omega*CONCOS(4,J)
        A(3,3)=+1./(2.*H)
        D(3,3)=-1./(2.*H)
        B(3,17)=+1.0
        B(3,8)=omega
```

```
C       FOR HOLES-MEB-Imaginary
        G(4)=(FLUXOS(4,J+1)-FLUXOS(4,J-1))/(2.*H)
     1        -RXNOS(4,J)+omega*CONCOS(3,J)
        A(4,4)=+1./(2.*H)
        D(4,4)=-1./(2.*H)
        B(4,18)=+1.0
        B(4,7)=-omega

C       FOR ELECTRON-FLUX-REAL

        G(5)=-DIFF(1)*(CONCOS(1,J+1)-CONCOS(1,J-1))/(2.*H)
     1        -AMOBE*Z(1)*F*CNS(J)*(POTOS(1,J+1)-POTOS(1,J-1))/(2.*H)
     2        -AMOBE*Z(1)*F*(POTS(J+1)-POTS(J-1))/(2.*H)*CONCOS(1,J)
     3        -FLUXOS(1,J)

        A(5,5)=-DIFF(1)/(2.*H)
        B(5,5)=+AMOBE*Z(1)*F*(POTS(J+1)-POTS(J-1))/(2.*H)
        D(5,5)=DIFF(1)/(2.*H)
        A(5,9)=-AMOBE*Z(1)*F*CNS(J)/(2.*H)
        D(5,9)=+AMOBE*Z(1)*F*CNS(J)/(2.*H)
        B(5,1)=+1.0

C       FOR ELECTRON-FLUX-Imaginary

        G(6)=-DIFF(1)*(CONCOS(2,J+1)-CONCOS(2,J-1))/(2.*H)
     1        -AMOBE*Z(1)*F*CNS(J)*(POTOS(2,J+1)-POTOS(2,J-1))/(2.*H)
     2        -AMOBE*Z(1)*F*(POTS(J+1)-POTS(J-1))/(2.*H)*CONCOS(2,J)
     3        -FLUXOS(2,J)

        A(6,6)=-DIFF(1)/(2.*H)
        B(6,6)=+AMOBE*Z(1)*F*(POTS(J+1)-POTS(J-1))/(2.*H)
        D(6,6)=DIFF(1)/(2.*H)
        A(6,10)=-AMOBE*Z(1)*F*CNS(J)/(2.*H)
        D(6,10)=+AMOBE*Z(1)*F*CNS(J)/(2.*H)
        B(6,2)=+1.0

C       FOR HOLES-FLUX-Real
        G(7)=-DIFF(2)*(CONCOS(3,J+1)-CONCOS(3,J-1))/(2.*H)
     1        -AMOBH*Z(2)*F*CPS(J)*(POTOS(1,J+1)-POTOS(1,J-1))/(2.*H)
     2        -AMOBH*Z(2)*F*(POTS(J+1)-POTS(J-1))/(2.*H)*CONCOS(3,J)
     3        -FLUXOS(3,J)

        A(7,7)=-DIFF(2)/(2.*H)
        B(7,7)=+AMOBH*Z(2)*F*(POTS(J+1)-POTS(J-1))/(2.*H)
        D(7,7)=DIFF(2)/(2.*H)
        A(7,9)=-AMOBH*Z(2)*F*CPS(J)/(2.*H)
        D(7,9)=+AMOBH*Z(2)*F*CPS(J)/(2.*H)
        B(7,3)=+1.0

C       FOR HOLES-FLUX-Imaginary
        G(8)=-DIFF(2)*(CONCOS(4,J+1)-CONCOS(4,J-1))/(2.*H)
     1        -AMOBH*Z(2)*F*CPS(J)*(POTOS(2,J+1)-POTOS(2,J-1))/(2.*H)
     2        -AMOBH*Z(2)*F*(POTS(J+1)-POTS(J-1))/(2.*H)*CONCOS(4,J)
     3        -FLUXOS(4,J)

        A(8,8)=-DIFF(2)/(2.*H)
        B(8,8)=+AMOBH*Z(2)*F*(POTS(J+1)-POTS(J-1))/(2.*H)
```

```
580         D(8,8)=DIFF(2)/(2.*H)
581         A(8,10)=-AMOBH*Z(2)*F*CPS(J)/(2.*H)
582         D(8,10)=+AMOBH*Z(2)*F*CPS(J)/(2.*H)
583         B(8,4)=+1.0
584
585 C       FOR POISSON'S Equation-Real
586         G(9)=(POTOS(1,J+1)-2.*POTOS(1,J)+POTOS(1,J-1))/H**2.
587        1       +RHOOS(1,J)/ELE
588         A(9,9)=-1./H**2
589         B(9,9)=+2./H**2
590         D(9,9)=-1./H**2
591         B(9,11)=-1./ELE
592
593 C       FOR POISSON'S Equation-Imaginary
594
595         G(10)=(POTOS(2,J+1)-2.*POTOS(2,J)+POTOS(2,J-1))/H**2.
596        1       +RHOOS(2,J)/ELE
597         A(10,10)=-1./H**2.
598         B(10,10)=+2./H**2.
599         D(10,10)=-1./H**2.
600         B(10,12)=-1./ELE
601
602 C       FOR CHARGE DENSITY-Real
603
604         G(11)=F*(Z(1)*CONCOS(1,J)+Z(2)*CONCOS(3,J))-RHOOS(1,J)
605
606         B(11,5)=-F*Z(1)
607         B(11,7)=-F*Z(2)
608         B(11,11)=+1.0
609
610 C       FOR CHARGE DENSITY-Imaginary
611
612         G(12)=F*(Z(1)*CONCOS(2,J)+Z(2)*CONCOS(4,J))-RHOOS(2,J)
613
614         B(12,6)=-F*Z(1)
615         B(12,8)=-F*Z(2)
616         B(12,12)=+1.0
617
618 C       For current density-Real
619         G(13)=F*(Z(1)*FLUXOS(1,J)+Z(2)*FLUXOS(3,J))-CURRENTOS(1,J)
620         B(13,1)=-F*Z(1)
621         B(13,3)=-F*Z(2)
622         B(13,13)=+1.0
623
624 C       For current density-Imaginary
625
626         G(14)=F*(Z(1)*FLUXOS(2,J)+Z(2)*FLUXOS(4,J))-CURRENTOS(2,J)
627         B(14,2)=-F*Z(1)
628         B(14,4)=-F*Z(2)
629         B(14,14)=+1.0
630
631
632 C       For homogeneous reaction of electrons-real
633         G(15)=-RATEE*(CNS(J)*CONCOS(3,J)+CPS(J)*CONCOS(1,J))
634        1       -RXNOS(1,J)
635         B(15,7)=RATEE*CNS(J)
636         B(15,5)=RATEE*CPS(J)
637         B(15,15)=+1.0
```

```
C      For homogeneous reaction of electrons-Imaginary
       G(16)=-RATEE*(CNS(J)*CONCOS(4,J)+CPS(J)*CONCOS(2,J))
      1       -RXNOS(2,J)
       B(16,8)=RATEE*CNS(J)
       B(16,6)=RATEE*CPS(J)
       B(16,16)=+1.0

C      For homogeneous reaction of holes-real
       G(17)=-RATEE*(CNS(J)*CONCOS(3,J)+CPS(J)*CONCOS(1,J))
      1       -RXNOS(3,J)
       B(17,7)=RATEE*CNS(J)
       B(17,5)=RATEE*CPS(J)
       B(17,17)=+1.0

C      For homogeneous reaction of holes-Imaginary
       G(18)=-RATEE*(CNS(J)*CONCOS(4,J)+CPS(J)*CONCOS(2,J))
      1       -RXNOS(4,J)
       B(18,8)=RATEE*CNS(J)
       B(18,6)=RATEE*CPS(J)
       B(18,18)=+1.0

       CONTINUE
C     SAVE G OUT DATA
   212 DO 11 I=2,NJ-1
    11 If (I.EQ.J) WRITE(12,301) J, (G(K),K=1,N)

C    888 if (J.EQ.2) WRITE(88,866) J,(B(1,1)),(B(2,2)),(B(3,1)),(B(3,3)),
C       1             (B(3,5)),(B(4,2)),(B(4,4)),(B(4,5)),(B(5,5)),(B(5,6)),
C       2             (B(6,3)),(B(6,4)),(B(6,5)),(B(6,6))
       RETURN
       END
c      SUBROUTINE BCNJ(J)
       SUBROUTINE BCNJ(J)
       IMPLICIT DOUBLE PRECISION (A-H, O-Z)
       COMMON/BAB/ A(18,18),B(18,18),C(18,100001),D(18,37),G(18)
      1              ,X(18,18),Y(18,18)
       COMMON/NSN/ N,NJ
       COMMON/NSNP/ NPTS
       COMMON/VAR/ FLUXOS(4,100001),CURRENTOS(2,100001)
       COMMON/DVAR/ CONCOS(4,100001),POTOS(2,100001),RHOOS(2,100001)
       COMMON/VARR/ H,EBIG,Y1,JCOUNT
       COMMON/CONSTANT/ F,R,DPBULK,DRHOBULK,CURRPER,AMOBH,AMOBE
       COMMON/CONCENRATION/ DCBULK(2),CBULK(2)
       COMMON/VARSSA/ DCONCSS(2,1000001),DPOTSS(1000001),DRHOSS(1000001)
       COMMON/VARSSB/ FLUXSS(2,1000001),CURRENTSS(1000001)
       COMMON/DCOMCENTRATION/ PBULK,RHOBULK
       COMMON/SURF/ CSURF,ATEM,DOP,ELE
       COMMON/REFERENCE/ REF(3),DIFF(2),Z(2)
       COMMON/CHARGE/ DQCHARGE,QCHARGE,CHARCOE
       COMMON/CONSTRAIN/ CONCU,CONCD
       COMMON/REACTION/ RXNSS(2,1000001),RXNOS(4,100001)
       COMMON/REARATE/ RATEE,RATEF,CONCIN
       COMMON/FRE/ FREQ(100001),omega
       COMMON/POTFRE/DPOTII(1000,10001),CURNTII(1000,10001)
       COMMON/CONCRE/CONCEII(1000,10001)
       COMMON/OLDVARA/ FNS(100001),FPS(100001),CNS(100001),CPS(100001)
       COMMON/OLDVARB/ POTS(100001),RHOS(100001),CURS(100001)
```

```
696       COMMON/OLDVARC/ RNS(100001),RPS(100001)
697       COMMON/GUESS/ NCOUNTMAX
698
699   301 FORMAT (5x,'J=' I5,  18E18.9)
700 C   866 FORMAT (5x,'J=' I5, 36E18.9)
701
702
703
704 C       FOR ELECTRON-MEB-Real
705       G(1)=FLUXOS(1,J)
706       B(1,1)=-1.0
707
708 C       FOR ELECTRON-MEB-Imaginary
709       G(2)=FLUXOS(2,J)
710       B(2,2)=-1.0
711
712
713 C       FOR HOLES-MEB-Real
714
715       G(3)=(FLUXOS(3,J)-FLUXOS(3,J-1))/H
716      1     -0.5*RXNOS(3,J)-0.5*RXNOS(3,J-1)
717      2     -0.5*omega*CONCOS(4,J)-0.5*omega*CONCOS(4,J-1)
718       A(3,3)=+1./H
719       B(3,3)=-1./H
720       B(3,17)=+0.5
721       A(3,17)=+0.5
722       B(3,8)=0.5*omega
723       A(3,8)=0.5*omega
724
725 C       FOR HOLES-MEB-Imaginary
726
727       G(4)=(FLUXOS(4,J)-FLUXOS(4,J-1))/H
728      1        -0.5*RXNOS(4,J)-0.5*RXNOS(4,J-1)
729      2        +0.5*omega*CONCOS(3,J)+0.5*omega*CONCOS(3,J-1)
730       A(4,4)=+1./H
731       B(4,4)=-1./H
732       B(4,7)=-0.5*omega
733       A(4,7)=-0.5*omega
734       B(4,18)=+0.5
735       A(4,18)=+0.5
736
737 C       FOR ELECTRON-FLUX-REAL
738
739       G(5)=-DIFF(1)*(CONCOS(1,J)-CONCOS(1,J-1))/H
740      1     -0.5*AMOBE*Z(1)*F*(CNS(J)+CNS(J-1))*(POTOS(1,J)-POTOS(1,J-1))/H
741      2     -0.5*AMOBE*Z(1)*F*(POTS(J)-POTS(J-1))/H*(CONCOS(1,J)
742      3     +CONCOS(1,J-1))
743      4     -0.5*(FLUXOS(1,J)+FLUXOS(1,J-1))
744
745       A(5,5)=-DIFF(1)/H+0.5*AMOBE*Z(1)*F*(POTS(J)-POTS(J-1))/H
746       B(5,5)=+DIFF(1)/H+0.5*AMOBE*Z(1)*F*(POTS(J)-POTS(J-1))/H
747       A(5,9)=-0.5*AMOBE*Z(1)*F*(CNS(J)+CNS(J-1))/H
748       B(5,9)=+0.5*AMOBE*Z(1)*F*(CNS(J)+CNS(J-1))/H
749       A(5,1)=+0.5
750       B(5,1)=+0.5
751
752 C       FOR ELECTRON-FLUX-Imaginary
753       G(6)=-DIFF(1)*(CONCOS(2,J)-CONCOS(2,J-1))/H
```

```
     1     -0.5*AMOBE*Z(1)*F*(CNS(J)+CNS(J-1))*(POTOS(2,J)-POTOS(2,J-1))/H
     2     -0.5*AMOBE*Z(1)*F*(POTS(J)-POTS(J-1))/H*(CONCOS(2,J)
     3     +CONCOS(2,J-1))
     4     -0.5*(FLUXOS(2,J)+FLUXOS(2,J-1))

      A(6,6)=-DIFF(1)/H+0.5*AMOBE*Z(1)*F*(POTS(J)-POTS(J-1))/H
      B(6,6)=+DIFF(1)/H+0.5*AMOBE*Z(1)*F*(POTS(J)-POTS(J-1))/H
      A(6,10)=-0.5*AMOBE*Z(1)*F*(CNS(J)+CNS(J-1))/H
      B(6,10)=+0.5*AMOBE*Z(1)*F*(CNS(J)+CNS(J-1))/H
      A(6,2)=+0.5
      B(6,2)=+0.5

C     FOR HOLES-FLUX-Real
      G(7)=-DIFF(2)*(CONCOS(3,J)-CONCOS(3,J-1))/H
     1     -0.5*AMOBH*Z(2)*F*(CPS(J)+CPS(J-1))*(POTOS(1,J)-POTOS(1,J-1))/H
     2     -0.5*AMOBH*Z(2)*F*(POTS(J)-POTS(J-1))/H*(CONCOS(3,J)
     3     +CONCOS(3,J-1))
     4     -0.5*(FLUXOS(3,J)+FLUXOS(3,J-1))

      A(7,7)=-DIFF(2)/H+0.5*AMOBH*Z(2)*F*(POTS(J)-POTS(J-1))/H
      B(7,7)=+DIFF(2)/H+0.5*AMOBH*Z(2)*F*(POTS(J)-POTS(J-1))/H
      A(7,9)=-0.5*AMOBH*Z(2)*F*(CPS(J)+CPS(J-1))/H
      B(7,9)=+0.5*AMOBH*Z(2)*F*(CPS(J)+CPS(J-1))/H
      A(7,3)=+0.5
      B(7,3)=+0.5


C     FOR HOLES-FLUX-Imaginary
      G(8)=-DIFF(2)*(CONCOS(4,J)-CONCOS(4,J-1))/H
     1     -0.5*AMOBH*Z(2)*F*(CPS(J)+CPS(J-1))*(POTOS(2,J)-POTOS(2,J-1))/H
     2     -0.5*AMOBH*Z(2)*F*(POTS(J)-POTS(J-1))/H*(CONCOS(4,J)
     3     +CONCOS(4,J-1))
     4     -0.5*(FLUXOS(4,J)+FLUXOS(4,J-1))

      A(8,8)=-DIFF(2)/H+0.5*AMOBH*Z(2)*F*(POTS(J)-POTS(J-1))/H
      B(8,8)=+DIFF(2)/H+0.5*AMOBH*Z(2)*F*(POTS(J)-POTS(J-1))/H
      A(8,10)=-0.5*AMOBH*Z(2)*F*(CPS(J)+CPS(J-1))/H
      B(8,10)=+0.5*AMOBH*Z(2)*F*(CPS(J)+CPS(J-1))/H
      A(8,4)=+0.5
      B(8,4)=+0.5

C     FOR POSSON'S EQUATION-REAL
      G(9)=POTOS(1,J)-1.E-6
      B(9,9)=-1.0

C     FOR POSSON'S EQUATION-Imaginary

      G(10)=POTOS(2,J)
      B(10,10)=-1.0

C     FOR CHARGE DENSITY-Real

      G(11)=F*(Z(1)*CONCOS(1,J)+Z(2)*CONCOS(3,J))-RHOOS(1,J)

      B(11,5)=-F*Z(1)
      B(11,7)=-F*Z(2)
      B(11,11)=+1.0

```

```
C      FOR CHARGE DENSITY-Imaginary

       G(12)=F*(Z(1)*CONCOS(2,J)+Z(2)*CONCOS(4,J))-RHOOS(2,J)

       B(12,6)=-F*Z(1)
       B(12,8)=-F*Z(2)
       B(12,12)=+1.0

C      For current density-Real
       G(13)=F*(Z(1)*FLUXOS(1,J)+Z(2)*FLUXOS(3,J))-CURRENTOS(1,J)
       B(13,1)=-F*Z(1)
       B(13,3)=-F*Z(2)
       B(13,13)=+1.0

C      For current density-Imaginary

       G(14)=F*(Z(1)*FLUXOS(2,J)+Z(2)*FLUXOS(4,J))-CURRENTOS(2,J)
       B(14,2)=-F*Z(1)
       B(14,4)=-F*Z(2)
       B(14,14)=+1.0


C      For homogeneous reaction of electrons-real
       G(15)=-RATEE*(CNS(J)*CONCOS(3,J)+CPS(J)*CONCOS(1,J))
      1       -RXNOS(1,J)
       B(15,7)=RATEE*CNS(J)
       B(15,5)=RATEE*CPS(J)
       B(15,15)=+1.0

C      For homogeneous reaction of electrons-Imaginary
       G(16)=-RATEE*(CNS(J)*CONCOS(4,J)+CPS(J)*CONCOS(2,J))
      1       -RXNOS(2,J)
       B(16,8)=RATEE*CNS(J)
       B(16,6)=RATEE*CPS(J)
       B(16,16)=+1.0

C      For homogeneous reaction of holes-real
       G(17)=-RATEE*(CNS(J)*CONCOS(3,J)+CPS(J)*CONCOS(1,J))
      1       -RXNOS(3,J)
       B(17,7)=RATEE*CNS(J)
       B(17,5)=RATEE*CPS(J)
       B(17,17)=+1.0

C      For homogeneous reaction of holes-Imaginary
       G(18)=-RATEE*(CNS(J)*CONCOS(4,J)+CPS(J)*CONCOS(2,J))
      1       -RXNOS(4,J)
       B(18,8)=RATEE*CNS(J)
       B(18,6)=RATEE*CPS(J)
       B(18,18)=+1.0

       CONTINUE

  206  WRITE(12,301) J, (G(K),K=1,N)

C   888  WRITE(88,866) J, (B(1,1)),(B(2,2)),(B(3,1)),(B(3,3)),(B(3,5)),
C     1 (B(4,2)),(B(4,4)),(B(4,5)),(B(5,5)),(B(5,6)),(B(6,3)),(B(6,4)),
C     2 (B(6,5)),(B(6,6))

```

```
      PRINT *, 'ITERATION=', JCOUNT
      RETURN
      END

C     SUBROUTINE MATINV
      SUBROUTINE MATINV(N,M,DETERM)
      IMPLICIT DOUBLE PRECISION (A-H,O-Z)
      COMMON/BAB/ A(18,18),B(18,18),C(18,100001),D(18,37),G(18)
     1           ,X(18,18),Y(18,18)
      COMMON/NSN/ NTEMP, NJ
      DIMENSION ID(18)
      DETERM=1.01
      DO 1 I=1,N
    1 ID(I)=0
      DO 18 NN=1,N
      BMAX=1.1
      DO 6 I=1,N
      IF(ID(I).NE.0) GO TO 6
      BNEXT=0.0
      BTRY=0.0
      DO 5 J=1,N
      IF (ID(J).NE.0) GO TO 5
      IF (DABS(B(I,J)).LE.BNEXT) GO TO 5
      BNEXT=DABS(B(I,J))
      IF (BNEXT.LE.BTRY) GO TO 5
      BNEXT=BTRY
      BTRY=DABS(B(I,J))
      JC=J
    5 CONTINUE
      IF(BNEXT.GE.BMAX*BTRY) GO TO 6
      BMAX=BNEXT/BTRY
      IROW=I
      JCOL=JC
    6 CONTINUE
      IF (ID(JC).EQ.0) GO TO 8
      DETERM=0.0
      RETURN
    8 ID(JCOL)=1
      IF (JCOL.EQ.IROW) GO TO 12
      DO 10 J=1,N
      SAVE=B(IROW,J)
      B(IROW,J)=B(JCOL,J)
   10 B(JCOL,J)=SAVE
      DO 11 K=1,M
      SAVE=D(IROW,K)
      D(IROW,K)=D(JCOL,K)
   11 D(JCOL,K)=SAVE
   12 F=1.0/B(JCOL,JCOL)
      DO 13 J=1,N
   13 B(JCOL,J)=B(JCOL,J)*F
      DO 14 K=1,M
   14 D(JCOL,K)=D(JCOL,K)*F
      DO 18 I=1,N
      IF (I.EQ.JCOL)  GO TO 18
      F=B(I,JCOL)
      DO 16  J=1,N
   16 B(I,J)=B(I,J)-F*B(JCOL,J)
      DO 17 K=1,M
```

```
   17   D(I,K)=D(I,K)-F*D(JCOL,K)
   18   CONTINUE
        RETURN
        END

C       SUBROUTINE  BAND(J)
        SUBROUTINE BAND(J)
        IMPLICIT DOUBLE PRECISION (A-H,O-Z)
        DIMENSION E(18,19,100001)
        COMMON/BAB/ A(18,18),B(18,18),C(18,100001),D(18,37),G(18)
       1           ,X(18,18),Y(18,18)
        COMMON/NSN/ N,NJ
        SAVE E, NP1
  101   FORMAT(15H DETERM=0 AT J=,I5)
        IF (J-2) 1,6,8
    1   NP1=N+1
        DO 2 I=1,N
        D(I,2*N+1)=G(I)
        DO 2 L=1,N
        LPN=L+N
    2   D(I,LPN)=X(I,L)
        CALL MATINV(N, 2*N+1,DETERM)
        IF (DETERM) 4,3,4
    3   PRINT 101,J
    4   DO 5 K=1,N
        E(K,NP1,1)=D(K,2*N+1)
        DO 5 L=1,N
        E(K,L,1)=-D(K,L)
        LPN=L+N
    5   X(K,L)=-D(K,LPN)
        RETURN
    6   DO 7 I=1,N
        DO 7 K=1,N
        DO 7 L=1,N
    7   D(I,K)=D(I,K)+A(I,L)*X(L,K)
    8   IF (J-NJ) 11,9,9
    9   DO 10 I=1,N
        DO 10 L=1,N
        G(I)=G(I)-Y(I,L)*E(L,NP1,J-2)
        DO 10 M=1,N
   10   A(I,L)=A(I,L)+Y(I,M)*E(M,L,J-2)
   11   DO 12 I=1,N
        D(I,NP1)=-G(I)
        DO 12 L=1,N
        D(I,NP1)=D(I,NP1)+A(I,L)*E(L,NP1,J-1)
        DO 12 K=1,N
   12   B(I,K)=B(I,K)+A(I,L)*E(L,K,J-1)
        CALL MATINV(N,NP1,DETERM)
        IF (DETERM) 14, 13, 14
   13   PRINT 101,J
   14   DO 15 K=1,N
        DO 15 M=1,NP1
   15   E(K,M,J)=-D(K,M)
        IF (J-NJ) 20,16,16
   16   DO 17 K=1,N
   17   C(K,J)=E(K,NP1,J)
        DO 18 JJ=2,NJ
        M=NJ-JJ+1
```

```
      DO  18  K=1,N
      C(K,M)=E(K,NP1,M)
      DO  18  L=1,N
   18 C(K,M)=C(K,M)+E(K,L,M)*C(L,M+1)
      DO  19  L=1,N
      DO  19  K=1,N
   19 C(K,1)=C(K,1)+X(K,L)*C(L,3)
   20 RETURN
      END
```

REFERENCES

[1] P. Agarwal, M. E. Orazem, and L. H. García-Rubio, "Measurement models for electrochemical impedance spectroscopy: 1. Demonstration of applicability," *Journal of the Electrochemical Society*, vol. 139, pp. 1917–1927, July 1992.

[2] P. Agarwal, O. D. Crisalle, M. E. Orazem, and L. H. García-Rubio, "Measurement models for electrochemical impedance spectroscopy: 2. Determination of the stochastic contribution to the error structure," *Journal of the Electrochemical Society*, vol. 142, pp. 4149–4158, 1995.

[3] P. Agarwal, M. E. Orazem, and L. H. García-Rubio, "Measurement models for electrochemical impedance spectroscopy: 3. Evaluation of consistency with the Kramers–Kronig relations," *Journal of the Electrochemical Society*, vol. 142, pp. 4159–4168, 1995.

[4] B. A. Boukamp, "A linear Kramers–Kronig transform test for immittance data validation," *Journal of The Electrochemical Society*, vol. 142, pp. 1885–1894, June 1995.

[5] G. Brooks, "A short history of the candu nuclear power system," tech. rep., INIS International NuclearInformation System, 1993.

[6] NWMO, "What is used nuclear fuel?." https://www.nwmo.ca/~/media/Site/Files/PDFs/2021/03/15/20/45/Backgrounder-2021-What-is-used-nuclear-fuel.ashx?la=en, Accessed: 25-Nov-2021.

[7] NWMO, "Canada's used nuclear fuel: How is it stored today?." https://www.nwmo.ca/en/Canadas-Plan/Canadas-Used-Nuclear-Fuel/How-Is-It-Stored-Today, Accessed: 04-Mar-2022.

[8] NWMO, "Canada's used nuclear fuel: About adaptive phased management." https://www.nwmo.ca/en/Canadas-Plan/About-Adaptive-Phased-Management-APM, Accessed: 04-Mar-2022.

[9] NWMO, "Deep geological repository." https://www.nwmo.ca/en/A-Safe-Approach/Facilities/Deep-Geological-Repository, Accessed: 04-Mar-2022.

[10] J. Noronha, "Deep geological repositoryconceptual design reportcrystalline / sedimentary rockenvironment," tech. rep., Nuclear Waste Management Organization, 2016.

[11] NWMO, "Multiple-barrier system." https://www.nwmo.ca/en/A-Safe-Approach/Facilities/Deep-Geological-Repository/Multiple-Barrier-System, Accessed: 25-Nov-2021.

[12] F. King, D. S. Hall, and P. G. Keech, "Nature of the near-field environment in a deep geological repository and the implications for the corrosion behaviour of the container," *The International Journal of Corrosion Processes and Corrosion Control*, vol. 52, pp. 25–30, 2017.

[13] D. S. Hall, M. Behazin, W. Jeffrey Binns, and P. G. Keech, "An evaluation of corrosion processes affecting copper-coated nuclear waste containers in a deep geological repository," *Progress in Materials Science*, vol. 118, p. 100766, 2021.

[14] T. S. C. I. R. Group, "The corrosion resistance of a copper canister for spent nuclearfuel—follow up," Tech. Rep. report no. SKBF/KBS TR 83-24, Swedish Corrosion Institute, 1983.

[15] N. K. Lars Werme, Patrik Sellin, "Copper canisters for nuclear high level wastedisposal. corrosion aspects," Tech. Rep. technical report no. TR 92-26, Swedish Nuclear Fuel and Waste Management Co, 1992.

[16] Å. Björkbacka, S. Hosseinpour, M. Johnson, C. Leygraf, and M. Jonsson, "Radiation induced corrosion of copper for spent nuclear fuel storage," *Radiation Physics and Chemistry*, vol. 92, no. 80-86, 2013.

[17] F. King and M. Kolar, "The copper container corrosion model used in aecl's second case study," Nuclear Waste Management Division Report 06819 REP 01200 10041 R00, Ontario Power Generation, 2000.

[18] F. King, C. Litke, M. Quinn, and D. LeNeveu, "The measurement and prediction of the corrosion potential of copper in chloride solutions as a function of oxygen concentration and mass transfer coefficient," *Corros. Sci*, vol. 37, pp. 833–851, 1995.

[19] F. King and M. Kolar, "Mechanistic modelling of the corrosionbehaviour of copper nuclear fuel wastecontainers. in proc. int. conf. deep geological disposal of radioactive waste," Tech. Rep. p. 5-39 to 5-50, Canadian Nuclear Society, Toronto, ON, 1996.

[20] F. King and M. Kolar, "A numerical model for the corrosion of copper nuclear fuel waste containers. in scientific basis for nuclear waste management xix, (w.m. murphy and d. knecht, editors," *Material Research Society Proceedings*, vol. 412, pp. 555–562, 1996.

[21] F. King and M. Kolar, "The effect of geosphere conditions on the lifetimes of copper containers," Atomic Energy of Canada Limited Report AECL 11717, COG 96 565, Atomic Energy of Canada, 1997.

[22] F. King and M. Kolar, "Corrosion of copper containers prior to saturation of a nuclear fuel waste disposal vault," Atomic Energy of Canada Limited Report AECL 11718, . Atomic Energy of Canada, 1997.

[23] F. King and M. Kolar, "Simulation of the consumption of oxygen in long-term in situ experiments and in the third case study repository using the copper corrosion model ccm-uc.1.1.," Nuclear Waste Management Division Report 06819 REP 01300 10084 R00, Ontario Power Generation, 2006.

[24] F. King, "Theory manual for the copper corrosion model for uniform corrosion in sedimentary rock ccm-uc.1.1," Nuclear Waste Management Organization Technical Report NWMO TR 2008 07, Nuclear Waste Management Organization, 2008.

[25] L. H. Johnson, D. LeNeveu, F. King, D. Shoesmith, M. Kolar, D. Oscarson, S. Sunder, C. Onofrei, and J. Crosthwaite, "The disposal of canada's nuclear fuel waste: A study of postclosure safety of in-roomemplacement of used c andu fuel in coppercontainers in permeable plutonic rockvolume 2: Vault model," Atomic Energy of Canada Limited Report AECL-11494-2, COG-96-552-2, Atomic Energy of Canada Ltd, 1996.

[26] F. King and S. Briggs, "Development and validation of a comsol version of the copper corrosion model," Tech. Rep. NWMO TR-2022-08, Nuclear Waste Management Organization, 2022.

[27] U. R. Evans, *The Corrosion of Metals*. E. Arnold & Company, London, 1926.

[28] J. Jiang, J. Wang, W. Wang, and W. Zhang, "Modeling influence of gasliquid/solid three-phase boundary zone on cathodic process of soil corrosion," *Electrochimica Acta*, vol. 54, pp. 3623–3629, May 2009.

[29] I. Cole, T. Muster, N. Azmat, M. Venkatraman, and A. Cook, "Multiscale modelling of the corrosion of metals under atmospheric corrosion," *Electrochimica Acta*, vol. 56, pp. 1856–1865, Jan. 2011.

[30] Y.-C. Chang, R. Woollam, and M. E. Orazem, "Mathematical models for under-deposit corrosion: I. aerated media," *Journal of the Electrochemical Society*, vol. 161, no. 6, pp. C321–C329, 2014.

[31] A. Ekimov, A. Efros, and A. Onushchenko, "Quantum size effect in semiconductor microcrystals," *Solid State Communications*, vol. 56, no. 11, pp. 921 – 924, 1985.

[32] R. Rossetti, S. Nakahara, and L. E. Brus, "Quantum size effects in the redox potentials, resonance raman spectra, and electronic spectra of cds crystallites in aqueous solution," *The Journal of Chemical Physics*, vol. 79, no. 2, pp. 1086–1088, 1983.

[33] L. E. Brus, "Electron–electron and electron-hole interactions in small semiconductor crystallites: The size dependence of the lowest excited electronic state," *The Journal of Chemical Physics*, vol. 80, pp. 4403–4409, May 1984.

[34] I. V. Martynenko, A. P. Litvin, F. Purcell-Milton, A. V. Baranov, A. V. Fedorov, and Y. K. Gun'ko, "Application of semiconductor quantum dots in bioimaging and biosensing," *Journal of Materials Chemistry B: Materials for Biology and Medicine*, vol. 5, pp. 6701–6727, 2017.

[35] K. W. J. Barnham and G. Duggan, "A new approach to high—efficiency multi—band—gap solar cells," *Journal of Applied Physics*, vol. 67, no. 7, pp. 3490–3493, 1990.

[36] C. S. Lent and P. D. Tougaw, "A device architecture for computing with quantum dots," *Proceedings of the IEEE*, vol. 85, pp. 541–557, Apr. 1997.

[37] J. Zhao, M. Holmes, and F. Osterloh, "Quantum confinement controls photocatalysis: A free energy analysis for photocatalytic proton reduction at cdse nanocrystals," *ACS nano*, vol. 7, Apr. 2013.

[38] V. Colvin, M. Schlamp, and A. Alivisatos, "Light-emitting diodes made from cadmium selenide nanocrystals and a semiconducting polymer," *Nature*, vol. 370, pp. 354–357, Aug. 1994.

[39] P. O. Anikeeva, J. E. Halpert, M. G. Bawendi, and V. Bulović, "Quantum Dot Light-Emitting Devices with Electroluminescence Tunable over the Entire Visible Spectrum," *Nano Letters*, vol. 9, pp. 2532–2536, July 2009.

[40] L. Qian, Y. Zheng, J. Xue, and P. Holloway, "Stable and efficient quantum-dot light-emitting diodes based on solution-processed multilayer structures[j]," *Nature Photonics - NAT PHOTONICS*, vol. 5, pp. 543–548, Aug. 2011.

[41] T. Ding, X. Yang, L. Ke, Y. Liu, W.-Y. Tan, N. Wang, X.-H. Zhu, and X. W. Sun, "Improved quantum dot light-emitting diodes with a cathode interfacial layer," *Organic Electronics*, vol. 32, pp. 89 – 93, 2016.

[42] B. Hirschorn, M. E. Orazem, B. Tribollet, V. Vivier, I. Frateur, and M. Musiani, "Constant-phase-element behavior caused by resistivity distributions in films: 1. Theory," *Journal of the Electrochemical Society*, vol. 157, pp. C452–C457, 2010.

[43] B. Hirschorn, M. E. Orazem, B. Tribollet, V. Vivier, I. Frateur, and M. Musiani, "Constant-phase-element behavior caused by resistivity distributions in films: 2. Applications," *Journal of the Electrochemical Society*, vol. 157, pp. C458–C463, 2010.

[44] M. E. Orazem, B. Tribollet, V. Vivier, S. Marcelin, N. Pébère, A. L. Bunge, E. A. White, D. P. Riemer, I. Frateur, and M. Musiani, "Dielectric properties of materials showing constant-phase-element (CPE) impedance response," *Journal of the Electrochemical Society*, vol. 160, pp. C215–C225, 2013.

[45] S. Amand, M. Musiani, M. E. Orazem, N. Pébère, B. Tribollet, and V. Vivier, "Constant-phase-element behavior caused by inhomogeneous water uptake in anti-corrosion coatings," *Electrochimica Acta*, vol. 87, pp. 693–700, 2013.

[46] M. E. Orazem, B. Tribollet, V. Vivier, D. P. Riemer, E. A. White, and A. L. Bunge, "On the use of the power-law model for interpreting constant-phase-element parameters," *Journal of the Brazilian Chemical Society*, vol. 25, pp. 532–539, 2014.

[47] H. Liao, W. Watson, A. Dizon, B. Tribollet, V. Vivier, and M. E. Orazem, "Physical properties obtained from measurement model analysis of impedance measurements," *Electrochimica Acta*, vol. 354, p. 136747, Sept. 2020.

[48] Y. Sakamoto, M. Ishiguso, and G. Kitigawa, *Akaike Information Criterion Statistics*. Boston: D. Reidel, 1986.

[49] M. E. Orazem and B. Tribollet, *Electrochemical Impedance Spectroscopy*. Hoboken: John Wiley & Sons, 2 ed., 2017.

[50] J. Cho, H. Kim, K. Jang, H. Sohn, J. Kim, J. Heo, J. Yi, S. Sohn, E. Nam, and D. Jung, "Electrical properties of organic light-emitting diodes fabricated on hfox-treated indium-tin-oxide surfaces by using an impedance spectroscopy analysis," *Journal of The Korean Physical Society*, vol. 53, Dec. 2008.

[51] S. Nowy, W. Ren, J. Wagner, J. A. Weber, and W. Brütting, "Impedance spectroscopy of organic hetero-layer OLEDs as a probe for charge carrier injection and device degradation," in *Organic Light Emitting Materials and Devices XIII* (F. So and C. Adachi, eds.), vol. 7415, pp. 79 – 90, International Society for Optics and Photonics, SPIE, 2009.

[52] C.-C. Hsiao, C.-H. Chang, T.-H. Jen, M.-C. Hung, and S.-A. Chen, "High-efficiency polymer light-emitting diodes based on poly[2-methoxy-5-(2-ethylhexyloxy)-1,4-phenylene vinylene] with plasma-polymerized chf3-modified indium tin oxide as an anode," *Applied Physics Letters*, vol. 88, no. 3, p. 033512, 2006.

[53] K. Kwak, K. Cho, and S. Kim, "Analysis of thermal degradation of organic light-emitting diodes with infrared imaging and impedance spectroscopy," *Optics express*, vol. 21, pp. 29558–66, Dec. 2013.

[54] S. D. Cai, C. H. Gao, D. Y. Zhou, W. Gu, and L. S. Liao, "Study of hole-injecting properties in efficient, stable, and simplified phosphorescent organic light-emitting diodes by impedance spectroscopy," *ACS Applied Materials & Interfaces*, vol. 4, no. 1, pp. 312–316, 2012.

[55] P. Chulkin, M. Lapkowski, M. R. Bryce, J. Santos, and P. Data, "Determination of standard redox rate constants of oled active compounds by electrochemical impedance spectroscopy," *Electrochimica Acta*, vol. 258, pp. 1160 – 1172, 2017.

[56] P. Chulkin, O. Vybornyi, M. Lapkowski, P. J. Skabara, and P. Data, "Impedance spectroscopy of oleds as a tool for estimating mobility and the concentration of charge carriers in transport layers," *Journal of Materials Chemistry C: Materials for Optical and Electronic Devices*, vol. 6, pp. 1008–1014, 2018.

[57] P. Tyagi, R. Srivastava, L. I. Giri, S. Tuli, and C. Lee, "Degradation of organic light emitting diode: Heat related issues and solutions," *Synthetic Metals*, vol. 216, pp. 40 – 50, 2016.

[58] F. So and D. Kondakov, "Degradation mechanisms in small-molecule and polymer organic light-emitting diodes," *Advanced Materials*, vol. 22, no. 34, pp. 3762–3777, 2010.

[59] R. Zheng, W.-B. Huang, W. Xu, and Y. Cao, "Analysis of intrinsic degradation mechanism in organic light-emitting diodes by impedance spectroscopy," *Chinese Physics Letters*, vol. 31, p. 027703, Feb. 2014.

[60] S. Chen, W. Cao, T. Liu, S.-W. Tsang, Y. Yang, X. Yan, and L. Qian, "On the degradation mechanisms of quantum-dot light-emitting diodes," in *Nature Communications*, 2019.

[61] A. Sacco, "Electrochemical impedance spectroscopy: Fundamentals and application in dye-sensitized solar cells," *Renewable and Sustainable Energy Reviews*, vol. 79, pp. 814–829, Nov. 2017.

[62] X. Yuan, H. Wang, J. Colinsun, and J. Zhang, "AC impedance technique in PEM fuel cell diagnosis—a review," *International Journal of Hydrogen Energy*, vol. 32, pp. 4365–4380, Dec. 2007.

[63] F. Huet, "A review of impedance measurements for determination of the state-of-charge or state-of-health of secondary batteries," *Journal of Power Sources*, vol. 70, pp. 59–69, Jan. 1998.

[64] S. Zhang, K. Xu, and T. Jow, "EIS study on the formation of solid electrolyte interface in li-ion battery," *Electrochimica Acta*, vol. 51, pp. 1636–1640, Jan. 2006.

[65] I. J. Gordon, S. Grugeon, H. Takenouti, B. Tribollet, M. Armand, C. Davoisne, A. Débart, and S. Laruelle, "Electrochemical impedance spectroscopy response study of a commercial graphite-based negative electrode for li-ion batteries as function of the cell state of charge and ageing," *Electrochimica Acta*, vol. 223, pp. 63–73, Jan. 2017.

[66] M. Ates, "Review study of electrochemical impedance spectroscopy and equivalent electrical circuits of conducting polymers on carbon surfaces," *Progress in Organic Coatings*, vol. 71, pp. 1–10, May 2011.

[67] E. Cano, D. Lafuente, and D. M. Bastidas, "Use of EIS for the evaluation of the protective properties of coatings for metallic cultural heritage: a review," *Journal of Solid State Electrochemistry*, vol. 14, pp. 381–391, Aug. 2009.

[68] V. M. Huang, S.-L. Wu, M. E. Orazem, N. Pébère, B. Tribollet, and V. Vivier, "Local electrochemical impedance spectroscopy: A review and some recent developments," *Electrochimica Acta*, Apr. 2011.

[69] T. Muselle, H. Simillion, D. V. Laethem, J. Deconinck, and A. Hubin, "Feasibility study and cell design for performing local electrochemical impedance spectroscopy measurements using an atomic force microscopy set-up," *Electrochimica Acta*, vol. 245, pp. 173–185, Aug. 2017.

[70] R. Montoya, F. García-Galván, A. Jiménez-Morales, and J. Galván, "Effect of conductivity and frequency on detection of heterogeneities in solid/liquid interfaces using local electrochemical impedance," *Electrochemistry Communications*, vol. 15, pp. 5–9, Feb. 2012.

[71] M. Mouanga, M. Puiggali, B. Tribollet, V. Vivier, N. Pébère, and O. Devos, "Galvanic corrosion between zinc and carbon steel investigated by local electrochemical impedance spectroscopy," *Electrochimica Acta*, vol. 88, pp. 6–14, Jan. 2013.

[72] C. Gabrielli and M. Keddam, "Review of applications of impedance and noise analysis to uniform and localized corrosion," *CORROSION*, vol. 48, pp. 794–811, Oct. 1992.

[73] M. A. Zabara, C. B. Uzundal, and B. Ulgut, "Linear and nonlinear electrochemical impedance spectroscopy studies of li/SOCl2batteries," *Journal of The Electrochemical Society*, vol. 166, no. 6, pp. A811–A820, 2019.

[74] T. Osaka, D. Mukoyama, and H. Nara, "Review—development of diagnostic process for commercially available batteries, especially lithium ion battery, by electrochemical impedance spectroscopy," *Journal of The Electrochemical Society*, vol. 162, no. 14, pp. A2529–A2537, 2015.

[75] C. Andrade, V. Castelo, C. Alonso, and J. González, "The determination of the corrosion rate of steel embedded in concrete by the polarization resistance and AC impedance methods," in *Corrosion Effect of Stary Currents and the Techniques for Evaluating Corrosion of Rebars in Concrete*, pp. 43–43–21, ASTM International, 1986.

[76] J. L. Ramirez-Reyes, G. Galicia-Aguilar, J. M. Malo-Tamayo, and J. Uruchurtu-Chavarin, "Electrochemical studies on inorganic zero VOC coated steel in atmospheric exposure and REAP test," *ECS Transactions*, vol. 64, pp. 35–44, Apr. 2015.

[77] "Iviumstat.h standard." https://www.ivium.com/product/iviumstat-h-standard/, Accessed: 02-Nov-2019.

[78] S. C. Creason and D. E. Smith, "Fourier transform faradaic admittance measurements," *Journal of Electroanalytical Chemistry and Interfacial Electrochemistry*, vol. 36, pp. A1–A7, Apr. 1972.

[79] D. E. Smith, "The acquisition of electrochemical response spectra by on-line fast fourier transform. data processing in electrochemistry," *Analytical Chemistry*, vol. 48, pp. 221A–240, Feb. 1976.

[80] "Multisine eis implementation: Gamry optieis." https://www.gamry.com/application-notes/EIS/optieis-a-multisine-implementation/, Accessed: 02-Nov-2019.

[81] Bio-Logic, "Eis measurements with multisine." https://www.bio-logic.net/wp-content/uploads/20101209-Application-note-19.pdf, Accessed: 02-Nov-2019.

[82] J. Házì, D. M. Elton, W. A. Czerwinski, J. Schiewe, V. A. Vicente-Beckett, and A. M. Bond, "Microcomputer-based instrumentation for multi-frequency fourier transform alternating current (admittance and impedance) voltammetry," *Journal of Electroanalytical Chemistry*, vol. 437, pp. 1–15, Nov. 1997.

[83] J.-S. Yoo and S.-M. Park, "An electrochemical impedance measurement technique employing fourier transform," *Analytical Chemistry*, vol. 72, pp. 2035–2041, Mar. 2000.

[84] J. Garland, C. Pettit, and D. Roy, "Analysis of experimental constraints and variables for time resolved detection of fourier transform electrochemical impedance spectra," *Electrochimica Acta*, vol. 49, pp. 2623–2635, July 2004.

[85] Y. Van Ingelgem, E. Tourwé, O. Blajiev, R. Pintelon, and A. Hubin, "Advantages of odd random phase multisine electrochemical impedance measurements," *Electroanalysis*, vol. 21, pp. 730–739, Mar. 2009.

[86] C. jiang Yang, Y. Ko, and S.-M. Park, "Fourier transform electrochemical impedance spectroscopic studies on anodic reaction of lead," *Electrochimica Acta*, vol. 78, pp. 615–622, Sept. 2012.

[87] D. H. Griffiths, *Fourier Transform 2e C*. John Wiley & Sons, Apr. 2007.

[88] E. D. Becker and T. C. Farrar, "Fourier transform spectroscopy," *Science*, vol. 178, pp. 361–368, Oct. 1972.

[89] W. H. Smyrl, "Digital impedance for faradaic analysis: II . electrodissolution of cu in," *Journal of The Electrochemical Society*, vol. 132, pp. 1555–1562, July 1985.

[90] W. H. Smyrl and L. L. Stephenson, "Digital impedance for faradaic analysis: III . copper corrosion in oxygenated," *Journal of The Electrochemical Society*, vol. 132, pp. 1563–1567, July 1985.

[91] J. Ühlken, R. Waser, and H. Wiese, "A fourier transform impedance spectrometer using logarithmically spaced time samples," *Berichte der Bunsengesellschaft für physikalische Chemie*, vol. 92, pp. 730–735, June 1988.

[92] G. S. Popkirov and R. N. Schindler, "A new impedance spectrometer for the investigation of electrochemical systems," *Review of Scientific Instruments*, vol. 63, pp. 5366–5372, Nov. 1992.

[93] G. S. Popkirov and R. N. Schindler, "Optimization of the perturbation signal for electrochemical impedance spectroscopy in the time domain," *Review of Scientific Instruments*, vol. 64, pp. 3111–3115, Nov. 1993.

[94] E. V. Gheem, R. Pintelon, J. Vereecken, J. Schoukens, A. Hubin, P. Verboven, and O. Blajiev, "Electrochemical impedance spectroscopy in the presence of non-linear distortions and non-stationary behaviour," *Electrochimica Acta*, vol. 49, pp. 4753–4762, Oct. 2004.

[95] E. V. Gheem, R. Pintelon, A. Hubin, J. Schoukens, P. Verboven, O. Blajiev, and J. Vereecken, "Electrochemical impedance spectroscopy in the presence of non-linear distortions and non-stationary behaviour," *Electrochimica Acta*, vol. 51, pp. 1443–1452, Jan. 2006.

[96] M. Meeusen, P. Visser, L. F. Macía, A. Hubin, H. Terryn, and J. Mol, "The use of odd random phase electrochemical impedance spectroscopy to study lithium-based corrosion inhibition by active protective coatings," *Electrochimica Acta*, vol. 278, pp. 363–373, July 2018.

[97] T. Hauffman, Y. van Ingelgem, T. Breugelmans, E. Tourwé, H. Terryn, and A. Hubin, "Dynamic, in situ study of self-assembling organic phosphonic acid monolayers from ethanolic solutions on aluminium oxides by means of odd random phase multisine electrochemical impedance spectroscopy," *Electrochimica Acta*, vol. 106, pp. 342–350, Sept. 2013.

[98] G. Meyer, H. Ochs, W. Strunz, and J. Vogelsang, "Barrier coatings with high ohmic resistance: Comparison between relaxation voltammetry and electrochemical impedance spectrosscopy," *Materials Science Forum*, vol. 289-292, pp. 305–314, Aug. 1998.

[99] R. Jurczakowski and A. Lasia, "Limitations of the potential step technique to impedance measurements using discrete time fourier transform," *Analytical Chemistry*, vol. 76, pp. 5033–5038, July 2004.

[100] "Zahner-elektrik gmbh & cokg - germany • highend data acquisition systems for electrochemical applications — imsine - intelligent multi-sine excitation.." http://zahner.de/support/application-notes/imsine-intelligent-multi-sine-excitation.html, Accessed: 02-Nov-2019.

[101] M. Urquidi-Macdonald, S. Real, and D. D. Macdonald, "Application of Kramers–Kronig transforms in the analysis of electrochemical impedance data: II . transformations in the complex plane," *Journal of The Electrochemical Society*, vol. 133, pp. 2018–2024, Oct. 1986.

[102] B. Hirschorn and M. E. Orazem, "On the sensitivity of the Kramers–Kronig relations to nonlinear effects in impedance measurements," *Journal of The Electrochemical Society*, vol. 156, no. 10, p. C345, 2009.

[103] D. D. Macdonald, "Reflections on the history of electrochemical impedance spectroscopy," *Electrochimica Acta*, vol. 51, pp. 1376–1388, Jan. 2006.

[104] M. Urquidi-Macdonald, S. Real, and D. D. Macdonald, "Applications of Kramers–Kronig transforms in the analysis of electrochemical impedance data—III. stability and linearity," *Electrochimica Acta*, vol. 35, pp. 1559–1566, Oct. 1990.

[105] R. Srinivasan, V. Ramani, and S. Santhanam, "Multi-sine EIS- drift, non linearity and solution resistance effects," *ECS Transactions*, vol. 45, pp. 37–50, Feb. 2013.

[106] R. L. Sacci, F. Seland, and D. A. Harrington, "Dynamic electrochemical impedance spectroscopy, for electrocatalytic reactions," *Electrochimica Acta*, vol. 131, pp. 13–19, June 2014.

[107] J. R. Macdonald, "Some new directions in impedance spectroscopy data analysis," *Electrochimica Acta*, vol. 38, pp. 1883–1890, Oct. 1993.

[108] J. S. Newman, "Resistance for flow of current to a disk," *Journal of the Electrochemical Society*, vol. 113, no. 5, pp. 501–502, 1966.

[109] J. S. Newman, "Current distribution on a rotating disk below the limiting current," *Journal of the Electrochemical Society*, vol. 113, pp. 1235–1241, 1966.

[110] W. R. Parrish and J. Newman, "Current distribution on a plane electrode below the limiting current," *Journal of The Electrochemical Society*, vol. 116, no. 2, p. 169, 1969.

[111] W. Parrish and J. S. Newman, "Current distributions on plane, parallel electrodes in channel flow," *Journal of the Electrochemical Society*, vol. 117, pp. 43–48, January 1970.

[112] W. H. Smyrl and J. S. Newman, "Detection of nonuniform current distribution on a disk electrode," *Journal of the Electrochemical Society*, vol. 119, pp. 208–212, 1972.

[113] J. S. Newman, "Frequency dispersion in capacity measurements at a disk electrode," *Journal of the Electrochemical Society*, vol. 117, pp. 198–203, 1970.

[114] V. M.-W. Huang, V. Vivier, M. E. Orazem, N. Pébère, and B. Tribollet, "The apparent CPE behavior of a disk electrode with faradaic reactions," *Journal of the Electrochemical Society*, vol. 154, pp. C99–C107, 2007.

[115] M. E. Orazem and B. Tribollet, *Electrochemical Impedance Spectroscopy*. Hoboken: John Wiley & Sons, 2 ed., 2017.

[116] K. Nisancioglu and J. S. Newman, "The transient response of a disk electrode," *Journal of the Electrochemical Society*, vol. 120, pp. 1339–1346, 1973.

[117] K. Nisancioglu and J. S. Newman, "The short-time response of a disk electrode," *Journal of the Electrochemical Society*, vol. 121, pp. 523–527, 1974.

[118] P. Antohi and D. A. Scherson, "Current distribution at a disk electrode during a current pulse," *Journal of the Electrochemical Society*, vol. 153, pp. E17–E24, 2006.

[119] S. B. Adler, "Reference electrode placement in thin solid electrolytes," *Journal of The Electrochemical Society*, vol. 149, no. 5, p. E166, 2002.

[120] M. Ender, J. Illig, and E. Ivers-Tiffée, "Three-electrode setups for lithium-ion batteries," *Journal of The Electrochemical Society*, vol. 164, pp. A71–A79, Dec. 2016.

[121] P. Córdoba-Torres, T. J. Mesquita, and R. P. Nogueira, "Influence of geometry-induced current and potential distributions on the characterization of constant-pphase element behavior," *Electrochimica Acta*, vol. 87, pp. 676–685, 2013.

[122] V. M.-W. Huang, V. Vivier, M. E. Orazem, N. Pébère, and B. Tribollet, "The apparent CPE behavior of an ideally polarized blocking electrode: A global and local impedance analysis," *Journal of the Electrochemical Society*, vol. 154, pp. C81–C88, 2007.

[123] V. M.-W. Huang, V. Vivier, I. Frateur, M. E. Orazem, and B. Tribollet, "The global and local impedance response of a blocking disk electrode with local CPE behavior," *Journal of the Electrochemical Society*, vol. 154, pp. C89–C98, 2007.

[124] O. Gharbi, A. Dizon, M. E. Orazem, M. T. Tran, B. Tribollet, and V. Vivier, "From frequency dispersion to ohmic impedance: A new insight on the high-frequency impedance analysis of electrochemical systems," *Electrochimica Acta*, vol. 320, p. 134609, Oct. 2019.

[125] B. Hirschorn, M. E. Orazem, B. Tribollet, V. Vivier, I. Frateur, and M. Musiani, "Constant-phase-element behavior caused by resistivity distributions in films: 1. Theory," *Journal of the Electrochemical Society*, vol. 157, pp. C452–C457, 2010.

[126] B. A. Boukamp and J. R. Macdonald, "Alternatives to Kronig–Kramers transformation and testing, and estimation of distributions," *Solid State Ionics*, vol. 74, pp. 85–101, 1994.

[127] B. A. Boukamp, "A linear Kronig–Kramers transform test for immittance data validation," *Journal of the Electrochemical Society*, vol. 142, pp. 1885–1894, 1995.

[128] C. You, M. A. Zabara, M. E. Orazem, and B. Ulgut, "Application of the Kramers–Kronig relations to multi-sine electrochemical impedance measurements," *Journal of The Electrochemical Society*, vol. 167, p. 020515, Jan. 2020.

[129] M. E. Orazem, P. T. Wojcik, M. Durbha, I. Frateur, and L. H. García-Rubio, "Application of measurement models for interpretation of impedance spectra for corrosion," *Materials Science Forum*, vol. 289-292, pp. 813–828, 1998.

[130] C. You, A. Titov, B. H. Kim, and M. E. Orazem, "Impedance measurements on QLED devices: analysis of high-frequency loop in terms of material properties," *Journal of Solid State Electrochemistry*, vol. 24, pp. 3083–3090, Aug. 2020.

[131] J. S. Newman and K. E. Thomas-Alyea, *Electrochemical Systems*. Hoboken: John Wiley & Sons, 3 ed., 2004.

[132] Y. Jiang, P. Ni, C. Chen, Y. Lu, P. Yang, B. Kong, A. Fisher, and X. Wang, "Selective electrochemical h2 o2 production through two-electron oxygen electrochemistry," *Advanced Energy Materials*, vol. 8, p. 1801909, Sept. 2018.

[133] O. E. Barcia, O. R. Mattos, N. Pébère, and B. Tribollet, "Mass-transport study for the electrodissolution of copper in 1m hydrochloric acid solution by impedance," *Journal of the Electrochemical Society*, vol. 140, pp. 2825–2832, October 1993.

[134] F. King, M. Kolar, and P. Maak, "Reactive-transport model for the prediction of the uniform corrosion behaviour of copper used fuel containers," *Journal of Nuclear Materials*, vol. 379, no. 1, pp. 133–141, 2008.

[135] A. E. Warraky, H. E. Shayeb, and E. Sherif, "Pitting corrosion of copper in chloride solutions," *Anti-Corrosion Methods and Materials*, vol. 51, pp. 52–61, feb 2004.

[136] D. L. Parkhurst, D. C. Thorstenson, and L. N. Plummer, "Phreeqe–a computer program for geochemical calculations," *Water-Resources Investigations Report*, 1980.

[137] D. L. Parkhurst and C. Appelo, "Description of input and examples for PHREEQC version 3: a computer program for speciation, batch-reaction, one-dimensional transport, and inverse geochemical calculations," 2013.

[138] U. G. Survey, "Attachment B–description of database files and listing." https://wwwbrr.cr.usgs.gov/projects/GWC_coupled/phreeqc/html/final-90.html, Accessed: 04-March-2022.

[139] X. Yuan, A. N. Pham, G. Xing, A. L. Rose, and T. D. Waite, "Effects of pH, chloride, and bicarbonate on cu(i) oxidation kinetics at circumneutral pH," *Environmental Science&Technology*, vol. 46, pp. 1527–1535, Jan. 2012.

[140] S. Briggs, C. Lilja, and F. King, "Probabilistic model for pitting of copper canisters," *Materials and Corrosion*, vol. 72, pp. 308–316, June 2020.

[141] D. A. G. Bruggeman, "Berechnung verschiedener physikalischer konstanten von heterogenen substanzen. i. dielektrizitätskonstanten und leitfähigkeiten der mischkörper aus isotropen substanzen," *Annalen der Physik*, vol. 416, no. 7, pp. 636–664, 1935.

[142] M. T. T. Tran, B. Tribollet, V. Vivier, and M. E. Orazem, "On the impedance response of reactions influenced by mass transfer," *Russian Journal of Electrochemistry*, vol. 53, pp. 932–940, sep 2017.

[143] D. Riemer and M. Orazem, "Modeling coating flaws with non-linear polarization curves for long pipelines," in *Modelling of Cathodic Protection Systems*, pp. 225–257, WIT Press, Nov. 2005.

[144] R. Guo, "Thermal response of a canadian conceptual deep geological repository in crystalline rock and a method to correct the influence of the near-field adiabatic boundary condition," *Engineering Geology*, vol. 218, pp. 50–62, 2017.

[145] J. Daintith, *A dictionary of chemistry*. New York: Oxford University Press, 2008.

[146] C. C. Miller, "The stokes-einstein law for diffusion in solution," *Proceedings of the Royal Society of London. Series A, Containing Papers of a Mathematical and Physical Character*, vol. 106, pp. 724–749, Dec. 1924.

[147] E. Riecke, H. Simon, P. Debye, and M. Born, *Physikalische Zeitschrift*, vol. 22. S. Hirzel, 1921.

[148] G. S. Fulcher, "ANALYSIS OF RECENT MEASUREMENTS OF THE VISCOSITY OF GLASSES," *Journal of the American Ceramic Society*, vol. 8, pp. 339–355, June 1925.

[149] G. Tammann and W. Hesse, "Die abhängigkeit der viscosität von der temperatur bie unterkühlten flüssigkeiten," *Zeitschrift für anorganische und allgemeine Chemie*, vol. 156, pp. 245–257, Oct. 1926.

[150] L. R. F. Allen J. Bard, *Electrochemical Methods: Fundamentals and Applications*. WILEY, Dec. 2000.

[151] C. Cleveland, M. E. Orazem, and S. Moghaddam, "Response to "comment on nanometer-scale corrosion of copper in de-aerated deionized water" [j. electrochem. soc., 161, c107 (2014)]," *Journal of The Electrochemical Society*, vol. 163, pp. Y5–Y11, Dec. 2015.

[152] R. E. Zeebe, "On the molecular diffusion coefficients of dissolved , and and their dependence on isotopic mass," *Geochimica et Cosmochimica Acta*, vol. 75, pp. 2483–2498, May 2011.

[153] J. Fritz and E. Koenigsberger, *Copper(I) Halides and Pseudohalides*, vol. 65. Oxford University Press, 1996.

[154] T. Dirkse, *Copper, Silver, Gold and Zinc, Cadmium, Mercury Oxides and Hydroxides*. Pergamon Press, 1986.

[155] E. Stricker, Z. Adler, J. Wainright, and R. Savinell, "Diffusion coefficients of cuprous and cupric ions in electrolytes with high concentrations of bromide ions," *Journal of Chemical&amp: Engineering Data*, vol. 64, pp. 1095–1100, Feb. 2019.

[156] A. C. F. Ribeiro, M. A. Esteso, V. M. M. Lobo, A. J. M. Valente, S. M. N. Simões, A. J. F. N. Sobral, and H. D. Burrows, "Diffusion coefficients of copper chloride in aqueous solutions at 298.15 k and 310.15 k," *Journal of Chemical&amp: Engineering Data*, vol. 50, pp. 1986–1990, Sept. 2005.

[157] J. Buffle, Z. Zhang, and K. Startchev, "Metal flux and dynamic speciation at (bio)interfaces. part i: Critical evaluation and compilation of physicochemical parameters for complexes with simple ligands and fulvic/humic substances," *Environmental Science&Technology*, vol. 41, no. 22, pp. 7609–7620, 2007. PMID: 18075065.

[158] J. V. Macpherson and P. R. Unwin, "Determination of the diffusion coefficient of hydrogen in aqueous solution using single and double potential step chronoamperometry at a disk ultramicroelectrode," *Analytical Chemistry*, vol. 69, pp. 2063–2069, June 1997.

[159] G. E. Dorfman, Leon M. ; Adams, "Reactivity of the hydroxyl radical in aqueous solutions," tech. rep., NATIONAL STANDARD REFERENCE DATA SYSTEM, 1973.

[160] M. Abdekhodaie, J. Cheng, and X. Wu, "Effect of formulation factors on the bioactivity of glucose oxidase encapsulated chitosan–alginate microspheres: In vitro investigation and mathematical model prediction," *Chemical Engineering Science*, vol. 125, pp. 4–12, Mar. 2015.

[161] C. R. Wilke and P. Chang, "Correlation of diffusion coefficients in dilute solutions," *AIChE Journal*, vol. 1, pp. 264–270, June 1955.

[162] M. Okuda, T. Tsuruta, and K. Katayama, "Lifetime and diffusion coefficient of active oxygen species generated in TiO2 sol solutions," *Physical Chemistry Chemical Physics*, vol. 11, no. 13, p. 2287, 2009.

[163] R. Sander, "Compilation of henry's law constants (version 4.0) for water as solvent," *Atmospheric Chemistry and Physics*, vol. 15, pp. 4399–4981, Apr. 2015.

[164] K. Yin, Y.-Y. Zhang, Y. Zhou, L. Sun, M. F. Chisholm, S. T. Pantelides, and W. Zhou, "Unsupported single-atom-thick copper oxide monolayers," *2D Materials*, vol. 4, p. 011001, Oct. 2016.

[165] X. Sun, W. Yu, B. Wu, and G. Yang, "Kinetics of dissolution of copper in liquid tin with ultrasonic waves," *Materials Research*, vol. 23, no. 1, 2020.

[166] R. Ghosh, V. Sudha, and S. Harinipriya, "Thermodynamic analysis of electrodeposition of copper from copper sulphate," *Bulletin of Materials Science*, vol. 42, Feb. 2019.

[167] D. Lloyd, T. Vainikka, L. Murtomäki, K. Kontturi, and E. Ahlberg, "The kinetics of the cu2+/cu+ redox couple in deep eutectic solvents," *Electrochimica Acta*, vol. 56, no. 14, pp. 4942–4948, 2011.

[168] B. M. Stühmeier, M. R. Pietsch, J. N. Schwämmlein, and H. A. Gasteiger, "Pressure and temperature dependence of the hydrogen oxidation and evolution reaction kinetics on pt electrocatalysts via PEMFC-based hydrogen-pump measurements," *Journal of The Electrochemical Society*, vol. 168, p. 064516, June 2021.

[169] A. B. Anderson, J. Roques, S. Mukerjee, V. S. Murthi, N. M. Markovic, and V. Stamenkovic, "Activation energies for oxygen reduction on platinum alloys: theory and experiment," *The Journal of Physical Chemistry B*, vol. 109, pp. 1198–1203, Jan. 2005.

[170] B. Hirschorn, B. Tribollet, and M. E. Orazem, "On selection of the perturbation amplitude required to avoid nonlinear effects in impedance measurements," *Israel Journal of Chemistry*, vol. 48, pp. 133–142, 2008.

[171] B. Hirschorn and M. E. Orazem, "On the sensitivity of the Kramers–Kronig relations to nonlinear effects in impedance measurements," *Journal of the Electrochemical Society*, vol. 156, no. 10, pp. C345–C351, 2009.

[172] G. Popkirov and R. Schindler, "A new approach to the problem of "good" and "bad" impedance data in electrochemical impedance spectroscopy," *Electrochimica Acta*, vol. 39, pp. 2025–2030, Sept. 1994.

[173] J. Giner-Sanz, E. Ortega, and V. Pérez-Herranz, "Total harmonic distortion based method for linearity assessment in electrochemical systems in the context of EIS," *Electrochimica Acta*, vol. 186, pp. 598–612, Dec. 2015.

[174] J. J. Giner-Sanz, E. M. Ortega, and V. Pérez-Herranz, "Optimization of the perturbation amplitude for impedance measurements in a commercial PEM fuel cell using total harmonic distortion," *Fuel Cells*, vol. 16, pp. 469–479, Feb. 2016.

[175] "Total harmonic distortion: Theory and practice." https://www.gamry.com/application-notes/EIS/total-harmonic-distortion/, Accessed: 02-Nov-2019.

[176] "THD: parameters affecting its value and comparison with other methods of linearity assessment.." https://www.bio-logic.net/wp-content/uploads/AN65{_}more{_}details{_}on-THD.pdf, Accessed: 02-Nov-2019.

[177] C. You, A. Dizon, M. Gao, V. Vivier, and M. E. Orazem, "Experimental observation of ohmic impedance," *Electrochimica Acta*, vol. 413, p. 140177, May 2022.

[178] T. von Kármán, "Über laminaire und turbulente reibung," *Zeitschrift für angewandte Mathematik und Mechanik*, vol. 1, pp. 233–252, 1921.

[179] W. G. Cochran, "The flow due to a rotating disc," *Proceedings of the Cambridge Philosophical Society*, vol. 30, pp. 365–375, 1934.

[180] S.-L. Wu, *Influence of Disk Electrode Geometry on Local and Global Impedance Response*. PhD thesis, University of Florida, Gainesville, FL, Aug. 2010.

[181] J. S. Newman, "Effect of ionic migration on limiting currents," *I & EC Fundamentals*, vol. 5, pp. 525–528, Nov. 1966.

[182] B. Tribollet and J. S. Newman, "The modulated flow at a rotating disk electrode," *Journal of the Electrochemical Society*, vol. 130, pp. 2016–2026, 1983.

[183] S. Havriliak and S. Negami, "A complex plane representation of dielectric and mechanical relaxation processes in some polymers," *Polymer*, vol. 8, pp. 161–210, Jan. 1967.

[184] M. Petrowsky and R. Frech, "Application of the compensated arrhenius formalism to dielectric relaxation," *The Journal of Physical Chemistry B*, vol. 113, pp. 16118–16123, Nov. 2009.

[185] W. Watson and M. E. Orazem, "EIS: Measurement model program," Sept. 2020.

[186] J. More, B. Garbow, and K. Hillstrom, "User guide for MINPACK-1. [in FORTRAN]," tech. rep., Argonne National Lab, Aug. 1980.

[187] P. Agarwal, M. E. Orazem, and L. H. García-Rubio, "Measurement models for electrochemical impedance spectroscopy: 1. Demonstration of applicability," *Journal of the Electrochemical Society*, vol. 139, pp. 1917–1927, July 1992.

[188] P. Agarwal, O. D. Crisalle, M. E. Orazem, and L. H. García-Rubio, "Measurement models for electrochemical impedance spectroscopy: 2. Determination of the stochastic contribution to the error structure," *Journal of the Electrochemical Society*, vol. 142, pp. 4149–4158, 1995.

[189] P. Agarwal, M. E. Orazem, and L. H. García-Rubio, "Measurement models for electrochemical impedance spectroscopy: 3. Evaluation of consistency with the Kramers–Kronig relations," *Journal of the Electrochemical Society*, vol. 142, pp. 4159–4168, 1995.

[190] G. J. Brug, A. L. G. van den Eeden, M. Sluyters-Rehbach, and J. H. Sluyters, "The analysis of electrode impedances complicated by the presence of a constant phase element," *Journal of Electroanalytical Chemistry*, vol. 176, pp. 275–295, 1984.

[191] M. E. Orazem, M. Durbha, C. Deslouis, H. Takenouti, and B. Tribollet, "Influence of surface phenomena on the impedance response of a rotating disk electrode," *Electrochimica Acta*, vol. 44, pp. 4403–4412, 1999.

[192] S. Wang, J. Zhang, O. Gharbi, V. Vivier, M. Gao, and M. E. Orazem, "Electrochemical impedance spectroscopy," *Nature Reviews Methods Primers*, vol. 1, June 2021.

[193] B. Tribollet and J. S. Newman, "Analytic expression for the warburg impedance for a rotating disk electrode," *Journal of the Electrochemical Society*, vol. 130, pp. 822–824, 1983.

[194] X. Tang, C. R. Ma, M. E. Orazem, C. You, and Y. Li, "Local electrochemical characteristics of pure iron under a saline droplet i: Effect of droplet size on electrochemical distribution," *Electrochimica Acta*, vol. 354, p. 136633, Sept. 2020.

[195] X. Tang, C. R. Ma, M. E. Orazem, C. You, and Y. Li, "Local electrochemical characteristics of pure iron under a saline droplet II: Local corrosion kinetics," *Electrochimica Acta*, vol. 354, p. 136631, Sept. 2020.

[196] S. Li and L. H. Hihara, "Atmospheric-corrosion electrochemistry of NaCl droplets on carbon steel," *Journal of The Electrochemical Society*, vol. 159, no. 11, pp. C461–C468, 2012.

[197] R. Avci, B. H. Davis, M. L. Wolfenden, L. R. Kellerman, K. Lucas, J. Martin, and M. Deliorman, "A practical method for determining pit depths using x-ray attenuation in EDX spectra," *Corrosion Science*, vol. 93, pp. 9–18, Apr. 2015.

BIOGRAPHICAL SKETCH

Chen You graduated with Bachelor of Science degree cum laude in chemical engineering at the University of Missouri-Columbia in May 2016 and received his Bachelor of Engineering degree in chemical engineering at the China University of Petroleum-Beijing in June 2016. During his undergraduate study, he won the Lloyd and Alfreida Macom Scholarship and has been an active member of the Tau Beta Pi. Chen came to the University of Florida in August 2016 and started his master's program in chemical engineering. He joined Professor Mark E. Orazem's research group in January 2017 and conducted his master's thesis project on the evaluation of the Gerischer impedance assumptions. During that time, he become a member of International Society of Electrochemistry and the Electrochemical Society. He earned Master of Science-thesis degree of chemical engineering from the University of Florida in May 2018.

In August 2018, he continued to stay in the Professor Mark E. Orazem's research group to pursue his doctorate degree in chemical engineering. His research focus on the experimental and simulation work on multiple electrochemical systems including development of a mathematical model for localized corrosion of copper, interpretation of impedance on QLED devices, and fundamental studies of several topics on electrochemical impedance spectroscopy. He served as Treasurer of Electrochemical Society Student Chapter and peer mentor for the course of impedance spectroscopy. He received several awards during his PhD studies. He received 240th ECS meeting Travel Award from Electrochemical Society, and Graduate Student Council Travel Award from University of Florida in Summer 2021. He also received Outstanding Achievement Merit Award from University of Florida in Fall 2021, First Place Student Oral Presentation Award at 23rd Grace Symposium from the Department of Chemical Engineering in Fall 2021, and Chemical Engineering PhD Research Excellence Award from the Department of Chemical Engineering in Spring 2022. He graduated with doctoral degree in chemical engineering from the University of Florida in August 2022.